

Dissertation zur Erlangung des Doktorgrades
an der Fakultät für Chemie und Pharmazie
der Ludwig-Maximilians-Universität München

Exploring the impact of structure directing agents on the synthesis and structure of imidazolate frameworks

von
Erik Andreas Flügel
aus
München, Deutschland

2015

ERKLÄRUNG

Diese Dissertation wurde im Sinne von § 7 der Promotionsordnung vom 28. November 2011 von Frau Prof. Dr. Bettina Lotsch von der Fakultät für Chemie und Pharmazie betreut.

EIDESSTATTLICHE VERSICHERUNG

Diese Dissertation wurde eigenständig und ohne unerlaubte Hilfe erarbeitet.

München, den 20.07.2015

.....

(Erik Flügel)

Dissertation eingereicht am 23.07.2015

1. Gutachter: Prof. Dr. Bettina Lotsch

2. Gutachter: Prof. Dr. Konstantin Karaghiosoff

Mündliche Prüfung am 08.09.2015

Copyrights

Parts of this work have been published or are under review in peer-reviewed journals and are subject to the following copyrights. They have been reproduced with permission of the corresponding publisher and have only been adapted with respect to the format of this thesis.

Surfactant-directed syntheses of mesostructured zinc imidazoles: formation mechanism and structural insights

E. A. Flügel, M. T. Aronson, S. C. Junggeburth, B. F. Chmelka and B. V. Lotsch, *CrystEngComm*, **2015**, 17, 463-470. DOI: 10.1039/C4CE01512F

Copyright © 2015 Royal Society of Chemistry

Homonuclear mixed-valent cobalt imidazolate framework for oxygen evolution electrocatalysis

E. A. Flügel, V. W.-h. Lau, H. Schlömmberg, R. Glaum and B. V. Lotsch, *J. Mater. Chem. A* **2015**, submitted.

Copyright © 2015 Royal Society of Chemistry

Synthetic routes toward MOF nanomorphologies

E. A. Flügel, A. Ranft, F. Haase and B. V. Lotsch, *J. Mater. Chem.* **2012**, 22, 10119-10133.

Copyright © 2012 Royal Society of Chemistry

Danksagungen

...Prof. Bettina Lotsch, welche mir die Anfertigung dieser Arbeit erst ermöglicht hat. Vielen Dank für die Aufnahme in die Gruppe und die konstanten, konstruktiven Diskussionen, welche die Arbeit zu dem gemacht haben, was sie heute ist.

...Prof. Konstantin Karaghiosoff für die Übernahme des Zweitgutachtens.

...Prof. D. Fattakhova-Rohlfing, Prof. O. Oeckler, Prof. D. Johrendt und Prof. C. Scheu für den Beisitz in der mündlichen Prüfung.

...Viola Duppel für die vielen SEM und TEM Messungen von Proben mit denen ich dich teilweise überschüttet habe.

...Christian Minke für zahlreiche EDX/SEM/Festkörper-NMR Messungen.

...Hartmund Hartl und Marie Luise Schreiber für ICP-Messungen.

...Christine Neumann, Peter Meyer und Prof. K. Karaghiosoff für Lösungs-NMR Messungen.

...Dr. Sophia Mankowski und Daniel Weber für DTA-TG Messungen.

...Wolfgang Wünschheim für konstanten IT-Support.

...allen Mitgliedern des AK-Johrendt und AK-Schnick für Wandertage, gemeinsame Pokerabende und die netter Atmosphäre.

...der, mittlerweile leider nicht mehr existenten, Kochgruppe für das gute Essen und die netten Gespräche: Florian Pucher, Dominik Baumann, Stephan Werner, Alexy Marchuk, Sebastian Junggeburch, Linus Stegbauer und Eva Wirnhier.

...dem gesamten AK-Lotsch, egal ob in Stuttgart oder München, aktuell oder schon gegangen. Die Zeit mit euch war großartig. Vielen, vielen Dank: Leo Diehl, Viola Duppel, Roland Eger, Primin Ganter, Kerstin Gottschling, Frederik Haase, Willi Hölle, Tanja Holzmann, Claudia Kamella, Prof. Jürgen Köhler, Vicent Lau, Claudia Lermer, Filip Podjaski, Hendrik Schlomberg, ...

... Marie-Luise Schreiber, Katharina Schwinghammer, Linus Stegbauer, Katalin Szendrei, Brian Tuffy, Olaf Alberto von Mankowski, Vijay Vyas, Christian Ziegler, Annkathrin Ranft, Friedrich Kögel, Olalla Sánchez-Sobrado, Ida Pavlichenko, Stephan Hug, Stephan Werner, Alexander Kuhn, Sebastian Junggeburth, Cheng Li und Hongji Wang.

...der Skatrunde für die kleinen Pausen zwischendurch.

...Albi fürs Korrekturlesen der vielen Kapitel. Es ist echt beeindruckend was du alles an Fehlern findest.

...Basti für die Einführung in das Thema und die Projekte welche du mir vererbt hast.

...meinen Laborkollegen über die Zeit in D2.049 und D2.102 für die schön Zeit: Stebbo, Linus, Anna, Albi, Basti, Ida, Katalin, Erwin, Christine und Tobi.

...meinen Praktikanten ohne die ich das alles nicht geschafft hätte. Die Arbeit mit euch hat viel Spaß gemacht: Stephan Gleich, Robert Dejak, Hendrik Schlomberg, Sabrina Rager, Cornelia Unger, Philipp Strobel, Evgeniia Shlaen und Jasmin Dums.

...meiner Familie für die Unterstützung während des Studiums. Wenn ihr mit den Rücken nicht so frei gehalten hättet und auch in schwereren Zeiten für mich da gewesen wärt, hätte ich das alles nicht geschafft.

...meiner Partnerin Claudia welche lange Abende ohne mich verbringen musste und viel Stress mit abgekriegt hat. Ich hoffe du weißt, dass ich dich nie wieder gehen lassen möchte.

Abstract

This thesis describes the synthesis and characterisation of a plethora of coordination polymers and metal-organic frameworks, that are based on syntheses assisted by surfactants. The effects of surfactants on the formation of coordination polymers can be manifold and range from size confinement effects to structural reorganisation on the mesoscale as well as the crystal lattice itself.

Detailed investigation of the atomic and supramolecular structure of most coordination polymers is hindered, due to the low crystallinity and scattering-cross section of the predominantly organic materials. A combination of X-ray powder diffraction, solid-state NMR spectroscopy, elemental analysis, electron spectroscopy (SEM, TEM, EDX) and atomic force microscopy were utilized in this work, in order to develop structural models of the synthesized materials.

In chapter 4 of this work, the synthesis of MIFs with gemini surfactants is explored, in order to investigate the effects of surfactant charge density and geometry on the formed structures. Whilst previous results showed that changes in the length of the used surfactants do not translate into changes of the geometry of obtained mesostructures, the question whether or not cubic or hexagonal mesostructures of zeolitic imidazolate frameworks (ZIFs) are accessible via microemulsion synthesis remained unanswered. The experiments presented in chapter 4 are addressing this issue by using gemini-surfactants in order to control charge density and geometry of the used surfactants to a higher degree as compared to single chain-surfactants, such as the previously used CTAB. Whilst the synthesis of cubic or hexagonally mesostructured materials was not successful, the experiments provided improved understanding of the formation mechanism of MIFs, which are formed due to the presence of halogenides during the microemulsion synthesis. Whilst a plethora of lamellar structured mesostructured imidazolate frameworks (MIFs) with different spacings, however identical inner-layer structure, are accessible this way, the proposed formation mechanism also provides explanation, to why the used surfactants need to be altered with regard to the used counter-ion in order to suppress the formation of the lamellar MIFs in favor for differently structured mesomaterials.

In another application of surfactant assisted synthesis procedures, the known two-dimensional poly[μ_2 -acetato- μ_2 -benzimidazolato zinc(II)] coordination polymer could previously be exfoliated in our group in a one-pot synthesis approach. In chapter 5, this thesis reports advances in the synthesis of functionalized analogs carrying nitro- or amine-groups and the subsequent use of the

amine-group in post-synthetic modification reactions with isocyanates. Through IR, solid-state NMR and fluorescence measurements, the chemical accessibility of the functional groups was shown.

In chapter 6 the effects of bromine-free surfactants to overcome the formation of MIFs, as discussed in chapter 4, are shown. Without the presence of halogenides in the microemulsion synthesis, neither the commonly obtained ZIFs nor the lamellar mesostructured MIFs are formed, but instead a crystalline material with a general composition of $\text{Zn}(\text{Im})_2$ is obtained. The material features a complex crystal structure consisting of helical chains as one main feature and was previously solely accessible via hydrothermal synthesis. The hydrothermally obtained $\text{Zn}(\text{Im})_2 \cdot \text{H}_2\text{O}$ exhibits no accessible porosity due to the retained solvent in the microporous material. Whilst the analogue obtained *via* microemulsion synthesis show significantly decreased solvent contents, even taking the increased dynamic radius of iso-propanol compared to water into account, at a composition of $\text{Zn}(\text{Im})_2 \cdot 0.1 \text{ C}_3\text{H}_8\text{O}$, the pore system is still blocked due to the contained solvent.

In chapter 7 the synthesis and characterization of the first mixed-valent, purely cobalt-based zeolitic imidazolate framework, $\text{Co}^{\text{II}}_3\text{Co}^{\text{III}}_2(\text{C}_3\text{H}_3\text{N}_2)_{12}$, is presented. The material, which was obtained in a surfactant assisted microwave-synthesis, adopts the cubic garnet-type structure and combines high thermal stability of up to 350 °C with excellent chemical stability. The existence of mixed-valent cobalt in the structure was confirmed using UV/VIS and XPS measurements. Electrochemical characterization shows that the cobalt centres are redox active and efficiently support oxygen evolution, thus rendering this framework a potential candidate as a single-site heterogeneous catalyst based on earth-abundant elements.

In the final chapter of this work, an overview over MOF nanostructuring techniques is given in form of a review. Whilst surfactant based nanoparticle syntheses are one part of this chapter, the discussed techniques and results are extending beyond surfactant based techniques and cover topics such as oriented growth of MOFs on substrates, layer-by-layer MOF deposition or microfluidic synthesis approaches. This diversity of synthesis techniques that are available to scientists striving for nano- and mesostructured coordination frameworks, highlights the huge potential for new discoveries that is present today in this field of research.

Contributions

E. Flügel, M. T. Aronson, S. Junggeburth, B. F. Chmelka and B. V. Lotsch, "Surfactant-directed syntheses of mesostructured zinc imidazoles", *CrystEngComm*, 2015, 17, 463–470.

This project was based on previous work performed by Sebastian Junggeburth in our group. He was able to synthesize a new class of materials, the so called "mesostructured imidazolate frameworks" (MIFs) *via* a microemulsion synthesis approach. These materials are composed of one dimensional $\text{ZnBr}_2(\text{Im})_{2/2}$ chains, that arrange into two-dimensional sheetlike structures which are in turn intercalated by the used surfactant (CTAB). Following up on this work, I was able to extend the range of known materials by using gemini-surfactants, which offer increased control over important surfactant parameters such as surfactant geometry, charge density of critical micelle concentration. By altering the used surfactant, I was able to prove that the unusual structure of MIFs is a direct product of the presence of bromide ions during the reaction, which are present in all used surfactants for charge compensation.

In collaboration with Prof. Chmelka's group at UCSB, Matthew Aronson performed 2D solid-state NMR measurement on MIFs structured by CTAB, in order to shed light on the local structure of the material. Due to observed interactions between the surfactant and the imidazolate backbone of the chain-like structures, the previously proposed structure model for MIFs could be confirmed. By combining these results with detailed analytical efforts, a structure model for the new variants of MIFs, including the complex geometry of the gemini surfactants, could be developed. The results published in this paper are a substantial step towards understanding the formation of mesostructured derivatives of zeolitic imidazolate frameworks (ZIFs) and thereby towards ZIFs and MOFs with hierarchical pore structures obtained via templating, in general. I wrote the manuscript regarding the characterization of the MIF materials and the proposed structure model, whilst Matthew contributed the parts of the manuscript about the performed 2D solid-state NMR measurements.

E. Flügel, S. Junggeburth "Introducing functionality into 2D exfoliable Metal-Organic Frameworks", Chapter 5, unpublished results.

In this part of the thesis, experiments revolving around the 2D exfoliable Metal-Organic frameworks discovered by Sebastian Junggeburth are discussed. Sebastian was able to synthesize $\text{Zn}[\text{Belm}]\text{OAc}$ as well as provide detailed insight into an exfoliation procedure for this material,

relying on a microemulsion approach. He could additionally synthesize the functionalized analoga $\text{Zn}[\text{NO}_2\text{-Belm}]\text{OAc}$ and $\text{Zn}[\text{NH}_2\text{-Belm}]\text{OAc}$ via solid-state synthesis procedures, yet was unable to adapt the microemulsion based approach and the subsequent exfoliation to the functionalized materials. I was able to synthesize both functionalized analoga, as well as $\text{Zn}[\text{Belm}]\text{OPr}$ and $\text{Zn}[\text{Belm}]\text{OBut}$ via microemulsion based synthesis procedures. Subsequent exfoliation attempts yielded nanosheets of $\text{Zn}[\text{NO}_2\text{-Belm}]\text{OAc}$ and $\text{Zn}[\text{Belm}]\text{OPr}$, which were previously unknown. Additional experiments regarding the chemical accesibily of the amine-group in $\text{Zn}[\text{NH}_2\text{-Belm}]\text{OAc}$ were performed in order to investigate if the material is a suitable candidate for postsynthetic modification reactions. Experimental work could show that the amine-groups are indeed reactive and can undergo coupling reactions with isocyanates, such as phenylisocyanat. In subsequent experiments with the fluorescence marker 4-(6-Methyl-2-benzothiazolyl)phenyl isocyanate, I was able to synthesize a fluorescent framework derived from $\text{Zn}[\text{NH}_2\text{-Belm}]\text{OAc}$.

E. Flügel, P. Strobl, "Microemulsion Synthesis of $\text{Zn}(\text{Im})_2$ ", Chapter 6, unpublished results.

The synthesis of $\text{Zn}(\text{Im})_2$ via microemulsion synthesis was first performed by Phillip Strobl as part of an internship under my supervision. With these experiments we were able to develop a technically less challenging synthesis procedure towards $\text{Zn}(\text{Im})_2$, a material that was previously only accessible via hydrothermal synthesis approaches. Philip performed the characterization of the material via pXRD, IR and solid-state NMR measurments under my supervision. The chapter was written by me.

E. Flügel, V. Lau, H. Schlomberg, R. Glaum and B. V. Lotsch, "Homonuclear mixed-valent cobalt imidazolate framework for oxygen evolution electrocatalysis", *Chem Eur J*, 2015, submitted.

The synthesis protocol for this publication were devoloped by Hendrik Schlomberg as part of an internship under my supervision. Hendrik was able to synthesize the material and determine the crystal structure via powder XRD measurements as well as confirm the purity through IR and elemental analysis. Due to the complex structure of the materials with mixed-valent metal-modes, I performed further analysis including rietveld refinement of the structure based on powder XRD data and XPS measurements in order to investigate the oxidation state of the metal-nodes. Whilst XPS data already indicated the presence of mixed-valent cobalt in the structure, UV/VIS measurements performed by Prof. Glaum were able to prove the coexistence of Co^{2+} and Co^{3+} in the structure.

The electrochemical characterization of the material was performed by Vincent Lau, who could show that $\text{Co(II)}_3\text{Co(III)}_2(\text{Im})_{12}$ is suitable as electrocatalyst for the oxygen evolution reaction. With activities comparable to Co_3O_4 , this ZIF is one of only two known MOFs known to date, capable of catalysis of this reaction. In additional experiments, Vincent was able to prove long-term stability of the materials without loss of the catalytic properties. I wrote the manuscript that was published together with Vincent Lau, resulting in my first authorship of this paper.

E. Flügel, A. Ranft, F. Haase and B. V. Lotsch, "Synthetic routes toward MOF nanomorphologies", *J. Mater. Chem.*, 2012, 22, 10119-10133.

The invited review "Synthetic routes towards MOF nanomorphologies" was a collaborative effort between Annkathrin Ranft, Frederik Haase and myself. Whilst extensive literature research for this paper as well as the selection of figures and graphs for illustration purposes was performed in cooperation between all authors, most of the writing was performed by me which was recognized through first authorship of this paper.

LIST OF ABBREVIATIONS

All physical units agree with the International System of Units (SI).

Å	Ångström, 10^{-10} m
AFM	Atomic force microscopy
ATR	Attenuated total reflection (IR spectroscopy)
OBut	Butyric acid
calc.	calculated
C	Carbon
°C	Temperature in degree Celsius
cm	Centimeters
cm^{-1}	Wavenumbers
d	Days
DMF	Dimethylformamide
DTA-TG	Differential Thermal/Thermogravimetric Analysis
EDX	Energy-dispersive X-ray spectroscopy
<i>et al.</i>	<i>et alii</i> ; And others
eV	Electron volts
exp	experimental
g	Grams
h	Hours
IR	Infrared
L	Liters
LMU	Ludwig Maximilians University
MS	Mass Spectrometry
MIF	Mesostructured Imidazolate Framework
min	Minutes
mL	Milliliters, 10^{-3} L
μL	Microliters, 10^{-6} L
mm	Millimeters, 10^{-3} m
μm	Micrometers, 10^{-6} m
mmol	Millimols
MOF	Metal Organic Framework
nm	Nanometers, 10^{-9} m
NMR	Nuclear magnetic resonance
OAc	Acetyl
OPr	Propionic acid
ppm	Parts per million

pXRD	Powder X-ray diffraction
rpm	Revolutions per minutes
TEM	Transmission electron microscopy
SEM	Scanning electron microscopy
wt%	Weight percent
ZIF	Zeolitic Imidazolate Framework

TABLE OF CONTENTS

1	INTRODUCTION.....	1
1.1	POROUS MATERIALS	1
1.2	ZEOLITES.....	2
1.3	ZEOLITIC IMIDAZOLATE FRAMEWORKS (ZIF)	3
1.4	METAL-ORGANIC FRAMEWORKS (MOF).....	5
1.5	MESOPOROUS MATERIALS	8
1.5.1	TEMPLATING MECHANISMS.....	8
1.5.2	MESOPOROUS SILICA	10
1.5.3	GEMINI SURFACTANTS	11
1.5.4	TEMPLATING ON METAL-ORGANIC FRAMEWORKS	12
1.5.5	MESOSTRUCTURING OF ZEOLITIC IMIDAZOLATE FRAMEWORKS	13
1.6	POST-SYNTHETIC MODIFICATION OF METAL-ORGANIC FRAMEWORKS	14
2	CHARACTERIZATION METHODS.....	17
2.1	POWDER X-RAY DIFFRACTION (XRD).....	17
2.2	INFRARED SPECTROSCOPY (IR)	18
2.3	DIFFERENTIAL THERMAL/THERMOGRAVIMETRIC ANALYSIS (DTA-TG).....	19
2.4	ELEMENTAL ANALYSIS: CHNS AND INDUCTIVELY COUPLED PLASMA ATOMIC EMISSION SPECTROSCOPY (ICP-AES).....	19
2.5	ELECTRON MICROSCOPY	20
2.5.1	TRANSMISSION ELECTRON MICROSCOPY (TEM)	20
2.5.2	SCANNING ELECTRON MICROSCOPY (SEM) AND ENERGY-DISPERSIVE X-RAY SPECTROSCOPY (EDX) .	21
2.6	NUCLEAR MAGNETIC RESONANCE (NMR) SPECTROSCOPY	21
2.6.1	SOLUTION NMR SPECTROSCOPY.....	21
2.6.2	SOLID-STATE NMR SPECTROSCOPY ^[171, 172]	22
2.7	ULTRAVIOLETT-VISIBLE (UV-Vis) SPECTROSCOPY	22
2.8	ATOMIC FORCE MICROSCOPY (AFM) ^[173]	23
2.9	MASS SPECTROMETRY (MS)	24
3	OPERATIVE PROCEDURES.....	27
3.1	ORBITAL SHAKER	27
3.2	ULTRASONIC BATH.....	27
3.3	MICROWAVE	27

3.4	CENTRIFUGE	27
3.5	SPIN COATING	27
3.6	CHEMICALS	28
4	SURFACTANT-DIRECTED SYNTHESSES OF MESOSTRUCTURED ZINC IMIDAZOLATES	31
4.1	ABSTRACT	31
4.2	INTRODUCTION	32
4.3	EXPERIMENTAL SECTION	34
4.3.1	REAGENTS & INSTRUMENTS.....	34
4.3.2	SYNTHESIS OF GEMINI SURFACTANTS	34
4.3.3	SYNTHESIS OF MESOSTRUCTURED IMIDAZOLATE FRAMEWORKS	35
4.4	RESULTS AND DISCUSSION	35
4.5	CONCLUSIONS.....	44
4.6	ACKNOWLEDGEMENTS	45
5	INTRODUCING FUNCTIONALITY INTO 2D EXFOLIABLE COORDINATION FRAMEWORKS	47
5.1	INTRODUCTION	47
5.2	MODIFICATION OF THE ACETATE GROUPS.....	49
5.2.1	ZN[BEIM]OPR	50
5.2.2	ZN[BEIM]OBUT	55
5.3	MODIFICATION OF THE BENZIMIDAZOLATE GROUP.....	59
5.3.1	ZN[NO ₂ -BEIM]OAC	59
5.3.2	ZN[NH ₂ -BEIM]OAC	63
5.3.3	ZN[NO ₂ -BEIM] _{1-x} [NH ₂ -BEIM] _x OAC - MIXED LINKER SYNTHESSES.....	67
5.4	EXFOLIATION ATTEMPTS	71
5.4.1	BEIM-MIF(OPR)	72
5.4.2	BEIM-MIF(OBUT)	73
5.4.3	NO ₂ -BEIM-MIF(OAC).....	75
5.4.4	NH ₂ -BEIM-MIF(OAC).....	77
5.4.5	ZN(NO ₂ -BEIM) _{1-x} (NH ₂ -BEIM) _x OAC - MIXED LINKER SYNTHESSES.....	78
5.5	POST-SYNTHETIC MODIFICATION OF AMINE-GROUP CONTAINING LINKERS.....	80
5.6	CONCLUSION	84
5.7	EXPERIMENTAL DETAILS	86
5.7.1	SYNTHESIS OF ZN(C ₄ H ₇ O ₂) ₂	86

5.7.2	SOLUTION BASED SYNTHESIS OF BEIM-MIF(R), R = PRO, BUTO.....	86
5.7.3	SOLID-STATE SYNTHESIS OF [ZN(BEIM)OBUT]	86
5.7.4	SOLUTION BASED SYNTHESIS OF BEIM-MIF(R), R = PRO, BUTO WITH CTAB FOR EXFOLIATION.....	86
5.7.5	POST-SYNTHETIC MODIFICATION OF ZN[NH ₂ -BEIM]OAC WITH PHENYLISOCYANATE	87
6	MICROEMULSION SYNTHESIS OF ZN(IM)₂	89
6.1	EXPERIMENTAL DETAILS	89
6.1.1	MICROEMULSION ROUTE	89
6.1.2	SOLVOTHERMAL ROUTE	90
6.2	XRD POWDER DIFFRACTION AND STRUCTURAL DISCUSSION	90
6.3	INFRARED SPECTROSCOPY	92
6.4	ELEMENTAL ANALYSIS	92
6.5	SOLID-STATE NMR SPECTROSCOPY	93
6.6	THERMAL ANALYSIS	94
6.7	SCANNING ELECTRON MICROSCOPY	95
6.8	DISCUSSION.....	96
7	HOMONUCLEAR MIXED-VALENT COBALT IMIDAZOLATE FRAMEWORK FOR OXYGEN EVOLUTION ELECTROCATALYSIS.....	97
7.1	ABSTRACT	97
7.2	INTRODUCTION	FEHLER! TEXTMARKE NICHT DEFINIERT.
7.3	EXPERIMENTAL DETAILS	FEHLER! TEXTMARKE NICHT DEFINIERT.
7.4	RESULTS AND DISCUSSION	FEHLER! TEXTMARKE NICHT DEFINIERT.
7.5	CONCLUSIONS.....	FEHLER! TEXTMARKE NICHT DEFINIERT.
7.6	ACKNOWLEDGEMENTS	105
8	SYNTHETIC ROUTES TOWARD MOF NANOMORPHOLOGIES	107
8.1	ABSTRACT	107
8.2	INTRODUCTION	107
8.3	ZERO-DIMENSIONAL NANOSTRUCTURES	109
8.3.1	SONOCHEMICAL AND MICROWAVE-ASSISTED SYNTHESIS.....	109
8.3.2	MICROEMULSION SYNTHESIS	111
8.3.3	INTERFACIAL SYNTHESIS	112
8.4	ONE-DIMENSIONAL NANOSTRUCTURES	114
8.4.1	SURFACTANT-ASSISTED SYNTHESIS IN REVERSE MICROEMULSIONS.....	114
8.4.2	INTERFACIAL CONTROL IN A MICROFLUIDIC ENVIRONMENT	115

8.4.3	COORDINATION MODULATORS.....	116
8.4.4	GROWTH TEMPLATES	118
8.5	TWO-DIMENSIONAL NANOSTRUCTURES	120
8.5.1	DEPOSITION OF MOF COLLOIDS.....	120
8.5.2	GEL-LAYER APPROACH.....	121
8.5.3	LAYER-BY-LAYER GROWTH (LIQUID PHASE EPITAXY)	122
8.5.4	TOP-DOWN FABRICATION.....	124
8.6	HYBRID NANOMORPHOLOGIES.....	126
8.6.1	CORE-SHELL PARTICLES.....	127
8.6.2	MOF-ON-MOF HETEROEPITAXY.....	128
8.7	MECHANISTIC INSIGHTS AND DIMENSION CONTROL – A CASE STUDY	130
8.7.1	GROWTH MECHANISM OF ZIF-8 NANOPARTICLES.....	130
8.7.2	MORPHOLOGY CONTROL OF ZIF-7 NANOSTRUCTURES.....	132
8.8	CONCLUSION	133
8.9	ACKNOWLEDGEMENT.....	134
9	APPENDIX	135
9.1	CHAPTER 4 - SUPPORTING INFORMATION	135
9.2	CHAPTER 5 - SUPPORTING INFORMATION	149
9.3	CHAPTER 6 - SUPPORTING INFORMATION	151
9.4	CHAPTER 7 - SUPPORTING INFORMATION	153
9.4.1	EXPERIMENTAL PROCEDURES	153
9.4.2	STRUCTURE ELUCIDATION	155
10	REFERENCES	165

1 INTRODUCTION

1.1 POROUS MATERIALS

Porous materials have been a focus of research interests due to their numerous applications across a broad range of technologies such as catalysis,^[1] adsorption,^[2, 3] gas separation and purification,^[2, 4] drug delivery,^[5, 6] electrode materials^[7-9] and supercapacitors^[10, 11] as well as sensoric devices.^[12-14]

This broad range of applications puts high requirements on the pore systems of the created material with respect to pore size as well as pore shape. Whilst most gas separation applications rely on narrow pore size distributions and small pore diameters for the purpose of ensuring strong interactions with the guest molecules, catalysis is usually based on larger pores to allow the reactants to diffuse into the pore space and perform the reactions within the confined space of the pore.

In order to distinguish and categorize different pore sizes, the International Union of Pure and Applied Chemistry (IUPAC) introduced a classification system of three groups.^[15] Microporous materials, such as zeolites, exhibit pores with diameters below 2 nm which are well suited for gas adsorption or ion exchange based applications. Mesoporous materials, such as mesostructured silica materials, feature pores ranging from 2 to 50 nm, enabling good diffusion possibilities in combination with decent host-guest interactions as required for catalysis, whilst macroporous materials, such as sponges or bio-foams, show pores with diameters larger than 50 nm. (Fig. 1.1.1)

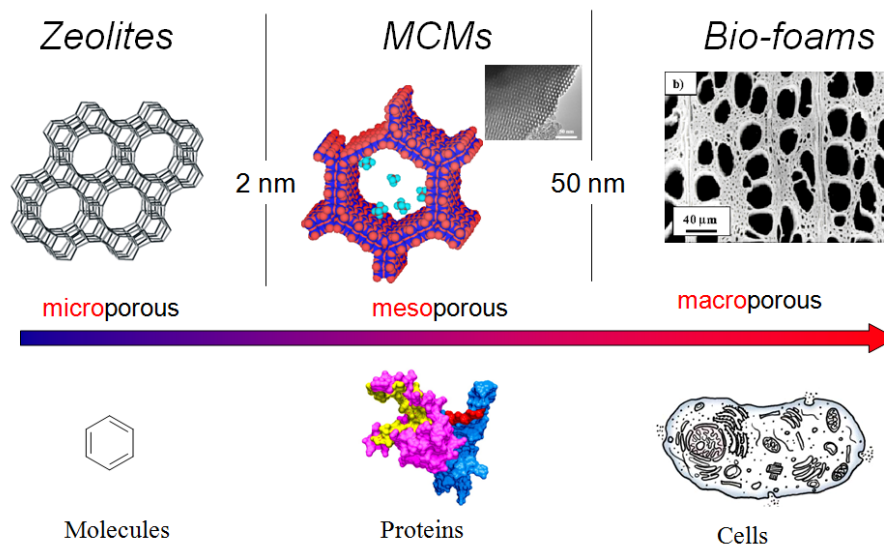


Figure 1.1.1: Classification of porous materials based on pore sizes as proposed by IUPAC.^[16]

1.2 ZEOLITES

Zeolites are amongst the industrially most commonly used microporous materials due to their high thermal and chemical stability as well as the vast variety of available structural motifs, pore sizes and shapes. In 1756 the porosity of zeolites was first observed when Axel F. Cronstedt discovered the water capturing capabilities of stilbite, a naturally occurring mineral.^[17] Upon heating the mineral, water vapor is released from the material, leading Cronstedt to name the material zeolite, from the greek words ζέω (*zéō*), meaning "to boil" and λίθος (*lithos*), meaning "stone". The reason for the observed water sorption capability of the material was not discovered until almost 200 years later, when in 1930, Taylor and Pauling were able to provide a structure solution of stilbite. The XRD analysis revealed a structure built up of corner- and edge-sharing $[\text{SiO}_4]$ and $[\text{AlO}_4]$ tetrahedra, featuring channels and cavities with diameters ranging from 3 to 15 Å.^[18, 19] Following up on the structure solutions of natural occurring zeolites, Barrer and Milton were able to synthesize zeolites with new structures, not found amongst the 48 naturally occurring zeolites, using hydrothermal synthesis conditions.^[20-22] In 1950 zeolite X, a material isotypic with faujasite, was first synthesized which led to important industrial applications of zeolites such as air separation and purification as well as fluidized catalytic cracking of high-molecular weight fractions of petroleum crude oils into gasoline and olefinic gases.^[23] In order to further broaden the range of available stable, porous materials, various other zeolite-like materials (zeotypes) have been synthesized by replacing silicon and aluminum in the structures with phosphate, creating (silico-)-aluminophosphates.^[24] Up to today more than 150 synthetic zeolite structures have been discovered.^[25]

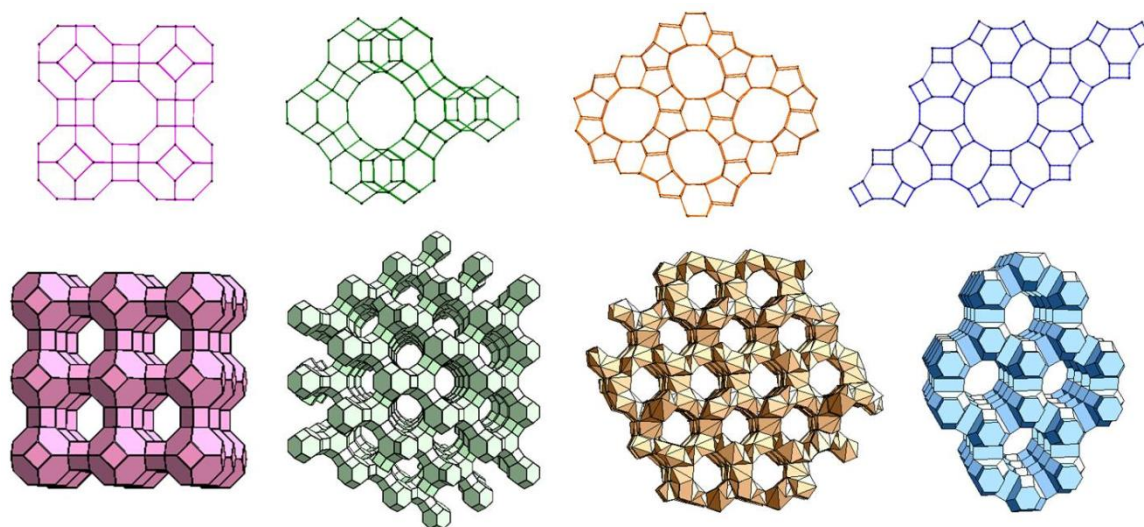


Figure 1.2.1: Variety of naturally occurring zeolite structures, showcasing the huge structural variability of the materials.^[26]

Despite all zeolite structures sharing the same building blocks and principles as mentioned before, the variety of structures formed by different connection patterns of the $[\text{SiO}_4]$ and $[\text{AlO}_4]$ tetrahedra enables the materials to form specific Lewis- and Brønsted-acid cation exchange centers, enabling zeolites to act as catalysts in numerous possible acid-catalyzed reactions. Applications today – apart from heterogeneous acid catalysis^[27, 28] – include the use as ion exchange materials^[29], heat storage applications^[30] or various uses in medicine for drug delivery or magnetic resonance imaging.^[31–33] Additional applications as biological carriers due to protein absorption,^[34] chemical sensors^[5], as materials in photovoltaic devices^[35] and for gas storage^[36–38] have been explored.

1.3 ZEOLITIC IMIDAZOLATE FRAMEWORKS (ZIF)

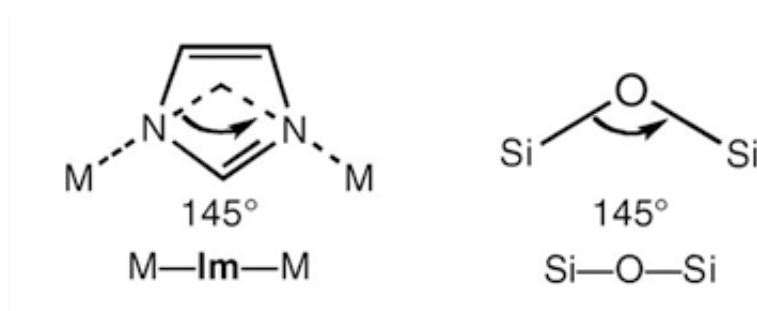


Figure 1.3.1: Binding angles found in zeolitic imidazolate frameworks (left) and zeolites (right).

The utilization possibilities that arise from the structures of zeolites can be extended beyond the substitution of silica or alumina, by altering the chemical compositions of the materials. Zeolite structures can be mimicked by so-called zeolitic imidazolate frameworks (ZIF),^[39] which are a subclass of MOFs featuring more than 100 different topologies composed of M^{2+} -ions ($\text{M} = \text{Zn}, \text{Co}, \text{Cu}$) bridged

by organic imidazoles.^[40] These similarities are based on the geometry of the metal-imidazolate-metal coordination featuring a binding angle of 145° , which is very similar to the Si-O-Si binding angle found in zeolites. (Fig. 1.3.1) The structural variety of ZIFs comprises most known zeolite structures,^[41, 42] yet is not limited to those as other structural motifs such as garnet structures could also be created.^[43] (Fig. 1.3.2)

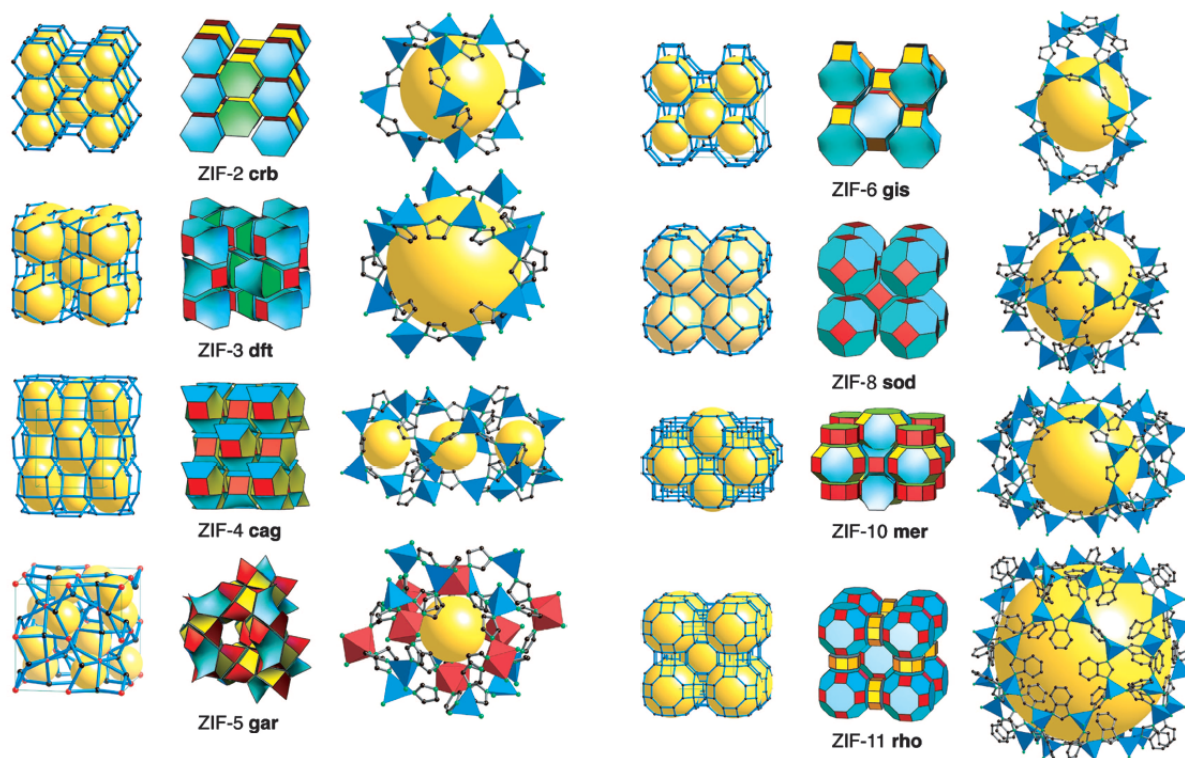


Figure 1.3.2: Structural diversity of zeolitic imidazolate frameworks, including zeolite and non-zeolite framework topologies. Taken from [42] with permission. Copyright (2006) National Academy of Sciences, U.S.A.

Taking the comparably weak coordinative interactions between linkers and nodes into account, ZIFs show remarkable thermal stability up to 550°C .^[42] Stability under reflux conditions in various solvents for extended periods of time without thermal decomposition was also demonstrated on ZIF-8 ($\text{Zn}(\text{MeIM})_2$, sodalite topology, sod) and ZIF-11 ($\text{Zn}(\text{BeIM})_2$, rho), making ZIFs one of the most robust coordination frameworks known.^[41] Additional applications of ZIFs revolve around the exceptionally high CO_2 uptake and selectivity of many known ZIF-materials, which could be demonstrated on ZIF-69 [$\text{Zn}(\text{Cl-BeIM})(2\text{-NO}_2\text{-IM})$; Cl-BeIM = 5-chlorobenzimidazole, 2- $\text{NO}_2\text{-Im}$ = 2-nitroimidazole], a material exhibiting gmelinite (gme) structure, which is capable of storing 83 liters CO_2 per liter ZIF-69 at 273 K under ambient pressure.^[42] Selectivity with regards to gas uptake has been shown on various ZIF-materials, such as modified ZIF-8, going up to a selectivity for CO_2/N_2 of 23 at 0.1 bar.^[44] Apart from applications such as gas selective membranes to separate H_2 or CO_2 from N_2 ,^[45, 46] sensor devices comprising ZIF-8 and TiO_2 nanoscale layers, yielding color-tunable photonic crystals that can

selectively detect gases due to changes in the effective refractive indices of the constituent materials upon gas adsorption, have been built.^[14, 47] Furthermore, uses in medical applications for drug delivery have been explored by encapsulation of organic molecules such as caffeine into ZIF-7^[48] or by incorporation of fluorescence markers for medical imaging.^[49]

1.4 METAL-ORGANIC FRAMEWORKS (MOF)

As mentioned previously, ZIFs are a subclass of metal-organic frameworks (MOFs), a family of hybrid organic-inorganic materials consisting of crystalline networks of metal-ions or clusters, coordinatively bridged by organic linkers. Despite the first MOF prototypes being known since 1965,^[50] their full potential was not recognized until Yaghi and co-workers systematically revived and extended this class of materials and named them MOFs in 1995.^[51]

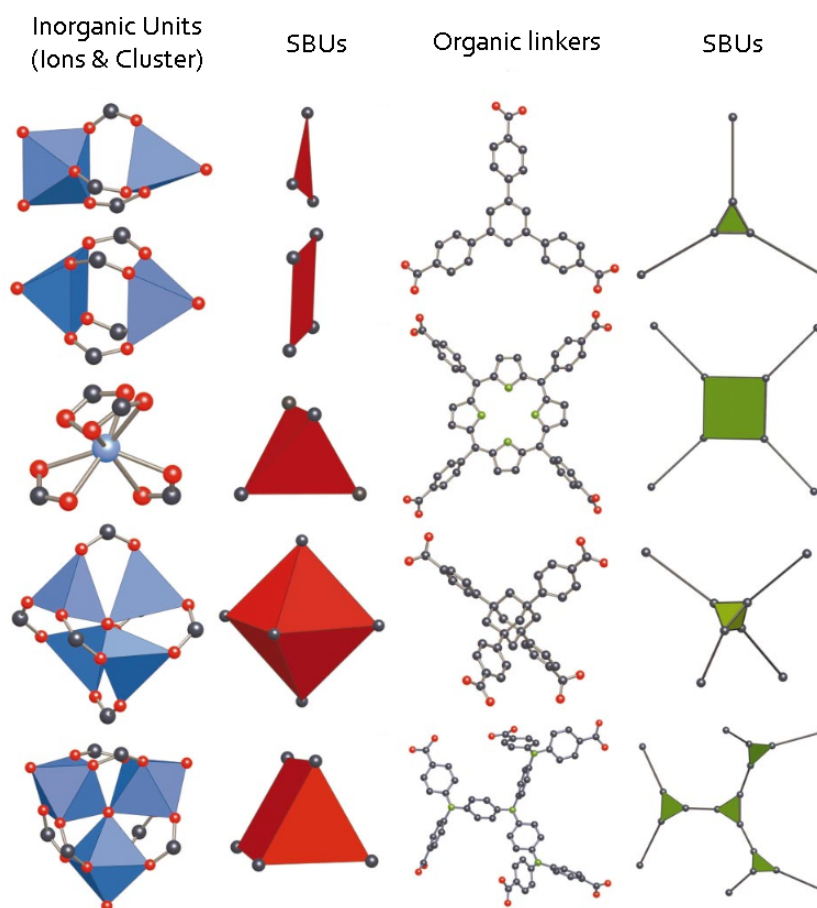


Figure 1.4.1: From left to right: inorganic units found in MOF topologies and their respective secondary building units (SBUs), organic linkers used in MOF synthesis and their respective SBUs. Reprinted with permission from Macmillan Publishers Ltd: Nature 2003, 423, 705., copyright 2015.

MOFs are a subclass of coordination polymers, three-dimensional periodic networks exhibiting permanent accessible porosity as well as a crystalline structure. They consist of inorganic units such

as metal ions and/or clusters, which are connected by two-, three-, four- or six fold coordination of the metal centers with different polytopic organic linkers (mono-, di-, tri- or tetravalent ligands), leading to a huge variety of structural motifs. The used organic linkers and metal nodes can be simplified into secondary building units (SBUs), based on their connectivity. (Fig. 1.4.1) By combining SBUs featuring certain geometries, the resulting structure of the obtained MOF material can be readily predicted, enabling rational design approaches to MOF materials. This rational synthesis approach is exemplified by a series of materials - the so-called isorecticular MOFs (IRMOFs) - which feature identical network topologies with vastly varying chemical and physical properties, such as pore size, hydrophobicity or reactivity. Yaghi *et al.* demonstrated the possibility to use 16 different linkers having the same SBU, in a MOF synthesis, while retaining the network topology.^[52] Starting from MOF-5 (also referred to as IRMOF-1), a structure consisting of a cubic network of zinc oxo clusters, sixfold coordinated by terephthalic acid, Yaghi used functionalized terephthalic acid linkers carrying organic groups such as -Br, -NH₂, -OC₃H₇ or -C₂H₅ to show the possibility to alter material properties such as hydrophobicity, pore size, or reactivity. By expanding the used dicarbonate linkers with long molecular struts such as biphenyl, tetrahydropyrene and terphenyl, they were able to increase the observed pore size drastically. Using this technique IRMOFs with up to 91.1% open space of the crystal volume could be obtained and the homogeneous periodic pores could be incrementally varied from 3.8 to 28.8 Å. (Fig. 1.4.2) However this series of experiments also outlined the boundaries and limitations of MOFs with regard to pore sizes, as the use of longer linkers in the synthesis resulted in interpenetration effects, lowering the pore diameter but in turn increasing the gas storage abilities in contrast to non-catenated structures due to interactions between linkers and adsorbents in the micropores.^[53, 54] Whilst interpenetration can be counteracted by using alkyl-modified ligands such as dioxidoterephthalate (MOF-74), creating a series of IRMOFs up to 85 Å pore size,^[55] problems arising due to the bad solubility of the very hydrophobic, large linkers cannot be easily overcome. Following up on interpenetration effects, Yaghi and co-workers were additionally able to show that reversible interpenetration of MOF networks is possible. In 2012, they were able to demonstrate using $\text{Zn}_7\text{O}_2(\text{NBD})_5(\text{DMF})_2$ (NBD = 2-nitrobenzene-1,4-dicarboxylate, DMF = N,N-dimethylformamide) that by addition or removal of the solvent (DMF) interpenetration effects can be established or suppressed.^[56]

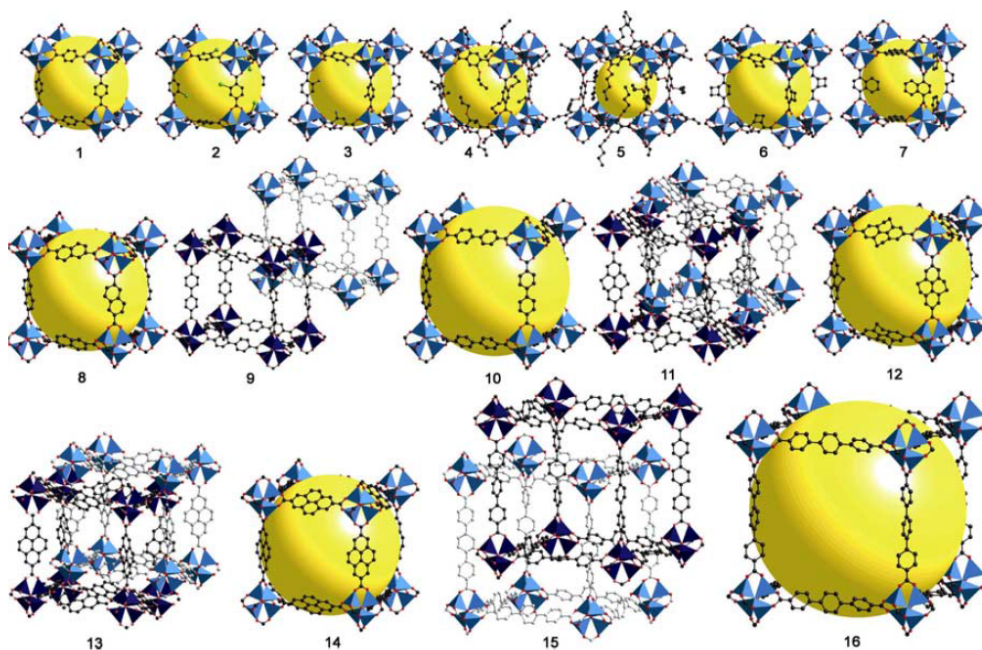


Figure 1.4.2: Series of isorecticular MOF frameworks (IRMOFs), highlighting the possibilities for framework modification (1-7), pore volume increase (8, 10, 12, 16), as well as interpenetration effects (9, 11, 13, 15). Reprinted from [57] with permission from Elsevier.

The possibility to rationally design a MOF based on the used SBUs is referred to as “reticular chemistry”, which is seen as a concept towards new materials with peerless diversity.^[58-60] This term describes the linking of molecular building blocks into predefined structures.^[61] Combined with the huge variability offered by the use of manifold organic linkers including functional groups such as carboxylates,^[52, 62, 63] phosphonates,^[64, 65] sulfonates,^[66] pyridine,^[67] imidazole,^[41, 68] triazole^[69] or tetrazole derivatives,^[70] amongst others, the amount of accessible structures and materials seems boundless. A limiting factor to take into account is the need to use mostly aromatic systems as linkers in order to create rigid and chemically stable backbones to ensure good thermal and chemical stability of the resulting materials while retaining permanent porosity. Recently, more unusual linkers such as chiral ligands^[71] and crown ethers,^[72] as well as bioavailable linkers such as chiral gamma-cyclodextrin,^[73] amino acids^[74] and polypeptides^[75] have been explored.

Whilst MOFs are commonly thermally less stable than zeolites, a fact that is especially true for zinc centered and redox-active MOFs,^[76] some of these coordination based materials show exceptional thermal stability, peaking at up to 300°C for MIL-101(Cr).^[77] Similar to zeolites, the hybrid organic-inorganic frameworks are generally synthesized under solvothermal conditions in various solvents such as water, dimethylformamide, ethanol, methanol or acetonitrile at room temperature^[78] and up to 300°C,^[79, 80] yet also solvent-free approaches^[81] and syntheses in ionic liquids^[82] are known.

1.5 MESOPOROUS MATERIALS

As previously mentioned, one of the main limitations to the porosity of MOFs is the occurring interpenetration upon using longer linkers to increase the pore volume. Apart from the use of linkers including functionalities that prevent interpenetration, such as the afore mentioned dioxidoterephthalate,^[55] the use of MOFs featuring complex crystal structures that are geometrically unable to interpenetrate is a known way to address these problems.^[43] Whilst these methods enable high pore volumes, they significantly lower the amount of available framework topologies and functional groups, thereby limiting the practical uses of larger pores for applications such as catalysis. Silicate-based materials have suffered from similar restrictions in the past, as possible applications with regards to the inherent porosity of many crystalline silicates, such as zeolites, have been limited due to the comparably small sizes of the formed Si-O cages and the resulting constrictions in the diffusion of reactants into the material. In 1992, Kresge *et al.* were able to create a new class of materials by adding surfactant templates to the synthesis of silica materials. The resulting MCM materials (mobile composition of matter), have uniform mesopores ranging from 3 to 5 nm in diameter, regular pore arrangements in various geometries such as cubic (MCM-48), 2D hexagonal (MCM-41) or lamellar (MCM-50) depending on the used surfactant and surfactant concentration, and exhibit amorphous silica pore walls.^[83, 84] The combination of narrow pore size distribution^[85] and high specific surface areas up to 1000 m²/g enable MCM materials to perform well as molecular sieves,^[84] for dye adsorption^[85] and as templates for the synthesis of other porous materials.^[86, 87]

1.5.1 TEMPLATING MECHANISMS

Until today two different templating mechanisms have been discussed based on the used surfactants and inorganic precursors. (Fig. 1.5.1)

True liquid crystal templating takes advantage of the self-ordering effects that many amphiphilic surfactants show in various solvents. After adding the surfactant to a solvent, a lyotropic liquid crystalline phase begins to form. The structure and geometry of the liquid crystalline phase can be altered by adjusting the solvent, the surfactant used, its concentration as well as the reaction temperature. The inorganic component such as silica precursors is added after the liquid crystal has formed, leading to a condensation around the preformed structure, embedding the liquid crystal as a template. In order to achieve permanent porosity, the surfactant has to be removed from the structure after the condensation reaction is complete. Various methods have been developed, based on the used surfactant as well as the inorganic material, such as template removal by calcination at high temperatures,^[88, 89] which is common for thermally stable, oxide based materials, the use of plasma,^[90] microwave irradiation^[91], the exchange of the used charged surfactants with smaller

molecules, such as the exchange of trimethylammonium based surfactants with ammonium nitrate in ethanol,^[92] or the use of supercritical CO₂.^[93]

In cooperative self-assembly driven reactions, the inorganic precursors are added at the start of the reaction, at the same time as the surfactants. The used charged surfactants generate micelles due to intermolecular attraction under hydrothermal conditions. The charged micellar structures then attract the oppositely charged inorganic precursor based on coulomb interactions. Due to the drastically increased charge density on the boundary surface between micelles and inorganic precursors, stable oligomeric structures are formed, which then in turn condensate through polymerisation and cross-linking into larger mesostructures. Whilst the driving force for this polymerisation is the minimization of interfacial energy, the reaction conditions such as pH-value, temperature, used solvents and surfactant-to-inorganic precursor ratio determine the final structure and thereby pore size, stability and topology of the obtained mesostructure.

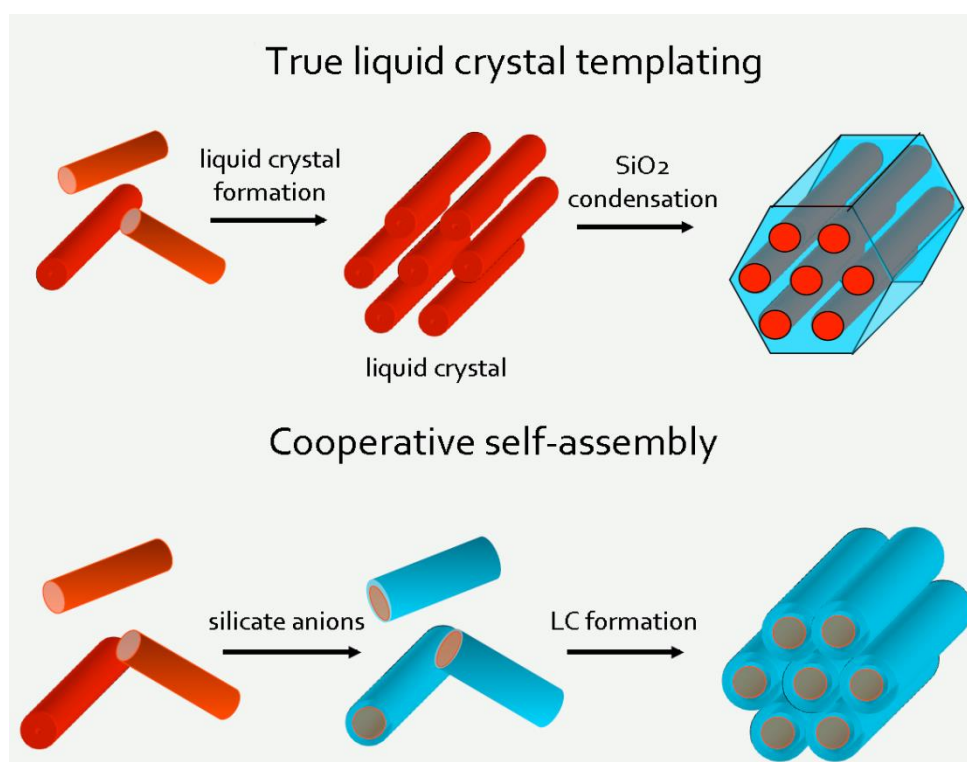


Figure 1.5.1: Reaction mechanisms used in supramolecular templating. Top: True liquid crystal templating; bottom: Cooperative self-assembly. Figure taken from [94] with adaptations.

Both mechanisms can lead to a variety of different mesostructures which range from lamellar to hexagonal and cubic. In Figure 1.5.2, a simplified phase diagram of the surfactant trimethyldodecyl chloride is shown, showcasing the possibilities to alter the resulting mesostructures by changing the used amount of surfactants.

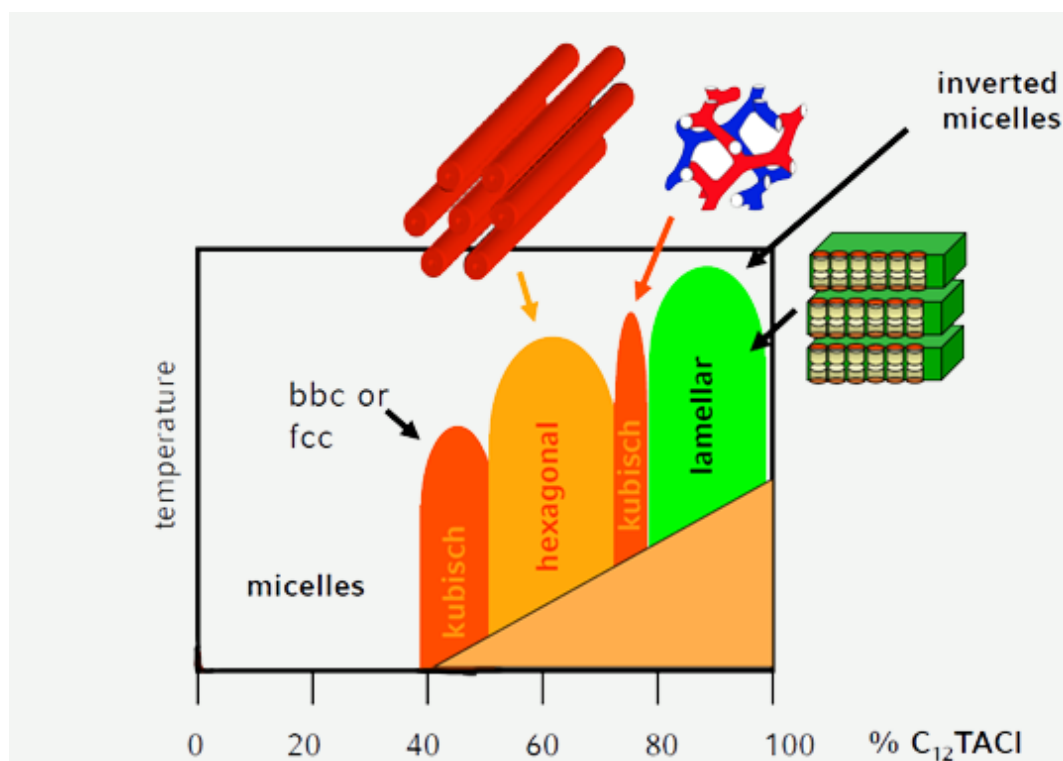


Figure 1.5.2: Simplified phase diagram of trimethyldodecyl chloride as function of concentration and temperature.

1.5.2 MESOPOROUS SILICA

Starting in 1992 with the first report on MCM materials, various other materials and templates have been explored, leading to a plethora of available mesostructured inorganic materials today. In 1995, Tanev et al. reported the synthesis of hexagonal mesoporous silica (HMS) by using primary amines as templates.^[95] By using poly(ethylene oxides) as a template for silica-based materials, groups at the Michigan State University were able to obtain a series of mesostructured silicates named MSU materials.^[96] By extending the range of available surfactants for the templating of silica materials to pluronic triblock copolymers, Stucky et al. were able to obtain SBA (Santa Barbara)-type materials with robust mesoporosity.^[88] Due to the amphiphilic nature and long carbon chains of these triblock copolymers featuring a central hydrophobic chain built of poly(propylene oxide) and on both ends hydrophilic chains of poly(ethylene oxide), reaching molecular weights up to 5800 $M_{avg.}$, remarkable mesopore sizes up to 15 nm and a vast morphological variety could be achieved.^[97] Due to templating effects of the poly(ethylene oxide) side chains, additional micropores in the amorphous silica pore walls could be observed,^[88, 98] as well as an increase in thermal and chemical stability compared to MCM materials, due to thicker pore walls.^[99]

Up until 2011, the vast majority of reports on mesostructured silica or metal-oxide based materials described systems based on amorphous walls combined with mesostructural templating by surfactants. The range of known mesostructured materials was extended to materials featuring

crystalline walls when Ryoo et al. reported on a new group of materials with hierarchical micro-mesoporous structures. By using the supramolecular templating effect of gemini surfactants, a class of surfactants featuring two charged head groups, mesoporosity was generated in a zeolite, while microporous, crystalline walls were created due to charge compensation effects between the surfactant head groups and the silica-based walls.^[100]

1.5.3 GEMINI SURFACTANTS

Gemini surfactants are an important class of surfactants that have received attention due to their low critical micelle concentration, high surface activity and unusual viscosity behavior.^[101-104] Their structure consists of two hydrophobic side chains, each attached to one of two polar head groups which are linked by a spacer. Whilst most known gemini surfactants possess a symmetric structure with identical side chains, recently dissymmetric surfactants have been used as well.^[105-107] The surfactants can in general be abbreviated as n - s - m , where s represents the number of carbon atoms in the spacer and n and m refer to the number of carbon atoms in the hydrophobic side chains.^[108-110] (Fig. 1.5.3) Up to today, a vast variety of gemini surfactants with different functionalities included into the side chains and spacers have been synthesized, such as acetylenic spacers,^[111] OH-groups included into alkyl spacers,^[112] ranging from cationic variants with ammonium based head groups^[113] to anionic dicarboxylate gemini surfactants.^[114] Due to the manifold modification possibilities of the formed surfactant mesophases by altering the surfactant spacer as well as the length of the hydrophobic side chains, gemini surfactants have been used as templates for silica based materials as well, resulting in the generation of hexagonal and lamellar mesophases depending on the used surfactants.^[115]

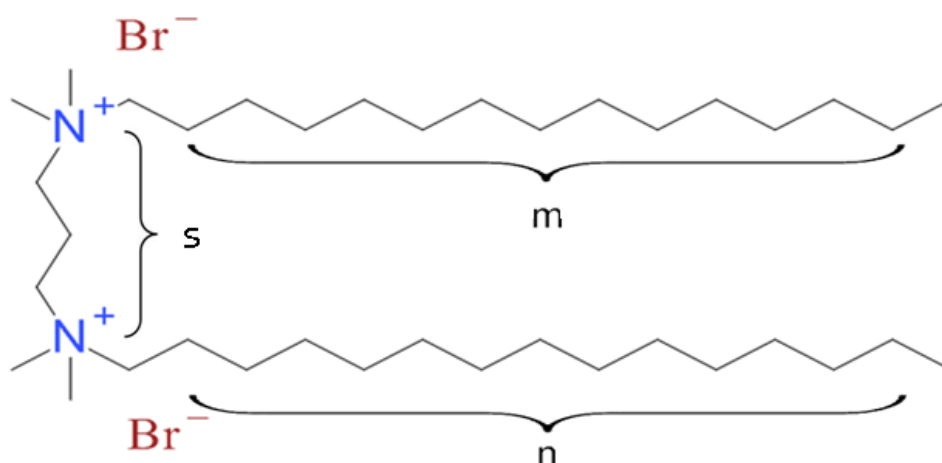


Figure 1.5.3: n - s - m gemini surfactant molecule with $n = m = 15$, $s = 3$.

1.5.4 TEMPLATING ON METAL-ORGANIC FRAMEWORKS

Supramolecular templating of MOFs has been another focus of research, due to the previously mentioned challenges and limitations arising from systematically enlarging the pore sizes of MOFs by altering the used linker. Hierarchically structured MOFs featuring a wide range of topologies, useable linkers and therefore catalytic possibilities as well as mesopores to facilitate diffusion and accessibility of the material for larger molecules and oligomers, are in high demand. In 2011, the first report of the successful synthesis of a meso-MOF using supercritical CO₂ in ionic liquids (1,1,3,3-tetramethylguanidinium acetate (TMGA)) and N-ethyl perfluorooctylsulfonamide (N-EtFOSA) as template was published.^[116] The obtained zinc-based 1,4-benzenedicarboxylic acid (BDC) MOF features micropores averaging 0.7 nm with a narrow pore size distribution and mesopores ranging from 2 nm to 6 nm in diameter. However, no evidence for the crystallinity of the MOF walls was provided, raising doubts about the crystal structure of the material.

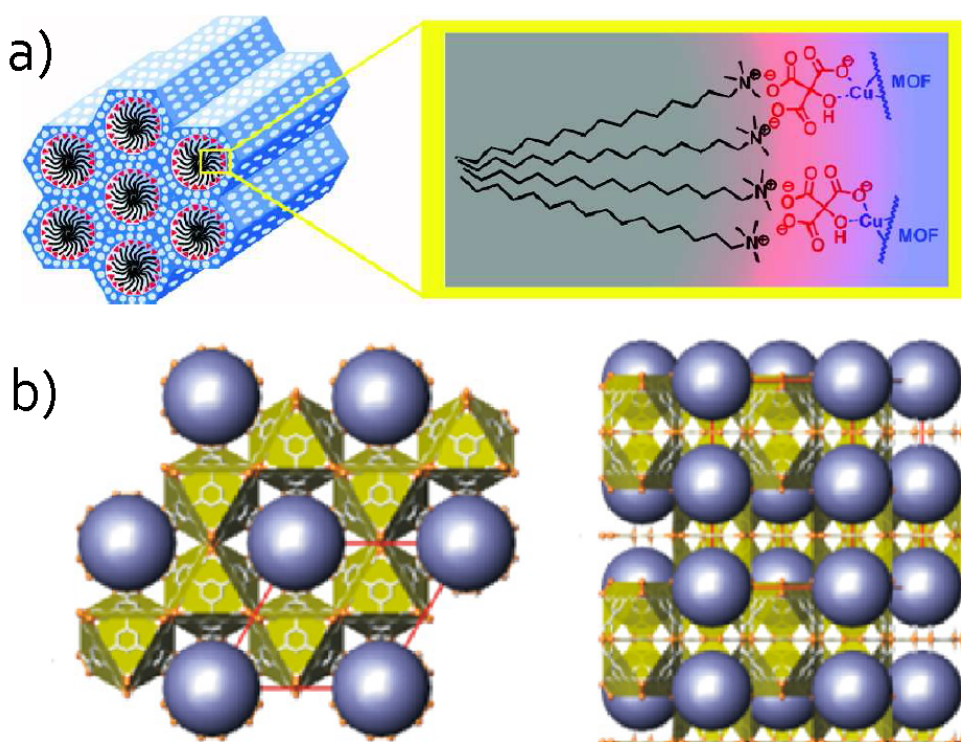


Figure 1.5.4: Supramolecular templating of MOFs. a) Stabilization of the MOF structure by utilizing citric acid as chelating agent. b) Encapsulation of Keggin Ions (blue) into the framework to stabilize the pore system. Reprinted with permission from [117] (a) and [118] (b). Copyright 2015 American Chemical Society.

The first reports that provided evidence for the crystallinity of the pore walls were based upon the use of a chelating agent (citric acid) to act as a mediator between the used trimethylammonium surfactant and the metal-organic framework.^[117] Citric acid coordinates the surfactant head groups on one side and the copper ions on the other, which are in turn coordinated by benzene-1,3,5-

tricarboxylic acid, creating the prototypic structure of the HKUST-1 (Hong Kong University of Science and Technology) MOF. (Fig. 1.5.4a) Whilst the mesopore structure could be proven *via* TEM measurements, the pore arrangement was not sufficiently regular to be detectable *via* powder X-ray diffraction. In addition, the used surfactants could not be removed from the structure without collapse of the framework, rendering this material unable to show improved molecule diffusion. The same principle was demonstrated by using pluronic surfactants to template carboxylic acid based MIL (Matériaux de l'Institut Lavoisier) into mesoporous structures.^[119, 120]

A different approach towards the mesostructuring of HKUST-1 was provided by Marteens et al., who focused on stabilizing the crystal structure of the MOF by integrating Keggin ions into the pores. (Fig. 1.5.4b) Upon addition of cetyltrimethylammonium bromide (CTAB) as a surfactant to the Keggin ion-assisted MOF synthesis, the formation of a mesostructured MOF (COK-15, Centrum voor Oppervlaktechemie en Katalyse) with uniform 5 nm mesopores and crystalline micropore walls of about 5 nm thickness was observed.^[118] The used Keggin ion templates could however not be removed at a later point, due to their superior thermal and chemical stability, compared to the surrounding MOF framework.

1.5.5 MESOSTRUCTURING OF ZEOLITIC IMIDAZOLATE FRAMEWORKS

Approaches towards the mesostructuring of ZIFs performed in our group, have resulted in the discovery of the class of "mesostructured imidazolate frameworks" (MIF).^[121] The first known materials of this new class resemble the previously discussed MCM-51 phase, featuring lamellar mesostructures combined with pore walls exhibiting low crystallinity. By altering the used trimethylammonium-type surfactants with regards to their polycarbonchain lengths, the interlayer spacing of the obtained mesostructures could be varied, showing a direct correlation between the length of the surfactant tail and the obtained spacing. Upon surfactant extraction by refluxing the material in ethanol, the structure of ZIF-8 could be obtained. These MIF materials were obtained for 2-methylimidazolate and imidazolate-based ZIFs, which possess sodalite-type topologies in the respective MOF crystal structure.

Whilst exfoliation of MIF materials into nanosheets proved unsuccessful since a transition of the materials into ZIF structures was observed during exfoliation attempts, exfoliation of zinc benzimidazolate based layered MOFs turned out to be viable.^[122] By using the surfactants as a structure directing agent during the synthesis procedure, the layered MOF Zn(BeIM)OAc could be pre-structured into a lamellar hybrid mesostructure with a lattice period of about 8 nm. Exfoliation with organic solvents such as THF resulted in slim nanosheets with minimum heights of 4 nm and lateral extension of several micrometers, which could in turn be deposited on silicon wafers *via* spin-coating, showcasing good processability of the obtained sheets.

1.6 POST-SYNTHETIC MODIFICATION OF METAL-ORGANIC FRAMEWORKS

One major advantage of MOFs compared to silica-based materials is the possibility to use the linker molecules for manifold organic reactions, introducing functionalities into the obtained frameworks, whilst retaining their topology and porosity. The concept of post-synthetic modification (PSM) was developed by Cohen et al. on IRMOF-3, a network containing the linker 2-amino-1,4-benzene dicarboxylic acid. Utilizing the reactivity of the amine-group with acetic acid, Cohen et al. were able to prove that functional groups in MOFs are accessible to organic reactions whilst retaining the framework crystallinity, leading to a single-crystal-to-crystal reaction.^[123] Subsequently, they were able to establish the validity of PSM as a widely valid concept by presenting numerous possible PSMs on IRMOF-3, including reactions with anhydrides, isocyanates as well as various carboxylic acids.^[124-128] Whilst these experiments have been the first to utilize the organic toolbox in the postsynthetic modification of MOFs, Lee and Kim had previously managed to include a metal complex into the pore system of a homochiral MOF, resulting in catalytic activity for enantioselective transesterification.^[129] Today, PSM reactions include covalent modifications of the networks as well as coordinative modifications, such as attaching a covalently bound chelating ligand which is suitable for complexing Pd(II), in turn enabling the MOF to perform heterogeneous catalysis.^[130] Additionally, multi-step reactions^[131] as well as diastereoselective reactions^[132] on the organic linkers could be performed under suitable reaction conditions, proving that a plethora of organic reactions can be done on MOFs without loss of crystallinity or porosity.

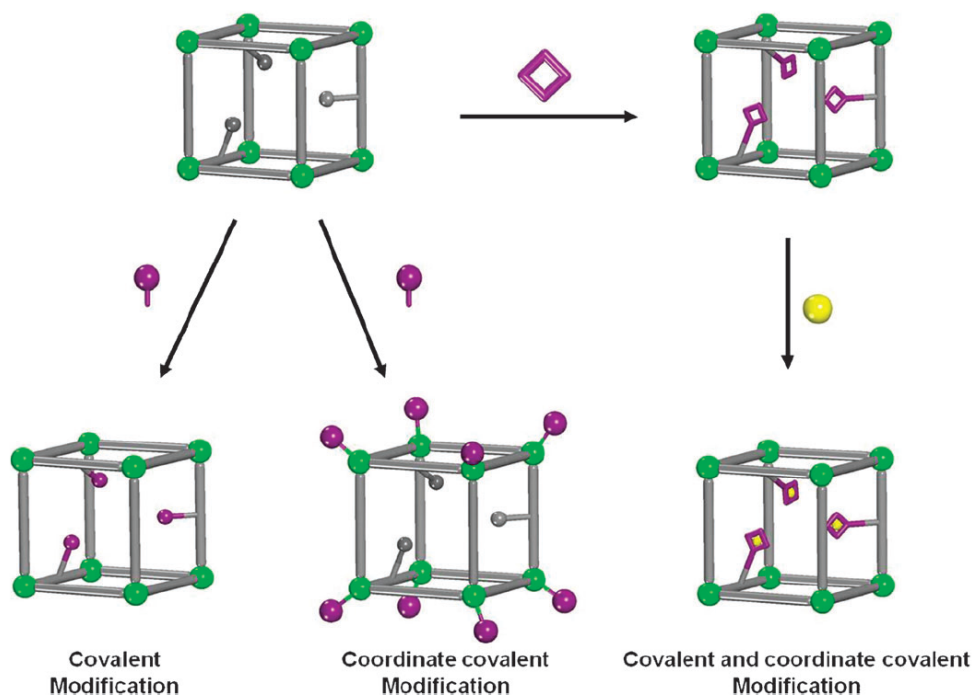


Figure 1.6.1: Schematic of various PSM routes, including covalent modification, coordinative covalent modification as well as multi-step covalent and coordinative modification approaches. Reproduced from ^[128] with permission of The Royal Society of Chemistry.

Potential applications are manifold, including heterogeneous catalysis,^[130, 133, 134] the modulation of gas sorption abilities^[135-137] as well as biomedical applications, where MOFs such as (Fe)-MIL-101 have been functionalized with drugs and imaging contrast agents and were successfully tested in cell cultures.^[138]

Apart from choosing a suitable organic reaction and creating a MOF bearing the desired organic functionality, problems arise due to instabilities of MOFs under PSM conditions, as a consequence of framework collapse due to acids, bases or high temperatures. However some MOFs show remarkable stability against certain external factors, such as ZIF-8, modified with additional carboxaldehyde functionalities, which can be reduced even by strong reducing agents such as NaBH_4 ,^[139] or (Cr)-MIL-101, which withstands PSM through nitration with $\text{HNO}_3/\text{H}_2\text{SO}_4$.^[140] Nevertheless, PSM under mild conditions can be performed through techniques such as the use of protective groups, removable *via* light irradiation, to include more reactive groups into the frameworks during synthesis.^[141] Additionally, PSM reactions initiated by irradiation with UV light are known, such as *cis/trans* isomerization in (Cr)-MIL-101- NH_2 treated with *p*-phenylbenzoylchloride/4-(phenylazo)-phenylisocyanate.^[142]

A more universal approach towards mild PSM conditions was discovered by Sharpless et al., who were able to perform the copper catalyzed alkyne and azide [3+2] Huisgen-cycloaddition inside a MOF framework.^[143] This so called click-chemistry combines high yields even at micromolar concentrations, mild reaction conditions and readily available starting materials, resulting in a broad

range of applications in various fields such as polymer science^[144-146] and bioconjunction (*in vitro*^[147, 148] and *in vivo*^[149, 150]). By adding this technique to the toolbox of known PSM reactions, the range of applicable modifications has been significantly increased, as amines, which can be integrated into a broad range of framework topologies, can be readily transformed into azides, which in turn can be used for click-chemistry on a vast variety of MOFs.

Apart from the previously mentioned applications of MOFs after PSM, there is also a plethora of uses that have been explored for as-synthesized MOFs. (Mg)-MOF-74 has been used to effectively separate CO₂ from a gas mixture of CO₂ in CH₄ due to interactions at open metal sites,^[151] whilst other MOFs also have been used to efficiently store H₂, CO₂ or CH₄.^[152] The storage and release of nitric oxides has been explored in the context of biomedical applications, as nitric oxides are an important factor for wound sealing^[153] and are used as signaling molecules for various targets such as the cardiovascular system.^[154] Other biomedical applications for MOFs include drug delivery and the use of frameworks containing Gd³⁺ ions as MRI contrast agents.^[155] The use of MOFs in fields such as non-linear optics,^[156] catalysis^[157-159] or sensor devices^[14, 47, 160] have been reported as well. With respect to catalysis, two approaches have to be highlighted specifically: heterogenous catalysis on one hand and electrocatalysis on the other. Whilst heterogeneous catalysis with MOFs using the linker as well as metal nodes or post-synthetically introduced metal-ions as catalytic active centers has been thoroughly explored,^[134, 161, 162] electrocatalysis is so far a much less explored topic. Reports have focused on i) the use of MOF pyrolysis products in electrocatalysis, creating a N-doped carbon matrix for metal-ions,^[163-165] ii) the incorporation of redox-active metal complexes into MOFs,^[166] or iii) the formation of surface-bound iron hydroxides on Basolite™ F300 by an initial electrochemical scanning step.^[167]

The focus of this work is on the improvement of the understanding of MOF mesostructuring techniques. Detailed investigations on the effects of different surfactants and solvents on the structure of MIFs will be presented. The provided insights are leading to a possible reaction mechanism that deepens the understanding of the formation of the obtained mesophases and will provide information towards future synthesis approaches. In the second part of the thesis, the focus lies on catalytic applications of MOFs by presenting a series of MOF nanosheets, obtained through exfoliation that are suitable for functionalization through various reactions, providing a basis for applications such as catalysis, photocatalysis or surface modification as well as one of the first electrochemically active ZIFs that retains its crystal structure during electrocatalytic processes.

2 CHARACTERIZATION METHODS

2.1 POWDER X-RAY DIFFRACTION (XRD)

In order to determine symmetry, phase purity, crystallinity and particle size of materials, powder X-ray diffraction (XRD) can be used. During XRD analysis the sample is irradiated with monochromatic X-rays, which are scattered by crystal lattice planes that are made up by the periodically arranged atoms in a crystal, following Bragg's law^[168]

$$\sin\theta = \frac{n \cdot \lambda}{2d} \quad (1)$$

where θ is the scattering angle, d the lattice plane, λ the wavelength and n the reflection order (see Figure 2.1.1). The so-called Bragg angle θ describes the angle at which constructive interference between radiation scattered at different lattice planes occurs. Thus, only materials composed of periodic structures, such as crystal lattices, equally spaced layers or highly ordered pore systems, are well suited for analysis by XRD.

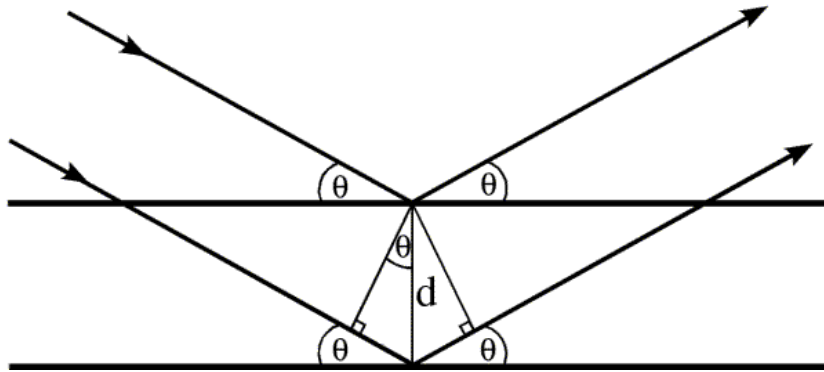


Figure 2.1.1: Geometric derivation of the Bragg equation.

XRD measurements performed in this work were measured on a STOE Stadi P Comi (STOE & Cie GmbH, Germany) high throughput device operating in Debye-Scherrer geometry, a BRUKER D8 Discover Avance (BRUKER AXS, USA) operating in Bragg-Brentano geometry, a STOE Stadi P (STOE & Cie GmbH, Germany) rotating capillary setup, or a HUBER G670 (HUBER Diffractionstechnik, Germany) working in Guinier geometry.

All measurements, except measurements for samples containing cobalt, were performed using a curved Ge(111) monochromator and Cu K $_{\alpha 1}$ radiation ($\lambda = 0.154$ nm). Samples containing cobalt were measured using Mo K $_{\alpha 1}$ radiation ($\lambda = 0.071$ nm) to prevent fluorescence of the samples. The data were evaluated using the software package WINX^{POW}.^[169] Whilst already known phases were identified by comparison with the database of the Joint Committee on Powder Diffraction Standards (JCPDS)^[170], indexing and Pawley fits of unknown powder patterns were carried out using the TOPAS Academic software (Version 4.1).

2.2 INFRARED SPECTROSCOPY (IR)

Infrared spectroscopy uses the infrared region of the electromagnetic spectrum to excite vibrational and rotational modes of molecules and extended solids. Excitation of different modes is limited to vibrational or rotational movements that alter the dipole moment during movement. The amount of absorbed radiation as a function of energy is detected and provides information about the different chemical bonds within the material under investigation due to the excitations of afore mentioned modes. The energies needed for the excitation can be estimated via the equation for harmonic oscillators.

$$\nu = \frac{1}{2\pi c} \sqrt{\frac{f}{\mu}} \quad (2)$$

The vibrational frequency ν can be calculated from equation (2) with c being the speed of light, μ being the reduced mass as defined by equation (3) and f being the force constant of the examined bond.

$$\mu = \frac{m_A m_B}{m_A + m_B} \quad (3)$$

The force constant f is a criterium for the strenght of the bond, influenced by various factors, such as the binding order and the chemical surrounding of the bond and the participating atoms.

All data presented in this work were measured on a Perkin Elmer Spektrum BXII FT-IR (Perkin Elmer Inc., USA) featuring an attenuated total reflectance unit (ATR).

2.3 DIFFERENTIAL THERMAL/THERMOGRAVIMETRIC ANALYSIS (DTA-TG)

To get insight into the thermal behaviour of the sample in order to detect phase transitions and decomposition processes in the material, differential thermal (DTA) and thermogravimetric analyses (TG) were performed. During differential thermal analyses the difference in temperature between the sample and an inert reference is measured as both are heated in an inert atmosphere. By recording all endothermic and exothermic processes, phase transitions can be detected. By simultaneously recording the sample weight for thermogravimetric analyses, the thermal stability of the materials can be explored as well as possible solvent removal from the potentially porous samples.

All measurements were performed on a Setaram DTG/TG-thermobalance 92-2400 (Setaram Engineering, France) under helium atmosphere from room temperature to 1000 °C with a heating rate of 5 °C/min using Al₂O₃ crucibles.

2.4 ELEMENTAL ANALYSIS: CHNS AND INDUCTIVELY COUPLED PLASMA ATOMIC EMISSION SPECTROSCOPY (ICP-AES)

To determine the elemental composition of the samples, CHNS analysis, titrometric halogenide determination and inductively coupled plasma atomic emission spectroscopy (ICP-AES) were used.

Analysis of carbon, hydrogen and nitrogen was done by high-temperature digestions in a highly oxygenated helium atmosphere. The evolving gases CO₂, H₂O, N₂ as well as various nitrous oxides are subsequently detected using a thermal conductivity measurement cell with an accuracy of about 0.30 %. All CHNS analyses were carried out using an Elementar vario EL (Elementar Analysensysteme, Germany) by the microanalytical laboratory of the Department of Chemistry (LMU).

The halogenide contents were determined by oxidative pulping followed by potentiometric titration with AgNO₃ using an automatic Titroprocessor 672 determining all halogenides at once.

To determine the content of metal ions in the samples, inductively coupled plasma atomic emission spectroscopy (ICP-AES) was carried out. The samples were heated in a plasma up to 7000 K, resulting in molecules dissociating into atoms and ions. Due to the recombination of formed electron-hole-pairs in the atoms at such temperatures, the ions emit irradiation of an element-characteristic wavelength. The emitted radiation was detected by a VARIAN VISTA RL simultaneous spectrometer (Agilent Technologies, USA) utilizing a CCD detector. All experiments were carried out by Helmut Hartl (LMU) or Marie-Luise Schreiber (MPI Stuttgart).

2.5 ELECTRON MICROSCOPY

In order to obtain high resolution images of materials to gain information about their morphology and elemental composition, different electron spectroscopic methods have been used. Whilst the resolution limit of optical microscopes is limited to about 200 nm due to diffraction limit, electron microscopy is able to improve the resolution up to about 0.1 nm. The electron beam is generated by a tungsten filament or a field emission gun, accelerated by voltages between 40 and 3000 kV and focused through electrostatic and electromagnetic lenses.

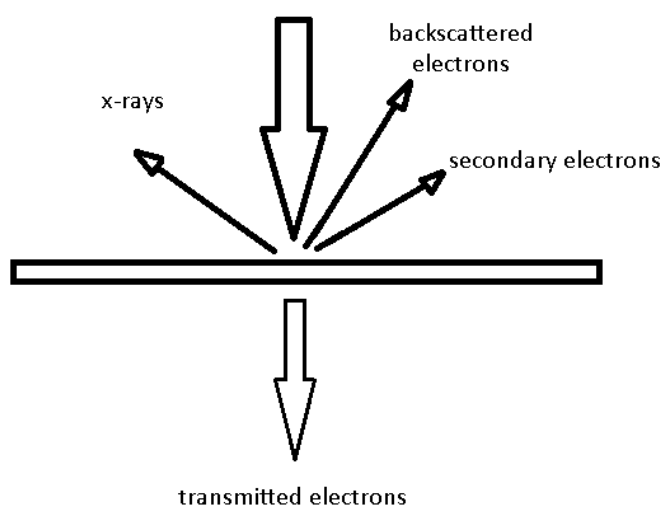


Figure 2.5.1: Electron interactions with a materials specimen during electron microscopy.

Elastic and inelastic scattering as well as transmission of the electrons through the sample can be used in transmission electron microscopy (TEM), scanning electron microscopy (SEM) and energy-dispersive X-ray spectroscopy (EDX).

2.5.1 TRANSMISSION ELECTRON MICROSCOPY (TEM)

In order to gain information about the morphology of nanostructured samples, as well as the elemental distribution in these, transmission electron microscopy was used. During scanning transmission electron microscopy (STEM), the sample is scanned with a focused electron beam spot and transmitted electrons are detected. The scattering angle of the detected electrons correlates to the atomic number of the atoms in the sample as well as the sample thickness and can therefore be used to determine sample composition and morphology.

All experiments were carried out using a JEOL JEM-2011 (JEOL Ltd., Japan) equipped with a tungsten cathode at an accelerating voltage of 200 kV or a Philips CM 30 ST with a LaB_6 thermal source operating at 300 kV.

2.5.2 SCANNING ELECTRON MICROSCOPY (SEM) AND ENERGY-DISPERSIVE X-RAY SPECTROSCOPY (EDX)

By using lower accelerating voltages compared to TEM measurements (0.1 - 30 kV) and thicker specimen, backscattered and secondary electrons are obtained from the sample. Secondary electrons are inelastically scattered electrons with low energies and can be used to get insight into the topology of the sample by imaging the sample surface. Backscattered electrons are scattered elastically by the surface and have higher energies, providing element-specific information about the composition of the sample.

Additional information about the composition of the sample is obtained by exciting inner-shell electrons of the atoms in the sample. By relaxing back to energetically lower levels, higher-shell electrons emit specific X-ray radiation that can be detected with energy-dispersive X-ray (EDX) spectroscopy.

The SEM and EDX measurements were performed using a JEOL JSM-6500F (JEOL Ltd., Japan) with accelerating voltages from 2 to 25 kV by Christian Minke (LMU).

2.6 NUCLEAR MAGNETIC RESONANCE (NMR) SPECTROSCOPY

Nuclear magnetic resonance (NMR) spectroscopy is an analytical technique used for determination of the local structure of molecules or solids having at least one NMR active isotope. These isotopes with nonzero nuclear spin possess intrinsic magnetic moments that interact with external magnetic fields. The resonance frequency of the interaction is dependent on the magnetic properties of the nuclear isotope and the external field. The magnetic properties of the isotopes are influenced by various factors including structure, dynamics, oxidation state and chemical environment, rendering NMR spectroscopy able to act as a comprehensive analytical technique with regards to the local structure of molecules.

2.6.1 SOLUTION NMR SPECTROSCOPY

During solution NMR spectroscopic measurements, all molecules in the sample are rotate due to Brownian motion. This movement averages out all orientation-dependent interactions between different nuclei, resulting in information about the connectivities and structure of the molecule, yet only limited information about intermolecular interactions. All measurements were performed on a Varian Gemini 200, Varian Gemini 300, Bruker DRX 200, Bruker AMX 400 or Bruker AMX 600 using TMS as an external standard for ^{13}C and ^1H measurements and nitromethane for ^{15}N measurements.

2.6.2 SOLID-STATE NMR SPECTROSCOPY^[171, 172]

During solid-state NMR spectroscopy measurements the orientation-dependent interactions are not averaged out by Brownian motion, leading to significant line-broadening caused by effects such as chemical shift anisotropy, dipolar coupling and quadrupole coupling. Amongst these orientation-dependent effects, the dipolar coupling is the most general one and the one most commonly observed for abundant NMR active cores such as ^1H . The orientation of isotopes for this interaction with respect to the external magnetic field can be described by

$$\Delta B = \frac{\mu_0}{4\pi} (3 \cos^2 \theta - 1) \mu r^{-3} \quad (4)$$

with ΔB being the variation in the local magnetic field, μ_0 being the permeability of free space, μ the magnetic moment of the isotope, r the distance vector and θ referring to the angle between r and the direction of the external magnetic field. If θ equals 54.74° , the term $(3 \cos^2 \theta - 1)$ turns 0, thus averaging out the effects of dipolar coupling on the measurement to a large extent. This technique is referred to as magic-angle spinning (MAS). Additionally, cross-polarisation (CP) can be used to increase the signal strength of isotopes with low natural abundance and low gyromagnetic ratio such as ^{15}N by transferring magnetization from more abundant isotopes such as ^1H to the desired core.

All measurements were performed using ZrO_2 rotors (BRUKER) using a Bruker Avance-III spectrometer operating at 500 MHz. Detailed measurement parameters for each shown measurement can be found in the appendix.

2.7 ULTRAVIOLETT-VISIBLE (UV-Vis) SPECTROSCOPY

The absorption of visible and UV light by a sample, exciting electronic states from the ground state to an excited state, can be used analytically to examine transition metal ions that exhibit color and highly conjugated organic compounds, as well as biological macromolecules. The absorption processes can be used for quantitative analysis of known adsorbents via the Beer-Lambert equation.

$$\log \frac{I_0}{I} = \epsilon c L \quad (5)$$

With I_0 being the intensity of the incident light beam, I the transmitted intensity, L the path length through the sample, c the concentration of the absorbing species and ϵ being a constant known as molar absorptivity or extinction coefficient, the concentration can be readily calculated from the measured intensity of the transmitted beam.

An additional application of UV-Vis spectroscopic measurements is the determination of oxidation states of transition metal ions and their coordination sphere, such as found in metal-organic frameworks. Due to different properties of chromophores of the same metal, this technique can be used to differentiate between different oxidation states as well as chemical surroundings of the metal ions. All measurements performed in this study have been recorded using a Varian Cary 500 Scan UV-Vis-NIR spectrometer (Agilent Technologies, USA).

2.8 ATOMIC FORCE MICROSCOPY (AFM)^[173]

To obtain information about the height profile and morphology of nanosheets spincoated onto a substrate with a lateral and vertical resolution below 0.1 nm, atomic force microscopy (AFM) was used. In tapping mode, a cantilever is oscillated close to its resonance frequency by a small piezoelectric element and moved into the vicinity of the sample surface. The oscillation frequency thereby becomes dependent on the distance between cantilever and surface. By scanning the cantilever over the sample surface while using piezoelectric crystals to keep the distance of the cantilever to the surface and thereby the oscillation frequency of the cantilever constant, a detailed image of the surface can be obtained. An attached computer calculates the surface topology by imaging the response of the piezo-crystals with respect to the used raster pattern.

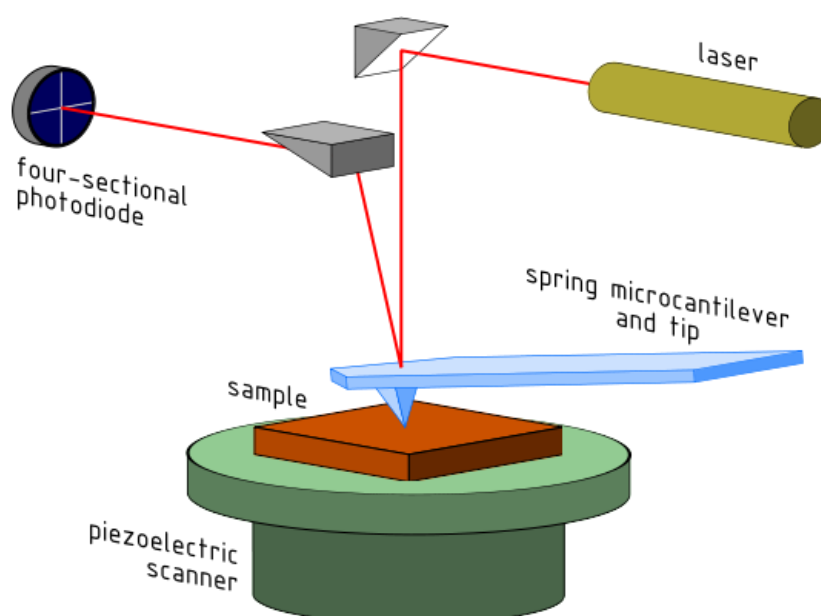


Figure 2.8.1: Working principle of an atomic force microscope, showcasing the detection of the cantilever displacement via laser on a four-sectional photodiode.^[174]

For AFM measurements, commonly three measurement techniques are utilized. In contact mode measurements the cantilever tip is dragged across the surface of the sample. Due to the texture of

the sample surface, the cantilever is displaced, which is detected via deflection of the laser signal or the feedback signal of the cantilever movements. To combat damages to the sample surface during the measurements as well as to increase the signal to noise ratio, cantilevers with low stiffness are used in this method. Contact mode measurements are only suitable for samples that can not be deformed due to the cantilever interactions on the surface and are additionally disturbed by attractive forces between cantilever and sample surface, that make the cantilever snap into position on the surface, thereby falsifying the measurement data.

To reduce the cantilever interactions with the surface due to close-range forces and interactions due to thin liquid meniscus layers on the sample under ambient conditions, tapping mode measurements are used. In tapping, or dynamic contact mode, the cantilever is oscillated by piezo crystals close to or at its resonance frequency, with an oscillation amplitude around 100 to 200 nm. Due to interaction between the oscillating cantilever and the surface, such as Van-der-Waals forces, dipole-dipole interactions and electrostatic forces, the oscillation is dampened. The cantilever is in turn moved by piezoelectric crystals in order to maintain a constant oscillation altitude and the height adjustments of the piezoelectric crystals are used to create an image of the sample surface.

Further improvement in terms of signal to noise ratio and regarding the limitation of damage to the sample surface, was achieved by employing non-contact measurements. In these measurements the cantilever is oscillated similar to tapping mode measurements, although at much lower amplitude, ranging between 10 nm and a few picometers. Depending on whether the cantilever is oscillated at resonance frequency or just above the resonance frequency, two different modulations are used to detect interactions with the sample and thereby determine the surface structure are used. At resonance frequency, the so called frequency modulation is used, by detecting changes in the frequency of the cantilever and subsequent correction of the changes via piezoelectric crystals. At frequencies slightly above the resonance frequency, amplitude modulation is used and changes in the amplitude of the oscillation are detected and in turn corrected by the piezoelectric control circuits.

An Asylum Research MFP 3D (Asylum Research, USA) operated in tapping mode was used to perform all measurements presented in this work.

2.9 MASS SPECTROMETRY (MS)

Information about detailed molecule weight distributions of the sample constituents can be obtained by ionizing a sample containing molecules that can be ionized, such as organic linkers in metal-organic frameworks, in order to break them into charged fragments. By applying an electric field, these fragments can be separated according to their mass-to-charge ratio during mass spectrometry (MS). In order to handle different types of samples, a variety of ionization methods has been

developed such as electron impact ionization (EI), chemical ionization (CI), electrospray ionization (ESI) and fast atom bombardment (FAB). In this work, MS measurements were performed to identify the products of linker syntheses as well as the modification reactions, such as hydrogenation, of linkers to be used in MOF syntheses.

Mass spectrometry performed during this work, was measured on a Thermo Finnigan MAT 95 (Thermo Fischer Scientific, USA) using electron impact ionization. The measurements were carried out by the microanalytical department of the Department of Chemistry (LMU).

3 OPERATIVE PROCEDURES

3.1 ORBITAL SHAKER

Exfoliation of suspended samples prestructured or dispersed by surfactants was carried out by using the orbital shakers GFL 3005 (max. 500 rpm) and GFL 3017 (max. 300 rpm) (Gesellschaft für Labortechnik mbH, Germany).

3.2 ULTRASONIC BATH

Additinal exfoliation attempts were carried out using an Elmasonic S100H (Elma Hans Schmidbauer GmbH & Co. KG, Germany) ultrasonic bath, operating with a power of 500W and a 9.5L tank volume.

3.3 MICROWAVE

Experiments at elevated pressure and temperature using microwave radiation as a heating source were carried out using a Biotage Initiator (Biotage AB, Sweden) microwave with 10-20 mL microwave vials from Biotage.

3.4 CENTRIFUGE

To gather formed precipitates from reaction suspensions, a sigma 3-30K centrifuge (Sigma Laborzentrifugen GmbH, Germany) with a fixed angle rotor (no. 12158) operating at a maximum rotation speed of 25000 rpm, resulting in a maximum gravitational force of 60628 x g, was used.

3.5 SPIN COATING

To produce high-quality samples of as-synthesized nanosheets on silicon wafers, spincoating was performed using a Laurell WS-650SZ-6NPP/LITE (Laurell Technologies Corporation, North Wales) spin coater. The silicon wafers were washed and kept under ethanol prior to the spincoating process. No further cleaning procedures were used.

3.6 CHEMICALS

Chemical	Formula	Purity	Supplier
Acetone	C ₃ H ₆ O	dry	Brenntag
Ammonium acetate	C ₂ H ₇ NO ₂	per analysis	Fluka
Benzimidazole	C ₇ H ₆ N ₂	99 %	Alfa Aesar
1,4-dibromobutane	C ₄ H ₈ Br ₂	99 %	Alfa Aesar
1,5-dibromopentane	C ₅ H ₁₀ Br ₂	98 %	Alfa Aesar
1,6-dibromohexane	C ₆ H ₁₂ Br ₂	97+ %	VWR
1,7-dibromoheptane	C ₇ H ₁₄ Br ₂	97 %	Acros Organics
1,8-dibromooctane	C ₈ H ₁₆ Br ₂	98 %	Acros Organics
1,9-dibromononane	C ₉ H ₁₈ Br ₂	97 %	Acros Ogranics
1,10-dibromodecane	C ₁₀ H ₂₀ Br ₂	97 %	Alfa Aesar
5-Brom-1H-benzimidazole	C ₇ H ₅ BrN ₂	97 %	Sigma Aldrich
Cetyltrimethylammoniumbromide	C ₁₉ H ₄₂ BrN	98 %	Alfa Aesar
Chloroform	CHCl ₃	puriss.	Merck
Cobalt(II) acetate tetrahydrate	Co(C ₂ H ₄ O ₂) * 4 H ₂ O	98+ %	Acros Organics
Cobalt(II) nitrate hexahydrate	Co(NO ₃) ₂ * 6 H ₂ O	>98 %	Roth
Diethylether	C ₄ H ₁₀ O	100 %	Prolabo
Dimethylformamide	C ₃ H ₇ NO	99.5 %	Acros Organics
N,N-dimethylhexadecylamine	C ₁₈ H ₃₉ N	≥95 %	Sigma Aldrich
N,N-dimethyloctadecylamine	C ₂₀ H ₄₃ N	≥95 %	Sigma Aldrich
N,N-dimethyltetradecylamine	C ₁₆ H ₃₅ N	≥95 %	VWR
Ethanol	C ₂ H ₆ O	99 %	Bundesmonopolverwaltung für Branntwein
n-Heptane	C ₇ H ₁₆	99 %	Grüssing
1-Hexanol	C ₆ H ₁₄ O	98 %	Sigma Aldrich
Imidazole	C ₃ H ₄ N ₂	for synthesis	Merck
Isopropanol	C ₃ H ₈ O	99 %	Sigma Aldrich
Methanol	CH ₄ O		Sigma Aldrich
2-Methylimidazole	C ₄ H ₆ N ₂	for synthesis	Merck
5-Nitrobenzimidazole	C ₇ H ₅ N ₃ O ₂	98 %	Alfa Aesar
5% Palladium on carbon			Alfa Aesar
Pyridine	C ₅ H ₅ N	90+ %	VWR
Silver nitrate	AgNO ₃	99.8 %	Fluka
Sodium hydroxide	NaOH	puriss.	Grüssing
Tetrahydrofuran	C ₄ H ₈ O		Chemetall

Tetramethylammonium hydroxide	$\text{N}(\text{CH}_3)_4\text{OH}$	0.06 mol/L	Acros
Toluol	C_7H_8	puriss.	Merck
Zinc acetate dihydrate	$\text{Zn}(\text{C}_2\text{H}_3\text{O}_2)_2 \cdot 2 \text{H}_2\text{O}$	98 %	Alfa Aesar
Zinc butyrate	$\text{Zn}(\text{C}_4\text{H}_7\text{O}_2)_2$		Synthesized in the workgroup
Zinc propionate	$\text{Zn}(\text{C}_3\text{H}_5\text{O}_2)_2$	98 %	Alfa Aesar

4 SURFACTANT-DIRECTED SYNTHESSES OF MESOSTRUCTURED ZINC IMIDAZOLATES

This chapter is based on the article “Surfactant-directed syntheses of mesostructured zinc imidazoles: formation mechanism and structural insights”, published by *CrystEngComm*, 2015, 17, 463-470. from E. A. Flügel, M. T. Aronson, S. C. Junggeburth, B. F. Chmelka and B. V. Lotsch.^[175]

4.1 ABSTRACT

Supramolecular templating techniques have been widely used to direct the formation of porous materials with the goal of introducing permanent mesoporosity. While surfactant-directed self-assembly has been exploited for inorganic materials such as titania, silica, organosilica, and zeolites, it has rarely been applied to metal-organic frameworks (MOFs) and coordination polymers. Here we introduce a new family of gemini surfactant-directed zinc imidazoles, referred to as mesostructured imidazolate frameworks (MIFs), and present a detailed study on the influence of different gemini-type surfactants on the formation mechanism and structures of the resulting zinc imidazoles. The proposed formation mechanism for MIF-type materials involves co-assembly and crystallization processes that yield lamellar mesostructured imidazolate frameworks. Understanding and controlling such processes also has implications for the syntheses of microporous zinc imidazolate framework (ZIF) materials, whose formation can be suppressed in surfactant-rich solutions, whereas formation of MIF materials is favored in the presence of surfactants and triggered by the addition of halogenides. Solid-state 2D ^{13}C HETCOR NMR measurements on prototypic CTAB-directed MIF-1 establish that the head group moieties of the surfactant molecules interact strongly with the zinc-imidazolate-bromide sheets.^[176] Additionally, the NMR analyses suggest that MIF-1 has a significant fraction of surfactant molecules that are interdigitated between the zinc-imidazolate-bromide sheets with an antiparallel stacking arrangement, consistent with the high thermal and chemical stability of the MIF hybrid materials.

4.2 INTRODUCTION

In recent years, metal-organic frameworks (MOFs) have received considerable attention due to their modularity and versatility, such as tunable pore sizes,^[57, 58] high specific surface areas^[177-179] and the possibility to alter their properties *via* post-synthetic modification of the organic linkers.^[128, 180] These desirable properties render MOFs multi-purpose scaffolds in a number of applications such as catalysis,^[162, 181] sensing,^[182, 183] gas storage^[70, 152] and drug delivery.^[155, 184] Limitations in the use of MOFs in catalysis mainly arise from a lack of chemical stability as well as small pore sizes in the micropore regime, as only a limited number of MOFs with pore sizes larger than 2 nm have been reported to date.^[185-187] With interpenetration effects limiting the possibility of using larger linkers to increase the pore size, other routes such as the use of more complex connection motifs^[186] or templating techniques have been utilized.^[120] The latter provide additional benefits by creating a hierarchical structure with bi- or multimodal pore-size distributions, including both micro- and mesopores, which facilitate the diffusion of bulky molecules and widen the potential applications in catalysis and drug delivery.

While exploring synthetic approaches to hierarchical ZIFs by soft templating, we have recently discovered the class of mesostructured imidazolate frameworks (MIFs), which combine structural elements of both coordination polymers and liquid crystalline mesophases to form hierarchical structures ordered on both the atomic- and nanoscale.^[121] MIFs are composed of zinc imidazolate chains or layers sandwiched between surfactant slabs, forming a mesoscopic layered hybrid structure similar to MCM-type lamellar silica or metal oxide mesophases.^[121, 122] Therefore, the well-known structural analogies between zeolitic imidazolate frameworks – a subclass of metal-organic frameworks – and zeolites can also be extended mesophase materials, where surfactant-directed lamellar zinc imidazolate mesophases find their analogue in MCM-50-type silica mesostructures (Fig. 4.2.1a). Lamellar MIFs have previously been obtained under reverse microemulsion conditions in the presence of the surfactant cetyltrimethylammonium bromide (CTAB). Given the structural similarities between MIFs and MCM-50 – both on the molecular level (Zn-Im-Zn vs. Si-O-Si bonding angles) and on the mesoscale (mesoscopic phase segregation into organic and inorganic lamellar domains) – design principles associated with mesostructured silica materials may ultimately enable the syntheses of MIFs with non-lamellar 3D hexagonal or cubic mesostructures.

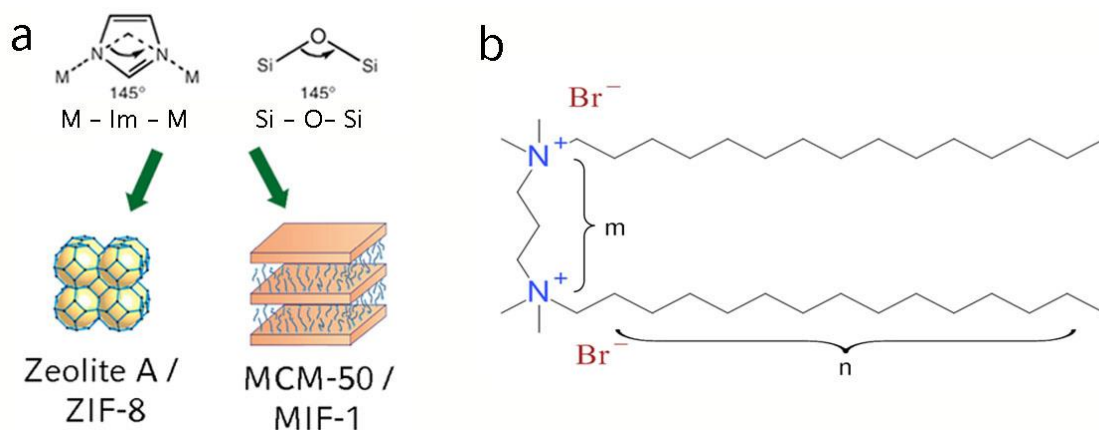


Figure 4.2.1: (a) Schematic diagram showing the similarities between ZIFs and zeolites on the one hand, and MIFs and MCM-type materials on the other hand. (b) Molecular structure of a representative gemini surfactant (here $n = 14$, $m = 4$). The spacer length m and the carbon tail length n can be altered to tune the properties of the surfactant.

Previous work on mesostructured silica materials has revealed the dominant role of the surfactant and its amphiphilic architecture and colloidal properties on the resulting mesostructures. Ryoo et al. reported the synthesis of a hierarchically nano- and mesoporous MFI zeolite, where gemini-type surfactants directed the formation of MFI nanosheets with a multilamellar structure.^[100, 188, 189] Gemini surfactants can be described by the general structure n - m - n , with n being a terminal aliphatic carbon chain and m being a linker between two quaternary nitrogen ions (Fig. 4.2.1b). Importantly, surfactant properties such as packing parameter and critical micelle concentration, which ultimately determine the micellar curvature, are a function of the size, geometry and charge density of the gemini surfactant molecules.^[109, 110, 190, 191] Earlier work on the influence of these surfactants on the formation of periodic mesoporous organosilica (PMO) has shown that n -6- n gemini surfactants ($n = 12$ -22) can form multiple mesostructures, depending on the length of the terminal carbon chains. For example, shorter chains ($n = 12$ -14) result in cubic phases, while longer chains often lead to 3D and 2D hexagonal ($n = 16$ -20) or lamellar ($n = 22$) structures.^[192] In this work, we use gemini surfactants with different lengths of their alkyl chains (from 14 to 18 carbon atoms) and spacer lengths (4 to 10 carbon atoms) to synthesize a homologous series of mesostructured imidazolate frameworks. To develop a better understanding of the mechanisms underlying MIF formation, we rely on a combination of spectroscopic analyses that provide complementary information across multiple length scales. In particular, two-dimensional solid-state nuclear magnetic resonance (NMR) spectra establish specific surfactant-framework interactions in zinc methylimidazolate – CTAB hybrid materials. The detailed insights provided by this work are expected to aid in the design of MIFs with a broader range of mesostructured compositions, topologies, and hierarchical structural ordering.

4.3 EXPERIMENTAL SECTION

4.3.1 REAGENTS & INSTRUMENTS

All reagents were commercially available and used as purchased without further purification.

Powder X-ray diffraction (PXRD) measurements were performed using a STOE *Stadi P* powder X-ray diffraction instrument, operated in Guinier geometry using a Mythen1K or an imaging plate detector. Infrared measurements were performed on a Perkin Elmer *Spektrum BX II* with an attenuated total reflectance unit. Elemental analysis was done in a thermal conductivity measurement cell of an *Elementar vario EL*. Analysis of halogenide content was done by titration with $\text{Ag}(\text{NO}_3)$ on a *Titroprocessor 672* by Metrohm. To determine the amount of zinc and other metal ions, the samples were analyzed based on optical emission of the elements in an Ar-plasma (ICP). Measurements were done on a *VARIAN VISTA* simultaneous spectrometer with autosampler and recorded with a CCD-detector. TEM measurements were performed on a Philips CM 30 ST microscope (LaB₆cathode, 300kV, C_s=1.15mm). Sample preparation was done by drop casting highly diluted samples (~ 50 µg mL⁻¹) on a carbon coated copper grid, followed by evaporation of the solvent. Solid-state NMR experiments were conducted at 11.7 T using Bruker AVANCE II and DSX-500 NMR spectrometers, both operating at frequencies of 500.24 MHz for ¹H, 125.78 MHz for ¹³C, and 50.70 MHz for ¹⁵N. The experiments were performed at room temperature under magic-angle-spinning (MAS) conditions using a 4 mm Bruker H-X double-resonance probehead and zirconia rotors. For the solid-state 2D ¹³C{¹H} HETeronuclear CORrelation (HETCOR) NMR experiments, high-power homonuclear ¹H-¹H decoupling was applied during the ¹H evolution period to enhance the resolution in the ¹H dimension, using the eDUMBO-1 pulse sequence^[193] with a phase-modulated radio frequency pulse of constant amplitude (100 kHz). The 2D ¹³C{¹H} HETCOR spectra were acquired with cross-polarization (CP) contact times of 1 ms or 5 ms, a recycle delay of 1 s, and SPINAL-64 ¹H heteronuclear decoupling (80 kHz). 128 transients (*t*₂) were signal-averaged for each of the 400 *t*₁ increments, resulting in a total experimental time of approximately 14 h for each spectrum. Thermogravimetric and differential thermal analysis measurements were performed on a combined DTA-TG-thermobalance (*Type 92-2400*, Setaram). The samples were transferred into an aluminum oxide crucible and heated from room temperature to 700 °C at a rate of 5 °C min⁻¹.

4.3.2 SYNTHESIS OF GEMINI SURFACTANTS

The gemini surfactants were synthesized by dissolving 3 mmol of the respective N,N-dimethylamine in 75 mL of acetone and adding 1.5 mmol of the respective α,ω-dibromoalkane to the solution (for details on all chemicals used see chapter 9.1, Table S1). The solution was refluxed for 4 days, leading

to the formation of a white precipitate that was obtained by centrifugation at 15000 rpm for 10 minutes. The product was dried at room temperature overnight and yielded a white, waxy substance. Purity of the obtained surfactants was confirmed by elemental analysis, IR spectroscopy and solution-state NMR.

4.3.3 SYNTHESIS OF MESOSTRUCTURED IMIDAZOLATE FRAMEWORKS

In a typical synthesis, 1 mmol of surfactant was dissolved in 25 mL of solvent (water, methanol, ethanol, 2-propanol, THF, acetone, ethylacetate, diethylether, dioxan or *n*-heptane/1-hexanol (10:1)). 0.603 mmol (603 μ L, 1 mol/L in water) zinc acetate and 0.603 mmol (335 μ L, 1.8 mol/L in water) of (methyl) imidazole were added to the solution and the resulting mixture was stirred overnight at room temperature. The formed precipitate was collected by centrifugation (20.000 rpm, 5 min), washed with 2-propanol and dried at room temperature.

4.4 RESULTS AND DISCUSSION

MIFs were obtained in the presence of *n-m-n* gemini surfactants ($n = 14-18$, $m = 4-10$, see Fig. 4.4.1b) as structure directing agents in a variety of solvents ranging from methanol to inverse microemulsion systems such as *n*-heptane/1-hexanol/water mixtures and THF. The materials could be obtained with imidazole (IM) and 2-methylimidazole (MeIM) as linkers, at room temperature as well as under reflux conditions. In order to obtain differently mesostructured materials, the ratio of IM to $\text{Zn}(\text{NO}_3)_2$ was altered between 8:1 and 1:4 and the surfactant concentration was varied between 0.01 M and 0.5 M. Although *n-m-n* gemini surfactants were reported to direct the formation of 3D cubic ($n = 16-18$, $m = 10-12$) and hexagonal ($n = 16-18$, $m = 6-10$) mesostructures in the MCM system,^[194] we found the signature of lamellar MIF mesophases in all cases, irrespective of the type of gemini surfactant/solvent combination used, over the whole range of surfactant concentrations tested. The stacking parameters varied slightly depending on the solvent used (see chapter 9.1, Table S2, Fig. S1), yet could not be correlated to specific solvent properties such as boiling point or dielectric constant. The obtained MIF phases exhibited varying degrees of crystallinity, and only a small fraction of the materials yielded powder patterns of suitable quality for indexing. Pawley refinement of the XRD pattern of 16-8-16 imidazolate MIF yielded metrics consistent with monoclinic symmetry ($C2$, $a = 11.5829 \text{ \AA}$, $b = 58.253 \text{ \AA}$, $c = 9.2415 \text{ \AA}$, $\beta = 88.94^\circ$, $wR = 7.57$, $\text{GoF} = 1.286$, chapter 9.1, Fig. S2). Similar metrics were determined for gemini-directed MIFs with $m \leq 8$. Although all samples are highly sensitive to the electron beam, transmission electron microscopy selected area diffraction (TEM SAED) data obtained for the 16-10-16 sample revealed a rectangular pattern with $a = 11.5 \text{ \AA}$ and $c = 9.2 \text{ \AA}$ and a lamellar stacking of 29 \AA along $[0k0]$ (Fig. 4.4.1), which is in principle agreement with the powder data. The doubled stacking parameter along b that can be observed in the Pawley fit may

be rationalized by a superstructure, which prominently was observed for MIFs based on gemini-surfactants with $m \leq 8$. The absence of higher order stacking reflections at around $2\theta = 5^\circ$ in hybrid materials with shorter linkers may be due to the discussed superstructure effects or accidental extinction.^[188, 195]

Elemental analysis revealed a composition of all hybrid materials of zinc : IM/MeIM : bromine : surfactant of 1:1:2:0.5, corresponding for example to the empirical formula $\text{Zn}_2\text{Br}_4(\text{C}_3\text{H}_3\text{N}_2)_2(\text{C}_{46}\text{H}_{96}\text{N}_2)$ for the 16-10-16 imidazolate MIF. (chapter 9.1, Table S3) The synthesized materials show good thermal stability up to $\approx 320^\circ\text{C}$ (chapter 9.1, Fig. S3), as well as chemical stability, withstanding even surfactant extraction procedures with supercritical CO_2 , yet showing the typical sensitivity of MOFs towards acids. Upon acid-induced decomposition of the material, the pristine surfactants and imidazoles were recovered, proving that all MIF constituents stay intact during the entire synthesis process.

Our data therefore suggest that all gemini-directed materials are composed of the same principal building units like the prototypic MIF-1,^[121] as sketched in Figure 4.4.1. The formerly proposed structure model consists of one-dimensional zinc-imidazolate chains with additional coordination of two bromine ions to the metal center. These chains of corner sharing tetrahedra are interleaved with surfactant layers, thus forming quasi two-dimensional layered assemblies. This structural motif for the zinc imidazolate subunit has previously been reported by Lin et al. in a coordination polymer without incorporated surfactant molecules.^[196, 197] Combination of the developed structure model with the metrics obtained from the Pawley fit shows good accordance between both (Fig. 4.4.1).

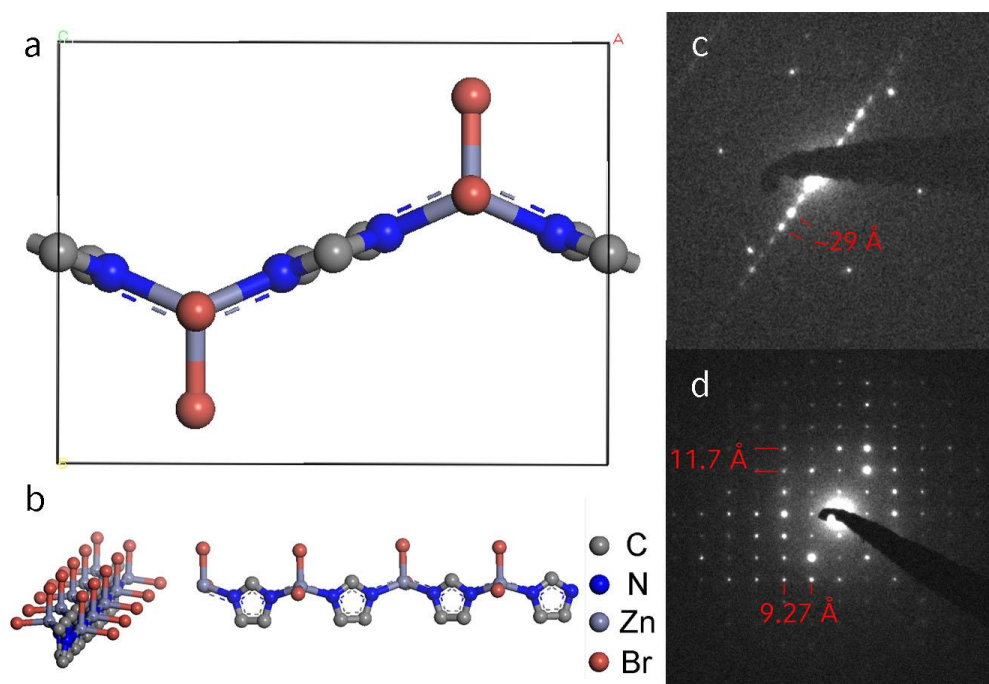


Figure 4.4.1: (a) Structure model of the zinc imidazolate bromide chain viewed along the *b*-axis and (b) along / onto the chains. (c,d) TEM SAED images of 16-6-16 IM MIF (c) perpendicular to the [010] direction and (d) of the (101) plane.

A solid-state ^{13}C MAS NMR spectrum of the 16-10-16 MeIM MIF material (Fig. 3b) exhibits two distinct high-frequency signals for MeIM ($\delta = 149.4, 125.1$ ppm for C3-C1), similar to the ^{13}C signals observed for ZIF-8 ($\delta = 150.0, 125.2$ ppm).^[121] The ^{13}C signals corresponding to the surfactant ($\delta = 67.1, 48.2, 43.0, 32.0, 29.8, 26.3, 23.0, 15.8, 14.8$ ppm), as well as those for MeIM are in good agreement with the ^{13}C signals previously reported for MIF-1 (Fig. 4.4.2a).^[121] The solid-state ^{15}N MAS NMR spectrum of the 16-10-16 MeIM MIF (Fig. 4.4.2d) exhibits two distinct ^{15}N signals associated with the surfactant head groups (-323.5 ppm) and the methylimidazolate ion (-168.4 ppm), respectively, consistent with similar local environments for both types of ammonium groups and both imidazolate nitrogen atoms.

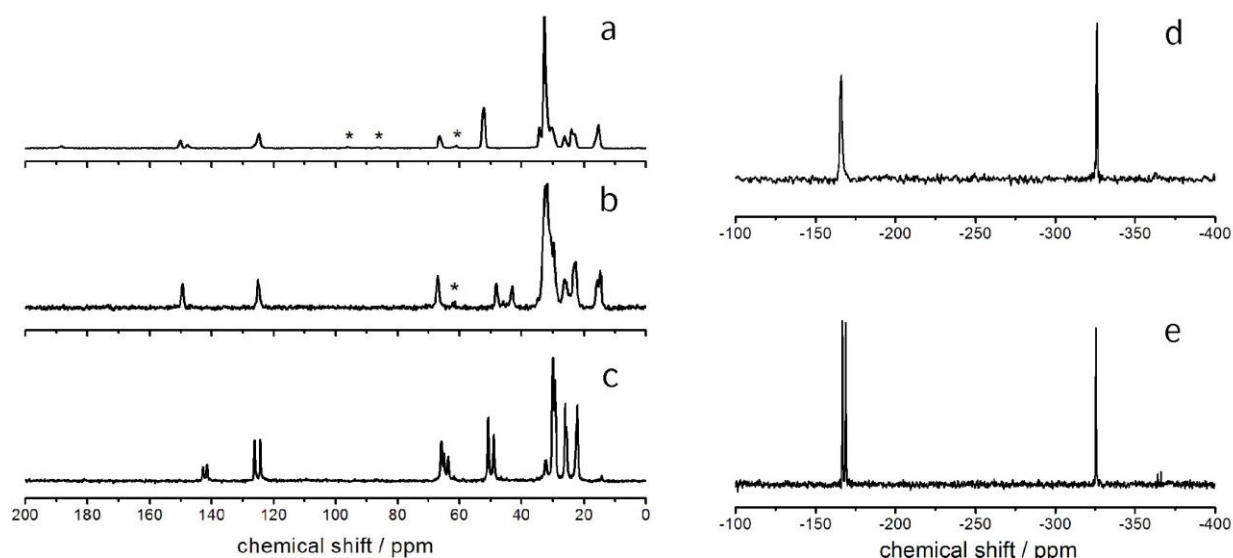


Figure 4.4.2: Solid-state ^{13}C MAS NMR spectra of (a) MIF-1,^[121] (b) 16-10-16 MeIM MIF and (c) 14-6-14 IM MIF and solid-state ^{15}N MAS NMR spectra of (d) 16-10-16 MeIM MIF and (e) 14-6-14 IM MIF. Asterisks indicate spinning side bands

For the 14-6-14 IM MIF material, additional signals are observed in the ^{13}C MAS NMR spectrum, revealing the presence of different ^{13}C local environments. As shown in Figure 4.4.2c, two different pairs of well-resolved ^{13}C signals are observed for the imidazolate carbon atoms (143.1 and 141.6 ppm, 126.1 and 124.4 ppm). These distinct pairs of ^{13}C signal intensities are consistent with two inequivalent ^{13}C local environments for the imidazolate species, likely due to superstructure effects, such as ABA-type stacking of the surfactant-inorganic slabs. Such a stacking arrangement would also give rise to a doubled b -axis as found for other hybrid materials^[198] and for pure CTAB.^[199] Interestingly, similar experiments on CTAB-directed MIF-1 (Fig. 4.4.2a) also exhibit two distinct ^{13}C signals (149.0 and 151.0 ppm) for the sp^2 carbon atom bonded to the nitrogen atoms of the methylimidazole moieties. These results, along with a detailed 2D NMR analysis of MIF-1, are discussed below.

Subtle but distinct differences are also observed in the ^{15}N local environments of the 14-6-14 IM MIF, as evidenced by ^{15}N MAS NMR (Fig. 4.4.2e) and consistent with the ^{13}C NMR analyses above. Two well-resolved and equally intense ^{15}N signals associated with the imidazolate nitrogen atoms are observed at -166.4 and -168.9 ppm for the 14-6-14 IM MIF, whereas only one corresponding ^{15}N signal (-166.2 ppm) is observed for the 16-10-16 MeIM MIF (Fig. 3d). These results indicate that the local environments of the imidazolate species are highly sensitive to surfactant architecture, such as spacer length, leading to inequivalent imidazolate and surfactant interactions predominantly for materials synthesized using surfactants with shorter spacers ($m \leq 8$).

The gemini MIFs obtained by syntheses with n - m - n gemini surfactants ($n = 14, 16, 18$; $m = 4$ -10) all exhibit similar layered zinc-imidazolate structures separated by surfactant molecules, while the stacking parameter of the mesostructures differs for the surfactants used. All synthesized materials exhibit a lamellar mesostructure, with layer stacking distances varying between 25.4 Å and 35.6 Å for IM bridged systems and between 25.3 Å and 35.9 Å for MeIM bridged systems, respectively, depending on the used surfactants (Fig. 4.4.3). We find that the stacking of the material depends on both the surfactant tail length (n) as well as on the length of the spacer (m), indicating a tilted arrangement of the surfactants with respect to the zinc-imidazolate slabs. Our data show a direct correlation between the d -spacing and the tail length, with an increase in d -spacing by 1.7 ± 0.3 Å for an increase of the tail length by two carbon atoms (Fig. 4.4.3, chapter 9.1, S4 and Table S4). The observable lamellar stacking also increases with longer spacer lengths, but by a variable amount depending on the used spacer. Whilst the stacking distance increases by 4.6 Å when switching from $m=9$ to $m=10$ in 18- m -18 IM MIFs, the lamellar stacking decreases by ≈ 0.1 Å when switching from $m=7$ to $m=8$ in the same MIF system.

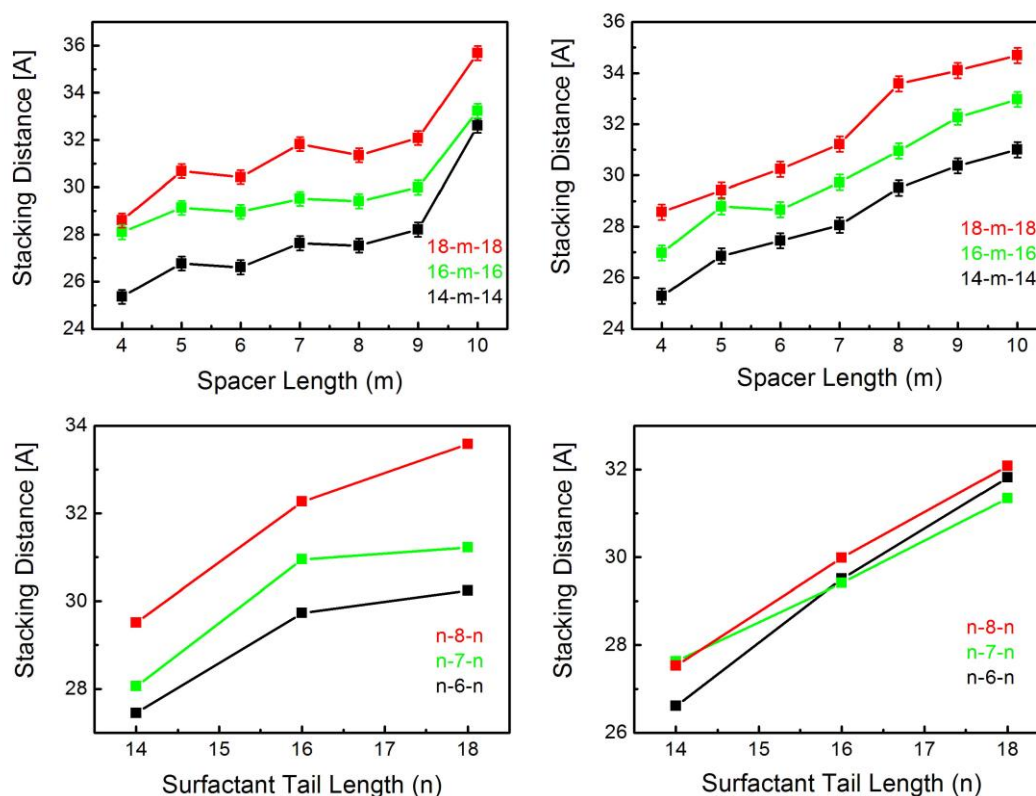


Figure 4.4.3: Graphical presentation of the d -values corresponding to the first observable stacking reflection in the PXRD measurements of all synthesized MIF materials as a function of spacer length (top) and tail length (bottom). Left: IM bridged MIFs, right: MeIM bridged MIFs.

A closer look at the proposed structure of the MIF materials provides an explanation for this phenomenon. The distance between two $[\text{ZnBr}_2]^-$ -units is roughly 6 Å, which is in good agreement with the distance between the two quaternary nitrogen ion headgroups of a $m = 5$ gemini surfactant. Up to a linker length of $m = 9$, we see that the surfactants appear to gradually tilt further away from the neighbouring $[\text{Zn}(\text{Me})\text{IMBr}_2]^-$ -units in order to comply with the charge density of the inorganic slabs (chapter 9, Scheme S5). The sudden increase in stacking distance at $m = 10$ for IM (Fig. 4.4.3, left) is likely accompanied by a more abrupt structural rearrangement, such as an increase in the tilt angle α , leading to a more perpendicular alignment of the surfactants with respect to the layers and, hence, increased d -spacing.

The tilted arrangement of the gemini surfactants seems contradictory to our previous observations, as this asymmetric arrangement of the surfactants is expected to manifest distinct ^{15}N NMR signals for the two nitrogen atoms of the gemini head groups due to differences in local environments of the two alkylammonium ions. However, the alkyl-groups surrounding the nitrogen atoms may well “screen” them and provide an overall similar local environment, rendering them less susceptible to direct interactions with the coordination polymer chains.

To complete our structural model of gemini-directed MIFs, we assume that the two surfactant carbon tails are oriented in a close-to-parallel conformation, in agreement with previous work on

gemini-surfactants with spacer sizes $m > 3$.^[101] This leads us to propose a model of the surfactant location in the material with both carbon tails parallel to each other with a fixed angle α of about 43° between the surfactant tail and the zinc imidazolate layers (chapter 9.1, Fig. S6).

Previously synthesized prototypic MIFs differ from the materials presented in this work only with respect to the type of surfactant used (alkyl ammonium vs gemini alkyl ammonium), the resulting d -spacings and the apparent structural order, as indicated by the presence of high-angle reflections in the PXRD data of the gemini surfactants as opposed to those of CTAB-directed MIF-1. Despite their similar composition (ratio of inorganic and organic building blocks) and mesostructure, we assume a more rigid anchoring of the doubly cationic ammonium head groups of the gemini surfactants to the inorganic slabs as compared to CTAB-directed MIFs, stabilized by multiple hydrophobic interactions of the antiparallel interdigitated surfactant layers.^[200]

To gain additional insights about the locations and interactions of the surfactants within MIF-type materials, solid-state 2D $^{13}\text{C}\{^1\text{H}\}$ HETeronuclear CORrelation (HETCOR) NMR measurements were performed on a CTAB-directed MIF material (MIF-1). MIF-1 was used instead of the gemini-directed MIFs because the CTAB-based system is less complicated and exhibits similar molecular-level interactions between different organic and inorganic moieties. Interactions among chemically distinct species in heterogeneous zinc imidazolate materials can be established by solid-state 2D NMR techniques that are sensitive to dipole-dipole couplings between molecularly proximate moieties. Here, solid-state 2D $^{13}\text{C}\{^1\text{H}\}$ HETCOR NMR spectra provide specific local and molecular-level information on CTA⁺-framework interactions in as-synthesized MIF-1. Furthermore, the intra- and intermolecular interactions can be distinguished by experimentally varying the ^{13}C - ^1H cross-polarization contact time from short (e.g., 1 ms) to long (e.g., 5 ms) durations, respectively.

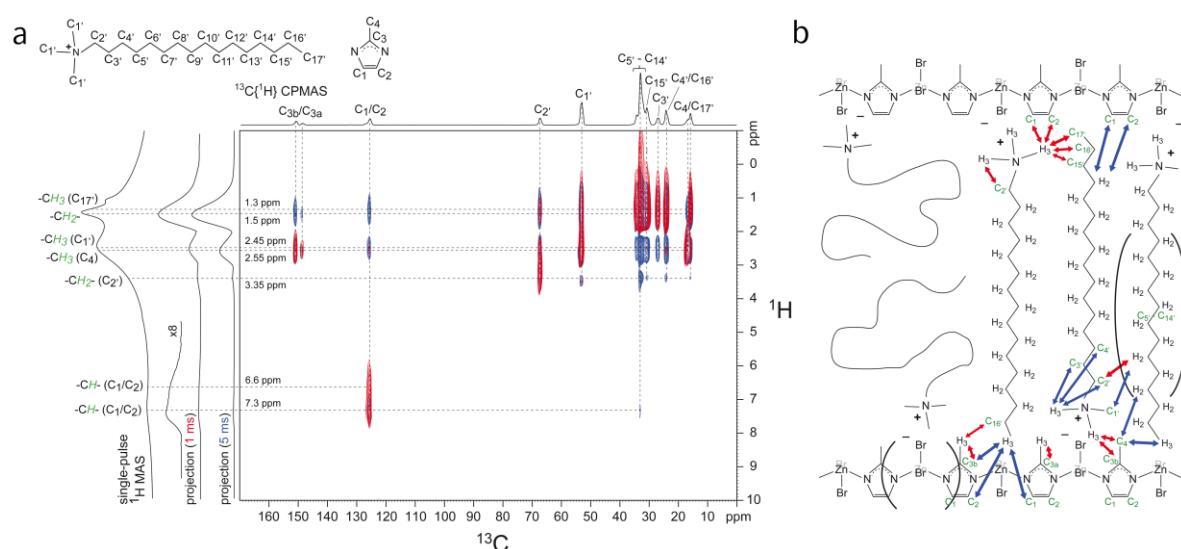


Figure 4.4.4: (a) Solid-state 2D $^{13}\text{C}\{^1\text{H}\}$ HETCOR NMR spectra acquired at room temperature for as-synthesized MIF-1 under MAS conditions of 12.5 kHz with 1 ms (red) or 5 ms (blue) cross-polarization (CP) contact times. For comparison, 1D single-pulse ^1H MAS and 1D $^{13}\text{C}\{^1\text{H}\}$ CPMAS spectra are shown along the vertical and horizontal axes, respectively, of the 2D

spectra. Schematic diagrams of the CTA⁺ surfactant and methylimidazole molecules are shown and their corresponding ¹³C and ¹H signal assignments are indicated in the 1D spectra. **(b)** Schematic diagram of MIF-1 (Zn/MeIM/CTAB) showing interactions between the zinc imidazolate chains and the CTA⁺ molecules that are consistent with the 2D ¹³C{¹H} HETCOR NMR analyses. Carbon and hydrogen atoms are labeled according to the assignments in Figure 1. Red and blue arrows indicate ¹³C-¹H dipolar interactions at short (1 ms) and long (5 ms) contact times, respectively. Note that Zn and Br atoms oriented into the page are colored gray. A fraction of the CTA⁺ molecules are thought to be interdigitated with an antiparallel stacking arrangement.

The solid-state 2D ¹³C{¹H} HETCOR NMR spectra in Figure 5a of as-synthesized MIF-1 exhibit strong and distinct intensity correlations between ¹³C and ¹H nuclei associated with the CTA⁺ surfactant molecules and the zinc-imidazolate-bromide sheets. A 1D ¹³C{¹H} CPMAS NMR spectrum is shown above the horizontal axis, along with ¹³C signal assignments corresponding to the various ¹³C species of the CTA⁺ surfactant and the methylimidazole moieties. Two 2D NMR spectra conducted with short (1 ms) and long (5 ms) CP contact times are shown in red and blue, respectively, for comparison. The 2D signal intensities observed for the short contact time arise from strongly dipolar-coupled nuclei that are associated principally with intramolecular interactions from covalently bonded ¹³C and ¹H nuclei. Strong intensity correlations are observed between the ¹³C signal of the methylimidazole aromatic carbon atoms (*C*₁/*C*₂) at 126 ppm and the ¹H signals at 6.6 ppm and 7.3 ppm corresponding to their aromatic protons, as expected. Similarly, correlated signal intensity is observed at 16 ppm (*C*_{17'}), 17 ppm (*C*₄), and 53 ppm (*C*_{1'}) in the ¹³C dimension associated with distinct methyl groups at 1.3 ppm, 2.55 ppm, and 2.45 ppm in the ¹H dimension from their respective covalently bonded hydrogen atoms. Additionally, 2D intensity correlations are observed at 67 ppm (*C*_{2'}) and 25–35 ppm (*C*_{3'}-*C*_{16'}) from alkyl chain ¹³C atoms with the ¹H signals at 3.35 ppm and 1.5 ppm, associated with the alkyl protons of the CTA⁺ molecules. Together, these intramolecular 2D intensity correlations allow the numerous partially resolved ¹³C and ¹H signals to be unambiguously assigned to as-synthesized MIF-1.

More interestingly, correlated signal intensity from intermolecular interactions between ¹³C and ¹H nuclei on different molecular species provide complementary information concerning the proximities of the CTA⁺ surfactant and the methylimidazole framework moieties. Correlated signal intensity is observed for a short cross-polarization contact time (1 ms, Fig. 4.4.4a, red) at 17 ppm (*C*₄) and 126 ppm (*C*₁/*C*₂) in the ¹³C dimension from the anionic zinc methylimidzolate chains and at 2.45 ppm in the ¹H dimension associated with the cationic CTA⁺ head group; these results are consistent with the expected charge-balancing electrostatic interactions between the surfactant species and the MIF-1 framework. In the accompanying 1D ¹³C{¹H} CPMAS spectrum, the two well-resolved ¹³C signals at 149 ppm and 151 ppm indicate the presence of two inequivalent ¹³C environments (*C*_{3a} and *C*_{3b}) associated with the *sp*² carbon atom bonded to the nitrogen atoms of the methylimidazole moieties.

This is clearly evidenced in the 2D HETCOR spectrum, in which different intensity correlations are observed for these ^{13}C signals: while they both are correlated with the ^1H signal at 2.55 ppm from the methyl protons of the methylimidazole group (C_4), only the ^{13}C signal at 151 ppm (C_{3b}) is correlated with the ^1H signal at 2.45 ppm from the CTA^+ head groups. This indicates that there are two distinct types of methylimidazole C_3 moieties, which differ according to their respective proximities to the CTA^+ head groups. Interestingly, the ^1H signal at 2.45 ppm from the CTA^+ head groups is also correlated with the alkyl ^{13}C signals at 16 ppm ($\text{C}_{17'}$), 24 ppm ($\text{C}_{16'}$), and 31 ppm ($\text{C}_{15'}$) associated with the ends of the CTA^+ alkyl chains; these specific intensity correlations reflect an interdigitated arrangement of a fraction of CTA^+ molecules where the head group and tail are in close proximity to each other, an arrangement known from the surfactant crystal structure. For this short contact time, correlated signal intensity is also observed between the ^1H signal at 2.55 ppm from the methyl protons of the methylimidazole moiety (C_4) and the ^{13}C signal at 24 ppm ($\text{C}_{16'}$) from the penultimate carbon atom on the end of the CTA^+ alkyl chain, which corroborates the interdigitated arrangement of some of the surfactant species. The molecular-level insights provided by these short-range intermolecular correlations (red arrows) are depicted in the schematic diagram in Figure 4.4.4b.

For a longer contact time (5 ms), the 2D $^{13}\text{C}\{^1\text{H}\}$ HETCOR NMR spectrum (Fig. 4.4.4a, blue) acquired under otherwise identical conditions yields correlated signal intensity from more weakly coupled ^{13}C and ^1H nuclei (for reasons of internuclear distance or molecular mobilities). Intensity correlations are observed for the ^{13}C signal at 126 ppm (C_1/C_2) with the ^1H signal at 1.3 ppm, revealing that the aromatic carbons (C_1/C_2) of the methylimidazole are also molecularly proximate to the methyl protons of the CTA^+ tail. As observed and discussed above, the blue spectrum also reveals 2D signal intensity between both of the ^{13}C signals at 149 ppm (C_{3a}) and 151 ppm (C_{3b}) and the ^1H signal at 1.5 ppm associated with the CTA^+ alkyl protons, while only the C_{3b} carbon atom is molecularly close to the CTA^+ tail, based on the intensity correlation between the ^{13}C signal at 151 ppm and the ^1H signal at 1.3 ppm. This difference between the two distinct signals for C_3 indicates a high degree of order in the material if the antiparallel arrangement of the surfactant chains is taken into account. These longer-range intermolecular correlations are depicted by the blue arrows in the schematic diagram of Figure 4.4.4b.

Collectively, the NMR results offer complementary and additional insights to previous X-ray diffraction analyses of MIF-1, which characterize the long-range order of the materials, though are insensitive to structural disorder or order that is present only locally (e.g., several nm). In particular, the absence of XRD reflections at high 2θ values – as opposed to the gemini-type MIFs – is consistent with a rather high degree of surfactant disorder commonly observed for other CTA^+ -directed mesostructured oxide materials.^[201, 202] Nevertheless, the 2D $^{13}\text{C}\{^1\text{H}\}$ HETCOR NMR spectra establish that the head group moieties of the cationic CTA^+ surfactants interact strongly with the anionic zinc

imidazolate framework, as previously observed for closely related CTA⁺-directed silicates with lamellar mesoscopic ordering.^[201, 202] However, whereas the surfactant chains are highly disordered in the layered CTA⁺-silicate materials, MIF-1 has a significant fraction of its CTA⁺ molecules that appear to be interdigitated between the zinc methylimidazolate chains with an anti-parallel stacking arrangement (Fig. 4.4.4b), as likewise inferred for the gemini-directed MIFs. Similar interdigitated, antiparallel arrangements of alkyl side chains on supramolecular assemblies of (linear) semiconducting polymers in bulk heterojunction materials have been observed, where the degree of ordering of the domains has a significant influence on the charge transfer properties.^[203, 204] The discrepancy between the order observed in the 2D NMR experiments and apparent absence of order at the molecular level in the PXRD experiments can be explained in two ways: First, CTA⁺ is an organic species that exhibits lower scattering factors compared to the inorganic layers, thus resulting in low scattering intensity especially at higher angles in the PXRD patterns. Secondly, the antiparallel arrangements of the alkyl side chains may be (confined to small domains and) broken up by significant conformational disorder, and therefore not detected by XRD methods.

To assess the importance of the halogenide counter-ions on the formation of lamellar MIF mesophases, the syntheses were conducted with gemini surfactant molecules without halogenide counter-ions. (The bromine counter-ions were exchanged by nitrate ions via treatment with AgNO₃.) For all combinations of solvents and surfactant concentrations tested, no mesostructured products were formed in the absence of the halogenide counter-ions, under otherwise identical conditions. By comparison, syntheses conducted with chlorine counter-ions yielded MIF products (chapter 9.1, Fig. S7). These results corroborate the important role of the halogenide counter-ions in syntheses of the MIF materials. In addition, the presence of the surfactant molecules appears to hinder the formation of ZIF structures, such as ZIF-8, which are typically obtained by mixing zinc nitrate and imidazole in methanol.^[205] However, adding halogenide ions to a reaction mixture containing methanol, zinc acetate, imidazole and surfactants with nitrate counter-ions led to the formation and rapid precipitation of a MIF product. Collectively, these observations underscore the importance of halogenide ions in the MIF syntheses.

Previously, a liquid crystal templating mechanism was proposed for the formation of MIF materials, according to which the mesostructure is directed by the surfactant molecules, while the coordination polymer nucleates and grows within the water reservoirs of the lamellar surfactant mesophase.^[121] As the curvature of the micellar structure formed by gemini surfactants is strongly dependent on the lengths of the tail and linker chains and is highly sensitive to the surfactant concentration and solvent composition,^[104, 190] this formation mechanism should in principle result in a wide variety of mesostructures, which is not observed in the present case where exclusively lamellar nanomorphologies are obtained. We therefore propose a formation mechanism in which the one-

dimensional structure composed of negatively charged $[\text{Zn}(\text{Me})\text{IMBr}_2]^-$ chains is formed first. These then assemble with the positively charged gemini surfactants by an electrostatically driven cooperative assembly process familiar from various MCM-type systems^[206], resulting in the 2D slab-like structures of the final lamellar mesostructured material (Fig. 4.4.5). Since the quasi-linear geometry of the zinc bromide imidazolate chains with vanishing curvature seems to direct and drive the mesostructure assembly, the formation of exclusively lamellar mesostructures with zero curvature is hence expected.

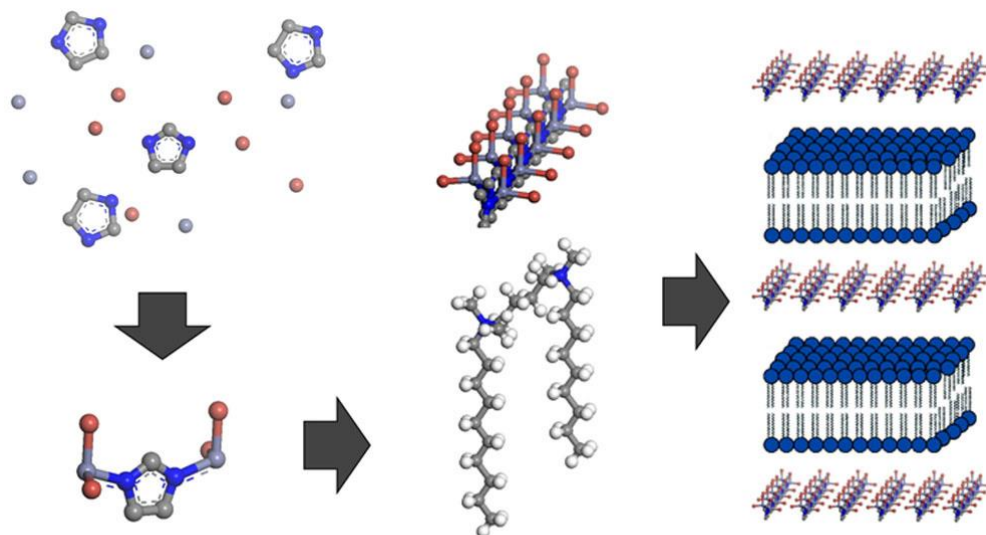


Figure 4.4.5: Proposed formation of MIF materials by electrostatically-driven cooperative self-assembly. Upon addition of bromide to the solution containing imidazole, zinc and the surfactant, one-dimensional chains form and arrange into quasi two-dimensional layers, intercalated by surfactant ions for charge compensation. Note that the surfactants are omitted on the left-hand side for clarity.

4.5 CONCLUSIONS

The solid-state NMR analyses yield detailed atomic-level insights on the structures of metal imidazolate framework materials, which support previously proposed structural models. Specifically, surfactant bilayers between the layers of one-dimensional zinc-imidazolate chains charge-compensate the chain structure. Although our efforts to obtain cubic or hexagonal mesostructured MIFs have so far been unsuccessful, the proposed formation mechanism of the gemini-directed MIFs – electrostatically driven co-assembly governed by the formation of linear zinc bromide imidazolate chains – sheds light on why exclusively lamellar structures have been found so far in the MIF system. The roles of halogenide counterions in surfactant-assisted syntheses MIF and ZIF materials are established, along with their influences on the selectivity and nanoscale morphologies of MIF versus ZIF products. These results have general implications for syntheses of nano- mesostructured

imidazolate framework materials and the molecular-level interactions that are responsible for the assembly and crystallization of their ordered frameworks.

4.6 ACKNOWLEDGEMENTS

Financial support from the Max Planck Society, the cluster of excellence “Nanosystems Initiative Munich” (NIM), the Center for NanoScience (CeNS), Chevron Energy Technology Company, and the U.S. National Science Foundation Graduate Research Fellowship under Grant no. 1144085 are gratefully acknowledged. The solid-state 2D NMR experiments were conducted at the UCSB MRL Shared Experimental Facilities, which is supported by the MRSEC Program of the NSF under award no. DMR-1121053. We thank C. Minke, V. Duppel, and C. Ziegler for their assistance with the material analyses and an MPG-UCSB exchange program that led to this collaborative work.

5 INTRODUCING FUNCTIONALITY INTO 2D EXFOLIABLE COORDINATION FRAMEWORKS

5.1 INTRODUCTION

The advances in studies of low-dimensional nanostructures have sparked large research interest due to the influence of size confinement effects and amplified surface areas on material properties and their applications.^[207] The following chapter describes the synthesis and exfoliation of a series of two-dimensional coordination polymers, based on $\text{Zn}[\text{BeIm}]\text{OAc}$ and $\text{BeIm-MIF}(\text{OAc})$, which were first introduced by Junggeburth et al. in 2013.^[122]

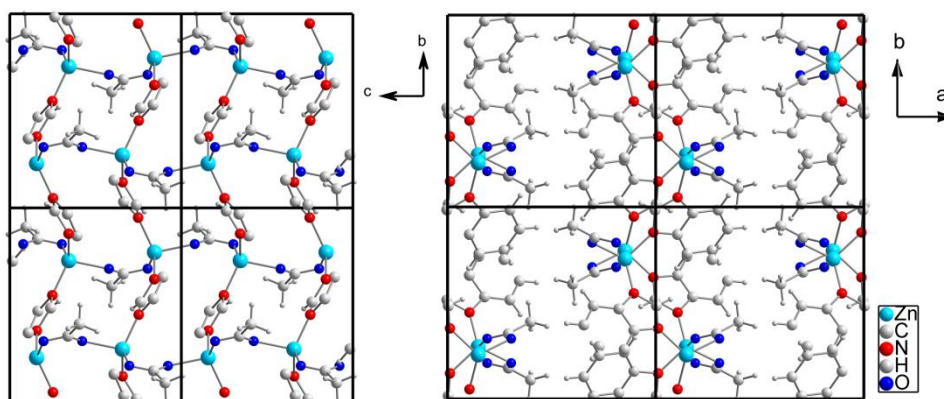


Figure 5.1.1: Crystal structure of $\text{Zn}[\text{BeIm}]\text{OAc}$ viewed along $[100]$, highlighting the 2D network structure (left), and along $[001]$, showing the interaction of the layers by van-der-Waals forces.

All presentend structures are based on the poly $[\mu_2\text{-acetate-}\mu_2\text{-benzimidazolato-zinc(II)}]$ coordiantion polymer, a material that has been discovered in 2007 by Li et al.^[208, 209] The structure consists of a two-dimensional network of zinc ions, which are coordinated by two benzimidazoles, resulting in one-dimensional chain-like structures. The chains are interconnected by acetate ions, bridging between the zinc centers of two neighbouring chains, which leads to a two-dimensional layered structure. The layers are helt together along the a -axis of the crystal structure by van-der-Waals forces. The metal-organic framework, which crystallizes in the space group $P2_1/c$ with $a = 10.81 \text{ \AA}$, $b = 9.83 \text{ \AA}$, $c = 8.81 \text{ \AA}$ and $\beta = 98.96^\circ$, was recently reported to be readily exfoliable into nanosheets

via a microemulsion synthesis approach based on the intercalation of CTAB between the sheetlike coordination polymer structure as a structure directing agent.^[122]

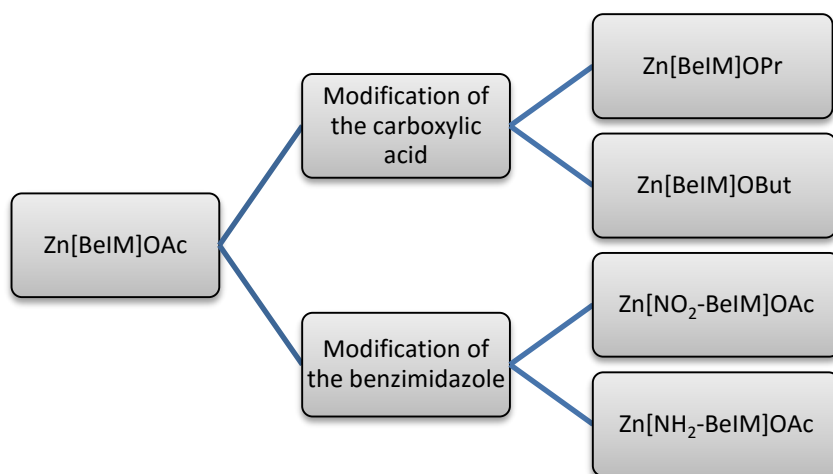


Figure 5.1.2: Schematic overview of the experiments performed as part of this chapter, showcasing the different modification approaches taken.

Whilst the first parts of this chapter describe the efforts of synthesizing materials with different carboxylic acids (chapter 5.2) or benzimidazolates (chapter 5.3), the later parts present the results of exfoliation experiments (chapter 5.4) and post-synthetic modification reactions on the obtained amino-functionalized material (chapter 5.5).

5.2 MODIFICATION OF THE ACETATE GROUPS

In the first part of this chapter, experiments aimed at replacing acetate in the material with other carboxylic acids in order to examine the effects of the longer carbon backbones on the structure, properties and the possibility to exfoliate the material.

The methyl-groups of the acetate ions are oriented parallel to the *a*-axis, thus by exchanging the acetate linkers with propionate or butyrate ions, an elongation of the crystal structure along *a* is to be expected. By elongating the *a*-axis through the use of longer carboxylic acid linkers, the interlayer-distance between the zinc-benzimidazolate backbones of the framework is increased, hence exfoliation should be facilitated due to reduced van-der-Waals forces as a result of the increased average distance between the benzimidazolate ring systems. Taking into account that the coordination spheres, angles and other in-plane parameters of the structure remain unchanged while altering the carboxylic acid, a structurally closely related material to the parent Zn[BeIM]OAc is expected to be formed.

Previous experiments performed in our group by Junggeburth, showed that the desired materials can be formed in Solid-state reactions, as Zn[BeIM]OPr and Zn[BeIM]OBut could be synthesized via this way. However due to the limitations for surfactant use in Solid-state syntheses, exfoliation of the synthesized materials into nanosheets was not achieved.^[210]

5.2.1 Zn[BeIM]OPr

By replacing zinc acetate ($\text{Zn}(\text{OAc})_2$) with zinc propionate ($\text{Zn}(\text{OPr})_2$), whilst leaving all other reaction parameters identical to the known synthesis procedure (see Chapter 5.7 for experimental details), a white crystalline powder was obtained. The powder pattern of the isolated product, named Zn[BeIM]OPr, is depicted in Figure 5.2.1. The obtained pattern neither contains signs of starting materials nor does it correspond to a known ZIF-structure.

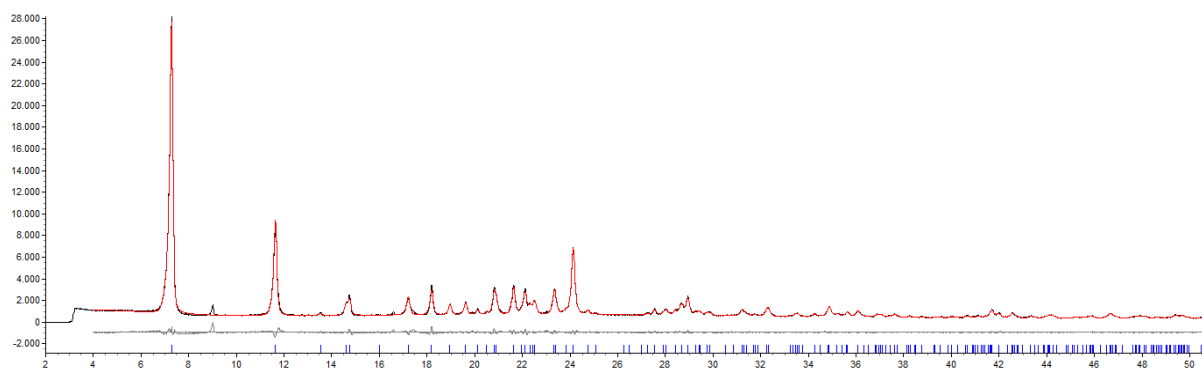


Figure 5.2.1: Pawley fit of the XRD powder pattern of Zn[BeIM]OPr, yielding space group and lattice parameters $P2_1/c$ with $a = 12.23 \text{ \AA}$, $b = 9.75 \text{ \AA}$, $c = 8.90 \text{ \AA}$ and $\beta = 97.47^\circ$ (GoF: 1.818).

Indexing and Pawley fitting of the obtained pXRD data was possible, confirming the synthesis of a phase pure material which crystallizes in $P2_1/c$ with $a = 12.23 \text{ \AA}$, $b = 9.75 \text{ \AA}$, $c = 8.90 \text{ \AA}$ and $\beta = 97.47^\circ$ (GoF: 1.818). The lattice parameters equal those of Zn[BeIM]OAc, with the exception of an elongated a-axis from 10.81 \AA to 12.23 \AA ($\Delta a = +1.41 \text{ \AA}$), which is in good agreement with the expected effects of using a carboxylic acid with a prolonged carbon backbone. The in-plane b- and c-axes show almost no deviation compared to Zn[BeIM]OAc ($\Delta b = -0.087 \text{ \AA}$, $\Delta c = +0.083 \text{ \AA}$), which confirms the assumption that the formed Zn[BeIM]OPr is featuring the same connectivity pattern as the parent material Zn[BeIM]OAc.

The peak at $2\theta = 9^\circ$ can however not be explained with the proposed space group. This peak is a first indication of a loss in symmetry, that could be observed for Zn[BeIM]OBut as well and is explained in detail in chapter 5.2.2. Due to the increasing length of the carboxylic acid backbone and the thereby created disorder in the arrangement of the carboxylic chain in the crystal structure, the glide plane found in $P2_1/c$ is resolved and the material crystallizes in $P2_1$ instead. This effect is only marginally observable in Zn[BeIM]OPr by the small, afore mentioned peak.

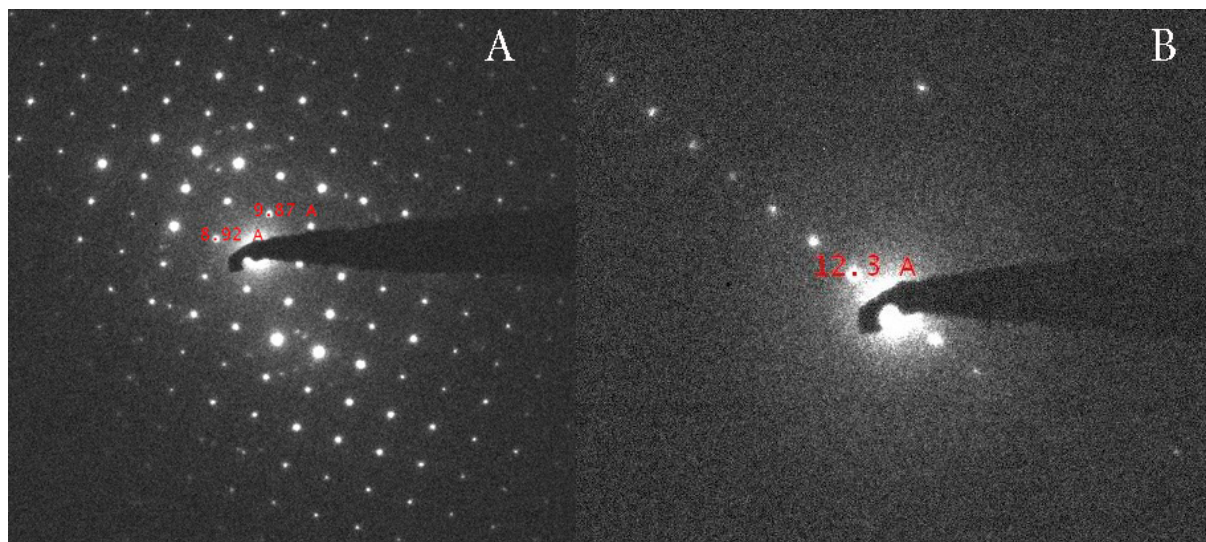


Figure 5.2.2: TEM SAED measurements of Zn[BeIM]OPr showing (A) the in-plane lattice parameters of the (100)-plane (9.87 Å and 8.92 Å) as well as (B) the stacking parameter of 12.30 Å along the a-axis of the crystal structure.

In order to confirm these results, TEM SAED measurements were performed on the material (Fig. 5.2.2). As known from other coordination polymers, the material is highly sensitive to the electron beam and decomposes rapidly upon irradiation. To address this sensitivity problem, all measurements were performed without prior alignment by scanning random points on the sample. The occurring decomposition even during short acquisition times results in a low signal to noise ratio of the measurements and the missing alignment prior to the measurements limits the accuracy of the measurements.

Despite the difficulties during acquisition, the observed diffraction patterns confirm the unit cell parameters obtained from pXRD measurements, with an orthogonal pattern of 8.92 (± 0.45) Å \times 9.87 (± 0.49) Å and a stacking parameter of 12.30 (± 0.62) Å, which is in good agreement with previously discussed values.

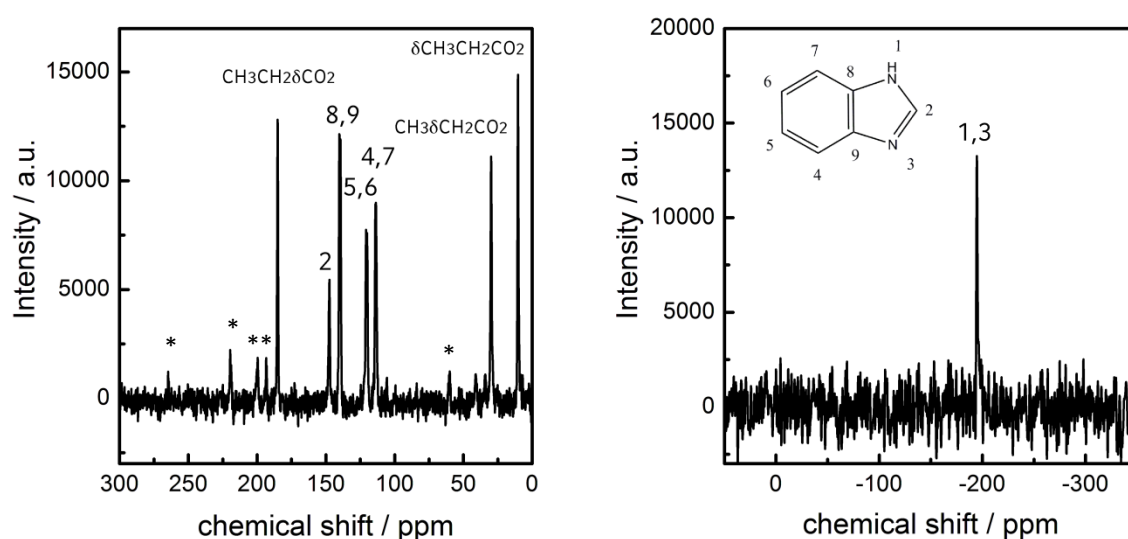


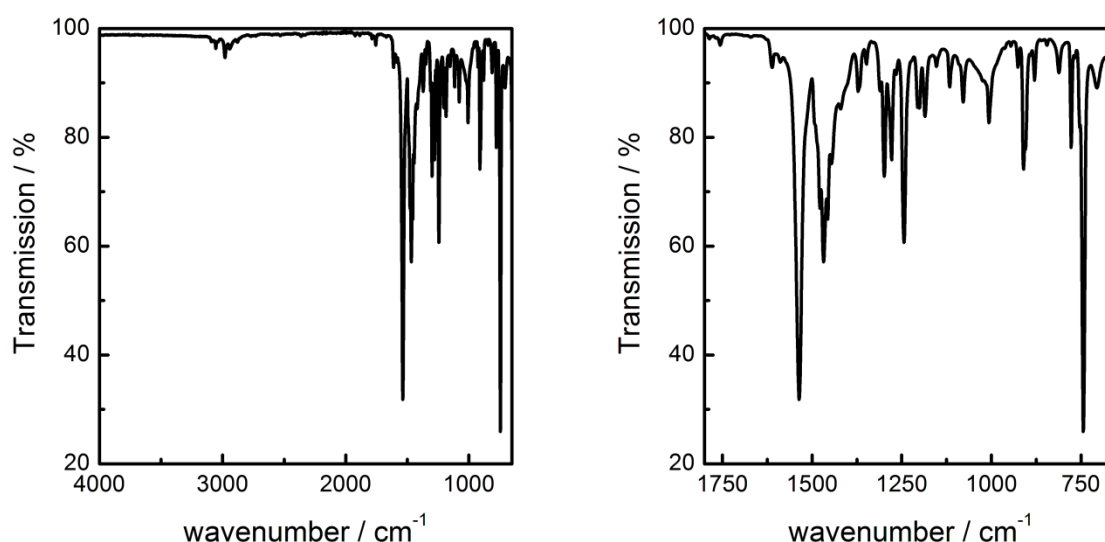
Figure 5.2.3: ^{13}C (left) and ^{15}N MAS (right) Solid-state NMR spectra of $\text{Zn}[\text{BeIm}]\text{OPr}$. Spinning side bands are marked with an asterisk.

To confirm the composition of the obtained material, ^{13}C MAS Solid-state NMR was performed (Fig. 5.2.3). Both spectra solely exhibit the signals of benzimidazolate and the propionate ions. In the range between 150 and 110 ppm, the signals of BeIm can be identified, with a shift to lower field when compared to BeIm(H). The largest shift is found for the signal corresponding to C2, located in between the coordinating nitrogen atoms, which is shifted from 141.5 ppm in BeIm(H) to 147.4 ppm, thus indicating the presence of anionic benzimidazolate as the only BeIm-species in the material. Comparing the observed chemical shifts of the benzimidazolate to those observed in the BeIm-based ZIF-7, a consistent upfield shift for the signals corresponding to $\text{Zn}[\text{BeIm}]\text{OPr}$ can be observed due to the electronic effects of the propionic acid. The splitting of the signals for C5, C6, C8 and C9, that is present in ZIF-7 Solid-state NMR measurements can not be observed for $\text{Zn}[\text{BeIm}]\text{OPr}$, thus leading to the assumption that all benzimidazolate species in the material have identical chemical surroundings. The assignment of the observed chemical shifts to the corresponding carbon signals can be found in Table 5.2.1. The signals of the anionic propionate are found at 10.4 ppm, 29.8 ppm and 185.3 ppm, respectively, which corresponds to a slight downfield shift when compared to $\text{Zn}(\text{Pro})_2$ (9.1 ppm, 26.5 ppm, 185.3 ppm).

Table 5.2.1: Experimental ^{13}C NMR chemical shifts (in ppm) and assignments to $\text{Zn}[\text{BeIM}]\text{OPr}$ as well as comparison to ZIF-7 and the used starting materials.

^{13}C NMR	$\delta\text{CH}_3\text{CH}_2\text{CO}_2$	$\text{CH}_3\delta\text{CH}_2\text{CO}_2$	$\text{CH}_3\text{CH}_2\delta\text{CO}_2$	δC2	$\delta\text{C4,7}$	$\delta\text{C5,6}$	$\delta\text{C8,9}$
$\text{Zn}[\text{BeIM}]\text{OPr}$	10.4	29.8	185.3	147.4	113.8	120.5	139.7
ZIF-7				149.9	114.9	122.5	138.1
						125.3	140.3
BeIM(H)				141.5	115.4	122.9	137.9
$\text{Zn}(\text{OPr})_2$	9.1	26.5	185.3				

In the ^{15}N CP-MAS Solid-state NMR spectrum (Fig 5.2.3) only a single peak is visible which corresponds to the signals of N1/N3 of anionic benzimidazolate (-194.7 ppm). The signal is significantly shifted compared to a solely imidazolate-bridged coordination framework such as ZIF-8 (-209 ppm).^[211] This shift can be readily explained by the close proximity of the acetate group and its electronic effects, as discussed above.

**Figure 5.2.4:** IR-spectrum of $\text{Zn}[\text{BeIM}]\text{OPr}$ (left) and enlarged view of the fingerprint region (right).

Infrared spectroscopy measurements were performed to confirm the purity of the material. The carboxylate vibrations at 1590 cm^{-1} (antisymmetric stretch) and 1460 cm^{-1} (symmetrical valence) can be clearly distinguished and can, in combination with the very low intensity of the usually very intense O-H vibrational modes in the range between 3500 cm^{-1} and 3000 cm^{-1} , as well as at 1620 cm^{-1} , be seen as an indication for complete deprotonation of the used carboxylic acid. The peaks between 3000 cm^{-1} and 2800 cm^{-1} can be assigned to the C-H valence vibrations of the propionic acid as well as to O-H vibrational modes corresponding to hydrogen bonds at the edge of the formed sheetlike structures. The complete deprotonation of the used benzimidazole can be

confirmed by the absence of N-H vibrations around 3400 cm^{-1} as well as around 1500 cm^{-1} , providing further proof to the discussed structural model.

Table 5.2.2: Elemental analysis of Zn[BeIM]OPr and comparison to the calculated values for an assumed molar ratio of $[\text{Zn}^{2+}] : [\text{BeIM}^-] : [\text{CH}_3\text{CH}_2\text{CO}_2^-] = 1 : 1 : 1$.

	Zn	N	C	H	O
Exp.	25,1	10,9	47,1	3,9	13,0
Calc.	25,6	11,0	47,0	3,9	12,5
Diff	- 0,5	- 0,1	0,10	0,0	0,5

Elemental analysis of the obtained material yielded a molar ratio of $[\text{Zn}^{2+}] : [\text{BeIM}^-] : [\text{CH}_3\text{CH}_2\text{CO}_2^-] = 1 : 1 : 1$, which is in agreement with the structural model with only small deviations from the calculated values.

5.2.2 Zn[BeIM]OBut

With the successful synthesis of Zn[BeIM]OPr and the confirmation of the proposed structural changes upon utilizing longer carboxylic acids, further elongation of the *a*-axis of the structure and thereby, as discussed in chapter 5.2.1, the average interlayer distance is the target of the following syntheses using zinc butyrate (Zn(OBut)₂) instead of the previously used acetates or propionates. By utilizing the known synthesis conditions in a solvent mixture of n-heptane/1-hexanol (9:1), a white crystalline powder was obtained with the empirical formula Zn[BeIM]OBut. The powder pattern of the material, shown in Figure 5.2.5, shows no traces of starting materials or known benzimidazolate-based ZIF-structures.

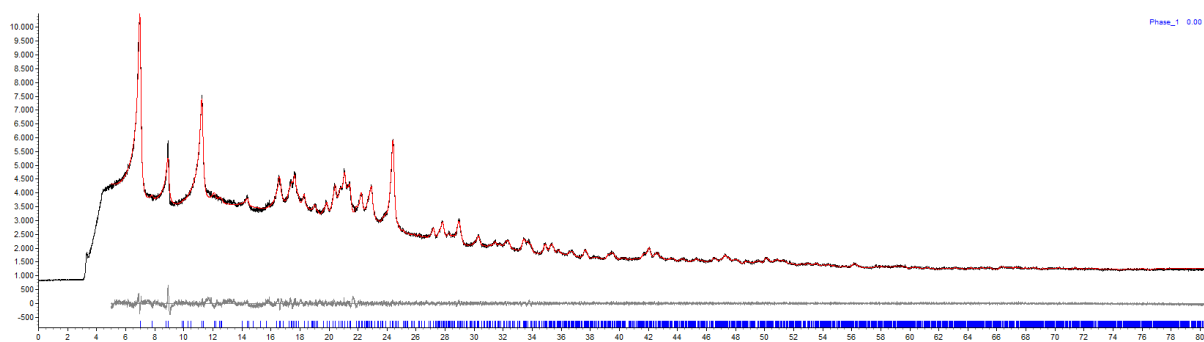


Figure 5.2.5: Pawley fit of the XRD powder pattern of Zn[BeIM]OBut, yielding space group and lattice parameters $P2_1$ with $a = 25.96 \text{ \AA}$, $b = 12.61 \text{ \AA}$, $c = 10.18 \text{ \AA}$ and $\beta = 103.36^\circ$ (GoF: 0.918).

The obtained powder pattern could not be indexed in $P2_1/c$, the space group found for the acetate and propionate based materials. Indexing and Pawley fitting was instead achieved by reducing the symmetry from $P2_1/c$ to $P2_1$, resulting in lattice parameters of $a = 25.96 \text{ \AA}$, $b = 12.61 \text{ \AA}$, $c = 10.18 \text{ \AA}$ and $\beta = 103.36^\circ$ (GoF = 0.918). The two space groups are related to one another by omitting the glide mirror plane in $P2_1/c$, which is expected to lead to a doubling of the *a*-axis assuming identical network connectivity. Due to the longer homologous carboxylic acid used, an *a*-axis of slightly more than twofold length with respect to the propionate phase is to be expected. This is in good agreement with the observed values, as the length of the *a*-axis in Zn[BeIM]OBut equals 2.12 times the length of the *a*-axis of Zn[BeIM]OPr. The loss of symmetry in the material can be attributed to the flexibility of arrangement of the butyrate carbon chain during the solvent based synthesis. During a Solid-state synthesis procedure, with an added tempering step in order to help facilitate the ordering of the carbon chain in the structure, the possibility of achieving the crystallization of the material in the known $P2_1/c$ space group should be increased.

To prove this concept, a Solid-state synthesis in a sealed glass ampulle under argon atmosphere was performed (see chapter 5.7 for experimental details). The pXRD data obtained from the resulting

white powder is shown in Figure 5.2.6 and shows no traces of starting materials or known benzimidazolate based ZIF-Phases.

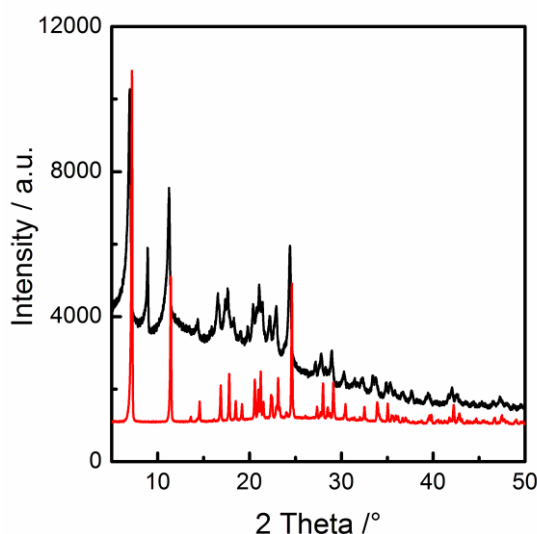


Figure 5.2.6: Comparison of XRD powder pattern of Zn[BeIM]OBut synthesized by microemulsion synthesis (black) and synthesized in Solid-state synthesis (red), yielding space group and lattice parameters $P2_1/c$ with $a = 11.69 \text{ \AA}$, $b = 9.92 \text{ \AA}$, $c = 8.77 \text{ \AA}$ and $\beta = 92.36^\circ$ (GoF: 1.128).

The obtained powder pattern can be indexed and Pawley fitted in $P2_1/c$ with $a = 11.69 \text{ \AA}$, $b = 9.92 \text{ \AA}$, $c = 8.77 \text{ \AA}$ and $\beta = 92.36^\circ$ (GoF: 1.128), which is in good agreement with the observed values for Zn[BeIM]OAc and Zn[BeIM]OPr. However a minor contraction of the a-axis with respect to the lattice parameters found for Zn[BeIM]OPr can be observed ($\Delta a = -0.54 \text{ \AA}$), which we attribute to the differences in the synthesis procedure and the tempering step in the Solid-state synthesis. The tempering is supposed to increase the crystallinity and to enable compact alignment of the carbon backbone of the used butyrate, which seems to lead to a more densely packed structure in the Solid-state synthesis than compared to the solution based syntheses of the other discussed materials. This finding provides further claim to the afore mentioned assumption, that the two found materials are polymorphs of the same network, that are only distinguished by the arrangement of the butyrate carbon-chains. The two different space groups of the structure can however only be accessed during the initial synthesis step, as later tempering experiments of the sample crystallizing in $P2_1$ did not result in a transformation to the higher symmetrical $P2_1/c$ space group.

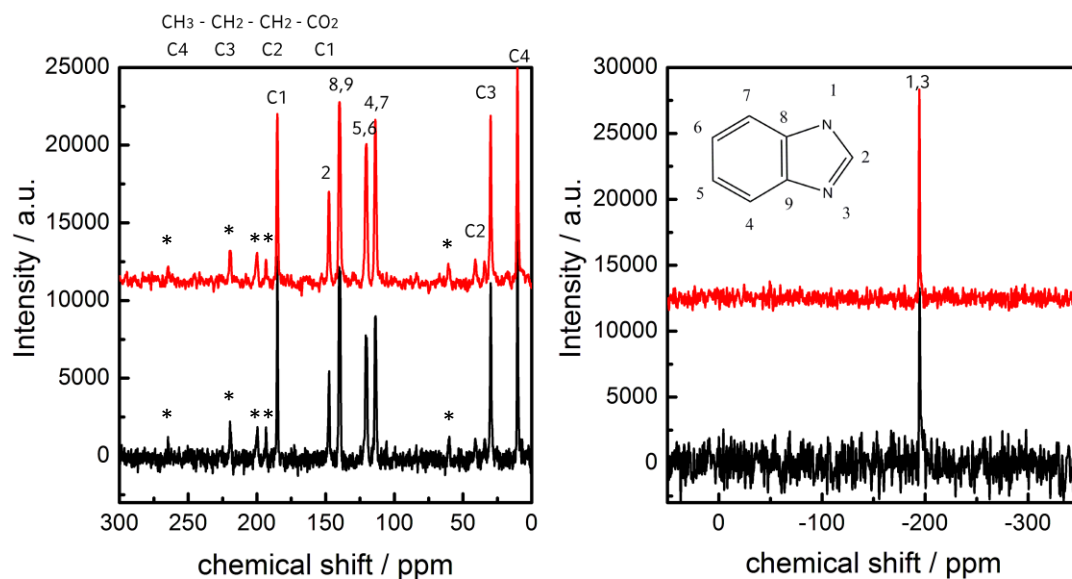


Figure 5.2.7: ^{13}C and ^{15}N Solid-state NMR of $\text{Zn}[\text{BeIM}]\text{OBut}$ synthesized by microemulsion synthesis (black) and Solid-state synthesis (red). Spinning side bands are marked with an asterisk.

^{13}C Solid-state NMR spectroscopy performed on the material synthesized in a microemulsion approach shows similar shifts of the peaks corresponding to the benzimidazolate carbon atoms between 115 and 150 ppm. The pronounced shift of the C2 signal at 147.1 ppm in comparison to $\text{BeIM}(\text{H})$ can be observed in this spectrum as well, indicating similar coordination and chemical surrounding for C2 as well as both neighbouring nitrogen atoms, including deprotonation of the benzimidazole moiety, which is further confirmed by ^{15}N Solid-state NMR. Both nitrogen atoms exhibit identical chemical shift at -187.0 ppm, which is in good agreement with the previously discussed structure and the symmetrical bridging position of the benzimidazolate.

Table 5.2.3: Experimental ^{13}C NMR chemical shifts (in ppm) and assignments to $\text{Zn}[\text{BeIM}]\text{OBut}$, as well as comparison to ZIF-7 and the used starting materials.

^{13}C NMR	$\delta\text{CH}_3\text{CH}_2$ CH_2CO_2	$\text{CH}_3\delta\text{CH}_2$ CH_2CO_2	$\text{CH}_3\text{CH}_2\delta$ CH_2CO_2	$\text{CH}_3\text{CH}_2\text{CH}_2$ δCO_2	δC2	$\delta\text{C4,7}$	$\delta\text{C5,6}$	$\delta\text{C8,9}$
$\text{Zn}[\text{BeIM}]\text{OBut}$	14.1	19.5	36.8	185.0	147.1	114.7	120.6	139.5
ZIF-7					149.9	114.9	122.5; 125.3	138.1; 140.3
$\text{BeIM}(\text{H})$					141.5	115.4	122.9	137.9
$\text{Zn}(\text{OBut})_2$	14.2	20.2	37.1	184.7				

The ^{13}C peaks corresponding to the butyrate carbon chain can be found at 14.1 ppm, 19.5 ppm and 36.8 ppm, respectively. The signal of the carboxylic carbon is shifted to lower field at 185.0 ppm from 180.7 ppm for proton-bearing butyric acid, which is comparable to the values found for $\text{Zn}(\text{OBut})_2$ (184.6 ppm).

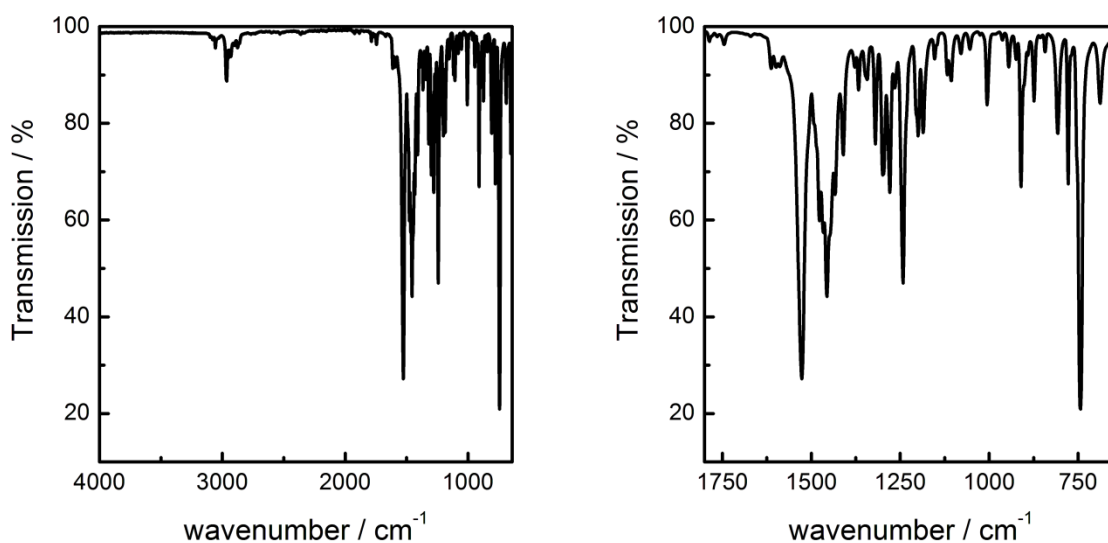


Figure 5.2.8: IR spectrum of Zn[BeIM]OBut (left) and close-up of the fingerprint region (right).

Infrared spectroscopy data are in good agreement with the data obtained from Zn[BeIM]OPr, however the C-H vibrations at 1550 cm⁻¹ exhibit increased intensity, which can be attributed to the prolonged carbon backbone of the butyric acid.

Table 5.2.4: Elemental analysis of Zn[BeIM]OBut and comparison to the calculated values for an assumed molar ratio of $[\text{Zn}^{2+}] : [\text{BeIM}^-] : [\text{CH}_3\text{CH}_2\text{CH}_2\text{CO}_2^-] = 1 : 1 : 1$.

	Zn	N	C	H	O
Exp.	23,4	10,4	49,0	4,5	13,2
Calc.	24,3	10,4	49,1	4,5	11,9
Diff	- 0,9	0,0	- 0,1	0,0	1,3

Elemental analysis is again in good agreement with the structure model by suggesting a molar ratio of $[\text{Zn}^{2+}] : [\text{BeIM}^-] : [\text{CH}_3\text{CH}_2\text{CH}_2\text{CO}_2^-] = 1 : 1 : 1$ with only slight deviations of the experimentally obtained values from calculated ratios.

5.3 MODIFICATION OF THE BENZIMIDAZOLATE GROUP

Following up on the successful modification of the carboxylic acid and the resulting alteration of the structure by elongation of the a-axis, modifications of the used benzimidazolate linker were carried out. In order to incorporate functional groups into the framework, different linkers such as nitro-benzimidazole and amino-benzimidazole were used. Nitro-benzimidazole is commercially available and features a spatially demanding functional group, rendering it a promising candidate to investigate the synthesis conditions required to integrate functional groups into the coordination polymer. However due to the low chemical accessibility of the nitro-groups with respect to reactions under mild conditions, nitro-benzimidazolate frameworks can only be seen as an intermediate step on the way to post-synthetic modification reactions on the synthesized materials. Thus amino-benzimidazole was synthesized, as the amine-group is known to react under mild conditions with a variety of other functional groups such as isocyanates or ketons.

The benzimidazolate groups in the framework are oriented parallel to the a-axis, similar to the previously modified carboxylic acids. Due to the flexibility of the material with respect to the interlayer distance, as shown previously, the inclusion of a benzimidazolate linker featuring functional groups seems feasible. In the following chapter the effects of incorporating the chemically functionalized linkers nitro-benzimidazole, amino-benzimidazole and mixtures of both on the resulting structures are discussed.

5.3.1 $\text{Zn}[\text{NO}_2\text{-BeIM}]\text{OAc}$

The synthesis using nitro-benzimidazole as a linker was carried out under identical conditions to the solvent-based synthesis of $\text{Zn}[\text{BeIM}]\text{OAc}$ in a mixture of n-heptane/1-hexanol (for synthesis details see chapter 5.7). The obtained light-brown powder was analysed by powder X-ray diffraction and was confirmed to be free of starting materials and other known benzimidazolate-based ZIF materials.

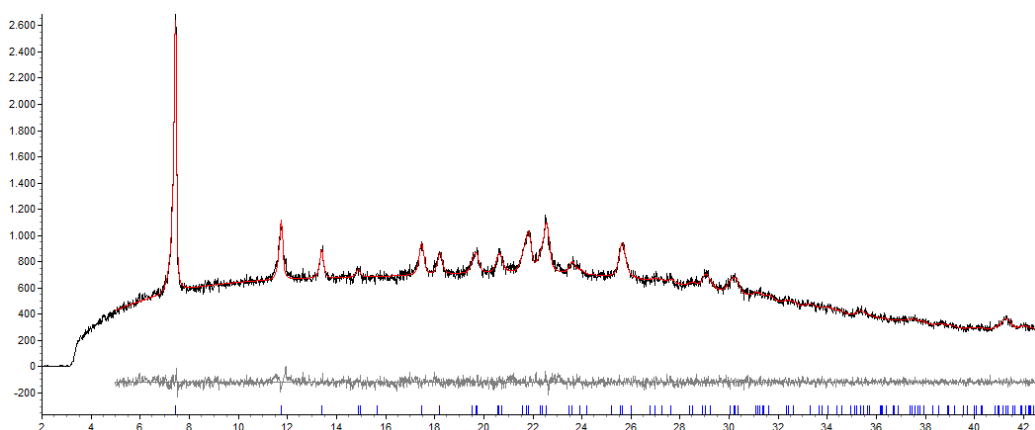


Figure 5.3.1: Pawley fit of the XRD powder pattern of $\text{Zn}[\text{NO}_2\text{-BeIM}]\text{OAc}$, yielding space group and lattice parameters $P2_1/c$ with $a = 11.91 \text{ \AA}$, $b = 9.69 \text{ \AA}$, $c = 8.97 \text{ \AA}$ and $\beta = 93.12^\circ$ (GoF: 3.423).

The obtained diffraction pattern was indexed in $P2_1/c$ and Pawley-fitting supplied the lattice parameters $a = 11.91 \text{ \AA}$, $b = 9.69 \text{ \AA}$, $c = 8.97 \text{ \AA}$, $\beta = 93.12^\circ$ (GoF: 3.423). Comparison of the obtained crystal lattice with the suspected isostructural $\text{Zn}[\text{BeIM}]\text{OAc}$ showed a close relation between both lattices, with an elongation of the a-axis from 10.81 \AA to 11.91 \AA ($\Delta a = +1.1 \text{ \AA}$) and a shift in the monoclinic angle from 98.96° to 93.12° , whilst b- and c-axis remain close to identical. Whereas the elongation of the a-axis was to be expected due to previously discussed reasons, the substantial shift in the monoclinic angle is surprising. However, this result can be rationalized by steric effects of the nitro-group in the interlayer space, rendering a less staggered structure preferable over the more staggered variants as the reduction in the monoclinic angle increases the distance between adjacent framework backbones and thus enables a better integration of the nitro-groups.

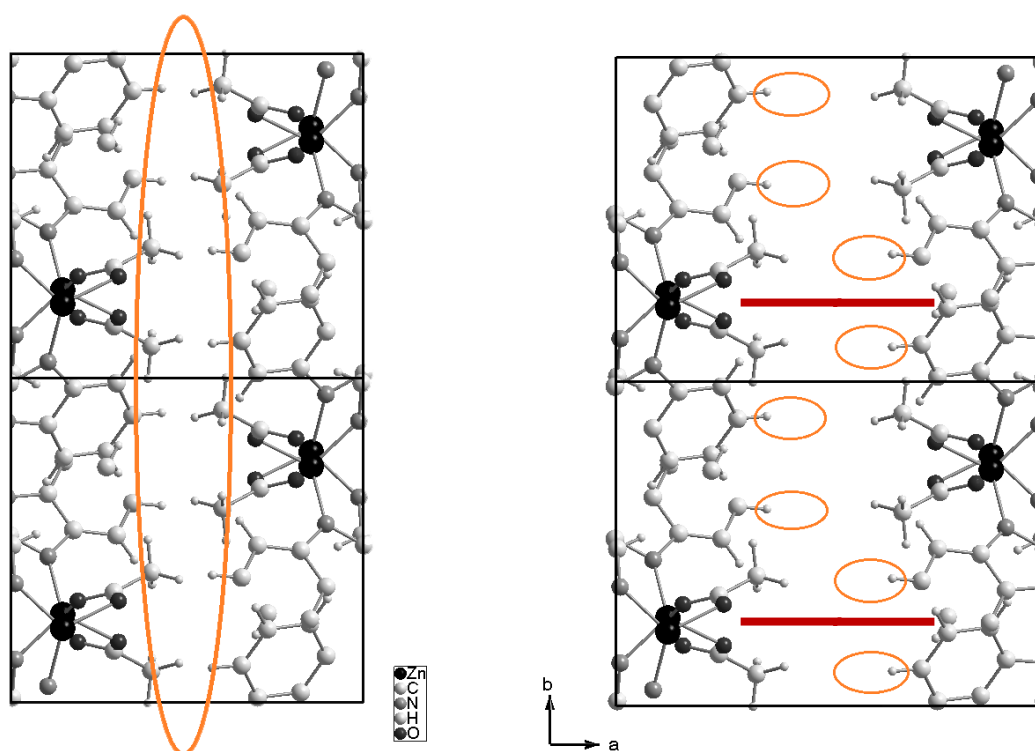


Figure 5.3.2: Schematic highlighting the structural adjustments needed to integrate nitro-benzimidazole into the structure. By increasing the monoclinic angle in addition to an increase in a-axis length, the distance between the backbone of adjacent chains is increased (highlighted in red), thereby minimizing steric interference between the two functional groups.

It is additionally noteworthy that the crystallinity of the sample and thereby the quality of the Pawley-fit has decreased significantly in comparison to previously discussed materials, which seems to be an effect of the spaceous nitro-group in the interlayer space and hence, less dense packing.

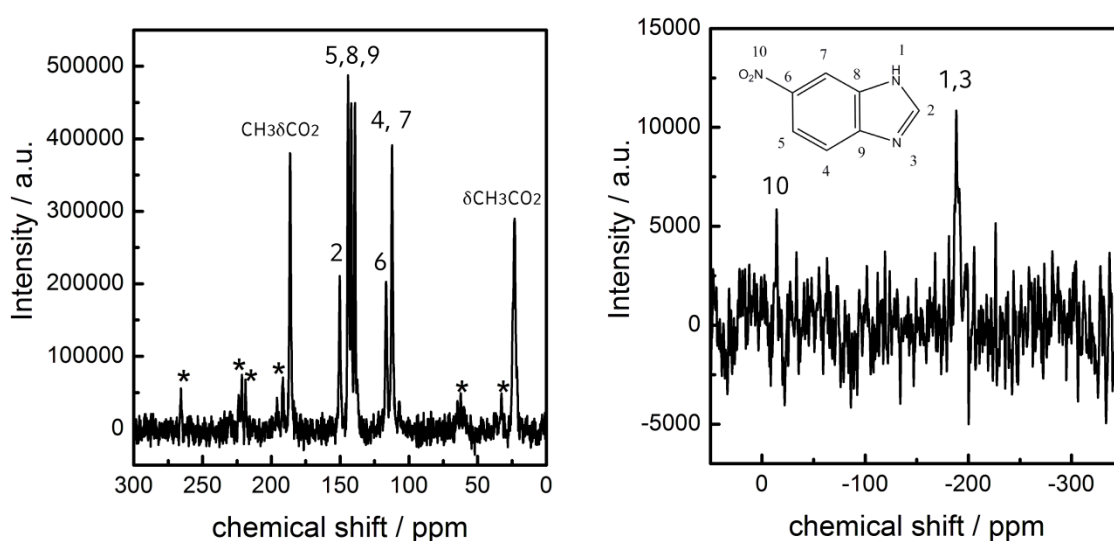


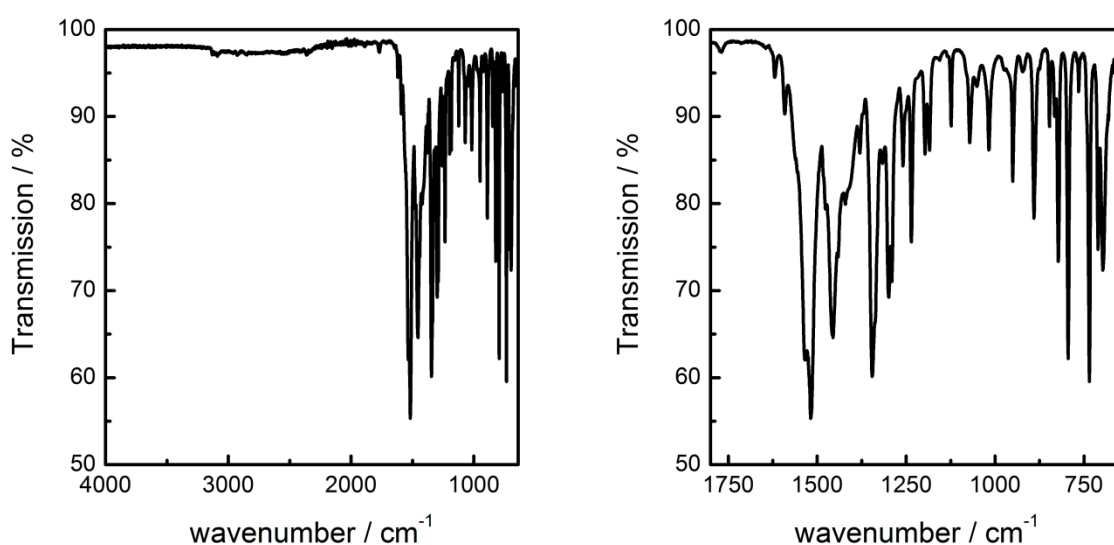
Figure 5.3.3: ^{13}C (left) and ^{15}N (right) Solid-state NMR of $\text{Zn}[\text{NO}_2\text{-BelM}]\text{OAc}$. Spinning side bands in the ^{13}C NMR spectrum are marked with asterisks.

The recorded ^{13}C Solid-state MAS NMR spectrum only exhibits the signals of nitro-benzimidazolate and the acetate ions. The peaks corresponding to nitrobenzimidazolate can be observed in the range between 145 and 110 ppm, which results in a slight shift to lower field compared to the previously discussed $\text{Zn}[\text{BelM}]\text{OPr}$ and $\text{Zn}[\text{BelM}]\text{OBut}$. These effects are more pronounced for carbon atoms close to the nitro-group, which is expected. The chemical shift for C2, which is positioned between both coordinating nitrogen ions in the benzimidazolate, shows identical chemical shift to C2 in $\text{Zn}[\text{BelM}]\text{OPr}$, indicating comparable chemical surrounding, which is, again, in good agreement with the assumed close structural relation between the two materials.

^{15}N Solid-state MAS NMR shows two distinct signals at -188.4 ppm, which can be assigned to the bridging nitrogen atoms in the benzimidazolate ring and another nitrogen at -13.9 ppm, which can be assigned to the nitro-group. The poor signal to noise ratio of the spectrum has to be attributed to the low natural abundance of ^{15}N as well as to a limited amount of sample obtained.

Table 5.3.1: Experimental ^{13}C NMR chemical shifts (in ppm) and assignments to $\text{Zn}[\text{NO}_2\text{-BeIM}]\text{OAc}$ as well as comparison to ZIF-7 and the used starting materials.

^{13}C NMR	$\delta\text{CH}_3\text{CO}_2$	$\text{CH}_3\delta\text{CO}_2$	δC2	$\delta\text{C4,7}$	δC5	δC6	$\delta\text{C8,9}$
$\text{Zn}[\text{NO}_2\text{-BeIM}]\text{OAc}$	23.2	185.8	150.6	112.4	117.5	144.4	139.3; 142.3
$\text{Zn}[\text{BeIM}]\text{OAc}$	23.1	182.9	147.6	114.6; 113.4	121.5	120.4	139.5; 140.3
ZIF-7			149.9	114.9	122.5	125.3	138.1; 140.3
$\text{NO}_2\text{-BeIM}(\text{H})$			141.5	115.4	122.9		137.9
$\text{Zn}(\text{OAc})_2$	9.1	185.3					

**Figure 5.3.4:** IR spectrum of $\text{Zn}[\text{NO}_2\text{-BeIM}]\text{OAc}$ (left) and zoom of the fingerprint region (right).

Infrared spectroscopy confirms the purity of the synthesized material and shows the absence of O-H and N-H vibrations, indicating complete deprotonation of the used linkers. Additionally the symmetrical (1340.0 cm^{-1}) and anti-symmetrical (1530.2 cm^{-1}) N-O vibrations can be observed.

Table 5.3.2: Elemental analysis of $\text{Zn}[\text{NO}_2\text{-BeIM}]\text{OAc}$ and comparison to the calculated values for an assumed molar ratio of $[\text{Zn}^{2+}] : [\text{NO}_2\text{-BeIM}^-] : [\text{CH}_3\text{CO}_2^-] = 1 : 1 : 1$.

	Zn	N	C	H	O
Exp.	25,5	14,8	38,4	2,9	18,4
Calc.	22,8	14,7	37,7	2,5	22,3
Diff	2,7	0,1	0,7	0,4	- 3,9

The data obtained by ICP and elemental analysis is in good agreement with the proposed structural model of $\text{Zn}[\text{NO}_2\text{-BeIM}]\text{OAc}$, indicating a molar ratio of $[\text{Zn}^{2+}] : [\text{NO}_2\text{-BeIM}^-] : [\text{CH}_3\text{CO}_2^-] = 1 : 1 : 1$.

5.3.2 Zn[NH₂-BeIM]OAc

In a second step, due to the limited chemical accessibility with respect to reactions under mild synthesis conditions of the previously used nitro-groups, amino-benzimidazole was used as a linker in the solvent-based synthesis procedure. Whilst amine-groups provide a well explored basis for a plethora of postsynthetic modification reactions utilizing reactants such as alcohols, ketons or isocyanates, the use of amino-benzimidazole requires various adaptations to the previously utilized synthesis procedures due to the limited solubility of the amine-functionalized linker. Whilst a Solid-state synthesis of the material had previously been performed by Junggeburth,^[210] a solution-based synthesis approach, which is fundamental for the known exfoliation procedures for materials such as Zn[BeIM]OAc, was previously unknown. By altering the used solvent mixture (n-heptane/1-hexanol) to a ratio of 7:1 and using the amino-benzimidazolate linker dissolved in DMF, a brown powder was obtained. The corresponding powder diffraction data is shown in Figure 5.3.5 and provide evidence that no starting material or known benzimidazolate-based ZIF phases are present in the sample.

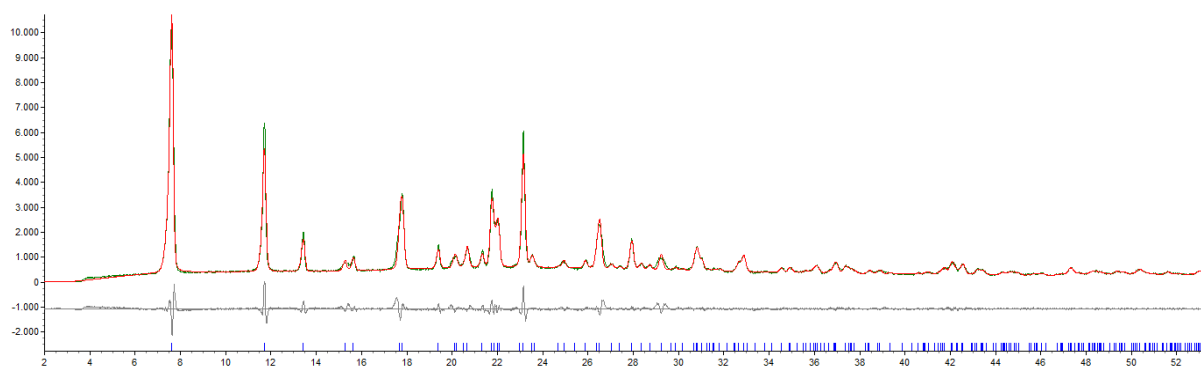


Figure 5.3.5: Pawley fit of the XRD powder pattern of Zn[NH₂-BeIM]OAc, yielding space group and lattice parameters $P2_1/c$ with $a = 11.61 \text{ \AA}$, $b = 9.76 \text{ \AA}$, $c = 8.80 \text{ \AA}$ and $\beta = 92.15^\circ$ (GoF: 2.168).

The obtained diffraction pattern was indexed and a Pawley-fit was carried out, again leading to the space group $P2_1/c$ with $a = 11.61 \text{ \AA}$, $b = 9.76 \text{ \AA}$, $c = 8.80 \text{ \AA}$ and $\beta = 92.15^\circ$ (GoF: 2.168). The found crystal lattice data are closely related to the known structures and shows a slight shortening of the a -axis, compared to the nitro-functionalized material. This is in line with expected behaviour, assuming that an amine-functionality is sterically slightly less demanding than a nitro-functionalized linker, thus enabling the reduction of the interlayer distance. Additionally, the possibility of the amine-groups to form hydrogen bonds with the adjacent layer results in a contraction of the crystal lattice along the a -axis, whilst the other parameters remain essentially unchanged between Zn[NH₂-BeIM]OAc and Zn[NO₂-BeIM]OAc.

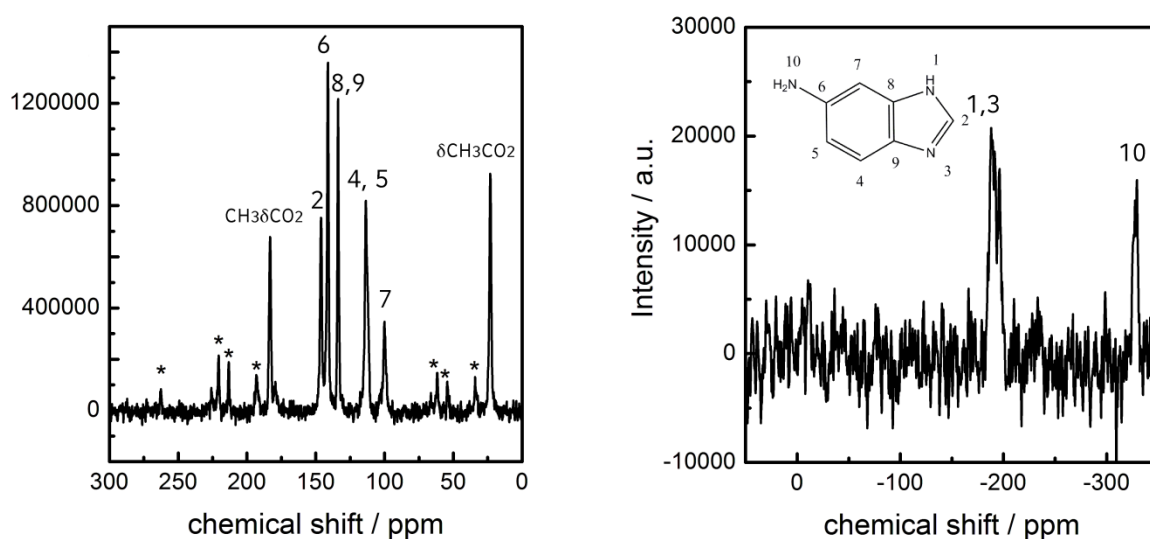


Figure 5.3.6: ^{13}C (left) and ^{15}N (right) Solid-state NMR of $\text{Zn}[\text{NH}_2\text{-BelM}]\text{OAc}$. Spinning side bands in the ^{13}C NMR spectrum are marked with asterisks.

The ^{13}C Solid-state MAS NMR measurements performed on the sample shows peaks at 23.7 ppm and 183.7 ppm which can be assigned to both carbon atoms of the carboxylic acid. Further peaks at 100.3 ppm, 114.5 ppm, 133.9 ppm, 141.3 ppm and 146.5 ppm can be attributed to the benzimidazolate ring system and again show an upfield shift of the benzimidazolate carbon signals in close proximity to the functional group, which is comparable to the shift observed for $\text{Zn}[\text{BelM}]\text{OPr}$ and $\text{Zn}[\text{BelM}]\text{OBut}$. The detailed assignment of the signals can be found in table 5.3.3.

Table 5.3.3: Experimental ^{13}C NMR chemical shifts (in ppm) and assignments to the $\text{Zn}[\text{NH}_2\text{-BelM}]\text{OAc}$ as well as comparison to ZIF-7 and the used starting materials.

^{13}C NMR	$\delta\text{CH}_3\text{CO}_2$	$\text{CH}_3\delta\text{CO}_2$	$\delta\text{C}2$	$\delta\text{C}7$	$\delta\text{C}4,5$	$\delta\text{C}6$	$\delta\text{C}8,9$
$\text{Zn}[\text{NH}_2\text{-BelM}]\text{OAc}$	23.7	183.7	146.5	100.3	114.5	141.3	133.9
$\text{Zn}[\text{BelM}]\text{OAc}$	23.1	182.9	147.6	114.6; 113.4	121.5	120.4	140.3; 139.5
ZIF-7			149.9	114.9	122.5	125.3	138.1; 140.3
$\text{NH}_2\text{-BelM}(\text{H})$			146.5	105.4	114.9		137.9
$\text{Zn}(\text{OAc})_2$	9.1	185.3					

^{15}N Solid-state NMR shows two distinct peaks at -329.8 ppm (N10) and between -188 and -198 ppm (N1/3). Whilst the peak corresponding to the amine group is very sharp, the signal corresponding to both nitrogen atoms in the benzimidazolate ring system shows a complex splitting pattern, which was not observed in the previously discussed samples. By comparison with the previously discussed $\text{Zn}(\text{NO}_2\text{-BelM})\text{OAc}$ it becomes apparent that the splitting is most likely the result of traces of

nitrobenzimidazole in the sample, remnants from the amino-benzimidazole synthesis. These traces could not be removed during the synthesis, due to the similar solubility properties of both chemicals. The left shoulder of the peak at around -188 ppm can be attributed to the nitrobenzimidazole impurities whilst the right parts around -198 ppm originate from amino-benzimidazole. The signal of the nitro-group, which would be expected at around -18 ppm, is not observed. However, even in the pure amino-benzimidazole sample the signal corresponding to the amine-group is barely visible (see Fig. 5.3.7, red graph), thus low amounts of nitrobenzimidazole in the framework are possible.

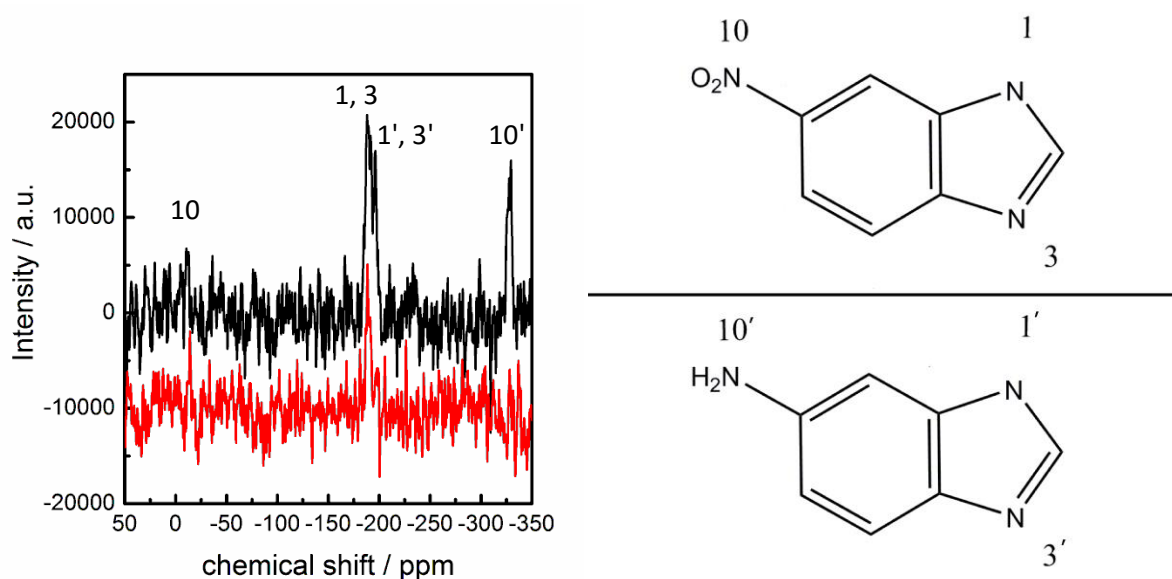


Figure 5.3.7: ^{15}N Solid-state NMR of $\text{Zn}[\text{NH}_2\text{-BelM}]\text{OAc}$ (black) and $\text{Zn}[\text{NO}_2\text{-BelM}]\text{OAc}$ (red).

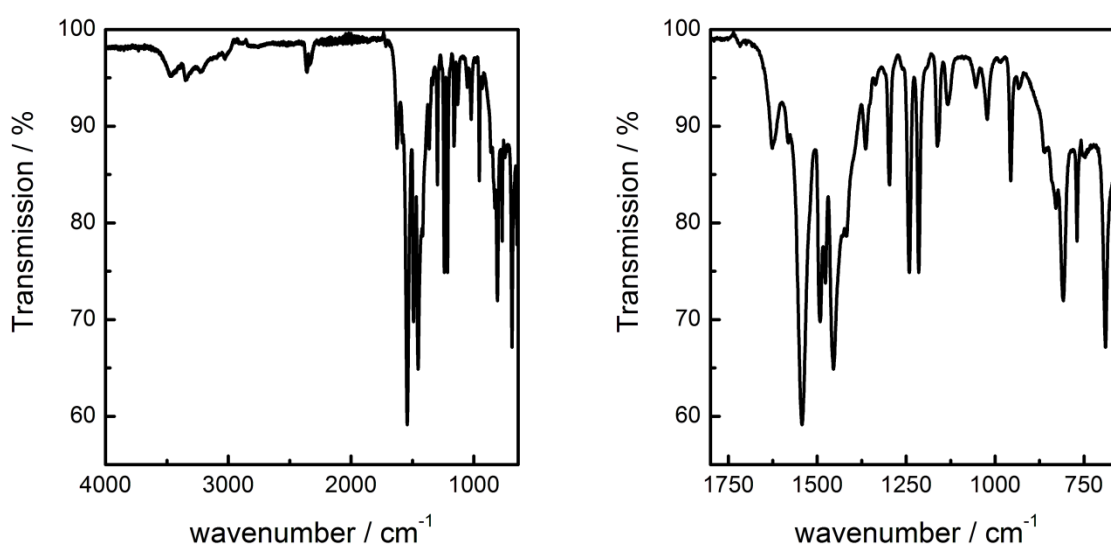


Figure 5.3.8: IR spectrum of $\text{Zn}[\text{NH}_2\text{-BelM}]\text{OAc}$ (left) and zoom on the fingerprint region (right).

IR measurement shows distinct N-H vibrations (N-H deformation of the N-H₂ group 1632.0 cm⁻¹, N-H valence vibration 3500 to 3200 cm⁻¹), proving the presence of the amino-groups in the framework material. Contradictory to the theory of a mixed-linker material with traces of nitro-benzimidazolate in an amino-benzimidazolate framework (see NMR results), the symmetrical N-O valence vibration expected to occur around 1350 cm⁻¹ is not present, as seen in Figure 5.3.9.

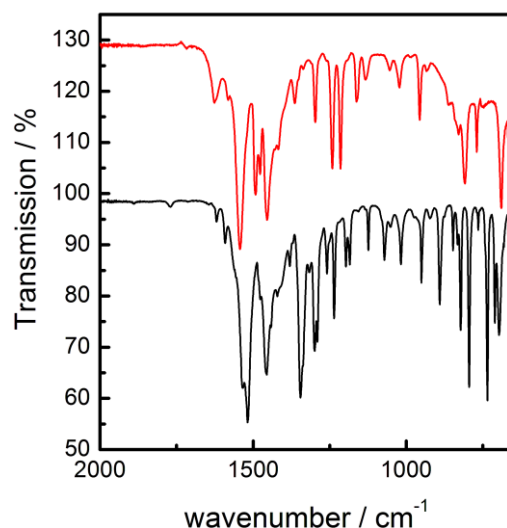


Figure 5.3.9: IR spectra of Zn[NH₂-BelM]OAc (black) and Zn[NO₂-BelM]OAc (red).

Elemental analysis again documents a composition of Zn[NH₂-BelM]OAc with only minor deviations which indicates that only traces of nitro-benzimidazolate can be present in the framework backbone.

Table 5.3.4: Elemental analysis of Zn[NH₂-BelM]OAc and comparison to the calculated values for an assumed molar ratio of [Zn²⁺] : [NH₂-BelM] : [CH₃CO₂] = 1 : 1 : 1

	Zn	N	C	H	O
Exp.	25,6	16,3	42,1	3,5	12,6
Calc.	25,50	16,4	42,1	3,5	12,5
Diff	0,1	- 0,1	0,0	0,0	0,1

5.3.3 $\text{Zn}[\text{NO}_2\text{-BeIM}]_{1-x}[\text{NH}_2\text{-BeIM}]_x\text{OAc}$ - MIXED LINKER SYNTHESSES

Mixed-linker syntheses are a commonly utilized approach to obtain MOFs suitable for "diluted" post-synthetic modifications, as they combine the stability and crystallinity of unfunctionalized (or partly functionalized) frameworks with the reactivity of the additionally introduced functional groups.^[212, 213]

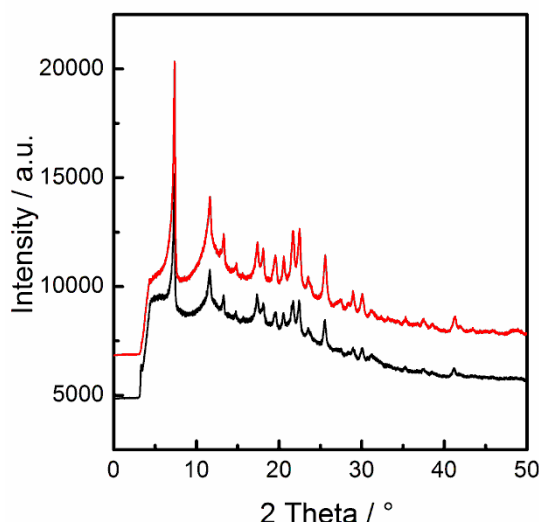


Figure 5.3.10: Powder XRD diffraction pattern of $\text{Zn}[\text{NO}_2\text{-BeIM}]_{1-x}[\text{NH}_2\text{-BeIM}]_x\text{OAc}$ with $x = 0.25$ (black) and $x = 0.5$ (red).

The obtained powder diffraction patterns for $x = 0.25$ and 0.5 are close to identical and could be indexed in $P2_1/c$ with $a = 11.93 \text{ \AA}$, $b = 9.74 \text{ \AA}$, $c = 9.02 \text{ \AA}$ and $\beta = 94.02^\circ$ (GoF = 0.895) for $x = 0.25$. The found crystal lattice is closely related to that of the pure nitro-benzimidazolate phase suggesting no significant structural changes due to the inclusion of the amine-functionalization into the nitro-benzimidazolate structure. Nonetheless the close relation of the found lattice parameters with almost no deviation from the lattice of $\text{Zn}[\text{NO}_2\text{-BeIM}]\text{OAc}$ gives rise to doubts if substantial amounts of amino-benzimidazolate linker were included into the framework.



Figure 5.3.11: Photographs of $\text{Zn}[\text{NO}_2\text{-BeIM}]\text{OAc}$ (left) and $\text{Zn}[\text{NO}_2\text{-BeIM}]_{1-x}[\text{NH}_2\text{-BeIM}]_x\text{OAc}$ with $x = 0.25$ (center) and $x = 0.5$ (right).

By taking a closer look at the photographs of the obtained powders in comparison to $\text{Zn}[\text{NO}_2\text{-BeIM}]\text{OAc}$, significant darkening of the samples that were synthesized with increased amounts of $\text{NH}_2\text{-BeIM}$ becomes apparent. This effect is an indication that the amine-functionalized linker was indeed integrated into the structure, as amino-benzimidazole and the corresponding $\text{Zn}[\text{NH}_2\text{-BeIM}]\text{OAc}$ are of dark brown coloration, whilst the materials based purely on nitro-benzimidazole are white in color.

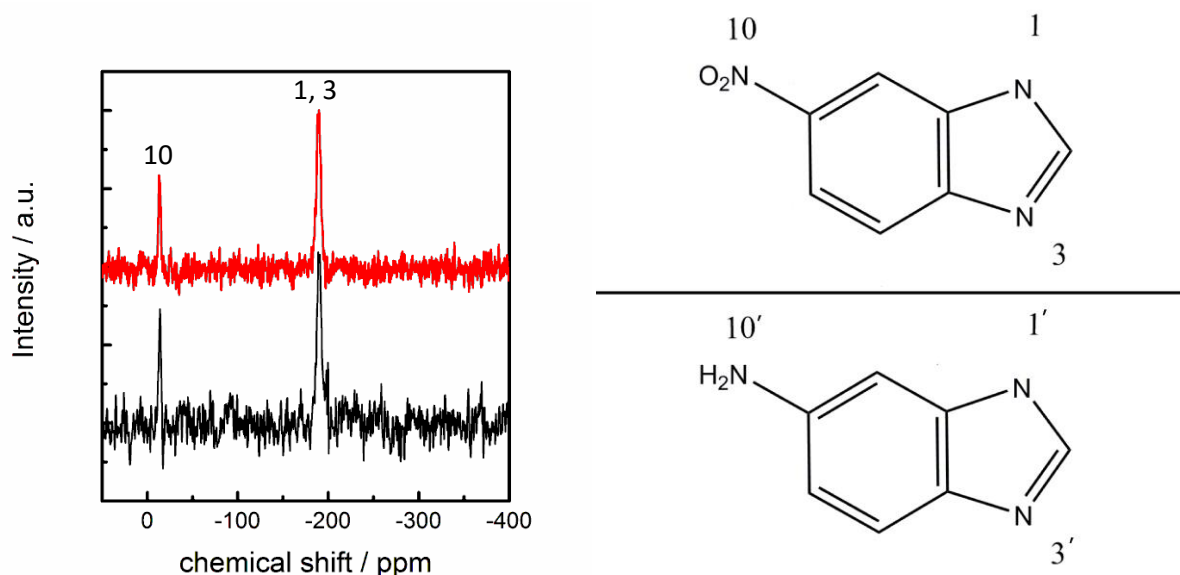


Figure 5.3.12: ^{15}N Solid-state NMR spectrum of $\text{Zn}[\text{NO}_2\text{-BeIM}]_{1-x}[\text{NH}_2\text{-BeIM}]_x\text{OAc}$ with $x = 0.25$ (black) and $x = 0.5$ (red).

^{15}N Solid-state MAS NMR was performed to confirm the presence of nitro- and amino-benzimidazolate groups in the synthesized material, however only two peaks can be observed, the signal corresponding to the nitro-group (N10) at -13.67 ppm and a peak at -189.79 ppm corresponding to both nitrogen atoms in the benzimidazole ring (N1/3) which are coordinating the zinc-ions in the lamellar framework structure. This result confirms the doubts about the presence of substantial amounts of amino-benzimidazolate in the structure, which can be attributed to the limited solubility of the amino-functionalized linker in comparison to nitro-benzimidazolate. These differences in accessibility of the different linkers during the synthesis procedure have already been discussed in chapter 1.3.2 and seem to prevent the formation of a mixed-linker material with quantitative amounts of amino-benzimidazole integrated into the framework. However due to the low natural abundance of ^{15}N , the NMR measurements are not contradicting the presence of small amounts of amino-benzimidazole (< 5-10 %) in the synthesized materials.

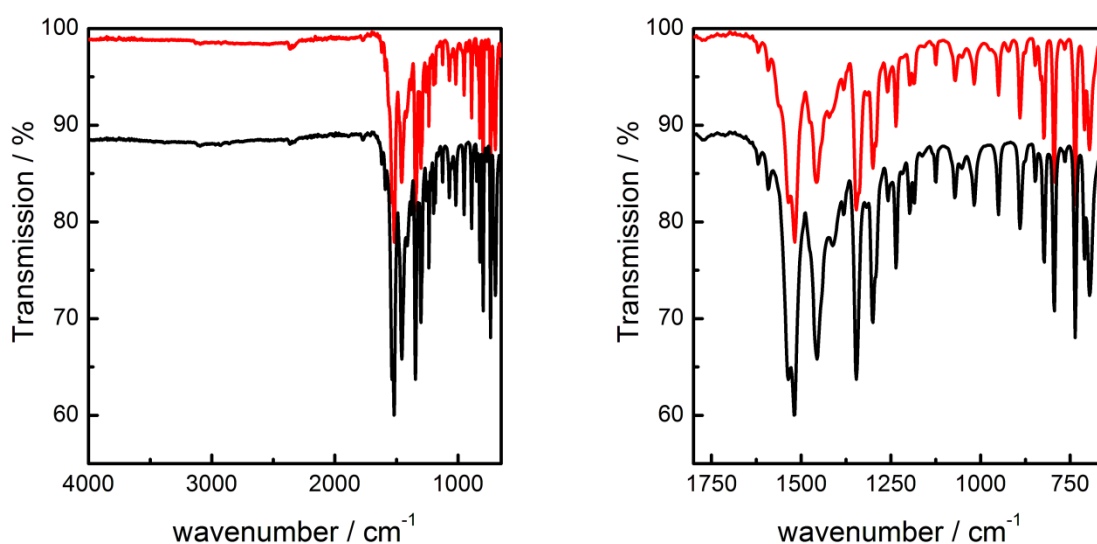


Figure 5.3.13: IR spectra of $\text{Zn}[\text{NO}_2\text{-BelM}]_{1-x}[\text{NH}_2\text{-BelM}]_x\text{OAc}$ with $x = 0.25$ (black) and $x = 0.5$ (red) and close up of the fingerprint region (right).

Whilst powder X-ray diffraction measurements suggested that no structural differences between both materials exists, however the color differences between the samples hint that slight deviations in the content of amino-benzimidazole in the sample might be possible. Infrared spectroscopy on materials obtained via mixed-linker syntheses show no difference between the materials with 25% or 50% amino-benzimidazolate in the starting mixture, which suggests that the chemical composition of both materials is equivalent, as the relative intensity of nitro- and amine-vibrations should shift due to the changing ratio between both in case of differences in composition. Additionally, even at 50% amino-benzimidazolate in the synthesis mixture, no N-H vibrations between 3500 and 3200 cm^{-1} can

be observed. This is a further indication, that the obtained materials are not mixed-linker coordination frameworks with the desired share of amino-benzimidazole, but rather nitro-benzimidazolate linked frameworks with trace amounts of amino-functionalized linkers integrated into the framework, causing the color changes.

Additional experiments to synthesize mixed-linker frameworks with unfunctionalized benzimidazole and amino-benzimidazole were performed in order to examine if the described synthetic challenges can be overcome by omitting the nitro-functionalized linker from the synthesis. However, these experiments led to pure Zn[BeIM]OAc according to all analytical measurements without any trace of amine-groups in pXRD, Solid-state NMR, IR, elemental analysis or optical impression of the resulting materials and are therefore not discussed further at this point.

5.4 EXFOLIATION ATTEMPTS

In order to investigate the synthesized materials with regard to their exfoliation properties and to provide further insight into the interlayer forces in the synthesized framework materials, syntheses with CTAB as a surfactant and structuring agent during the initial solution based synthesis step were carried out. Due to the lamellar structure of the previously discussed ternary materials, the presence of CTAB during the synthesis is expected to lead to a surfactant intercalated material with extended interlayer distances. By stacking CTAB and the lamellar material in an alternating fashion, reminiscent of lamellar liquid crystalline phases, artificial, soft "breaking points" are created in the material for subsequent exfoliation by surfactant extraction. The effects of CTAB on the ternary materials has been discussed by Junggeburth in the context of CTAB-intercalated $\text{Zn}[\text{BeIM}]\text{OAc}$, resulting in $\text{BeIM-MIF}(\text{OAc})$ interleaved with CTAB bilayers, which was subsequently exfoliated in THF into $1.5 \times 1.5 \mu\text{m}$ nanosheets.^[122] Exfoliation of the lamellar materials significantly increases the accessible surface area of the sheets and thereby facilitates post-synthetic modification reactions due to the easier accessability of functional groups.

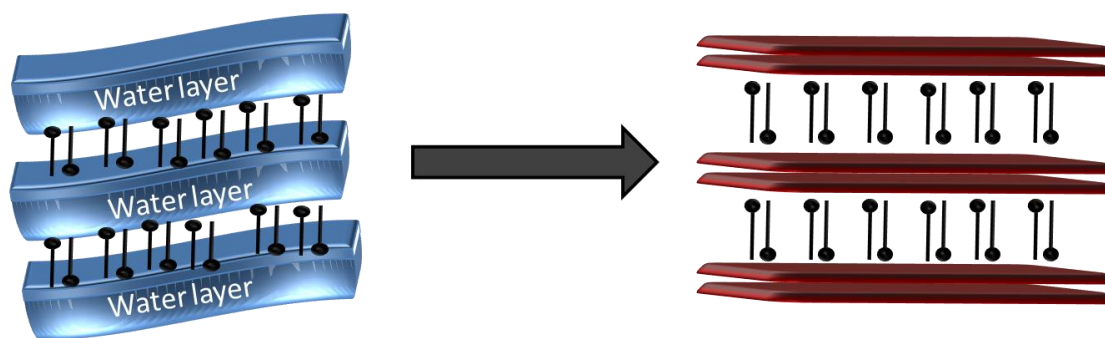


Figure 5.4.1: Proposed formation mechanism of the intercalated structure $\text{BeIM-MIF}(\text{OAc})$, leading to subsequent exfoliation at the CTAB layers.

Due to the influence of the different carboxylic acids, an increased tendency to exfoliate is expected for the materials with elongated carboxylic acids since the structuring agent should be able to infiltrate the propionate and butyrate based structures more readily, thus likely resulting in enhanced exfoliation and sheetlike structures.

5.4.1 BeIM-MIF(OPr)

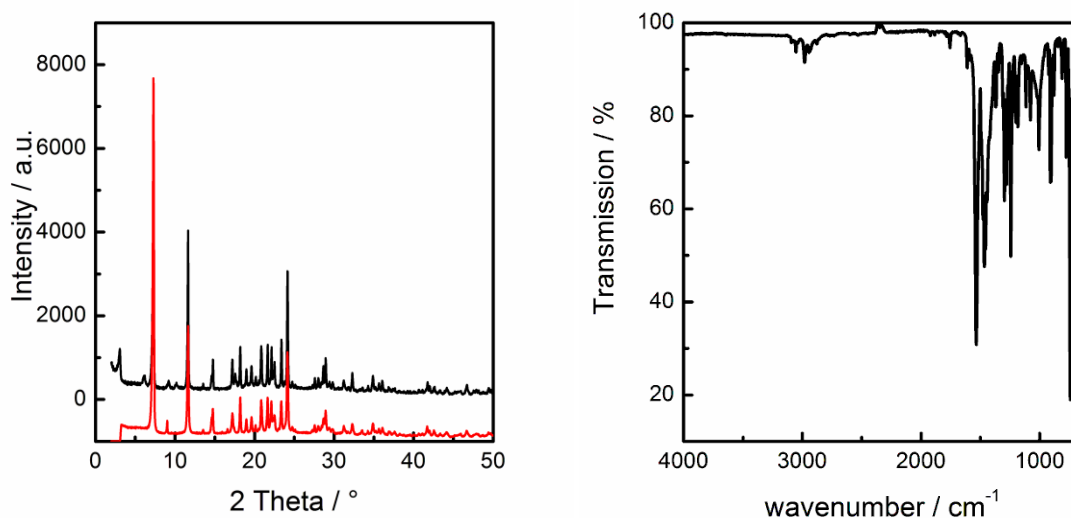


Figure 5.4.2: Powder diffractogram of BeIM-MIF(OPr) (black) and Zn[BeIM]OPr (red) (left) and IR spectrum (right) of BeIM-MIF(OPr).

Powder X-ray diffraction measurement of the sample obtained via synthesis containing CTAB yield identical diffraction patterns to those obtained from Zn[BeIM]OPr, however three distinct additional peaks can be observed. These peaks at $2\theta = 3.05^\circ$, 6.14° and 9.23° can be seen as a series corresponding to a *00l*-series, indicating a lamellar mesostructuring of the material with a corresponding distance of 28.97 Å. However compared to other known mesostructured materials such as the prototypical MIF-1,^[121] the intensity of the observed peaks is remarkably low.

Infrared spectra are identical to that of pure Zn[BeIM]OPr, synthesized without CTAB (see Fig. 5.2.3) showing C=O vibrations and the typical C-H, C=C and C=N vibrational modes of the benzimidazole ring system. The measurement does however not show C-H vibrational modes, giving rise to the notion that only trace amounts of CTAB might present in the material, either intercalated into the lamellar structure or as a residue on the particle surface.

Exfoliation of the obtained material was attempted with an orbital shaker using a dispersion of the material in THF resulting in a clear solution with no turbidity, which failed to deliver nanosheets that could be detected by AFM measurements. Additional efforts with different solvents such as diethylether, ethanol or iso-propanol as well as the use of ultrasound, did not improve the exfoliation step. Whilst all experiments with the orbital shaker did only result in clear solutions with no visible signs of suspended nanosheets and no material deposition at all on the investigated wafers, the use of ultrasound instead of an orbital shaker led to "shredding" of the material, leading to an opaque suspension of material in the solutions, however only the deposition of small unregular shaped particles with sizes below 0.1 µm on the wafer.

5.4.2 BeIM-MIF(OBuT)

Due to the structural flexibility of the butyrate materials, as demonstrated previously by the differences between solution based and Solid-state syntheses, exfoliation of Zn[BeIM]OBut was expected to be more facile.

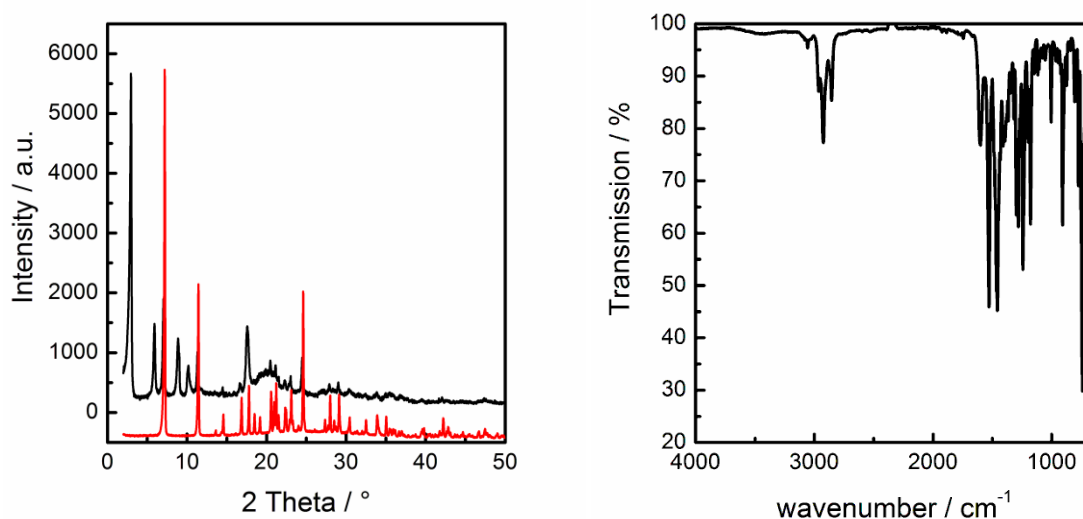


Figure 5.4.3: Powder diffractogram (left) and IR spectrum (right) of BeIM-MIF(OBuT).

Powder diffraction patterns of the formed material are in good agreement with data recorded of Zn[BeIM]OBut and exhibit a series of additional peaks at $2\theta = 2.94^\circ$, 5.91° and 8.87° , which can once again be seen as indication of a lamellar mesostructuring of the material, this time with a stacking parameter of 30.02 \AA . A direct comparison of the intensity of the observed peaks with those discussed in chapter 5.4.1 shows greatly increased intensity, which is in line with previous reports on lamellar mesostructured coordination frameworks.^[121, 175]

Infrared spectroscopic measurements further confirm the assumption of a surfactant induced mesostructuring of the material as the characteristic C-H valence vibrations of the alkyl-chains in CTAB can be seen at 2924.6 cm^{-1} and 2854.6 cm^{-1} , in addition to the peaks found in IR spectra of Zn[BeIM]OBut.

Subsequent exfoliation attempts in THF showed, that a weak mechanical force applied via orbital shaking is sufficient to create a stable suspension of the material for spincoating experiments. Spincoating of the prepared suspensions at 5.000 rpm onto Si wafers ($1.5 \times 1.5 \text{ cm}^2$), led to the deposition of the 2D material onto the substrate. AFM analysis of the wafer surface confirmed the presence of mostly rectangular nanosheets with dimensions of approximately $0.5 \times 0.5 \mu\text{m}^2$ with an average height of 2.5 nm, which equals the height of double-layers of Zn[BeIM]OBut based on the structure discussed in chapter 5.2.2. The nanosheets show a narrow size distribution in lateral

dimensions, ranging from $0.25 \times 0.25 \mu\text{m}^2$ to a maximum of about $0.7 \times 0.5 \mu\text{m}^2$, and height, confirming the assumed periodical intercalation of CTAB between the lamellae of $\text{Zn}[\text{BeIm}]\text{OBut}$.

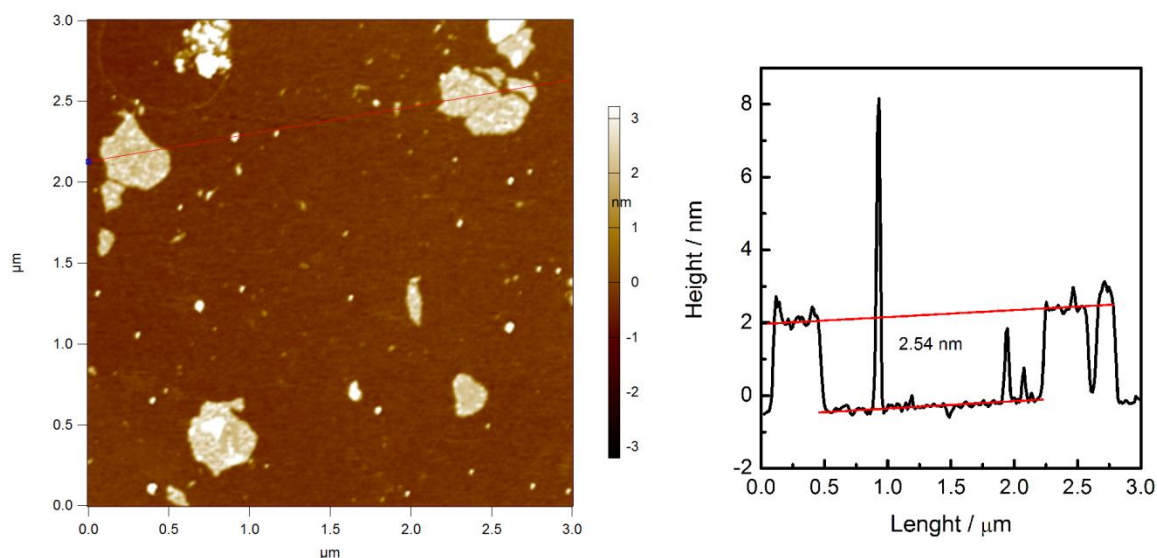


Figure 5.4.4: AFM surface topographies of BeIm-MIF(OBut) exfoliated in THF (left) and height profile (right).

Further exfoliation attempts using different pathways such as using an ultrasonic bath or simple stirring of BeIm-MIF(OBut) in THF, did not yield comparable results. Whilst stirring did only result in a clear solution and no observable nanosheets on the analysed wafers, the use of an ultrasonic bath led to an opaque suspension, however fragmentation of the sample occurred, leaving the wafer covered by small shreds with lateral dimensions below $0.1 \mu\text{m}$ with vastly varying height profiles.

5.4.3 NO₂-BeIM-MIF(OAc)

Based on the analysis of Zn[NO₂-BeIM]OAc, the corresponding NO₂-BeIM-MIF(OAc) is a promising candidate for exfoliation into nanosheets due to the significantly increased stacking parameter of the lamellar material – an advantage for the easy intercalation of CTAB into the sheet-like structure.

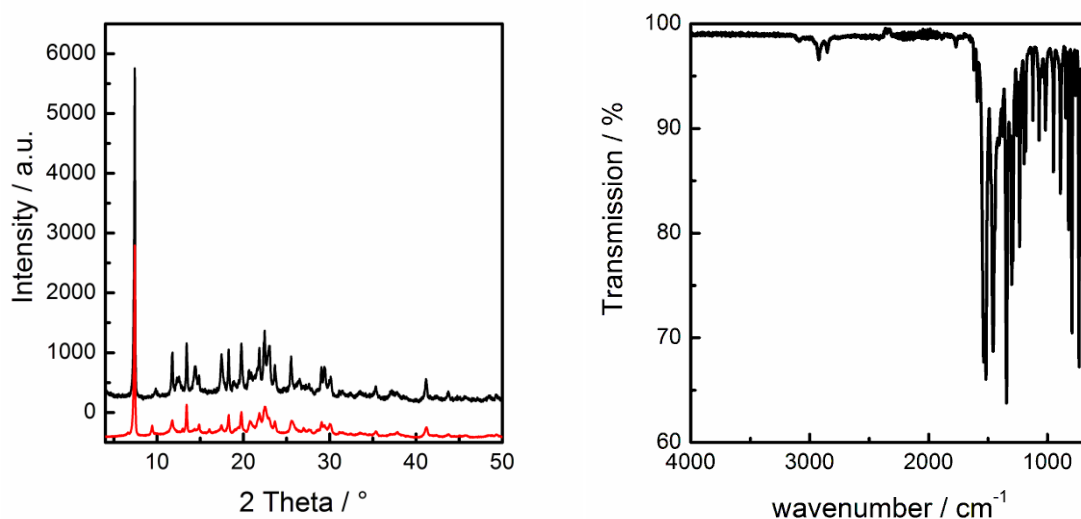


Figure 5.4.5: Powder diffractogram of NO₂-BeIM-MIF(OAc) (black) and Zn[NO₂-BeIM]OAc (red) (left) and IR spectrum (right) of NO₂-BeIM-MIF(OAc).

Powder diffraction analysis of the obtained white powder show that the material exhibits a similar diffraction pattern compared to Zn[NO₂-BeIM]OAc, however without any signs of a lamellar mesostructure as discussed in the previous chapters. This may be an indication that no mesostructure is formed, or if CTAB could be intercalated into the lamellar structure, the process did not lead to a crystalline mesostructure. The IR data match the spectrum obtained for Zn[NO₂-BeIM]OAc and suggests identical composition and coordination of nitro-benzimidazolate as well as acetate. In addition to the peaks originating from Zn[NO₂-BeIM]OAc, the of C-H stretching of the alkyl-chains are found at 2922.7 cm⁻¹ and 2852.1 cm⁻¹. This is a distinctive indication for the presence of CTAB in the formed NO₂-BeIM-MIF(OAc), bearing in mind that no other starting material exhibits aliphatic carbon chains. Due to lack of an observable mesostructure, these traces of CTAB might be found inserted between the lamellar structure, however not in a well ordered manner that is detectable via pXRD measurements or as residue on the surface of the formed particles.

Subsequent exfoliation experiments showed that despite the lack of an observable mesostructure, the material is prone to exfoliate, as even stirring of NO₂-BeIM-MIF(OAc) in THF at room temperature leads to a substantial covering of the surface of the spin-coated silicon wafers with nanosheets with lateral dimensions of 0.5 μm x 0.5 μm. Further exfoliation attempts, using orbital-shakers to apply shear forces to the material in , to further enhance the exfoliation step, yielded large clusters of

sheets in various stackings such as monolayers, double layers or triple layers with average dimensions of $0.5 \times 0.5 \mu\text{m}^2$ and a height of 2.7 nm per layer, corresponding to double layers of $\text{Zn}[\text{NO}_2\text{-BeIM}]\text{OAc}$.

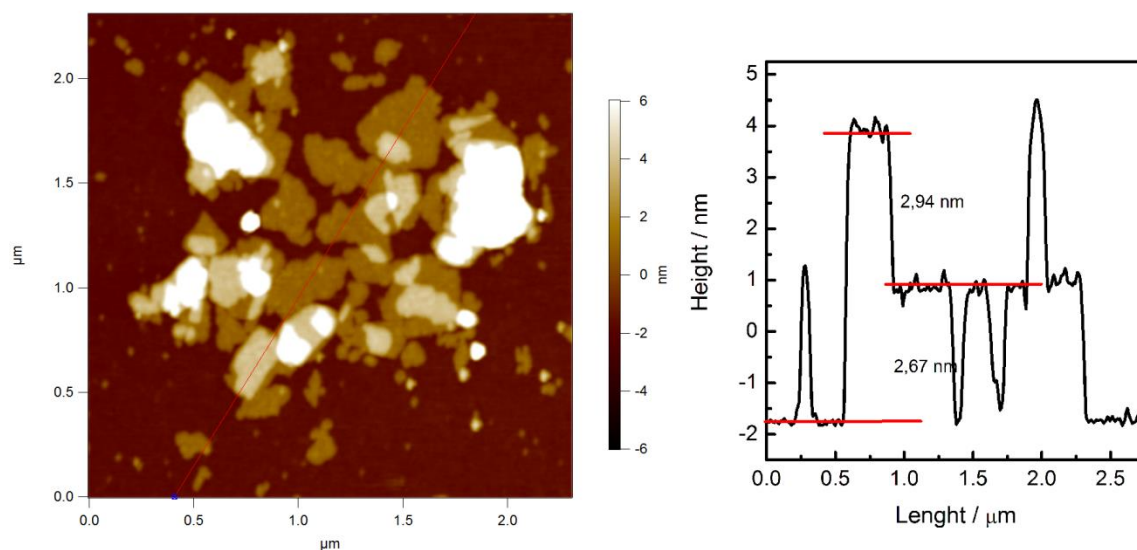


Figure 5.4.6: AFM surface topographies of $\text{NO}_2\text{-BeIM-MIF(OAc)}$ exfoliated by using orbital shakers and THF (left) and height profile (right),

These results indicate, that the effect of the nitro-groups integrated into the framework are indeed facilitating the exfoliation to a point where no detectable mesostructure is needed in order to create coordination polymer nanosheets. However the synthesis including CTAB is still a necessity, as exfoliation experiments using $\text{Zn}[\text{NO}_2\text{-BeIM}]\text{OAc}$ synthesized without CTAB did not yield nanosheets and only resulted in clear solutions without observable light scattering properties.

5.4.4 NH₂-BeIM-MIF(OAc)

Whilst the successful exfoliation of NO₂-BeIM-MIF(OAc) marks important progress on the way to nanosheets suitable for postsynthetic modification, nitro-groups are chemically unreactive under mild conditions. To overcome these obstacles, the synthesis of a quaternary phase containing amino-benzimidazolate units (NH₂-BeIM-MIF(OAc)) rather than their nitro-counterparts is desirable for obtaining nanosheets suitable for PSM reactions under mild conditions.

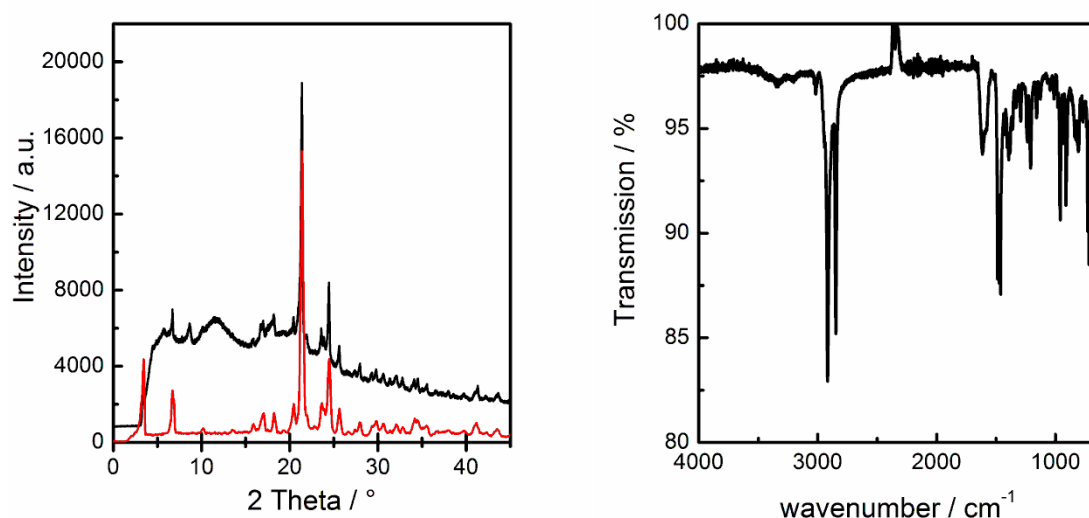


Figure 5.4.7: Powder diffractogram of NH₂-BeIM-MIF(OAc) (black) and CTAB (red) (left) and IR spectrum (right) of NH₂-BeIM-MIF(OAc).

The obtained powder diffraction pattern of the resulting white precipitate shows no resemblance with Zn[NH₂-BeIM]OAc. Comparison of the obtained pattern with the XRRD of pure CTAB reveals that all distinct peaks originate from CTA, rather than the desired hybrid material. The starting material seems to form an amorphous material, which contributes to the high background of the recorded diffraction pattern.

Infrared spectroscopy confirms that the main component of the material features aliphatic carbon chains, as seen by the very intense characteristic C-H stretching vibrations at 2913.3 cm⁻¹ and 2844.8 cm⁻¹ as well as the intense band corresponding to C-H deformation vibrational modes at 1460.4 cm⁻¹. The combination of these findings suggests that the formation of an NH₂-BeIM-MIF(OAc)-material similar to the previously discussed samples, was unsuccessful. An additional washing step with iso-propanol after the synthesis to remove any crystalline CTAB resulted in the complete decomposition of the powder with no residual material left.

5.4.5 $\text{Zn}(\text{NO}_2\text{-BeIM})_{1-x}(\text{NH}_2\text{-BeIM})_x\text{OAc}$ - MIXED LINKER SYNTHESSES

Due to the unsuccessful synthesis and exfoliation of CTAB structured $\text{Zn}[\text{NH}_2\text{-BeIM}]\text{OAc}$, the mixed linker materials synthesized in 5.3.3 were examined as candidates for intercalation and exfoliation, despite the uncertainty about the presence of amino-groups in the material. Ideally, the exfoliation properties of the pure nitro-benzimidazolate materials can thereby be combined with the presence of even a small amount of amine-groups in the material leading to nanosheets which are suitable for the proposed PSM reactions.

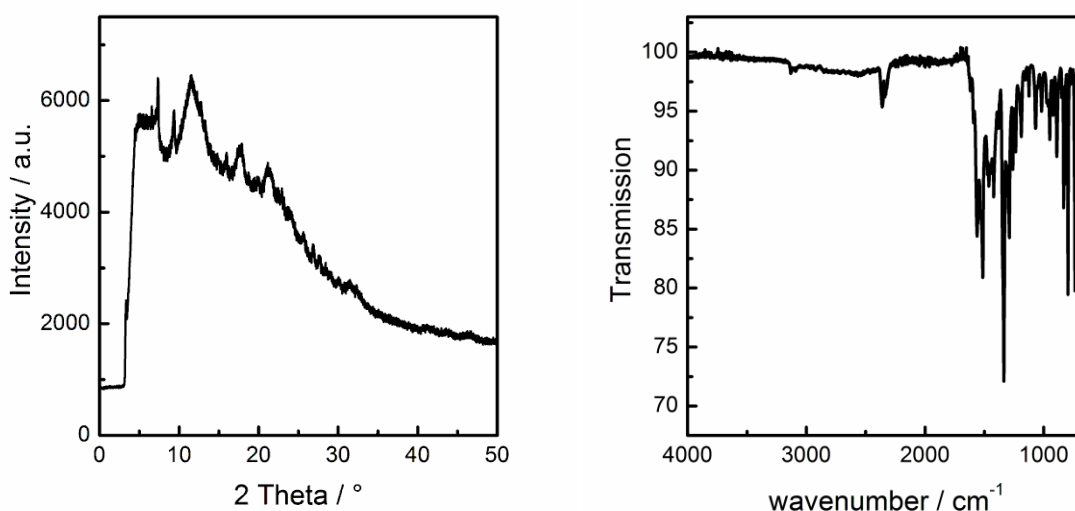


Figure 5.4.8: Powder diffractogram (left) and IR spectrum (right) of mixed linker BeIM-MIF(OAc).

Powder diffraction data obtained from the synthesis of a quaternary phase of $\text{Zn}(\text{NO}_2\text{-BeIM})_{1-x}(\text{NH}_2\text{-BeIM})_x\text{OAc}$ with $x = 0.25$ shows a vastly reduced crystallinity of the obtained material. Whilst the characteristic reflections of the ternary phase can still be observed, the overall signal-to-noise ratio has decreased drastically, indicating either a similar delamination phenomenon to what has been observed for the nitro-benzimidazolate based material (see chapter 5.4.3) or an overall loss in crystallinity during the synthesis.

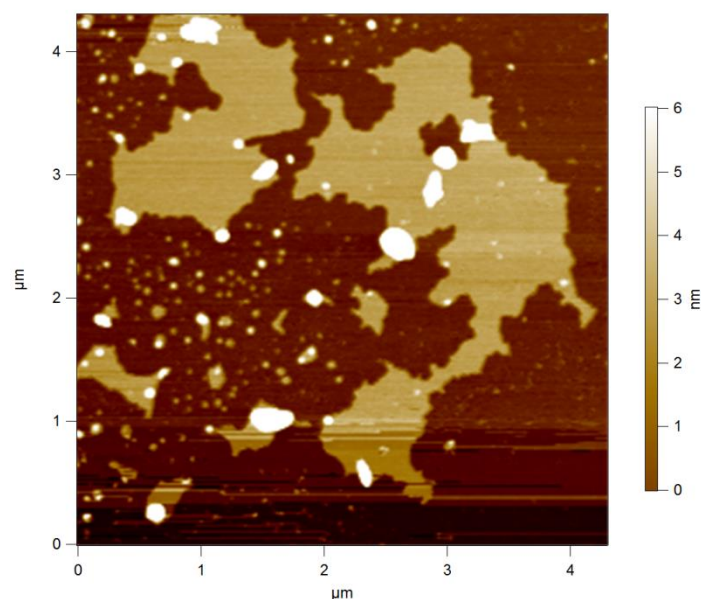


Figure 5.4.9: AFM surface topographies of depositions found after spincoating the mixed-linker $\text{Zn}[\text{NO}_2\text{-BeIM}]_{1-x}[\text{NH}_2\text{-BeIM}]_x\text{OAc}$ with $x = 0.25$.

Subsequent exfoliation attempts in THF, diethylether, ethanol and isopropanol using orbital shakers did not lead to nanosheet deposition on the used Si-wafers. Whilst the resulting solutions after the use of the orbital shaker showed slight opacity, the surface of the wafers was partially covered with material, with a thickness of about 4 nm. However, the irregular shape of edges and the rather smooth corners of the observed structures as well as the absence of any double-layers of deposited material points to the soft - and likely purely organic - composition of the layers, such as pure CTAB or benzimidazole. Subsequent washing steps were, in contrast to the previously discussed nanosheets, able to remove all structures from the wafer surface.

5.5 POST-SYNTHETIC MODIFICATION OF AMINE-GROUP CONTAINING LINKERS

Amine-functionalizations introduced into the framework, are a common way of achieving substrates for further post-synthetic modification reactions in MOFs, due to straightforward reactions with organic functional groups such as ketons or isocyanates already at low temperature. Despite the difficulties in exfoliation of the materials containing amine-groups and to prove whether the mixed linker framework actually does contain amine- as well as nitro-functionalizations, post-synthetic modification reactions were performed. In a one-step synthesis, the coordination polymer was stirred in freshly distilled chloroform and phenylisocyanate was added to the mixture (for detailed synthesis protocols, see chapter 5.7). The resulting white powder was collected and subsequently analyzed by pXRD, IR and ^{13}C Solid-state NMR spectroscopy.

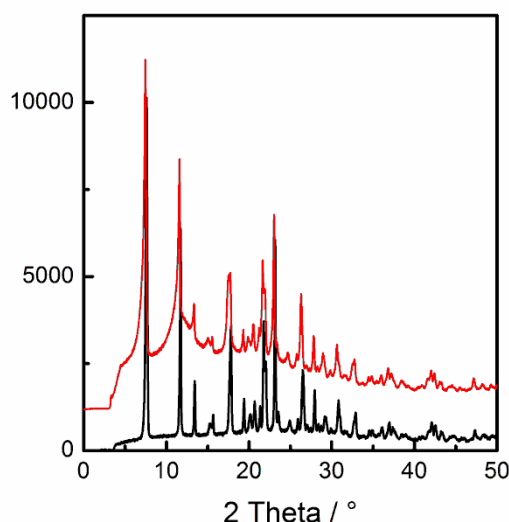


Figure 5.5.1: pXRD patterns of $\text{Zn}[\text{NH}_2\text{-BeIM}]\text{OAc}$ (black) and $\text{Zn}[\text{NH}_2\text{-BeIM}]\text{OAc}$ functionalized with phenylisocyanate (red).

Powder diffraction experiments performed on the material before and after the PSM reaction, show no difference in the resulting patterns apart from a slight broadening of peaks, which can be seen as indication of slightly decreasing particle size during the functionalization reaction. It is however, safe to assume that the framework structure has remained intact during the entire process. As the reaction between the amine-groups and isocyanate can only occur on the surface of the used bulk material and considering that the coordination polymer does not have adequately sized pores for the used phenylisocyanate to infiltrate the structure, the retained and unchanged crystal structure is in good agreement with the expected outcome of the reaction.

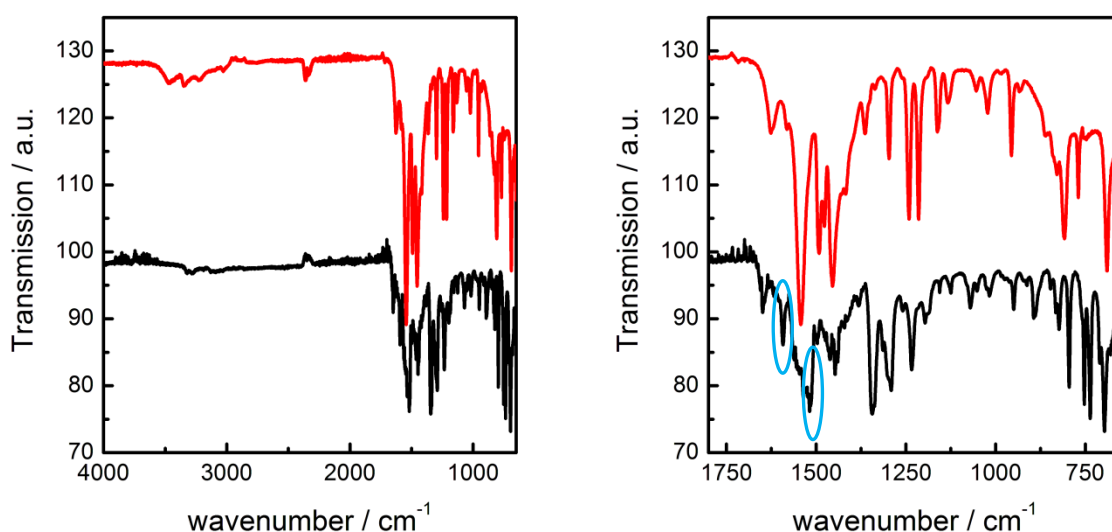


Figure 5.5.2: IR spectra of Zn[NH₂-BelM]OAc (red) and Zn[NH₂-BelM]OAc modified with phenylisocyanate (black). The peaks indicating the functionalization of the material are marked in blue.

Infrared spectroscopic measurements were performed to confirm the covalent modification of the accessible amino-groups with isocyanate. A reduction in intensity of the N-H vibrational modes between 3500 and 3200 cm⁻¹ is clearly visible, with the bands being almost not detectable any more in the sample after the PSM reaction. This indicates a mostly completed reaction, however no clear statement about the degree of functionalization can be made via this method. Additional confirmation for a successful PSM reaction is found in the peak at 1670.1 cm⁻¹ which can be attributed to the C=O valence vibrations of the amide group as well as an additional peak at 1517.7 cm⁻¹ corresponding to N-H bending vibrations of the amide bond.

Solid-state ¹³C MAS NMR analysis was performed in order to investigate the presence of amide bonds formed during the PSM process, which would be indicative of a successful modification. The obtained data is in good agreement with NMR data obtained for the unmodified Zn(NH₂-BelM)OAc with respect to the C1/C2 signals of acetate (23.7 ppm, 183.7 ppm) and the benzimidazolate backbone (100.3 ppm, 114.5 ppm, 133.9 ppm, 146.5 ppm). However, additional signals around 120 ppm can be observed, which correspond to the phenyl-ring system of the phenylisocyanate used in the PSM reaction as well as a signal at 182.0 ppm, corresponding to C10 in the amide bond.

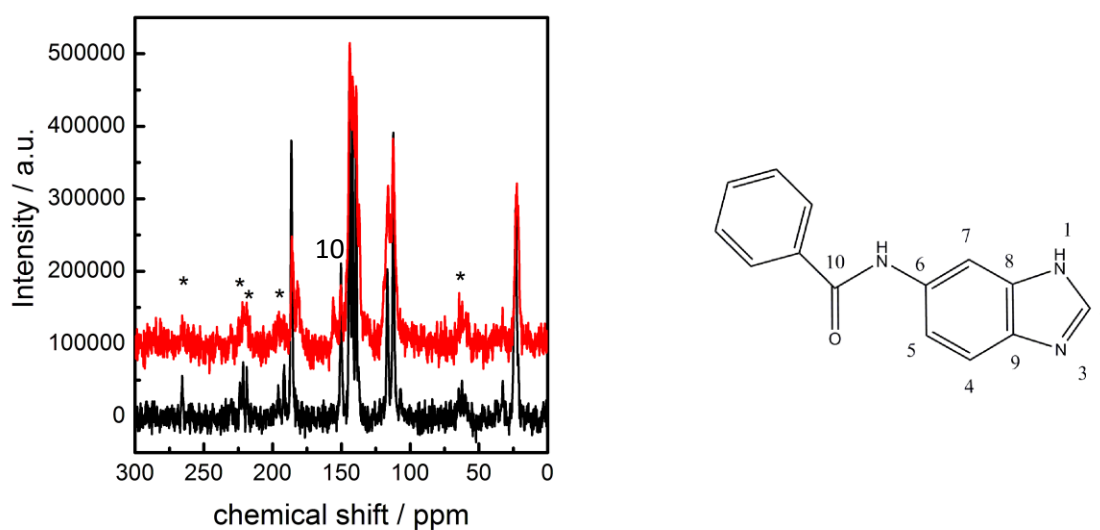


Figure 5.5.3: ^{15}N NMR spectra of $\text{Zn}[\text{NH}_2\text{-BelM}]\text{OAc}$ (black) and $\text{Zn}[\text{NH}_2\text{-BelM}]\text{OAc}$ modified with phenylisocyanate (red). Spinning side-bands are marked with an asterisk.

Table 5.5.1: Experimental ^{13}C NMR chemical shifts (in ppm) and assignments to $\text{Zn}[\text{NH}_2\text{-BelM}]\text{OAc}$ after PSM with isocyanate as well as comparison to ZIF-7 and the used starting materials.

^{13}C NMR			δC2	δC7	$\delta\text{C4,5}$	δC6	$\delta\text{C8,9}$
$\text{Zn}[\text{NH}_2\text{-BelM}]\text{OAc}$ (PSM)	23.2	185.8	145.8	101.0	115.6	140.4	134.2
$\text{Zn}[\text{NH}_2\text{-BelM}]\text{OAc}$	23.7	183.7	146.5	100.3	114.5	141.3	133.9
ZIF-7			149.9	114.9	122.5	125.3	138.1; 140.3
$\text{NH}_2\text{-BelM(H)}$			146.5	105.4	114.9		137.9
$\text{Zn}(\text{OAc})_2$	9.1	185.3					

^{15}N Solid-state MAS NMR would be a suitable way to provide additional information about the nitrogen atoms in the structure, especially those forming the amide bonds, however due to the low yield of the performed reaction, the amount of obtained substance was not sufficient for this analysis.



Figure 5.5.4: Image of $\text{Zn}[\text{NH}_2\text{-BeIM}]\text{OAc}$ (left) and $\text{Zn}[\text{NH}_2\text{-BeIM}]\text{OAc}$ modified with 4-(6-methyl-2-benzothiazolyl)phenyl isocyanate (black) under UV radiation.

In order to prove that the PSM reaction is not limited to small molecules such as phenylisocyanate and to provide proof that the PSM reaction on $\text{Zn}[\text{NH}_2\text{-BeIM}]\text{OAc}$ is a suitable method to introduce additional properties into the material, a fluorescence marker was used as a reagent. 4-(6-methyl-2-benzothiazolyl)phenyl isocyanate is a commonly used fluorescence marker with an absorption maximum at 350 nm and a corresponding emission maximum at 374 nm in its pristine form in chlorobenzene. The detailed synthesis procedure can be found in chapter 5.7.

The obtained powder exhibited white coloration in contrast to the brownish color of the parent $\text{Zn}[\text{NH}_2\text{-BeIM}]\text{OAc}$, which may be attributed to the reaction of the amine groups with impurities found in the material due to the difficulties in the synthesis procedure of amino-benzimidazole discussed in chapter 5.3.2. The white color of the labeled compound is in good agreement with the white color of the nitro- and pure benzimidazole based materials. Exposure of the material to UV light, readily leads to fluorescence of the sample, in contrast to its parent material (Figure 5.5.4). To ensure that the observed fluorescence is a result of covalently bound 4-(6-methyl-2-benzothiazolyl)phenyl isocyanate and does not merely result from the unreacted fluorescence marker, additional experiments using $\text{Zn}[\text{NO}_2\text{-BeIM}]\text{OAc}$ were performed, resulting in no observable fluorescence. Whilst unreacted fluorescence marker in the sample would also create fluorescence in the system, a covalent connection between the marker and the nitro-functionalized framework is not possible. Due to these findings, the absence of fluorescence in the nitrobenzimidazolate system can be seen as an additional strong indication of the successful PSM reaction between the surface amine-groups of the framework and the fluorescence linker in $\text{Zn}[\text{NH}_2\text{-BeIM}]\text{OAc}$.

5.6 CONCLUSION

In this chapter, the synthesis and close structural relationship between a group of coordination polymers with the general composition $\text{Zn}[\text{X-BeIM}]\text{R}$ ($\text{X} = \text{NO}_2, \text{NH}_2$; $\text{R} = \text{OAc}, \text{OPr}, \text{OBut}$) was shown.

The coordination polymer $\text{Zn}[\text{BeIM}]\text{OPr}$ was synthesized in a solution based synthesis route and characterized by pXRD, Solid-state NMR, elemental analysis, IR spectroscopy and TEM SAED measurements, showing that the obtained material exhibit close structural relations to $\text{Zn}[\text{BeIM}]\text{OAc}$. An elongation of the a-axis of the unit cell, parallel to the carbon backbone of the carboxylic acids can be observed, which is believed to be based on the use of the longer propionate during the synthesis. The use of CTAB in the solution-based synthesis with the goal to achieve mesostructuring of the material due to intercalation of the surfactant into the layered structure and thereby exfoliation into nanosheets, was not possible by the routes employed. Analysis of the material obtained in the CTAB-containing synthesis showed no presence of the surfactant and the subsequent exfoliation attempts yielded no nanosheets that could be detected via AFM measurements.

The synthesis of the analogous $\text{Zn}[\text{BeIM}]\text{OBut}$ via the known synthesis pathway leads to a material with reduced symmetry, yet still exhibits the same framework topology. Analysis by pXRD, Solid-state NMR, elemental analysis and IR spectroscopy proved that the obtained material has a doubled a-axis in comparison to the previously known frameworks, due to the loss of the glide mirror plane in the crystal structure, which is believed to be based on the increased orientation possibilities of the butyrate alkyl-chain in the structure in contrast to the previously used shorter carboxylic acids.

The synthesis of $\text{Zn}[\text{BeIM}]\text{OBut}$ was also achieved via a Solid-state route, leading to a materials with a slightly truncated a-axis, compared to $\text{Zn}[\text{BeIM}]\text{OPr}$, which is attributed to the differences in synthesis procedure. The additional tempering step as well as the solvent-free synthesis is supposed to assist in the arrangement of the carboxylic carbon backbone into a more dense packing and thereby reduce the interlayer distance.

Exfoliation experiments were performed on the material via a solution-based synthesis with CTAB added to the reaction, leading to $\text{BeIM-MIF}(\text{OBut})$, a material with CTAB intercalated between the sheetlike structure. pXRD analysis revealed an ordered lamellar mesostructure and subsequent exfoliation produced nanosheets sized $0.5 \times 0.5 \mu\text{m}^2$ with a height of 2.5 nm, indicating double layers of the exfoliated material, seeing that the thickness of a single lamellae in the crystal structure equals around 1.2 nm.

Experiments to introduce functional groups suitable for subsequent postsynthetic modification led to the synthesis of $\text{Zn}[\text{NO}_2\text{-BeIM}]\text{OAc}$ and $\text{Zn}[\text{NH}_2\text{-BeIM}]\text{OAc}$, two materials enriching the family of isostructural lamellar benzimidazolate-bridged coordination polymers known.

Both materials exhibit an increased stacking distance of the lamellar structure in comparison to the non-functionalized material, which can be rationalized by the increased sterical requirement of the nitro- and amine-groups in the interlayer space. Subsequent exfoliation experiments via the known intercalation synthesis with CTAB yielded different results for the two materials. The amino-functionalized framework showed decreased crystallinity and IR spectroscopy revealed the integration of small amounts of CTAB into the compound. Exfoliation in THF resulted in nanosheets with lateral dimensions of $0.5\ \mu\text{m} \times 0.5\ \mu\text{m}$ and an average height of 2.7 nm, indicating double layer-sheets of $\text{Zn}[\text{NO}_2\text{-BeIM}]\text{OAc}$ deposited onto the wafer. In contrast, exfoliation experiments with the amino-functionalized material did not lead to intercalation of CTAB but to the formation of an amorphous material and CTAB as the main crystalline phase.

Whilst the exfoliation experiments to synthesize nanosheets including amine-functionalities did not yield the desired materials, postsynthetic modification experiments on bulk- $\text{Zn}[\text{NH}_2\text{-BeIM}]\text{OAc}$ were performed to prove that the framework structure is suitable for the functionalization of the exposed amino groups with larger molecules on the surface of the bulk material. Experiments with phenylisocyanate and a fluorescence marker showed that the amine-groups are accessible and able to participate in reactions without destroying the framework structure. The reactions with the fluorescence marker additionally proved that properties such as fluorescence can be introduced into the material via PSM reactions.

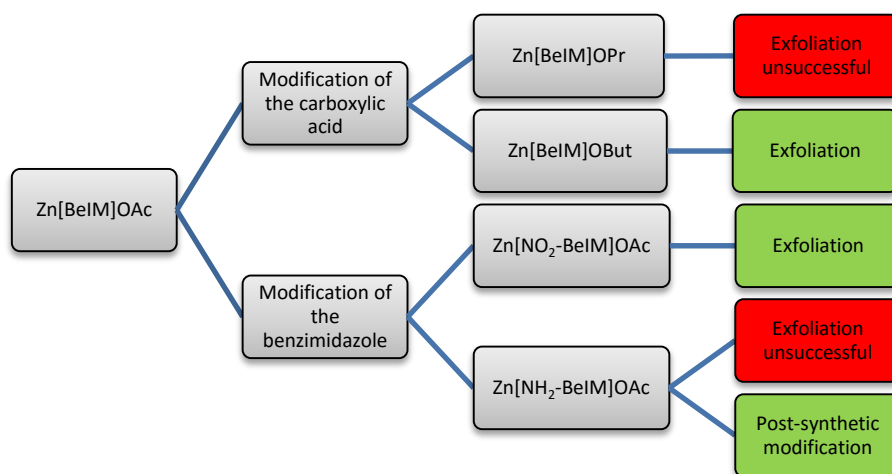


Figure 5.6.1: Schematic overview of the experiments performed as part of this chapter, showcasing the different modification approaches taken and the corresponding results.

5.7 EXPERIMENTAL DETAILS

5.7.1 SYNTHESIS OF $\text{Zn}(\text{C}_4\text{H}_7\text{O}_2)_2$

Zinc-butyrate was synthesized by mixing ZnO (10g, 0.112 mol) with butyric acid (33.63 mL, 0.368 mol) in 200mL EtOH. The mixture was heated to 85 °C for 2h under reflux conditions. The formed white precipitate was collected by centrifugation at 20.000 rpm, was washed subsequently with ethanol and petroleum ether and dried at room temperature.

The obtained white powder was analyzed by elemental analysis and ^{13}C Solid-state NMR.

Zn(OBut) ₂	13.5 ppm	19.3 ppm	37.1 ppm	184.6 ppm
HOBut	13.7 ppm	18.4 ppm	36.2 ppm	180.7 ppm

5.7.2 SOLUTION BASED SYNTHESIS OF BeIM-MIF(R) , R = PRO, BUTO

In a typical solution based synthesis, 5.4 mL BeIM (0.6 M in 1-hexanol) and 2.7 mL zinc propionate (or butyrate) (1.2 M in water) were added to 200 mL of a 9:1 mixture of n-heptane/1-hexanol. The mixture was heated for 16h and yielded a white precipitate that was collected by centrifugation (10k rpm for 5 minutes) and dried overnight at room temperature.

5.7.3 SOLID-STATE SYNTHESIS OF $[\text{Zn(BeIM)OBUT}]$

To obtain material via Solid-state synthesis, 0.118 g BeIM (1.0 mmol) and 0.239 g Zn(OBut)₂ (1 mmol) were thoroughly ground and filled in a dry Duran glass tube (diameter ext. 10mm, int 7 mm). The tube was evacuated, sealed under argon atmosphere at a length of 12 cm and placed in an inclined tube furnace. The oven was heated with a rate of 60°C / hour to 180 °C, held for 10 h, cooled to 105°C with 1°C/hour and cooled to RT with 60°C / hour. The obtained colorless product was washed with EtOH and dried overnight at RT.

5.7.4 SOLUTION BASED SYNTHESIS OF BeIM-MIF(R) , R = PRO, BUTO WITH CTAB FOR EXFOLIATION

To obtain material for exfoliation purposes, 5.4 mL BeIM (0.6 M in 1-hexanol) and 2.7 mL zinc propionate (or butyrate) (1.2 M in water) were added to a suspension containing 0.05 M CTAB in a 9:1 mixture of n-heptane/1-hexanol (200 mL). The mixture was heated for 16h and yielded a white precipitate that was collected by centrifugation (10k rpm for 5 minutes) and dried overnight at room temperature.

5.7.5 POST-SYNTHETIC MODIFICATION OF $\text{Zn}[\text{NH}_2\text{-BeIM}]\text{OAc}$ WITH PHENYLISOCYANATE

The PSM reaction was performed by dispersing 100 mg $\text{Zn}[\text{NH}_2\text{-BeIM}]\text{OAc}$ in 10 mL freshly distilled CHCl_3 . Under constant stirring, 0.3 mL (2.76 mmol) phenylisocyanate were added to the solution and the mixture was subsequently stirred for 3 days at room temperature.

The material was collected by filtration, washed with dry CHCl_3 and dried at room temperature.

6 MICROEMULSION SYNTHESIS OF $\text{Zn}(\text{Im})_2$

The effects of surfactants on a system can be manifold and are often determined by various factors such as the type of surfactants used, their concentration or the employed solvents, amongst others. While working on the synthesis of mesostructured imidazolate frameworks and upon realizing the importance of the used surfactant counter-ions such as bromide (see Chapter 4), multiple reactions without halogenides as counter-ions were carried out.

To obtain a halogenide-free surfactant, cetyltrimethylammonium bromide (CTAB) was treated with AgNO_3 to remove bromide and replace it by nitrate ions for charge compensation. The resulting nitrate containing surfactant (CTANO_3) is supposed to limit the possibility of structural changes in the obtained materials due to interactions of the framework with the surfactant counter-ion.

Experiments based on the previously discussed MIF syntheses using the halogenide-free surfactant, did not result in the formation of any precipitate. This outcome indicates that without the effects of the halogenide ions, other ways to enhance the reaction are needed. In further experiments, an organic base such as tetraethylammonium hydroxide (TEAOH) was added to the reaction mixture, in order to facilitate the deprotonation of the imidazole linker. This deprotonation prior to the reaction is supposed to enable the formation of a framework due to the significantly increase reaction speed of imidazolate with the used zinc ions, in comparison to imidazole.

6.1 EXPERIMENTAL DETAILS

6.1.1 MICROEMULSION ROUTE

1.) Bromine-free surfactant:

CTAB (27.4 mmol, 10.0g) was dissolved in 300ml water and AgNO_3 (25.5 mmol, 4.34 g) dissolved in 50 mL water was slowly added under constant stirring. The mixture was kept in the dark and stirred overnight, followed by subsequent centrifugation at 22.000 rpm for 15 min at 15 °C to remove precipitated AgBr , and the supernatant was dried at 70 °C to obtain CTANO_3 .

2.) Microemulsion synthesis

CTANO_3 (416 mg) was dissolved in 30 mL of iso-propanol. $\text{Zn}(\text{OAc})_2$ (603 μl ; 1 mol/l) and imidazole (670 μl , 1.8 mol/l) dissolved in water were added. Upon addition of a base (TEAOH, 295 mg) the formation of a white precipitate could be observed. In order to ensure complete reaction, the mixture was stirred at room temperature for two days, followed by filtration. The precipitate was washed with isopropanol and the obtained white powder was dried at room temperature.

6.1.2 SOLVOTHERMAL ROUTE

$\text{Zn}(\text{OAc})_2$ (3.3 mmol, 6072 mg), dissolved in 10 ml ethanol, and imidazole (6.67 mmol, 3.71 mg), dissolved in 10 ml pyridine, were combined and stirred for 12 hours. The solution was placed in a closed autoclave and heated under autogenic pressure to 140 °C for 24 hours.

The resulting white precipitate was collected by filtration, washed with isopropanol and subsequently dried at room temperature.

6.2 XRD POWDER DIFFRACTION AND STRUCTURAL DISCUSSION

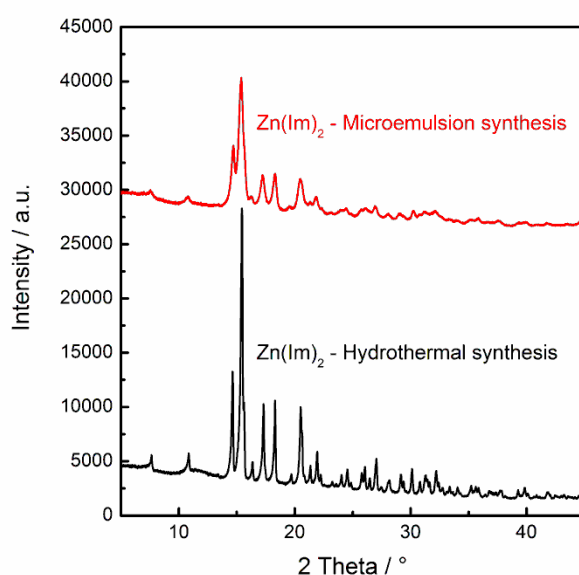


Figure 6.2.1: Powder x-ray diffraction pattern of $\text{Zn}(\text{Im})_2$, synthesized under microemulsion conditions (red) and through means of hydrothermal synthesis as reported by Tian et al. (black).

Powder X-ray diffraction measurements of the obtained materials after microemulsion synthesis were recorded and found to be in good agreement with the pattern of $\text{Zn}(\text{Im})_2$, a material which is usually accessible *via* hydrothermal methods as reported by Tian et al.^[214] A substantial broadening of the observed lines with concurrent reduction in the observed intensity, compared to the hydrothermally obtained material, is visible. This suggests that either the crystallinity of the material

is lower or the particle size is significantly reduced, likely due to surfactant effects. Both effects are known for metal-organic frameworks and have been explored previously.^[120, 215, 216] Templating effects such as mesostructure introduced into the material, cannot be observed in the powder pattern.

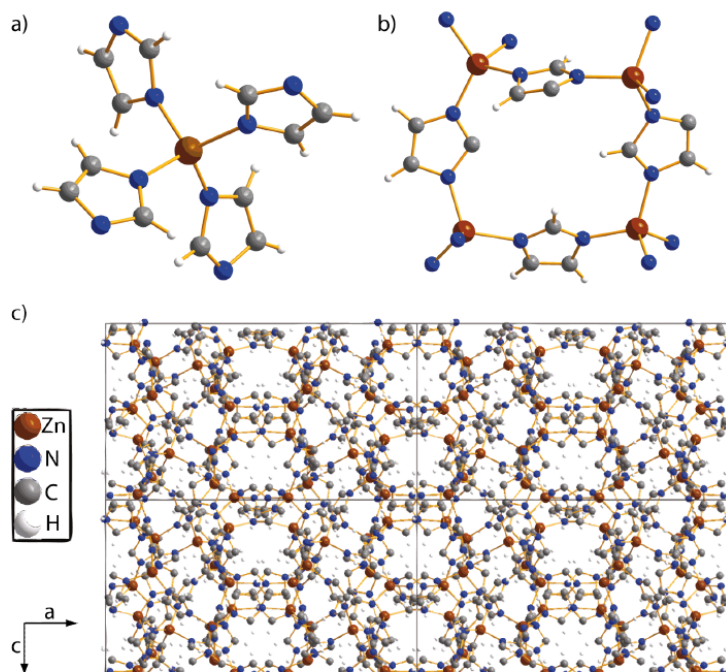


Figure 6.2.2: Crystal structure of $\text{Zn}(\text{Im})_2$: (a) tetrahedral coordination of Zn^{2+} ions by imidazolate; (b) characteristic Zn_4Im_4 4-rings; (c) 2×2 -supercell, viewing direction along $[010]$.^[214]

$\text{Zn}(\text{Im})_2$ has been characterized by multiple groups, which claim to have found different, yet closely related structures for the material. The first synthesis of this material was reported by Lehnert and Seel in 1980 during an investigation of Zn^{2+} and Mn^{2+} imidazolate salts.^[217] The synthesis was carried out by adding zinc acetylacetonate to a low melting ionic liquid, consisting of a mixture of imidazolate and tetramethylimidazolate. The resulting colorless crystals were described as $\text{Zn}(\text{Im})_2$ crystallizing in the space group $I4_1acd$ with $a = b = 22.872 \text{ \AA}$ and $c = 12.461 \text{ \AA}$.

In 2003, sparked by the growing interest in metal-organic frameworks, Tian et al. developed a hydrothermal synthesis for $\text{Zn}(\text{Im})_2 \cdot \text{H}_2\text{O}$ and its cobalt analogue, using acetate metal salts and imidazole in an organic solvent mixture.^[214] The obtained crystals were solved in $I4_1$ with $a = b = 22.874 \text{ \AA}$ and $c = 12.941 \text{ \AA}$.

The complex structure of the material has been described to consist of SBUs of M^{2+} 4-rings, that are doubly connected to wavelike or double-crankshaft-like chains. These chains are aligned parallel to the a -axis and intersect with identical chains running along the b -axis by means of common 4-rings at the wave peaks to form an open 3D framework with 12-ring openings. To complete the crystal structure, three open frameworks are interwoven and linked by imidazolates *via* the M^{2+} ions. The

resulting 3D framework is not an open framework, yet helical channels with dimensions of $3.5 \times 3.5 \text{ \AA}$ along the c-axis are accessible and contain water molecules in the crystal structure.

The same structural motifs are also known to occur in mixed-ligand syntheses as described by Yaghi *et al.*, who synthesized ZIF-61 [$\text{Zn}(\text{Im})(2\text{-MeIm})$] *via* hydrothermal synthesis routes and investigated this material alongside other materials featuring a $\text{Zn}(\text{Im})_2$ composition for their CO_2 capturing capabilities.^[42]

6.3 INFRARED SPECTROSCOPY

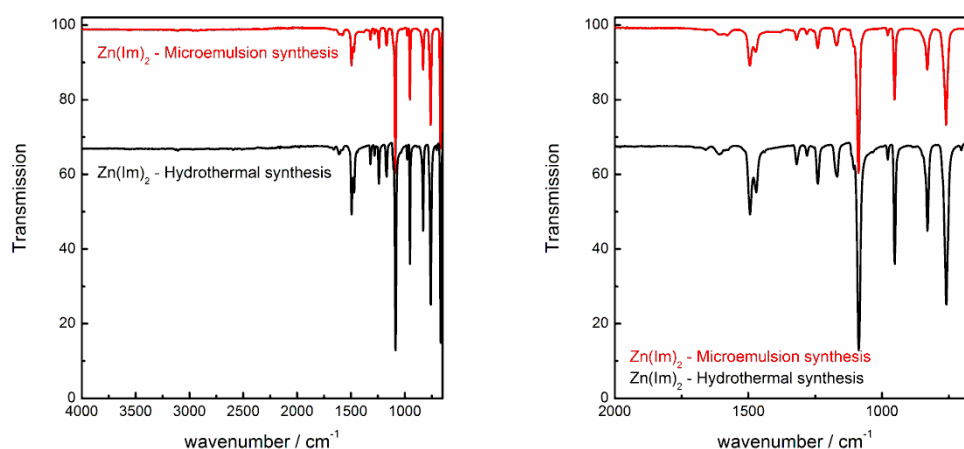


Figure 6.3.1: Infrared spectroscopic data of $\text{Zn}(\text{Im})_2$, synthesized under microemulsion conditions in *i*-PrOH (red) and *via* the hydrothermal synthesis route (black).

The absence of surfactant in the obtained material could be proven by infrared spectroscopy, showing no $\nu(\text{C-H})$ vibrations as commonly found for alkyl chains at around $2800\text{--}2900 \text{ cm}^{-1}$. A comparison with the hydrothermally obtained materials shows good agreement with no additional peaks found.

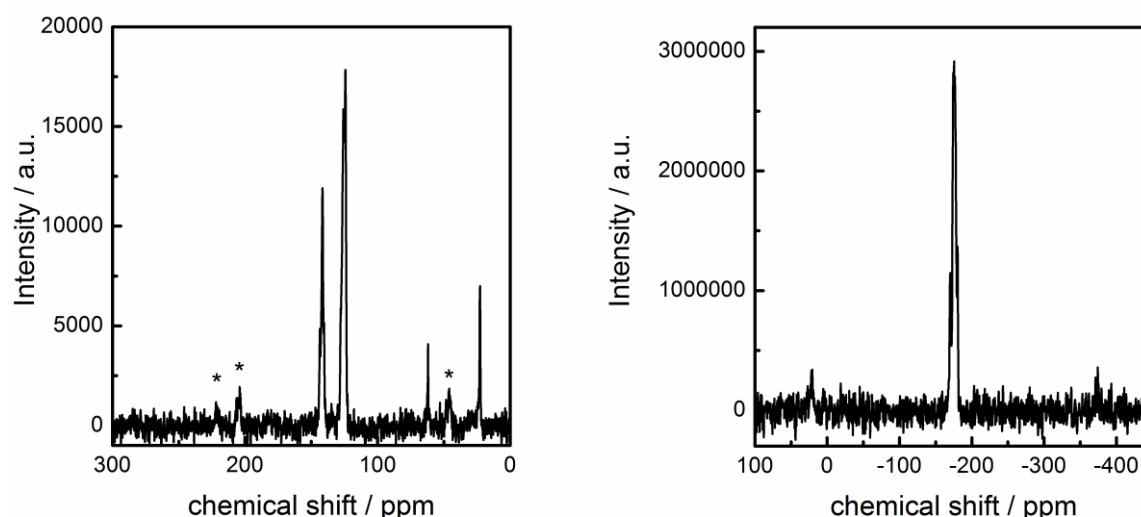
6.4 ELEMENTAL ANALYSIS

Elemental analysis confirms the composition of the found material under the assumption of small amounts of 2-propanol captured within the framework. In contrast to the previously reported $\text{Zn}(\text{Im})_2 \cdot \text{H}_2\text{O}$, the amount of isopropanol contained in the structure is lower, leading to a formula of $\text{Zn}(\text{Im})_2 \cdot 0.1 (\text{C}_3\text{H}_8\text{O})$ based on elemental analysis. Whilst the lower amount of iso-propanol compared to water is in part expected to be a result of the larger diameter of iso-propanol, the differences in the kinetic diameter (water 2.7 \AA , iso-propanol 4.7 \AA)^[218] do not support this being the sole reason for the observed difference in the amount of guest molecules.

Table 6.4.1: Elemental analysis of $\text{Zn}(\text{Im})_2$ obtained by microemulsion synthesis and comparison to the values calculated for solvent-free $\text{Zn}(\text{Im})_2$.

Element	N	C	H	Zn
Mass percentage	25.4	37.5	3.7	31.3
Molar ratio	1.8	3.1	3.6	1
Molar ratio, calc.	2	3	3	1

6.5 SOLID-STATE NMR SPECTROSCOPY

**Figure 6.5.1:** Solid-state NMR data of $\text{Zn}(\text{Im})_2$ via microemulsion synthesis. (left) ^{13}C NMR; (right) ^{15}N NMR. Spinning side bands are marked with asterisks.

Solid-state NMR measurements were used in order to determine if trace amounts of solvents were included into the channels of the material during the synthesis procedure. The signals in ^{13}C solid state NMR could be assigned to the deprotonated imidazolate ($\delta = 141.5$ ppm, 124.3 ppm) by comparison with the known literature values for the imidazolate based ZIF-4.^[41, 121] as well as to isopropanol ($\delta = 62.0$ ppm, 22.7 ppm) used as solvent in the synthesis. As the residual isopropanol could not be removed by thermal treatment at 150°C for 3 days, it can be assumed that the isopropanol is included into the structure in the same way as water is in the hydrothermally obtained material.^[214] In the ^{15}N NMR spectrum, a single signal at -184.1 ppm is found, which can be attributed to both imidazolate nitrogen atoms as they exhibit similar local chemical surroundings. The complex

splitting pattern of the peak in the ^{15}N NMR spectrum can be attributed to the effects of the different positions of the imidazolate molecules in the complex crystal structure, as described in chapter 6.2.

Table 6.5.1: Assignment of the observed signals in ^{13}C solid-state NMR and comparison to reported literature values.^[219]

Observed chemical shift			Literature values [ZIF-4]
[ppm]			[ppm]
Imidazolate	C ₁	141	148
Imidazolate	C _{2/3}	124	122
Isopropanol	C ₁	62	64
Isopropanol	C ₂	23	25

6.6 THERMAL ANALYSIS

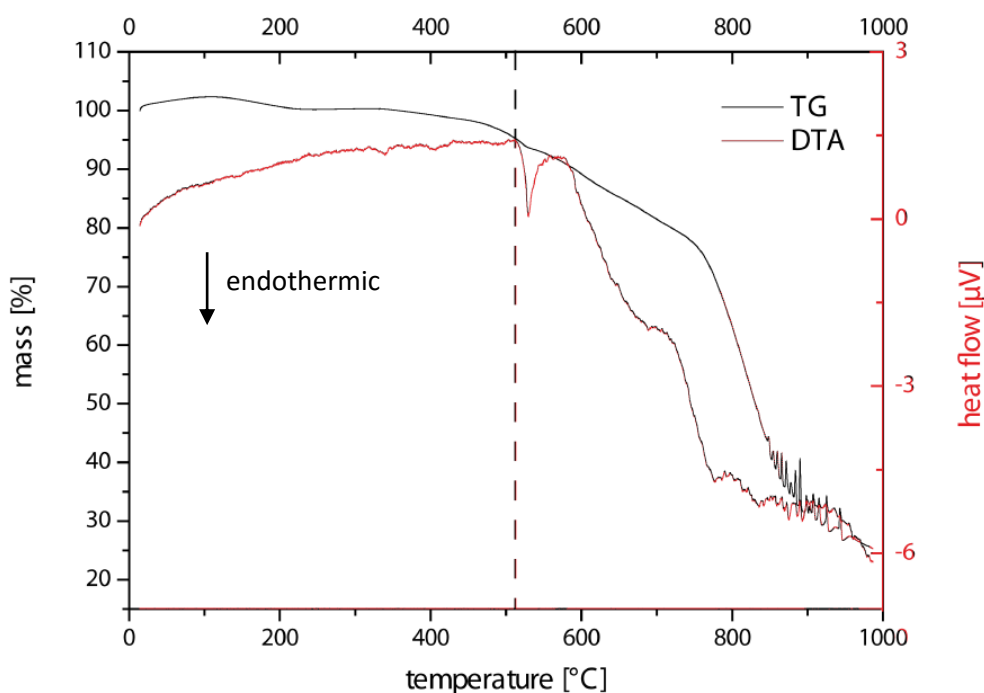


Figure 6.6.1: Thermogravimetry (TG, black) and differential thermal analysis (DTA, red) of $\text{Zn}(\text{Im})_2$ obtained via microemulsion synthesis.

Thermal analysis of the obtained material revealed thermal stability up to 500 °C. Starting at 500 °C, a gradual weight-loss step of about 25% until 775 °C can be observed, followed by a sharp decrease due to decomposition of the material. The first gradual step between 500°C and 775°C can most likely be attributed to the transformation of the material into amorphous N-doped carbon containing Zn^{2+} ions, as reported for various carbon based networks, commonly used in electrochemical

applications.^[220] The thermal stability of the material has not been investigated in the previous publications, yet is comparable to the properties of some of the thermally most stable MOFs, ZIF-8 (500°C) and ZIF-11 (525°C).^[41]

The endothermic process that can be observed starting at 510°C is related to the melting point of the material, which was confirmed by melting point analysis.

6.7 SCANNING ELECTRON MICROSCOPY

SEM images of $\text{Zn}(\text{Im})_2$ were obtained with an acceleration voltage of 5 kV. An overview image of the sample synthesized *via* microemulsion conditions at a magnification of 1800x shows rectangular shaped crystals with side lengths ranging from 2 to 10 μm (Figure 7.6.1). At higher magnification of 12000x, smaller particles become visible with lengths of about 300 nm.

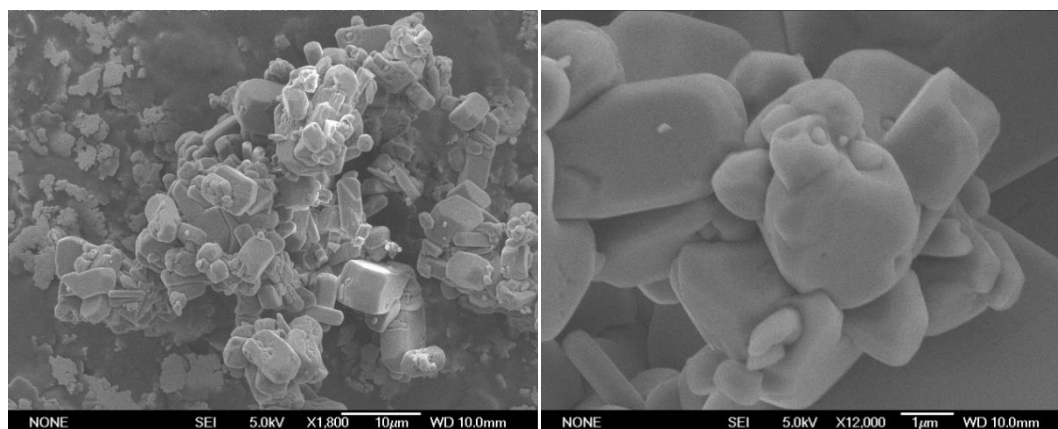


Figure 6.7.1: Scanning electron micrograph of $\text{Zn}(\text{Im})_2$ obtained *via* microemulsion synthesis at a magnification of x1800 (left) and x12000 (right).

SEM imaging of samples obtained *via* hydrothermal synthesis at a magnification of 6500x shows crystals that resemble the crystals obtained using microemulsion synthesis in shape as well as size, ranging from 500 nm to about 8 μm . At higher magnification of 12000x, smaller particles in the nanometer range can be seen in some chosen areas, which could not be observed for the microemulsion synthesis.

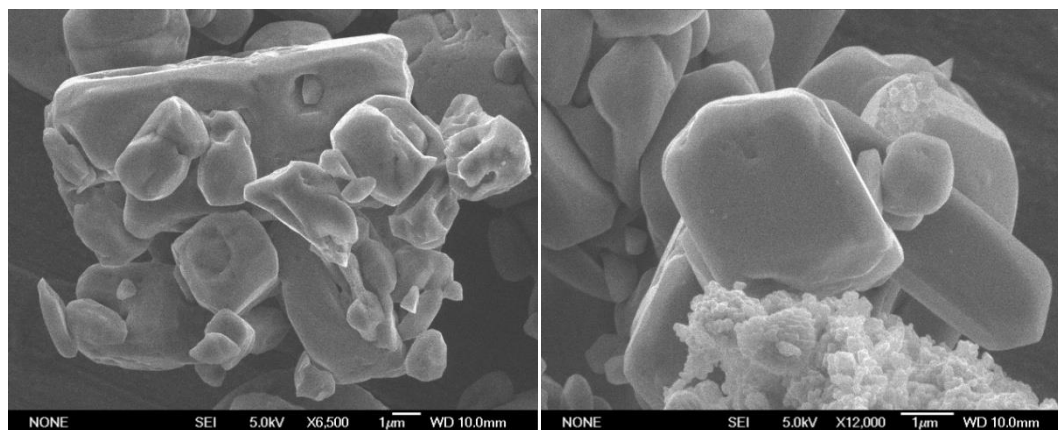


Figure 6.7.2: Scanning electron microscopical images of $\text{Zn}(\text{Im})_2$ obtained *via* hydrothermal synthesis at a magnification of x6500 (left) and x12000 (right).

Due to the particle size being comparable between the material synthesized utilizing microemulsion synthesis and hydrothermal methods, size effects cannot be invoked as the sole reason for wide peaks as well as the increase in background noise observed in the powder diffraction pattern.

6.8 DISCUSSION

The synthesis of $\text{Zn}(\text{Im})_2$ *via* microemulsion assisted routes offers a simple way to obtain the material using a room temperature synthesis as compared to the autoclave-based solvothermal synthesis reported in the literature. Whilst the crystallinity of the material obtained from microemulsion is lower than that of the solvothermally obtained $\text{Zn}(\text{Im})_2$, this is not unexpected since lower synthesis temperatures are known to lead to less crystalline materials. Nevertheless, the crystal size and thermal stability of the material obtained by microemulsion synthesis are comparable to those obtained in the solvothermal synthesis.

Similar to the synthesis described by Lehnert and Seel, the pore system of the material is host to traces of solvent molecules, in this case isopropanol. The presence of isopropanol in the pore system can only be detected by NMR spectroscopy and no trace of (O-H) vibrations can be observed in the corresponding IR data, leading to the conclusion, supported by elemental analysis, that only trace amounts (0.1 mol isopropanol per mol $\text{Zn}(\text{Im})_2$) are left within the material. As demonstrated by Yaghi et al. during their work on ZIF-67 [$\text{Zn}(\text{Im})(2\text{-MeIm})$], this material could be a potential candidate for CO_2 capture experiments. The capacity of $\text{Zn}(\text{Im})_2$ may even surpass that of ZIF-67 as a consequence of the increased pore volume due to the absence of methyl groups on the imidazolate linkers. Further experiments towards the use of $\text{Zn}(\text{Im})_2 \cdot 0.1 \text{ C}_3\text{H}_8\text{O}$ to capture CO_2 will have to be performed in order to determine if the previously discussed significant reduction in solvent contained in the framework assists in creating an efficient capturing material.

7 HOMONUCLEAR MIXED-VALENT COBALT IMIDAZOLATE FRAMEWORK FOR OXYGEN EVOLUTION ELECTROCATALYSIS

This chapter is based on the article “Homonuclear mixed-valent cobalt imidazolate framework for oxygen evolution electrocatalysis”, submitted to *Chem Eur J*, 2015 from E. A. Flügel, V. W.-h. Lau, H. Schlöbner, R. Glaum and B. V. Lotsch.

7.1 ABSTRACT

In this work we present the synthesis and characterization of the first mixed-valent, purely cobalt-based zeolitic imidazolate framework, $\text{Co}^{\text{II}}_3\text{Co}^{\text{III}}_2(\text{C}_3\text{H}_3\text{N}_2)_{12}$. The material adopts the cubic garnet-type structure and combines high thermal stability of up to 350 °C with excellent chemical stability. Electrochemical characterization shows that the cobalt centres are redox active and efficiently support oxygen evolution, thus rendering this framework a potential candidate for single-site heterogeneous catalysis based on earth-abundant elements.

7.2 ARTICLE

Metal-organic frameworks (MOFs), unlike microporous oxides such as zeolites, feature an exceptionally large range of compositions and network topologies owing to the diverse coordination modes and bonding geometries at the metal nodes and the essentially unlimited choice of organic linkers. Since the early stages of MOF science, tailored MOFs have been developed to serve a wide range of applications in gas separation and storage, as sensors and as single-site heterogeneous catalysts.^[42, 52, 221] Zeolitic imidazolate frameworks (ZIFs) represent a special subset of MOFs with structures analogous to those of zeolites, which is commonly rationalized by similar metal-imidazole-metal and Si-O-Si bonding geometries. ZIFs are zeotypes composed of metal ions (M = Zn, Co, Cu), which are bridged by imidazolate linkers, resulting in a large structural variety of tetrahedral ML_4 as well as octahedral ML_6 bonding motifs.^[41, 222, 223] ZIFs combine not only the

desirable properties of zeolites, including ordered microporosity as well as relatively high thermal and chemical stability,^[41] but also the chemical diversity inherent to the (functionalized) imidazolate linkers and different types of metal nodes.^[224, 225] Since their discovery, MOFs have been tested as catalysts for various reactions such as aldol condensations,^[226] oxidations^[158, 221] or the Knoevenagel reaction,^[159, 227] yet the use of ZIFs in such reactions has been rarely explored to date.^[161, 228, 229] Apart from the recent use of Co-ZIF-9 as oxidation catalyst, literature on redox active ZIFs is nearly absent, let alone their evaluation for electrochemical applications or electrocatalysis. While in a recent study Wang et al. explored the catalytic activity of Co-ZIF-9 towards water oxidation,^[230] most research is focused on the use of ZIF pyrolysis products in electrocatalysis.^[163, 164] A different approach towards electrocatalytically active MOFs is the incorporation of redox-active metal complexes into the framework of a MOF to perform electrocatalysis. Lin et al. reported the use of $\text{Zr}_6\text{O}_4(\text{OH})_4(\text{bpdc})_6$ MOFs modified with Ir-, Re- or Ru-based complexes capable of locally performing the oxygen evolution reaction (OER), whilst the MOF backbone stays catalytically inactive.^[166] Another approach to perform the OER using MOF materials was reported using the commercially available Fe-BTC MOF (Basolite™ F300).^[167] Babu et al. reported that during an initial preparation step the material was activated by scanning to potentials lower than 400 mV vs. SCE and suggested the formation of surface-bound iron hydroxides which then act as the electrochemically active species. We were thus interested in designing ZIFs containing redox active cobalt in the nodal position, which owing to the range of accessible valence states has been an abundant and well-documented species for applications in (electro)catalysis and energy storage.^[231-233]

In this study, we report the synthesis of the first redox-active, mixed-valent homonuclear Co-based ZIF structure, which was obtained by heating $\text{Co}(\text{OAc})_2$ and imidazole (ratio 1:5) under reverse microemulsion conditions using a solvent mixture of heptane/1-hexanol/water in a closed microwave vial in the presence of the stabilizer cetyltrimethylammonium bromide (CTAB). Further experimental details are provided in the Supporting Information. The product crystallizes in the form of cubic nanocrystals with sizes ranging from 100 nm to 500 nm. The product was identified by powder X-ray diffraction (PXRD), revealing a close structural relationship to ZIF-5 ($\text{Zn}_3\text{In}_2(\text{Im})_{12}$, $\text{Im} = \text{C}_3\text{H}_3\text{N}_2$). The crystal structure was solved from powder X-ray diffraction data and reveals a 3D framework structure which is isotypic with the cubic garnet structure similarly found in ZIF-5. Whereas in the heteronuclear ZIF-5 the two distinct metal positions are occupied by Zn^{II} and In^{III} , the basic structural motifs in the Co analogue reported here are Co^{2+} tetrahedrally coordinated by ditopic imidazolate ligands, and Co^{3+} octahedrally coordinated by imidazolate (Fig. 7.2.1b). As only cobalt(II) acetate was used in the synthesis without an oxidizing agent present, cobalt(III) is formed *in situ* by oxidation in air, as observed in a number of molecular mixed valence cobalt species.^[67, 234, 235] Elemental analysis (EA) is consistent with the composition $\text{Co}^{\text{II}}_3\text{Co}^{\text{III}}_2(\text{Im})_{12}$ and confirms the purity of the bulk material

(EA (%) calcd. for $\text{Co}^{\text{II}}_3\text{Co}^{\text{III}}_2(\text{Im})_{12}$: C, 39.3; H, 3.3; N, 30.5; Co, 26.8; Found: C, 38.7; H, 3.5; N, 29.5; Co, 27.2). The infrared (IR) spectrum of the obtained compound (Fig. 7.2.2b) exhibits a shift of the imidazole bands by up to 30 cm^{-1} to higher energies compared to free imidazole, indicating fairly strong metal – ligand coordination as expected for ZIFs.

Nitrogen and argon sorption analysis revealed no significant porosity with a measured surface area of $3.15\text{ m}^2\text{g}^{-1}$. This finding is in line with previous theoretical work on the structurally related ZIF-5,^[236] which indicates a dense packing with close to no accessible voids in the unit cell.

Due to the absence of porosity in the material, any electrochemical process is limited to the particle surface, thus necessitating small particle sizes and accordingly higher surface areas. In order to ensure the formation of nanoparticles, a microemulsion approach was utilized to facilitate the formation of nano- and small microscale particles within surfactant-stabilized water vesicles. Transmission electron microscopy measurements revealed that the surfactant-free material consists of cubic particles with an average size of about 300 nm (Fig. 7.2.1c,d).

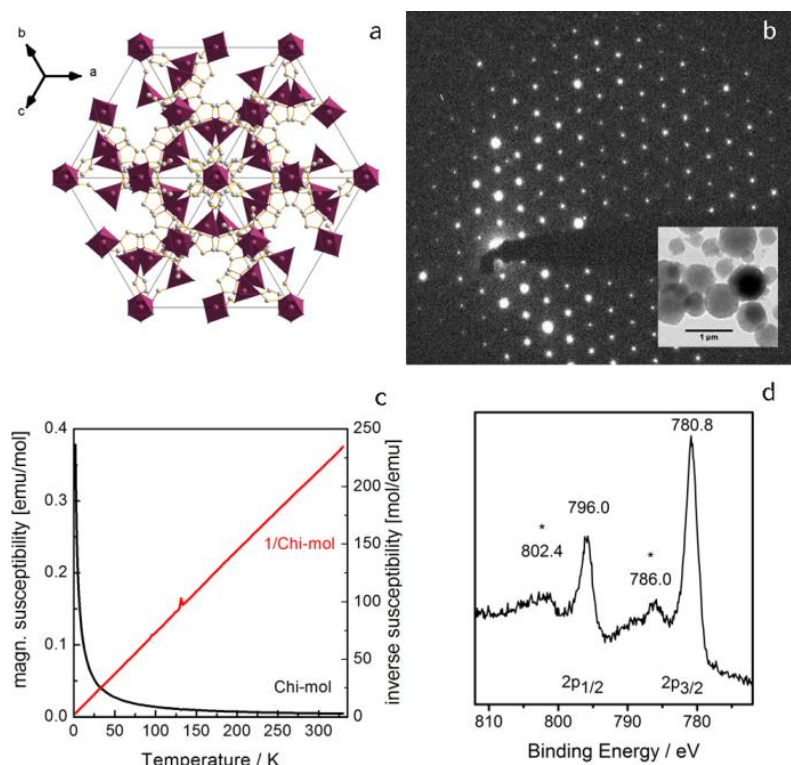


Figure 7.2.1. Crystal structure of $\text{Co}^{\text{II}}_3\text{Co}^{\text{III}}_2(\text{Im})_{12}$: **(a)** view of the unit cell along [111]. **(b)** Selected area electron diffraction (SAED) pattern of a nanocrystal along [111], showing the expected hexagonal symmetry. Inset TEM image of $\text{Co}^{\text{II}}_3\text{Co}^{\text{III}}_2(\text{Im})_{12}$ showing close to spherical particles with an average particle size of about 300 nm. **(c)** Magnetic susceptibility measurement. **(d)** XPS measurement showing the Cobalt 2p_{3/2} and 2p_{1/2} peaks. Satellites are marked with asterisks.

Thermogravimetric (TGA) analysis of the obtained crystals reveals only 2% weight loss up to 350 °C (chapter 9.4, Fig. S3), which we attribute to the removal of surface adsorbed material.^[237] With a thermal stability of up to 350 °C, $\text{Co}^{\text{II}}_3\text{Co}^{\text{III}}_2(\text{Im})_{12}$ surpasses many other coordination frameworks^[238] but does not reach the exceedingly high thermal stability up to 500 °C of the prototype compound ZIF-8.^[239] The chemical stability of the Co-MOF was demonstrated by suspending the as-synthesized samples in boiling methanol, toluene and water. After 3 days, no visible change in the resulting powder diffraction patterns was observed (Fig. 7.2.2a). The pronounced thermal and chemical stability renders this material a suitable candidate for applications in heterogeneous catalysis or electrochemistry where long-term stability and inertness towards solvents are key prerequisites.

To confirm the presence of mixed Co valence states, photoelectron spectroscopy (XPS) was performed (Fig. 2d, chapter 9.4, S4). According to Cook *et al.*^[240] satellite peaks, which can be found up to 6.5 eV above the respective main signals, are considered as indicative of cobalt(II), whilst cobalt(III) lacks such satellites. Here, we observe the main signals for $\text{Co}^{\text{II}}/\text{Co}^{\text{III}}$ at 780.8 eV (Co 2p_{3/2}) and 796.0 eV (Co 2p_{1/2}), while satellites can be found at ≈ 786.0 eV and 802.4 eV, which is well within the range discussed by Cook *et al.* Binding energies for both Co^{2+} and Co^{3+} 2p_{3/2} signals with similar coordination spheres were reported to be 780.8 eV and at 781.36 eV.^[241] Similar values are found for both Cobalt species in Co_3O_4 ,^[242] thus confirming that the XPS spectrum of our material is consistent with mixed valent cobalt materials.

Magnetic measurements (Fig. 7.2.2c) were performed on the material, revealing Curie-Weiss behavior with a temperature-independent magnetic moment of $\mu_{\text{eff}}/\mu_{\text{B}} = 3.36$ per mole $\text{Co}^{\text{II}}_3\text{Co}^{\text{III}}_2\text{Im}_{12}$. Assuming three high-spin Co^{2+} ions and neglecting any weak temperature independent paramagnetic moment for the Co^{3+} ions with low-spin configuration, $\mu_{\text{eff}}/\mu_{\text{B}} = 4.36$ per Co^{2+} ion is obtained. This value agrees quite well with $\mu_{\text{calc}}/\mu_{\text{B}} = 4.23$ per Co^{2+} obtained by angular overlap modelling^[243-245] for the tetrahedral $[\text{Co}^{\text{II}}\text{Im}_4]$ chromophore.

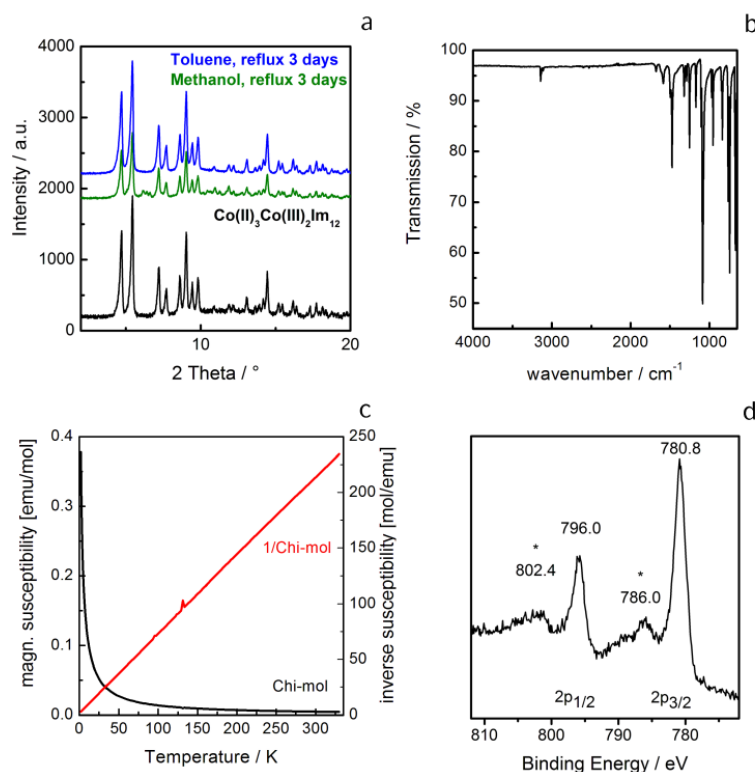


Figure 7.2.2: Powder XRD patterns of $\text{Co(II)}_3\text{Co(III)}_2\text{Im}_{12}$ before (black) and after 3 days refluxing in methanol (green) or toluene (blue). **(b)** IR spectrum of the sample. **(c)** Magnetic susceptibility measurement. **(d)** XPS measurement showing the Cobalt $2p_{3/2}$ and $2p_{1/2}$ peaks. Satellites are marked with asterisks.

The diffuse reflectance spectrum of $\text{Co(II)}_3\text{Co(III)}_2\text{Im}_{12}$ (chapter 9.4, Fig. S2) provides further evidence for the existence of two different oxidation states of the cobalt ions in the coordination polymer. The spectrum shows bands at 9100 cm^{-1} with a shoulder at 10000 cm^{-1} , and at 17500 cm^{-1} with a shoulder at 19000 cm^{-1} , corresponding to the electronic transitions from the $^4A_2(\text{F})$ ground state to the excited states $^4T_1(\text{F})$ and $^4T_1(\text{P})$ of the tetrahedral chromophore $[\text{Co(II)}\text{Im}_4]$. This assignment is backed by the results of angular overlap modelling of the electronic states of the $[\text{Co(II)}\text{Im}_4]$ chromophore (ticks in Fig. 7.2.3). In addition to the Racah parameters $B = 742\text{ cm}^{-1}$, $C = 3189\text{ cm}^{-1}$ ($C/B = 4.3$, $B_{\text{free-ion}} = 989\text{ cm}^{-1}$,^[245] $\beta = 0.75$) and spin-orbit coupling parameter $\zeta = \beta \cdot \zeta_{\text{free ion}} = 383.3\text{ cm}^{-1}$ ^[245] for the Co^{2+} ion, the AOM parameters ($e_\sigma(\text{N}) = 3500\text{ cm}^{-1}$, $e_{\pi, //}(\text{N}) = 0\text{ cm}^{-1}$, $e_{\pi, \perp}(\text{N}) = -525\text{ cm}^{-1}$) derived for the N atom of the quinoline ligand in tetrahedral $[\text{Co(II)}\text{QBr}_3]^-$ ^[246] have been used in the calculation without any additional fitting. Thus, in-plane ($//$) π -bonding for the *Im* ligand is assumed to be vanishing, while perpendicular (\perp) to the aromatic ring strong π -backbonding is expected. In this context it is also worth mentioning that the distances $d(\text{Co(II)}-\text{N}_{\text{Im}})$ for $\text{Co(II)}_3\text{Co(III)}_2\text{Im}_{12}$ are the same as $d(\text{Co(II)}-\text{N}_Q)$ in $[\text{Co(II)}\text{QBr}_3]^-$.^[247] In contrast to the presence of the $[\text{Co(II)}\text{Im}_4]$ chromophore only indirect evidence for the octahedral $[\text{Co(III)}\text{Im}_6]$ group can be drawn from the magnetic data and the powder reflectance spectrum of $\text{Co(II)}_3\text{Co(III)}_2\text{Im}_{12}$. By comparison to the absorption spectrum of the

$[\text{Co}^{\text{III}}(\text{NH}_3)_6]^{3+}$ chromophore^[248] the two weak shoulders at 21000 and 28400 cm^{-1} might be assigned to the transitions $^1\text{A}_1(\text{I}) \rightarrow ^1\text{T}_{1g}(\text{I})$ and $^1\text{A}_1(\text{I}) \rightarrow ^1\text{T}_{2g}(\text{I})$ of Co^{3+} with d^6 low-spin configuration.

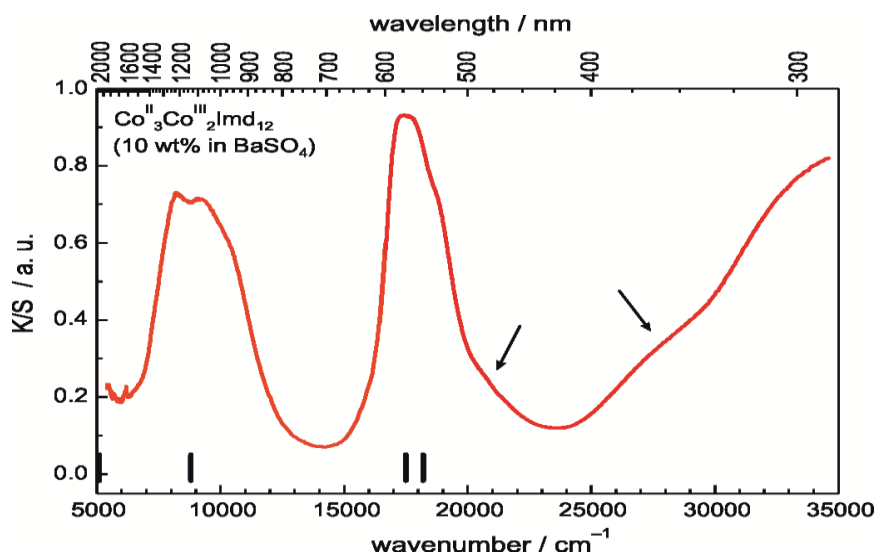


Figure 7.2.3: Powder reflectance spectrum of $\text{Co}^{\text{II}}_3\text{Co}^{\text{III}}_2(\text{Im})_{12}$ in the UV/vis/NIR region. Ticks at the bottom indicate transition energies from AOM calculations for the tetrahedral $[\text{Co}^{\text{II}}\text{Im}_4]$ chromophore. Arrows point to shoulders (21000 cm^{-1} , 28400 cm^{-1}) that possibly originate from the octahedral $[\text{Co}^{\text{III}}\text{Im}_6]$ chromophore.

To determine whether the simultaneous presence of $\text{Co}(\text{II})$ and $\text{Co}(\text{III})$ centers imparts redox activity to the ZIF, its electrochemical behaviour was characterized by cyclic voltammetry performed under non-aqueous conditions (Fig. 7.2.4b), using FTO with the coordination polymer deposited by drop-casting as the working electrode. We assign the redox event at approximately 25 mV vs ferrocene (*Fc*) to the $\text{Co}^{\text{II/III}}$ couple, and the irreversible reduction at -1.95 V vs *Fc* to the redox couple $\text{Co}^{\text{I/II}}$. Scanning further cathodic of -2.5 V or anodic of 2.5 V vs *Fc* led to bulk electrolysis. The former we assign to the bulk reduction to Co^0 , while the latter is associated with the oxidation of trace amounts of water in the electrolyte. The presence of the $\text{Co}^{\text{II/III}}$ oxidation states in the ZIF is important in terms of its possible utility in electrochemical and (electro)catalytic applications, since they are involved in numerous catalytic reactions, including oxidation reactions^[4, 10, 11, 231-233, 249] and in electrochemical energy storage, e.g. in Co-based cathode materials.^[250] Under alkaline conditions, the MOF exhibited an electrocatalytic oxidation activity comparable with the mixed valence spinel Co_3O_4 , a frequently used benchmark electrocatalyst for water oxidation,^[251, 252] requiring an only slightly higher overpotential of around 40 mV (Fig. 7.2.4a). Here, commercially available nanometer- and micrometer-sized Co_3O_4 were used. The electrocatalytic performance of the MOF is also comparable with the two Co_3O_4 benchmarks when an electrode other than FTO, namely glassy carbon, was used (chapter 9.4, Fig. S12), indicating that the substrate effect is small. However, for subsequent analyses (e.g. stability and faradaic yield), FTO was used as this electrode configuration allowed higher catalyst loading, reduced limitation of substrate diffusion, and better effusion of oxygen bubbles.

Measurements under acidic conditions have not been performed due to the known instability of all imidazolate frameworks under these conditions.

Material stability under the highly oxidizing alkaline environment was confirmed with chronoamperometry (chapter 9.4, Fig. S6); the OER current was steady at an applied potential of 556 mV vs SHE (800 mV vs SCE) for over 10 hours. A chronocoulometry experiment, together with quantification of oxygen, yields an estimate of the faradaic efficiency to be 50.1 % (chapter 9.4, Fig. S8 and S9). The spent catalyst remaining on the electrode was characterized by XRD and FTIR; the electrolyte was also analyzed for cobalt leaching by ICP-AES elemental analysis. No change was observed in the material by XRD and IR analysis (chapter 9.4, Fig. S9, S10), and the electrolyte contained a negligible amount of cobalt (50 ppb), thus confirming the ZIF was unaffected by the oxidizing environment. To verify whether the shown electrochemical capabilities and stability are determined by the ordered framework structure, the material was thermally decomposed at 500 °C under air and argon and the obtained residues were used in electrocatalytic measurements. In both cases, the electrochemical activity was slightly higher compared to the pure ZIF, yet the decomposed samples showed leaking of cobalt into the electrolyte, highlighting the importance of the stabilizing framework (chapter 9.4, Fig. S7). In terms of reaction mechanisms, analyses in the non-diffusion limited regime (< 0.4 V overpotential) show that the ZIF has a Tafel slope of 82 mV dec^{-1} (chapter 9.4, Fig. S8) and a reaction order (with respect to NaOH) of 1.4 (chapter 9.4, Fig. S9), similar to values of the nm-sized Co_3O_4 sample. Considering the proposed literature mechanism for oxygen evolution (chapter 9.4, Scheme S1),^[253, 254] these values are comparable to the calculated Tafel slope of 59 mV dec^{-1} and reaction order of 1.5 where the rate determining step is the chemical formation of surface-bound H_2O_2 (step 2). This is in fact considered to be the rate determining step for OER on Co_3O_4 , which likewise features both tetrahedral and octahedral coordination environments of the Cobalt centers in the same material. Note that the deviation from literature values of the Tafel slope and reaction order for both micro- and nano- Co_3O_4 has been attributed to variations in synthesis procedures, which can lead to differences in size and surface properties.^[253, 255] These results thus indicate that changing the ligand from O^{2-} to imidazolate does not seem to significantly affect the redox mechanism of the metal centers, and suggests the possibility of designing imidazolate MOFs for replicating, even improving, the electrocatalytic mechanism of metal oxides. The presence of organic linkers in this coordination framework, coupled with its electrocatalytic activity and stability, suggests that these and related electroactive MOFs may be applicable for other oxidation reactions, e.g. Knoevenagel reaction^[161, 228] and alcohol oxidation^[256] involving organic substrates and reagents.

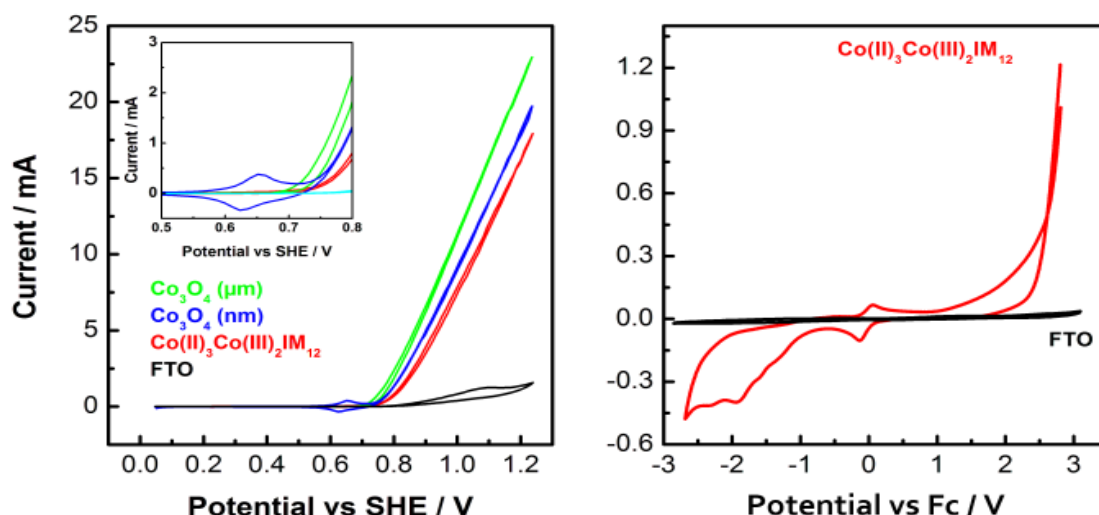


Figure 7.2.4: (a) Cyclic voltammogram at 1 mV s^{-1} of FTO as working electrode, with and without $\text{Co}^{\text{II}}_3\text{Co}^{\text{III}}_2(\text{Im})_{12}$ deposition, performed in NaOH (1 M) solution, with both nm- and μm -sized Co_3O_4 as the benchmark. (b) Cyclic voltammogram at 10 mV s^{-1} of $\text{Co}^{\text{II}}_3\text{Co}^{\text{III}}_2(\text{Im})_{12}$ on FTO in acetonitrile containing $[\text{TBA}][\text{PF}_6]$ as electrolyte.

In summary, we have reported on the first successful synthesis of a purely cobalt-based mixed-valent ZIF material with garnet-type structure and its characterization using various spectroscopic and diffraction techniques. The material combines the structural definition and known thermal stability of zeolitic imidazolate frameworks with redox active cobalt(II) and cobalt(III) centers located in close spatial vicinity, rendering it a good candidate material for heterogeneous catalysis. Whilst the activity of the material does not seem to be influenced significantly by the topology of the framework, the rigid integration of the cobalt centers into the garnet structure is crucial to the stability of the catalyst during electrochemical operation. These findings therefore provide a basis for the rational design of tailor-made MOF-based electrocatalysts with the prospect of synergistically combining molecularly tunable and substrate-selective framework topologies with sustained electrocatalytically active redox centers and possible high surface areas, as known from various MOFs. Although the cobalt framework is comparable with the earth-abundant benchmark electrocatalyst (Co_3O_4), it is as-yet not competitive with the noble metal benchmark IrO_x , which can achieve similar current using over 100 mV fewer overpotential.^[168] We nonetheless emphasise that, given the architectural flexibility of the framework (e.g. ligand choice) it may be possible to tailor this material for electrocatalytic applications to make it competitive with industry standards.

7.3 EXPERIMENTAL SECTION

In a typical synthesis, 948 mg (2.6 mmol) hexadecyltrimethylammonium bromide (CTAB) were added to a mixture of 22 mL n-heptane and 2.3 mL 1-hexanol. To the turbid mixture, 1675 μ L aqueous imidazole solution (1.8M) were added and the mixture was stirred until a clear solution was formed. To this solution, 150 mg (0.603 mmol) cobaltacetate tetrahydrate were added and the resulting mixture was refluxed at 105°C for 2 hours. The resulting precipitate was removed from the solution by filtration, washed with iso-propanol to remove unreacted species and dried at room temperature.

7.4 ACKNOWLEDGEMENTS

We thank Dr. Kremer for the performed magnetic measurements and his help with the calculations as well as Dr. Konuma for the performed XPS measurements.

Financial support by the Max Planck Society, Deutsche Forschungsgemeinschaft (SPP-1362), the Fond der Chemischen Industrie (FCI), the cluster of excellence “Nanosystems Initiative Munich” (NIM), and the Center for NanoScience (CeNS) is gratefully acknowledged.

8 SYNTHETIC ROUTES TOWARD MOF NANOMORPHOLOGIES

This chapter is based on the article “Synthetic routes toward MOF nanomorphologies”, published by *J. Mater. Chem.*, 2012, 22, 10119-10133. from E. A. Flügel, A. Ranft, F. Haase and B. V. Lotsch.^[257]

8.1 ABSTRACT

As metal-organic frameworks (MOFs) are coming of age, their structural diversity, exceptional porosity and inherent functionality need to be reduced to practice. Fashioning MOFs into various shapes and at the same time controlling their size constitutes an essential step toward MOF-based devices. Moreover, downsizing MOFs to the nanoscale triggers a whole new set of properties distinguishing nanoMOFs from their bulk counterparts. Therefore, dimensionality-controlled miniaturization of MOFs enables the customised use of nanoMOFs for specific applications where suitable size and shape are key prerequisites. In this feature article we survey the burgeoning field of nanoscale MOF synthesis, ranging from classical protocols such as microemulsion synthesis all the way to microfluidics-based techniques and template-directed epitaxial growth schemes. Along these lines, we will fathom the feasibility of rationally designing specific MOF nanomorphologies – zero-, one- and two-dimensional nanostructures – and we will explore more complex “second-generation” nanostructures typically evolving from a high level of interfacial control. As a recurring theme, we will review recent advances made toward the understanding of nucleation and growth processes at the nanoscale, as such insights are expected to further push the borders of nanoMOF science.

8.2 INTRODUCTION

Coordination chemistry has lived through a renaissance with the discovery of highly porous, crystalline framework materials composed of metal ions or clusters joined by rigid, polytopic organic linkers.^[57, 58] The triumphant success and rapid growth of this class of hybrid materials, dubbed metal-organic frameworks (MOFs) or porous coordination polymers (PCPs), is largely based on their

elegant yet simple synthesis and their versatility originating from the use of tailorable linkers and the resulting high surface areas and porosities. Although the validity of rational MOF synthesis is not universal and some doubt has been cast recently on the viability of true secondary building-block approaches,^[258] MOF chemistry continues to intrigue by offering modular and highly rational approaches to sophisticated network topologies, which is rarely seen in the synthesis of dense solid-state materials at elevated temperatures under thermodynamic control. The importance of the concepts “surface” and “porosity” associated with MOFs, together with their inherent functionality hosted by both organic and inorganic building blocks, gives rise to a kaleidoscope of properties and, hence, applications. The more traditional ones like adsorption,^[2, 160, 259] gas storage^[260, 261] and separation^[2, 262, 263] have been complemented in recent years by a host of emerging applications such as in sensor design,^[259, 264-266] light harvesting,^[239, 267] bioimaging,^[153, 268] drug delivery,^[155, 269, 270] and catalysis.^[157, 221, 271, 272]

Such applications have been propelled by the ongoing downsizing of MOFs to the nanoscale and the prospect of amplifying large internal surface areas by ever increasing external surface areas, and of combining inherent functionality with high sensitivity. The miniaturization of MOFs has already become one of the most prosperous disciplines in current MOF chemistry as it bridges the gap between fundamental MOF science and prospective applications by imprinting MOFs with morphologies suitable for device fabrication.

Nanosized MOF architectures (nanoMOFs), featuring at least one dimension at the nanoscale, offer significantly altered properties and reactivity compared to the bulk material. Increased textural porosity and external surfaces remove or diminish the mass transfer limits^[273] and therefore increase the activity of catalysts as well as the response time in sensor applications. Additionally, materials with structures matching visible light wavelengths may exhibit optical effects based on interference and diffraction.^[47] In biological applications, the internalization kinetics as well as blood half-life and the distribution of the particles throughout the biosystem have been found to be size-dependent.^[274] For example, smaller particles have been shown to exhibit increased plasma circulation times and can even be transported to the lymphatic system.^[275]

The exploration of synthesis strategies toward nanoMOFs and the exploitation of their small size constitutes a nascent field that has materialized already in promising studies on the use of nanoMOFs, for example in medical applications. However, apart from size effects, the shape and morphology of nanoMOFs play a key role and are inherently relevant to the type of application that is sought. As R. E. Morris states, “A burgeoning challenge in the field is therefore to prepare the materials with shapes tailored for specific purposes, for example as thin films for membrane applications.”^[276] While spherical shapes ensure uniform framework degradation and hence, drug release, non-spherical or anisotropic shapes may be preferred in catalysis or optics due to the

prominence of active sites at edges and corners or preferred orientation of channel systems. In contrast, MOF membranes or films exhibit suitable morphologies for gas separation or planar sensing platforms in devices such as vapor sensitive thin films^[47] or quartz crystal microbalance-based sensing systems.^[264, 277] Taken together, the specific size, shape and morphology imbue nanoMOFs with functionality and reactivity that can be tuned in a large range depending on the finesse of the fabrication procedures.

This feature article is geared towards recent advances in MOF nanoscale synthesis and nanofabrication that have set the stage for the rational design of MOF nanomorphologies ranging from 0D and 1D to 2D and other anisotropic and hybrid nanostructures. The article is designed to focus on benchmark studies rather than to give a comprehensive account of the rapidly evolving nanoMOF field, and as such, we will highlight selected examples that have paved the way toward a better understanding of nucleation and growth at the nanoscale, or which are trendsetting with respect to novel strategies in nanoscale MOF synthesis.

For a more comprehensive overview of emerging applications of MOF nanomorphologies, the reader is referred to a number of excellent reviews that have recently appeared on this topic, such as those by Lin,^[155] Spokoyny,^[278] or Shekhah.^[279]

8.3 ZERO-DIMENSIONAL NANOSTRUCTURES

8.3.1 SONOCHEMICAL AND MICROWAVE-ASSISTED SYNTHESIS

The synthesis of zero-dimensional MOF nanoparticles has been achieved by a number of protocols so far, which mainly rely on the spatial and temporal control of nucleation and growth of MOF crystals under solvo- or hydrothermal conditions. Along these lines, the concept of arrested particle growth has been implemented successfully by adding so called coordination modulators, i.e. inhibitors such as monocarboxylic acids,^[280, 281] or by the *in situ* activation of ligands as realized in the deprotonation of 2-methylimidazole to speed up ZIF-8 nucleation.^[237, 282] In general, the most convenient protocols for nanoMOF synthesis are those that require minimum *chemical* reaction control (addition of modifiers, surfactants, reactant ratio), but solely rely on growth control *via physical* parameters, such as the type of energy supply, reaction time and temperature. Therefore, a number of methodologies have been developed recently, exploiting either conventional electric (CE),^[283] ultrasonic (US)^[284, 285] or microwave (MW) assisted heating^[80, 286] for the synthesis of nanoMOFs. The use of US irradiation in the synthesis of nanosized MOFs has first been adapted from organic synthesis by Qiu *et al.*, who were able to synthesize a fluorescent microporous nanoMOF $[\text{Zn}_3(\text{btc})_2 \cdot 12\text{H}_2\text{O}]$ (*btc* = 1,3,5-benzenetricarboxylate) by using US treatment at room temperature^[284] and has since then been

successfully extended to various other systems like ZIF-8 and HKUST-1.^[287] US effects are originating from acoustic cavitation, which are generating local hot spots with high transient temperature (5000 K), high pressure (>1000 atm), and rapid heating and cooling rates (10^{10} Ks⁻¹).^[288, 289] The nucleation and growth of the particles is preferably taking place at these hot spots, which is limiting the particle size as the spots are cooling back to the temperature of the reaction medium within milliseconds.

MW-assisted synthesis has turned out to be another promising technique to achieve the formation of MOF nanoparticles. The method initially relied on a droplet liquid dispersion protocol taking advantage of the rapid evaporation of a reactant-containing organic solvent mixed with water by MW heating.^[290, 291] However, this method can be transferred to homogeneous solvent systems by taking advantage of the high dielectric absorptivity of polar solvents such as diethylformamide (DEF), which leads to rapid thermal energy conversion and efficient local heating of the reaction solution, thereby affording fast nucleation and crystal growth. Along these lines, Ni *et al.* reported the first successful synthesis of IRMOF-1, -2, and -3 nanoparticles by the so-called MW-assisted solvothermal synthesis, which has since then been picked up successfully by others to efficiently and size-selectively synthesize various MOF nanoparticles.^[80, 292-294]

Both sonochemical and microwave synthesis have been found to significantly accelerate MOF crystallization as compared to traditional electric heating, while the observed rate enhancement is typically larger for US than MW irradiation. Recent work has shown that both the rates of nucleation and crystal growth are greatly enhanced by US and MW irradiation compared to classical solvo-/hydrothermal syntheses, which is attributed to increased pre-exponential factors of the Arrhenius equation and hence, increased reaction probability (Fig. 8.3.1).^[292]

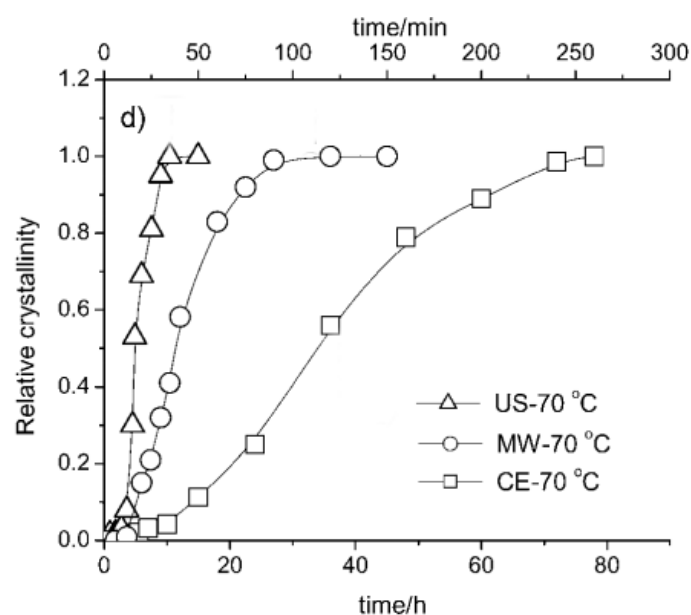


Figure 8.3.1: Increase in crystallinity of MIL-53 (Fe) with time compared for US, MW and CE heating. Reproduced with permission from ref. ^[292]. Copyright ©2011 by John Wiley & Sons, Inc.

It needs to be pointed out, however, that for different MOF systems different relative accelerations of nucleation and crystal growth, respectively, are observed. The impact of nucleation rate enhancement was found to be dominant in systems such as $\text{Cu}_3(\text{btc})_2$,^[295] while acceleration of crystal growth is more important in MIL-53(Fe).^[292] Taking into account the reaction yield and monodispersity of the resulting nanoparticles, which are key factors from a preparative point of view, Chalati *et al.* have found that for MIL-88A MW-assisted synthesis is superior to both conventional hydrothermal and US synthesis. Whilst both US and MW syntheses excel with respect to the rapid formation of nanoparticles smaller than 100 nm, US-assisted protocols require highly dilute solutions and the additional use of coordination inhibitors such as acetic acid, resulting in very small yields (< 10 %). In contrast, MW-assisted synthesis affords MIL-88A nanoparticles with good size control, being almost unaffected by the concentration (up to 1 mmol L^{-1}), and a relatively high yield independent of the reaction time.^[296]

8.3.2 MICROEMULSION SYNTHESIS

Besides size control by different types of energy transduction, zero-dimensional (0D) MOF nanoparticles have been synthesized by taking advantage of interfacial reactions providing shape control and confinement of the reaction zone at the same time. For example, a highly attractive route to MOF nanospheres has recently been reported by Zhao *et al.*, who used surfactants to limit the size of the resulting particles and as a template to create micro-mesoporous MOF structures at the same time.^[116] Highly ordered hierarchically porous structures were obtained by combining the solvating possibilities offered by ionic liquids (IL) and supercritical CO_2 (SCCO_2) with the templating properties of fluorocarbon-type surfactants. The surfactant N-ethyl perfluorooctylsulfonamide (N-EtFOSA) forms microemulsions in a solvent mixture of the IL 1,1,3,3-tetramethylguanidinium acetate (TMGA) and SCCO_2 , as the interactions between CO_2 and the fluorocarbon tails of the surfactants are strong.^[297, 298] In a standard synthesis procedure, $\text{Zn}(\text{NO}_3)_2$, 1,4-benzenedicarboxylic acid (H_2bdc) and N-EtFOSA were added to TMGA and heated in a high-pressure cell under 16.8 MPa CO_2 pressure at 80°C for 48 h. Transmission electron microscopy (TEM) images (Fig. 8.3.2) show nanoparticles of roughly 80 nm diameter with a uniform size distribution and a well ordered system of mesopores. The pore size was found to be 3.0 nm, whereas the microporous pore walls have a thickness of 2.5 nm. Although the structure of the pore walls could not be identified by comparison with known $\text{Zn}(\text{bdc})$ -type MOF structures, N_2 -sorption measurements reveal well-pronounced mesoporosity along with moderate microporosity and a bimodal pore size distribution centered at 3.6 nm and 0.7 nm.

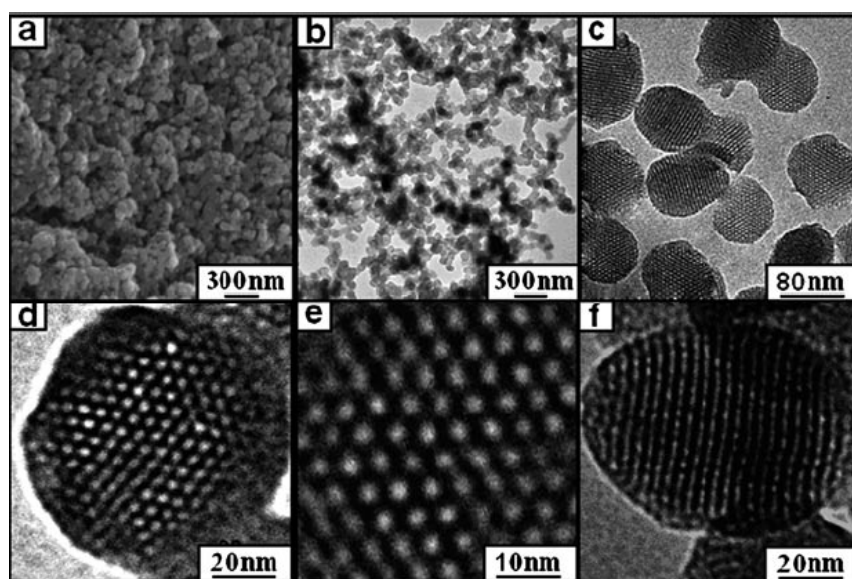


Figure 8.3.2: a) Scanning electron microscopy (SEM) and b-f) TEM images of hierarchically micro- and mesoporous MOF nanoparticles. Reprinted with permission from ref. [116]. Copyright ©2011 by John Wiley & Sons, Inc.

8.3.3 INTERFACIAL SYNTHESIS

A very elegant realization of interfacial control has been put forward by De Voss and co-workers, who demonstrated the fabrication of hollow MOF capsules at the interface between two immiscible liquids.^[299] The inorganic (copper acetate) and organic precursors (H_2btc) were separately dissolved in water and 1-octanol, respectively, and both liquids were supplied by syringe pumps to a T-junction, where water droplets were generated by breaking-off in the co-flowing organic ligand solution as demonstrated in Figure 8.3.3. The obtained micron-sized capsules ($\approx 375 \mu m$) feature defect-free walls of about $2 \mu m$ thickness due to a self-completing growth mechanism, which has nicely been demonstrated by the efficient retention of encapsulated Rose Bengal dyes within the intact walls of the MOF capsules.

While the thickness of the walls is clearly above the nanometer range, the interfacial formation of nanoscale MOF membranes based on this biphasic synthesis approach is clearly within reach. Moreover, the tuning of solvents, MOF precursors, concentrations and flow rates will further broaden the scope of this methodology and bodes well for the fabrication of freestanding MOF films as well as versatile MOF nanocontainers with microporous walls and, hence, size-selective storage and release properties. This could lead to future applications in catalysis by trapping molecular catalysts inside MOF capsules to form micro- or even nanoreactors.

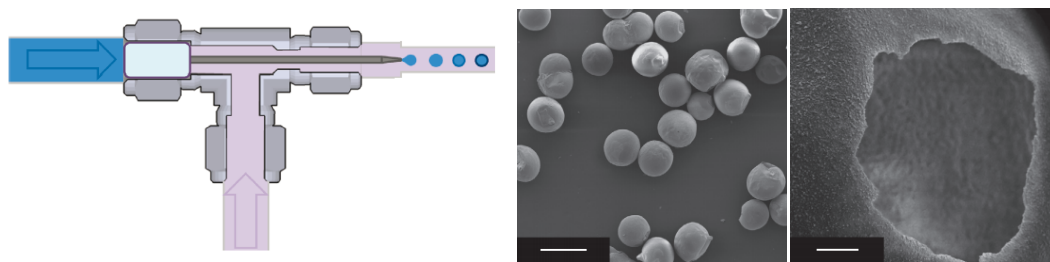


Figure 8.3.3: Left: Cut-away view of the T-junction showing details of the emulsification step. The metal-ion containing aqueous phase (blue) flows through a tapered capillary in the tubing, and the ligand-containing organic solution (purple) flows around it. Growing droplets detach when the force due to interfacial tension is exceeded by the drag force of the surrounding organic phase. Middle: SEM micrograph showing several capsules and their monodispersity. Scale bar 500 μm . Right: SEM micrograph of a capsule crushed with a needle tip showing its hollow interior. Scale bar 25 μm . Reprinted with permission from ref. [299]. Copyright ©2011 by Nature Publishing Group.

Table 8.3.1 Overview of various synthesis approaches towards 0D nanostructures and the resulting morphology and sorption properties of the formed particles in comparison to the respective bulk material.

0D Nanostructures				Bulk
Synthesis method	References	Selected examples	Properties	
Coordination modulation	[237, 280, 282, 286, 300-302]	ZIF-8	9 nm, rhombic dodecahedra, 1617 $\text{m}^2 \text{g}^{-1}$ (for 18 nm sized particles) [282]	micrometer sized, rhombic dodecahedra, 1630 $\text{m}^2 \text{g}^{-1}$ [303]
Ultrasonic synthesis	[237, 287, 292]	HKUST-1	10 nm, spherical particles, 1075 $\text{m}^2 \text{g}^{-1}$ [287]	micrometer sized, octahedra, 2260 $\text{m}^2 \text{g}^{-1}$ [304]
Microwave	[80, 281, 285, 291, 292]	IRMOF-3	(sub)micrometer sized, cubic crystals ^(a) 41	micrometer sized, cubes, 2160 $\text{m}^2 \text{g}^{-1}$ [52]
Interfacial synthesis	[299]	HKUST-1	375 μm , hollow capsules 620 $\text{m}^2 \text{g}^{-1}$ [299]	micrometer sized, octahedra, 2260 $\text{m}^2 \text{g}^{-1}$ [304]
Ionic liquids/ Microemulsion	[272]	$\text{Gd}_2(\text{btc})_3(\text{H}_2\text{O})_4$	100 nm (\varnothing) x 35 nm, irregularly shaped platelets ^(a) 22	blade-like crystals, no sorption observed for $\text{N}_2(\text{g})$ and $\text{CO}_2(\text{g})$ [305]

(a) no sorption data available

8.4 ONE-DIMENSIONAL NANOSTRUCTURES

8.4.1 SURFACTANT-ASSISTED SYNTHESIS IN REVERSE MICROEMULSIONS

While the synthesis of MOF nanoparticles has been rather widely explored, the search for a generalized approach to the synthesis of anisotropic and especially one-dimensional nanostructures such as wires and rods has received less attention. Nevertheless, progress has been made with respect to interfacial synthesis procedures in heterogeneous phase mixtures. Among these approaches, surfactant-assisted syntheses in reverse microemulsion systems have shown potential in controlling the shape and aspect ratio of nanoMOFs, although the direct correlation between emulsion composition and the resulting shapes is elusive in most cases.

Lin and co-workers developed a synthetic strategy utilizing the size limiting effects of reverse microemulsions to synthesize MOF nanostructures.^[306-308] Both shape and size of the micelles can be altered by adjusting the surfactant to water ratio ω , resulting in surfactant-stabilized water reservoirs in a continuous organic phase, which can be used as nanoreactors for MOF synthesis. The authors prepared $\text{Ln}(\text{bdc})_{1.5}(\text{H}_2\text{O})_2$ ($\text{Ln} = \text{Eu}^{3+}$, Gd^{3+} or Tb^{3+}) in a microemulsion system consisting of the cationic surfactant cetyltrimethylammonium bromide (CTAB), isooctane, 1-hexanol and water, using LnCl_3 and dimethylammonium-1,4-dicarboxylate as MOF precursors. By varying the ω -value from 5 to 10, the aspect ratio of the resulting MOF nanorods could be altered from 100-125 nm length and 40 nm diameter ($\omega = 5$) up to 2 μm length and a diameter of 100 nm ($\omega = 10$). While increasing the concentration does not affect the aspect ratio of the nanocrystals, it decreases the particle size, possibly due to the increased number of nucleation sites present in the higher concentrated synthesis solution. Additionally, the presence of the surfactant, which creates a shell-like structure around the growing particles, seems to enhance the stability of the particles against agglomeration.^[155] These nanoMOFs could lead to applications in bioimaging due to the high concentration of highly paramagnetic metal ions such as Gd^{3+} , which are administered to enhance magnetic resonance image contrast by increasing proton relaxation rates.^[306]

The above synthesis scheme was extended to MOFs with higher biocompatibility, while retaining MRI contrast enhancing properties, by the synthesis of Mn^{2+} -based MOFs with *bdc* and *btc* linkers. The resulting rod-shaped nanoMOFs of $\text{Mn}(\text{bdc})(\text{H}_2\text{O})_2$ crystallize in the bulk crystal structure and feature tuneable aspect ratios with lengths up to several microns. In contrast, nanoMOFs of composition $\text{Mn}_2(\text{btc})_3(\text{H}_2\text{O})_6$ exhibit an unusual spiral rod morphology (Fig. 8.4.1) with a crystal structure not corresponding to previously known Mn^{2+} -*btc*-based phases.^[308]

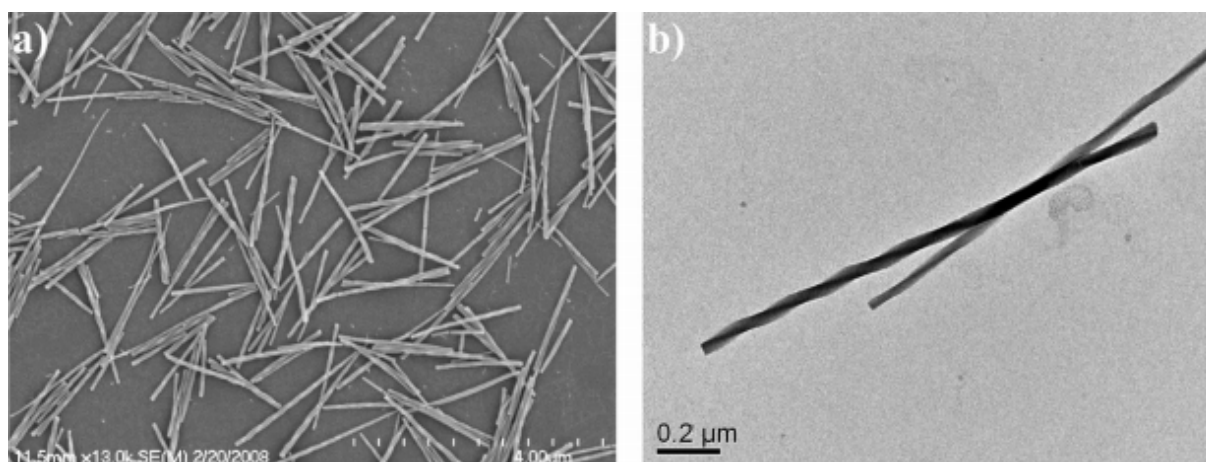


Figure 8.4.1: (a) SEM and (b) TEM image of $\text{Mn}_3(\text{btc})_2(\text{H}_2\text{O})_6$ spiral nanorods synthesized at room temperature. Reprinted with permission from ref. ^[308]. Copyright ©2008 American Chemical Society.

8.4.2 INTERFACIAL CONTROL IN A MICROFLUIDIC ENVIRONMENT

In recent years, “Lab-on-a-Chip” devices for the synthesis of 1D-nanostructures have entered the focus of synthetic chemists.^[309-311] An elegant method for the preparation of 1D nanowires of coordination polymers that exploits interfacial chemistry in a microfluidic environment has recently been presented by Dittrich and co-workers.^[312] The reactant solutions are injected parallel into a microfluidic chip creating a laminar flow of the reactant solutions, thereby enabling superior control of the interface region acting as reaction zone.

In Dittrich’s setup, two aqueous solutions of $\text{Cu}(\text{NO}_3)_2$ and L-Aspartate (Asp) in NaOH were injected into a microfluidic device with four input channels at a flow rate of $100 \mu\text{L min}^{-1}$. At the interface of both streams, nanowires formed within microseconds, which were identified as $\text{Cu}(\text{II})$ -Asp by XRD analysis. Scanning electron microscopy (SEM) measurements proved the formation of bundles of well-aligned nanowires (Fig. 8.4.2).

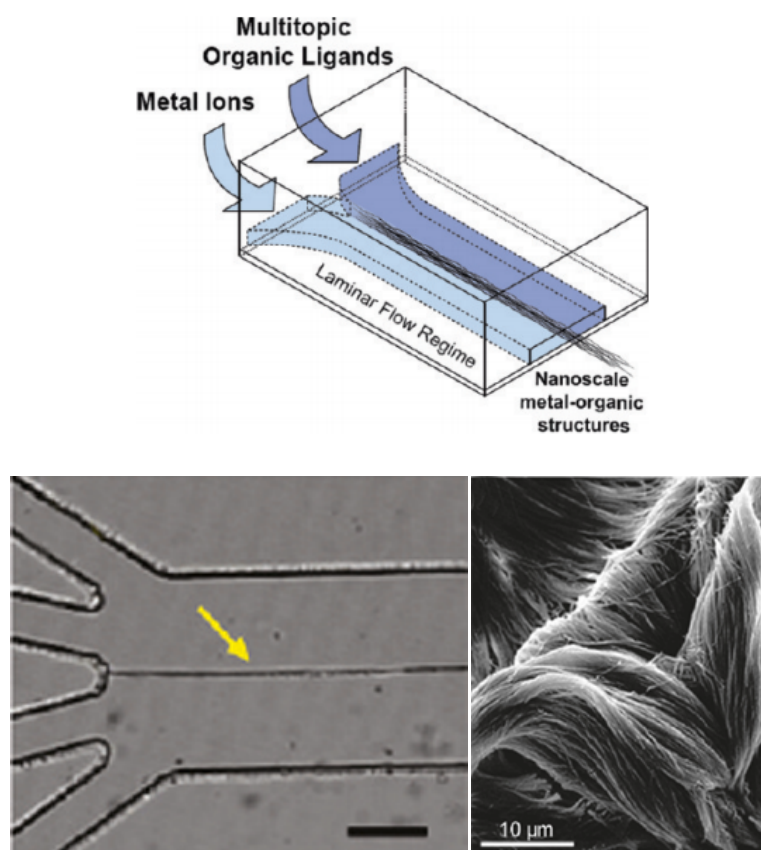


Figure 8.4.2: Top: Schematic drawing of the laminar flow of the reactants in a microfluidic device. Bottom left: Microscopic image of the formed nanowires at the interface between both reactant flows; bottom right: SEM image of a bundle of Cu(II)-Asp nanowires. Reprinted with permission from ref. ^[312]. Copyright ©2011 American Chemical Society.

The scope of this synthesis scheme has been extended to nanofibers of Ag(I)-cysteine (Cys) and Zn(II)-4,4'-bipyridine (4,4'-bipy) coordination polymers with rather uniform diameters in the sub-100 nm range. Although this intriguingly simple microfluidic scheme has not yet been used to produce porous MOF nanowires, it can in principle be utilized to fabricate a wide range of different 1D MOF nanostructures. A major drawback, however, is the lack of scalability, rendering this technique in its present form unsuitable for preparative chemistry and industrial production schemes.

8.4.3 COORDINATION MODULATORS

Capping agents have proven valuable in restricting particle growth by reacting with the surface of the particles and preventing further molecular addition from the mother liquor. Suitable capping agents, among others, are molecules having a single functionality able to form a bond with the metal ions of the metal-organic framework, termed monolinkers. The possibility to terminate the growth of nanoparticles by coordination modulation has been successfully demonstrated by Kitagawa and co-workers using $[\text{Cu}_3(\text{btc})_2]$ as a model system.^[286] Notably, the addition of such growth inhibitors may

permit valuable insights into MOF growth and can even be used to modulate the shape of nanosized MOFs.

Along these lines, Tsuruoka *et al.* have shown that the addition of monolinkers with a functionality identical with that of one of the framework constituents can yield crystals with anisotropic shapes (Fig. 8.4.3).^[280] In the three-dimensional layer-pillar-type framework $[\text{Cu}_2(\text{ndc})_2(\text{dabco})_n]$ (ndc = 1,4-naphthalene dicarboxylate; dabco = 1,4-diazabicyclo[2.2.2]octane), the ndc -linkers connect the copper-clusters in the [100] and [010] directions, while dabco connects the clusters in the [001] direction of the crystal. This inherent framework anisotropy based on two different coordination modes (copper- ndc and copper- dabco), which is imprinted in the tetragonal crystal structure, can be exploited to create different dimensionalities of the formed crystals. By adding a monocarboxylic acid such as acetic acid to the reaction mixture, further addition of ndc to the network is inhibited, leading to the formation of square-rod shaped nanocrystals with average lengths of 392 ± 210 nm and thicknesses of 82 ± 23 nm, respectively. The major axis of the nanorod was found to be coincident with the [001] direction of the framework, indicating preferred crystal growth along the copper- dabco interactions. The addition of a competitive linker to dabco should hence lead to the formation of nanosheets, but this hypothesis is yet to be proven. Interestingly, by studying the time evolution of the reaction by TEM, the growth mechanism was found to proceed by oriented attachment of medium-sized nanocubes (80 nm), as evidenced by the constant diameter of the formed nanorods of roughly 80 nm, and the stepwise increase of the aspect ratio. This is, perhaps not too surprisingly, the first strong evidence that the classical oriented attachment growth model familiar from a range of other nanomaterials^[313] likewise can occur in MOF systems.

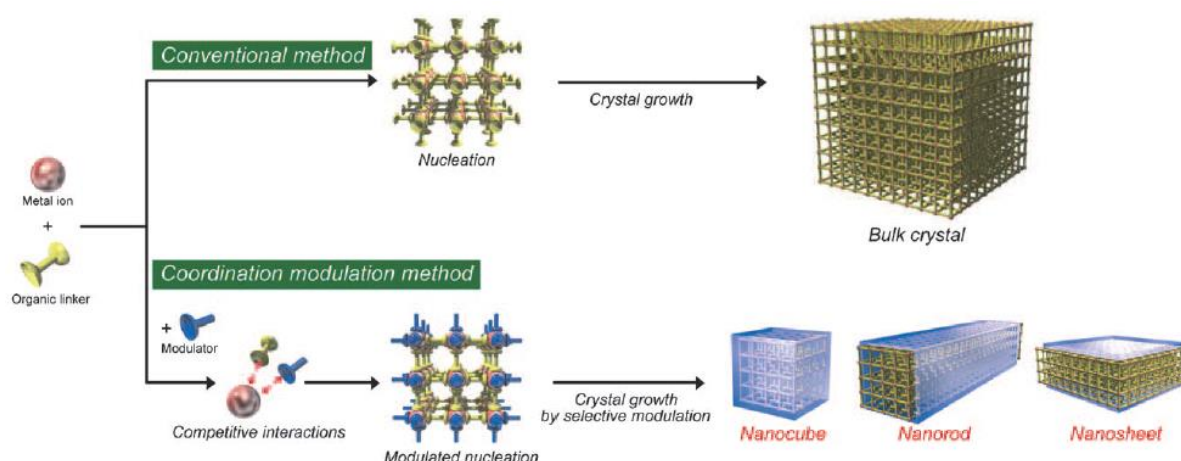


Figure 8.4.3: Conventional synthesis of metal-organic frameworks contrasted with the coordination modulation method to produce anisotropic nanostructures. Reprinted with permission from ref. ^[280]. Copyright © 2009 by John Wiley & Sons, Inc.

8.4.4 GROWTH TEMPLATES

An intriguing, yet unusual approach to grow MOF nanowires utilizes appropriately functionalized surfaces akin to SURMOFs grown from suitable organically modified substrates (see chapter 8.5.3). Recently, Jahan *et al.* elegantly transferred this concept to “freestanding surfaces”, i.e. to the use of chemically modified graphene nanosheets acting as nucleation sites for MOF-5 nanocrystals.^[314] Firstly, by modifying reduced graphene oxide (GO) sheets with benzoic acid, carboxylic acid groups were introduced at both sides of the graphene sheets. The so-called BFG (benzoic acid functionalized graphene) was then mixed with 1,4-*bdc* and $\text{Zn}(\text{NO}_3)_2$, forming a hybrid material consisting of MOF-5 and BFG sheets. Notably, at 5 wt% BFG a clear transformation into nanowire morphology was observed, which was accompanied by profound changes of the MOF crystal structure. Interestingly, the attachment of BFG to the tip of the resulting nanowires along with its integration into the body of the wire as evidenced by micro Raman analysis attests to a dual interaction between BFG and MOF and, hence, points to the following growth mechanism (Fig. 8.4.4): On the one hand, the average diameter of the graphene sheets amounts to roughly 300 nm, which coincides well with the diameter of the MOF nanowires. Hence, BFG acts as a nucleation template, providing a high density of carboxylic acid anchoring sites. On the other hand, TEM analyses reveal that the wires grow along the [220] direction with their (220) faces exposed. These facets incidentally exhibit the highest concentration of Zn_4O clusters, thus resulting in strong metal-carboxylate binding interactions favoring growth in this particular direction as well as the integration of BFG into the body of the growing MOF nanowire. Even if this discovery may have been driven by serendipity, it is trendsetting in revealing the potential of template-directed heterogeneous nucleation and growth for the design of anisotropic MOF nanostructures.

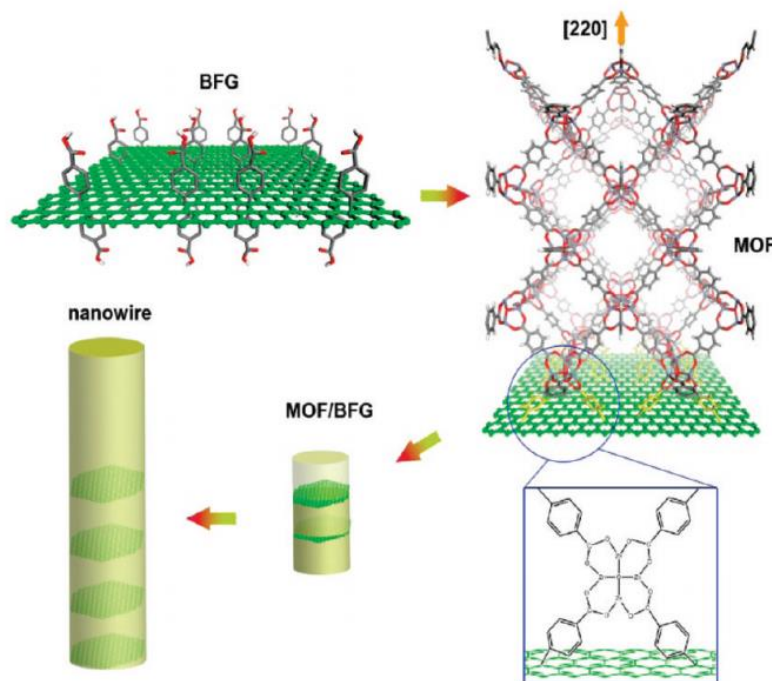


Figure 8.4.4: Schematic of the proposed bonding between BFG and MOF via COOH groups along the [220] direction, and the proposed assembly into nanowire structures with incorporated BFG. Reprinted with permission from ref. [314]. Copyright ©2010 American Chemical Society.

Table 8.4.1 Overview of the synthesis approaches towards 1D nanostructures and the resulting morphology and sorption properties of the formed structures in comparison to the respective bulk material.

1D Nanostructures				Bulk
Synthesis method	References	Selected examples	Properties	
Coordination modulation	[280]	$\text{Cu}_2(\text{ndc})_2(\text{dabco})_n$	392 nm x 82 nm rods ^(a) 33	microcrystalline powder, 1891 m ² g ⁻¹ [152]
Surfactant-assisted synthesis/ Reverse microemulsion	[116, 272, 307, 308]	$\text{Gd}_2(\text{bdc})_3(\text{H}_2\text{O})_4$	125 nm x 40 nm rods ^(a) 22	blade-like crystals, no sorption observed for N ₂ (g) and CO ₂ (g) [305]
Interfacial synthesis/ Microfluidics	[312]	Zn(II)-4,4'-bipyridine	10-75 nm (∅) fiber bundles ^(a) 69	micrometer sized, needle-like crystals ^(a) 69
Templating	[314]	MOF-5	300 nm (∅) wires, 809 m ² g ⁻¹ [314]	millimetre sized cubes, 2900 m ² g ⁻¹ [315]

(a) no sorption data available

8.5 TWO-DIMENSIONAL NANOSTRUCTURES

The fabrication of 2D-MOF nanostructures, i.e. thin films and membranes tailored to the need of specific applications, has dramatically picked up pace in recent years. This is because a number of complementary growth schemes has been devised that each address and imply different morphologies and substrate requirements. So far, MOF thin films have been obtained by six different synthetic schemes, including (a) direct oriented or non-oriented growth from preconditioned solvothermal mother liquors,^[262, 316-319] (b) electrochemical growth of MOF films on suitable metal substrates, including Galvanic displacement,^[320] (c) deposition from colloidal MOF suspensions,^[160, 281] (d) deposition of MOF films based on a gel-layer approach,^[321-323] (e) stepwise growth of thin MOF films utilizing a layer-by-layer (LbL) methodology,^[324-329] and (f) top-down fabrication of freestanding, atomically thin MOF layers.^[330] As a number of comprehensive reviews surveying each of the above growth methods exists,^[279, 301, 331] we will focus our attention to those schemes that furnish nanoscale thin films (primarily methods (c), (d), (e) and (f)), rather than micron-scale layers typically obtained by methods (a) and (b).

8.5.1 DEPOSITION OF MOF COLLOIDS

Though being a rather recent approach, the deposition of MOF thin films from colloidal suspensions is one of the key methods for film fabrication owing to its simplicity and facile production of films with high optical quality on various substrates. Horcajada *et al.* reported on the fabrication of thin films processed by dip-coating of an iron muconate (MIL-89) colloidal sol containing nanoparticles between 20 and 40 nm in size.^[281] The optical quality of the resulting films allowed *in situ* characterization by environmental ellipsometry, demonstrating the reversible increase in cell volume of the highly flexible MOF by adsorption of polar liquids, and the resulting decrease in the refractive index of the layer from 1.65 to 1.45 upon swelling. Similar films have been produced based on MIL-101(Cr) and other MOFs, featuring layer thicknesses typically below 80 nm, which could be increased by multiple dipping steps (Fig. 8.5.1).^[332]

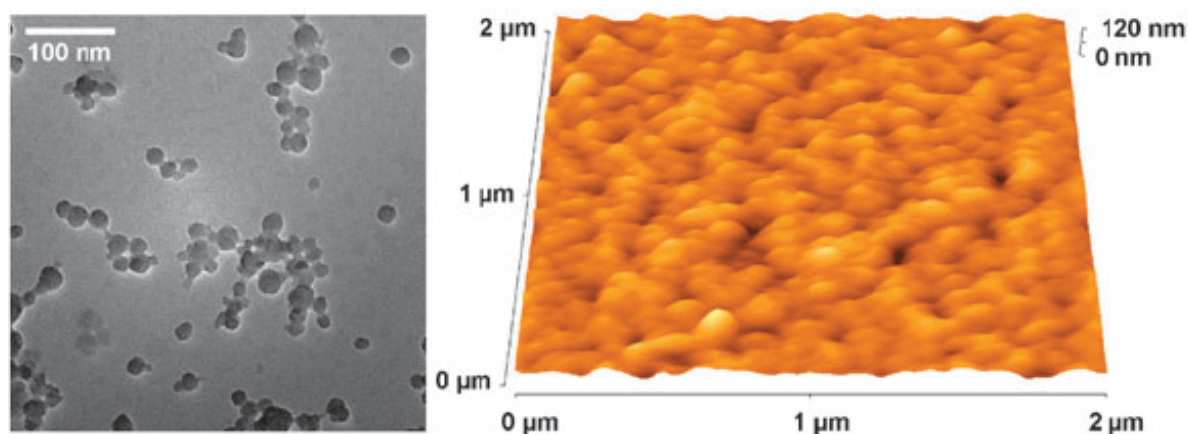


Figure 8.5.1: TEM (left) and atomic force microscopy (AFM) images of nanoparticles and a thin film of MIL-101 (Cr) made by nanoparticle deposition, respectively.^[332] Reproduced by permission of The Royal Society of Chemistry.

Owing to the deposition from colloidal suspensions, the films feature bimodal porosities resulting from both structural and textural porosity, the latter being introduced by inter-grain voids typically in the mesopore range. Hierarchical micro- and mesoporosity may turn out beneficial in applications where fast diffusion into the MOF micropores through mesoporous interparticle voids is key, such as in catalysis or size-selective adsorption from vapor mixtures. This increased sensitivity to guest molecules can be used to enhance MOF-based Fabry-Pérot sensor devices, which have already been synthesized *via* direct growth.^[47] Another advantage of the colloidal deposition method, which can easily be extended to spin- or spray-coating protocols, lies in its indiscriminate nature with respect to substrate requirements, as no surface modification prior to the coating step is necessary.

8.5.2 GEL-LAYER APPROACH

Colloidal deposition routes result in random orientation of the nanoparticles on the surface, hence not allowing for oriented MOF growth along specific crystallographic directions. On the contrary, oriented MOF growth has been observed in the gel-layer approach developed by Bein and co-workers,^[322] and is inherent to the LbL protocol that has been pioneered by the groups of Wöll and Fischer.^[323] In the novel gel-layer approach, a gold substrate primed by self-assembled monolayers (SAMs) as nucleation-directing templates^[321] is loaded with the metal-salt-containing poly(ethyleneglycol) gel layer and subsequently covered with a solution containing the linker molecules. Highly oriented and uniform submicron thick layers have successfully been grown with HKUST-1 and the flexible framework Fe-MIL-88B-NH₂ within reaction times of typically two days. As the layer thickness is tunable by adjusting the metal ion concentration in the gel layer, this approach represents a simple, yet highly efficient approach toward oriented MOF films with variable thicknesses. Although highly oriented films have also been grown from preconditioned mother

solutions in a direct fashion,^[317] the gel-approach allows for a more subtle control of the growth zone and hence, layer thickness.

8.5.3 LAYER-BY-LAYER GROWTH (LIQUID PHASE EPITAXY)

The technology of MOF thin film synthesis affording the highest level of control in terms of composition, crystallographic orientation and structure, thickness and even post-modification by selective pore loading, relies on the stepwise LbL growth christened „liquid phase epitaxy“ (LPE) owing to the unique orientation control possible with this technique.

The stepwise growth of surface immobilized MOFs (dubbed SURMOFs) was first introduced by Shekhah *et al.* in 2007, who could demonstrate the feasibility of controlling not only the orientation, but also the number of MOF layers grown on the surface.^[323] Instead of the single-pot solvothermal synthesis used by Fischer and Bein,^[322, 323] HKUST-1 was grown in a LbL fashion by repeated immersion cycles using two precursor solutions, each containing one reactant (Fig. 8.5.2). As with each immersion cycle another layer is added to the structure, the thickness of the resulting MOF film can be controlled by limiting the number of immersion cycles. Intriguingly, each immersion cycle can directly be observed *in situ via* quartz crystal microbalance analysis by monitoring the change in resonance frequency, or by surface plasmon resonance spectroscopy,^[329] demonstrating the precise growth of the film with sub-monolayer resolution.

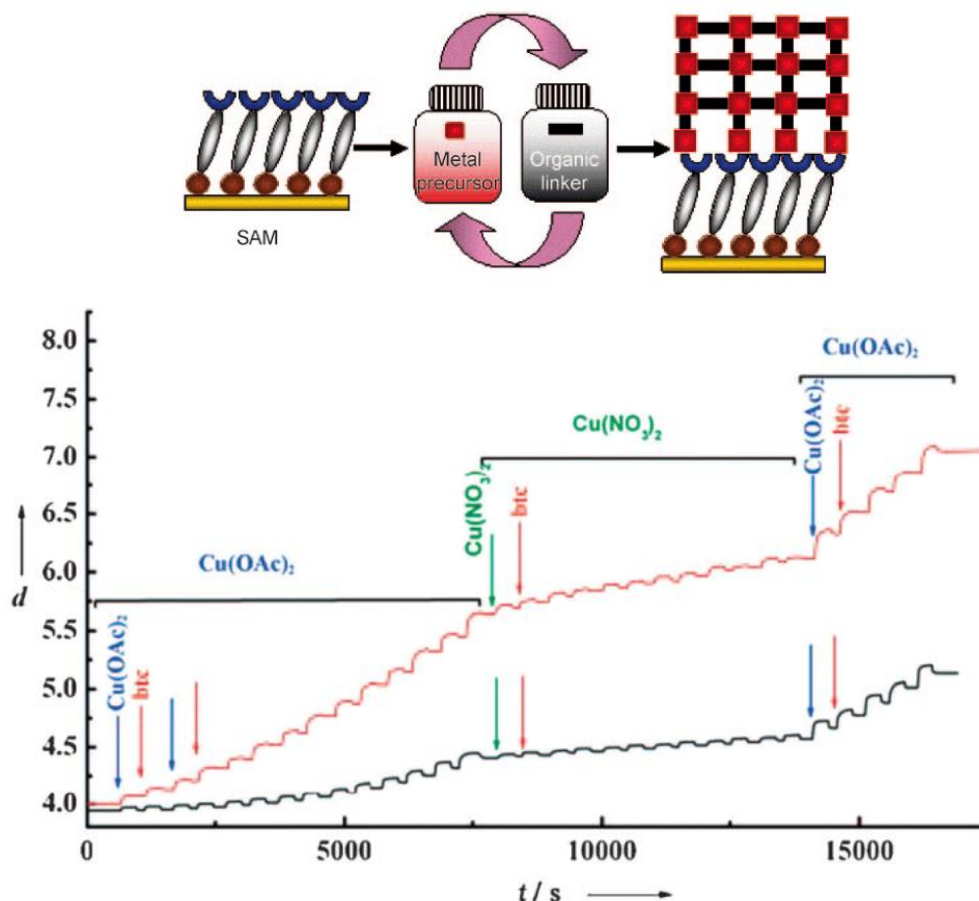


Figure 8.5.2: Top: Generalized scheme of a LbL synthesis of MOF thin films on SAM terminated surfaces. Bottom: SPR signal as a function of time recorded in situ during the stepwise treatment of two different SAMs (11-mercaptoundecanol (MUD) in red, 16-mercaptohexadecanoic acid (MHDA) in black) with Cu(OAc)₂, H₃btc, and Cu(NO₃)₂. Reprinted with permission from ref. [329]. Copyright ©2009 by John Wiley & Sons, Inc.

The effect of different SAMs on the orientation of the MOF layers has been demonstrated by Shekhah *et al.* who studied the influence of COOH- and OH-terminated SAMs on the orientation of HKUST-1.^[329] By functionalizing gold substrates with those SAMs, it could be shown by out-of-plane XRD measurements that COOH terminated surfaces lead to (100) oriented HKUST-1 films by strong interactions between exposed Cu₂ dimeric units and the carboxylic acid termini, while OH-groups provide a better surface for (111) orientation owing to beneficial Cu²⁺ - OH interactions.

Recently, the same groups proposed a new and faster synthesis route towards MOF thin films using a modified layer-by-layer approach. In contrast to previous LPE procedures, the reactants were now deposited *via* spray-coating on a surface modified with SAMs, thereby allowing for a significantly faster deposition speed as well as the fabrication of micron thick monolithic films. Washing steps between the sequential spray-coating of the individual reactant solutions have turned out to be crucial as they ensure that no additional substructures can be formed from excess reactants and the subsequently deposited reactant solution. Nevertheless, a substantially increased SURMOF thickness per deposition cycle is observed with spray coating as compared to the traditional LPE method, which

is likely due to incomplete reactant removal by the washing steps. Though being beneficial for rapid film growth (20 full cycles afford 200 nm film thickness in 30 min), these observations render the exact growth mode in the spray process still subject to debate.^[326]

The LPE surface growth of MOFs transcends classical LbL schemes introduced by Decher and others for oppositely charged polyelectrolytes^[325] in that it furnishes crystalline order both perpendicular and parallel to the substrate, combined with an exceptionally high level of compositional control at the atomic scale. It should be noted, however, that these achievements are intrinsically connected with the use of high quality SAM-modified substrates, as the crystalline order of the particular SAM chosen will be directly imprinted into the MOF film grown on top. Furthermore, it remains to be shown that the LPE scheme can be generalized to MOF compositions other than the typically used HKUST-1 and layer-pillar MOFs. An important step in this direction has recently been done by the selective growth of a so far unknown, non-interpenetrated MOF-508 structure based on Zn^{2+} , *bdc* and 4,4'-bipyridine building blocks by the LPE approach.^[324] The formation of the interpenetrated bulk structure is likely suppressed by the presence of the substrate, thus lifting the equivalence of the otherwise identical sublattices. This result bodes well for a more generalized approach toward surface-induced formation of new framework topologies *via* the LPE method.

8.5.4 TOP-DOWN FABRICATION

The final and most recent fabrication method for MOF thin films may be considered as a “top-down” or “deconstruction” method starting out from a bulk MOF material. Li *et al.* produced atomically thin MOF layers by delamination of a dried sample of bulk MOF-2 by ultrasonication in acetone.^[330] MOF-2, a 2D network constructed by paddle-wheel Zn_2 -clusters and terephthalates held together by hydrogen bonds,^[333] lends itself ideally as model system for exfoliation studies owing to its weak interlayer forces. The as-produced nanosheets were shown by AFM to have thicknesses between 0.7 and 6.0 nm and lateral dimensions between 100 nm and 1 μm (Fig. 8.5.3), corresponding well to the theoretical thickness of a single MOF-2 sheet (0.75 nm). Restacking in the presence of amines led to intercalated aggregates with increased layer spacings, yet more quantitative data will be needed in order to gauge the adsorption/intercalation capacities of MOF nanosheets and potential applications as sorption and storage media.

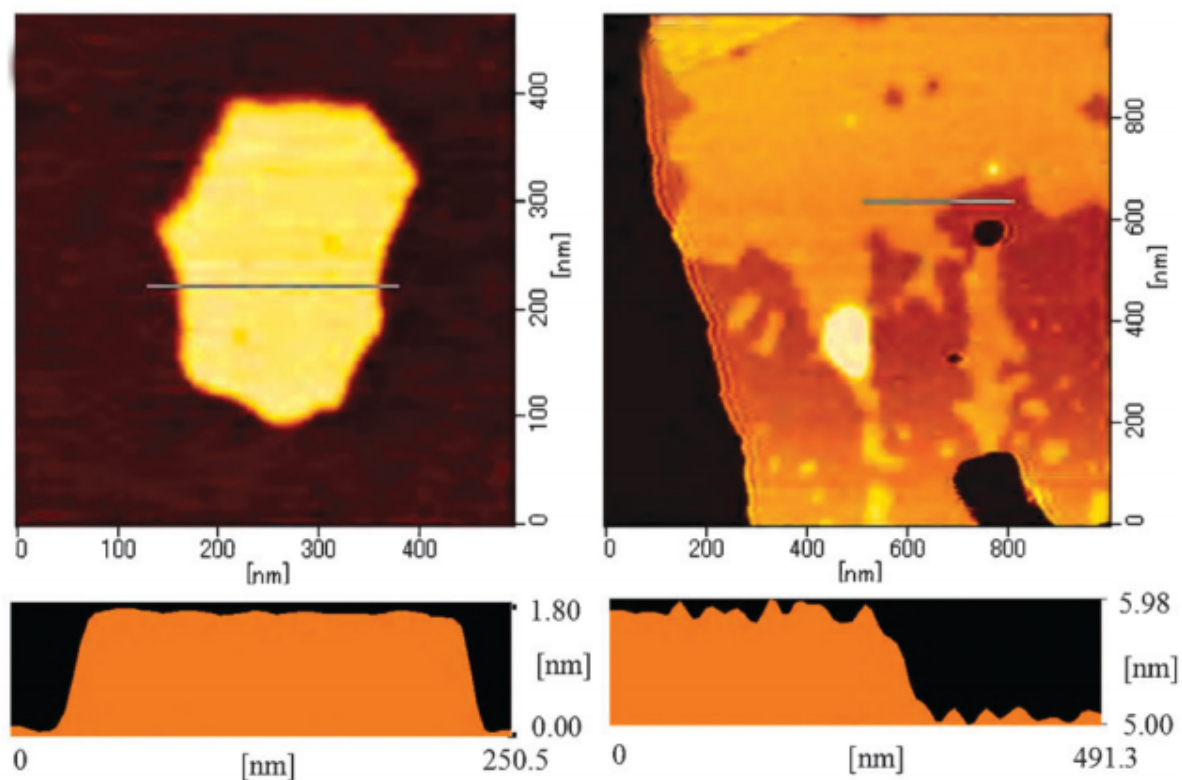


Figure 8.5.3: Tapping-mode AFM images of delaminated MOF-2 nanosheets deposited on a mica substrate showing (left) a MOF-2 nanosheet with the thickness of ~ 1.5 nm and (right) a profile of two neighbouring overlapped layers of delaminated MOF-2 nanosheets with a distance of ~ 0.7 nm between both layers.^[330] Reproduced by permission of The Royal Society of Chemistry.

Table 8.5.1 Overview of the synthesis approaches towards 2D nanostructures and the resulting morphology and sorption properties of the formed layers in comparison to the respective bulk material.

2D Nanostructures				Bulk
Synthesis method	References	Selected examples	Properties	
Coordination modulation	[280]	$\text{Cu}_2(\text{ndc})_2(\text{dabco})_n$	(a)	microcrystalline powder, $1891 \text{ m}^2 \text{ g}^{-1}$ [305]
Colloidal MOF-suspensions	[281, 332]	MIL-101(Cr)	22 nm spherical particles / 48 nm thin film, $4200 \text{ m}^2 \text{ g}^{-1}$ 90	microcrystalline powder, $5900 \text{ m}^2 \text{ g}^{-1}$ 90
Gel-layer deposition	[316-319], 79	HKUST-1	600 nm thin film (after 112 h) (a) 79	micrometer sized octahedra, $2260 \text{ m}^2 \text{ g}^{-1}$ [304]
Layer-by-layer growth/ Liquid phase epitaxy	[323, 327-329]	HKUST-1	200 nm thin films after 20 full cycles (a) 87	micrometer sized octahedra, $2260 \text{ m}^2 \text{ g}^{-1}$ [304]
Top-down fabrication	[330]	MOF-2	200 nm x 300 nm x 1.5 nm sheets (a) 88	micrometer sized prisms, $270 \text{ m}^2 \text{ g}^{-1}$ [315]

(a) no sorption data available

8.6 HYBRID NANOMORPHOLOGIES

While shape already imparts functionality to MOF nanocrystals, the level of functionality can significantly be raised by tuning the composition or by integrating different properties within one single MOF platform. This may be done by various schemes, the most prominent being post-synthetic modification (PSM) of the linkers in as-obtained frameworks, and the surface-modification of as-formed MOF nanoparticles. The former synthesis strategy can be used for materials having functional groups attached to the linker molecules, which can be modified with the desired reactant in the functionalization step. As a requirement, the frameworks must be stable under functionalization conditions as well as to by-products formed during the functionalization process. In contrast to surface modification schemes, the framework must exhibit pores, being large enough for the

reactants to enter in order to allow for a complete functionalization of the framework. The feasibility of PSM was already pointed out in 1990 by Hoskins *et al.*, who stated that “relatively unimpeded migration of the species throughout the lattice may allow chemical functionalization of the rods subsequent to the construction of the framework.”^[334] To this date, a variety of possible PSM approaches have been explored, with the two main foci being on biomedical applications^[138, 335, 336] and the exploration of otherwise inaccessible MOF compositions.^[124] However, PSM on nanoMOFs is still a surprisingly scarce topic in state-of-the-art MOF science and, hence, we will turn our focus on surface-modification of nanoMOFs rather than PSM.

8.6.1 CORE-SHELL PARTICLES

The groups of Férey and Lin have carried out pioneering works in the exploitation of biomedical applications based on surface-modified nanoMOFs, which have shown great potential for the encapsulation and controlled release of drugs.^[184, 337, 338] In order to ensure maximum biocompatibility, optimal blood circulation times and release kinetics, as well as suitable administration of the drugs, MOFs have been coated by hydrophilic polymers such as poly(ethylene glycol) (PEG), or thin silica shells that can further be modified by grafting functional molecules on the exposed surface.^[184, 335]

For example, in a seminal study Férey and co-workers were able to prove the general concept of using nanosized MOF particles as efficient carriers for anti-cancer drugs. To this end, protocols for the synthesis of MIL-100 (Fe) nanoparticles *via* microwave synthesis were developed,^[184] and the sub-200 nm particles were loaded with up to 25 wt% of busulfan, a commonly used anti-cancer drug. To enhance the stability of the MOF particles in biological systems, the authors coated the particles with bifunctional PEG (CH₃-O-PEG-NH₂, 5 mg/mL of water). Studies on human cell cultures showed that busulfan in nanosized MOFs and free busulfan exhibit the same activity, thereby paving the way for the use of suitably modified nanoMOFs as possible anti-cancer drug vehicles.

Lin and his group put forward studies on the biocompatibility of nanosized MOFs, thereby designing ways to enhance the stability of the particles inside biological systems.^[138] By adding an ethanolic solution of tetraethylorthosilicate (TEOS) containing 4 % aqueous ammonia to as-synthesized MIL-101 (Fe) nanoparticles, a silica shell is formed around the framework particles with thicknesses between 2 and 9 nm, depending on the reaction time (2-3 nm: 2 h, 8-9 nm: 7 h). As a consequence of the stabilizing shell, the half life in phosphate buffered saline (PBS) solution at 37 °C is increased from 2.5 hours to 16 hours.

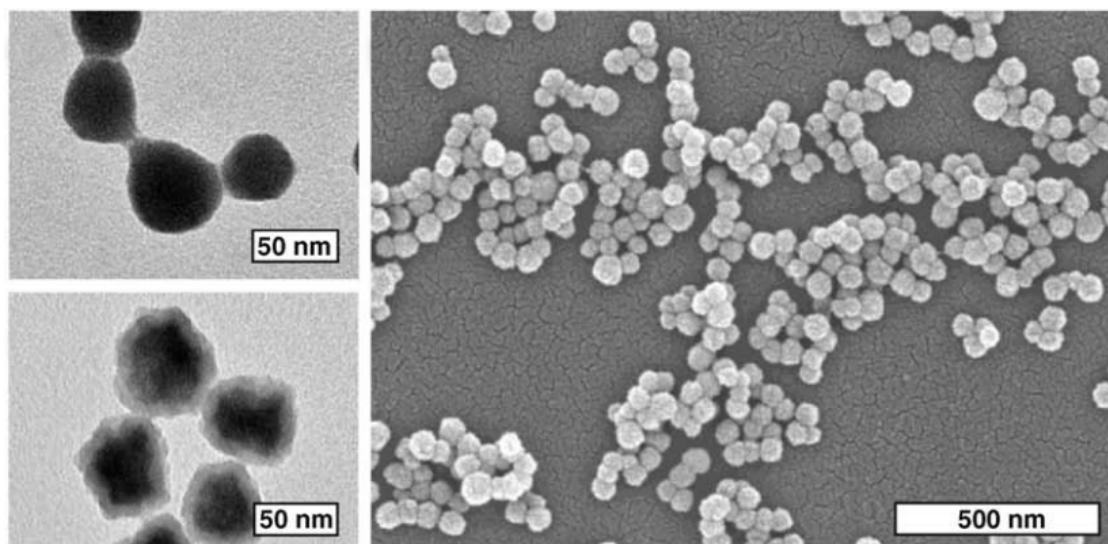


Figure 8.6.1: TEM micrographs of disuccinatocisplatin (DSCP)-loaded nanoMOFs (top left). TEM (right) and SEM (bottom left) micrographs of silica coated DSCP nanoMOF particles. Reprinted from ref. ^[339] with permission from Elsevier.

Furthermore, Lin and his group proved the possibility to functionalize nanoMIL-101 (Fe) particles (Fe^{2+} connected by $\text{NH}_2\text{-bdc}$ and 1,4-benzenedicarboxylate linkers) with organic fluorophores such as 4,4-dibromo-4-bora-3a,4a-diaza-s-indacene (Br-BODIPY). This modification enables the use of the nanoparticles as imaging vehicles, using the fluorophore as visible marker. The functionalisation with a prodrug of cisplatin (ethoxysuccinatocisplatin, ESCP) showed the possibility to use the particles also as drug carriers, as the cytotoxicity of the ESCP-functionalized particles on HT-29 human colon adenocarcinoma cells was comparable to other Pt-drugs.^[339] The combination of drug cytotoxicity with the increased biostability renders the nanoparticles capable to act as targeted drug vectors with a controllable release rate due to the slow diffusion of metal and organic constituents through the silica shell, thus boding well for a new generation of “nanobioMOFs”.

8.6.2 MOF-ON-MOF HETEROEPITAXY

The concept of MOF surface modification and protection can be taken to a higher level by precisely controlling the interfacial interactions between core and shell, that is, by epitaxial growth of the shell material on a well defined single crystal MOF core. This modified core-shell concept has been cast into a creative MOF-on-MOF growth scheme developed by Kitagawa and co-workers, which allows for the design of single-crystal MOF heterostructures with spatially modulated composition, porosity and, hence, functionality.^[340-342] These growth schemes have so far been demonstrated only based on micron-scale MOF single crystals and hence fall outside the nanoMOF focus adhered to in this review. Nevertheless, such aesthetic MOF@MOF architectures deserve to be discussed in some detail as they offer, in principle, a generic scheme for the design of multifunctional MOF heterostructures with spatial control of the composition down to the nanoscale.

The hybridization of a MOF core single crystal by epitaxial growth of a single crystalline shell with different structural and porosity properties has been demonstrated successfully based on the archetypal series of tetragonal layer-pillar MOFs with formula $\{M_2(\text{dicarboxylate})_2(\text{diamine})\}_n$.^[341] The authors convincingly demonstrate the implementation of well-resolved, spatially separated functionality by the presence of core and shell MOFs with distinct framework topologies and pore surfaces. For example, sequential functionalization was achieved by growing a $\{\text{Zn}_2(\text{adc})_2(\text{dabco})\}_n$ shell (adc = 9,10-anthracene dicarboxylate) on top of a $\{\text{Zn}_2(\text{bdc})_2(\text{dabco})\}_n$ core framework, resulting in heterostructures featuring size selective uptake of bulky hydrocarbons owing to the small apertures of the shell crystal and high storage capacities owing to the large pore volume of the core crystal.

The scope of framework topologies was extended by Koh *et al.* who were able to grow various core-shell architectures of the isorecticular cubic MOF-5 and IRMOF-3 using MOF-on-MOF heteroepitaxy.^[343]

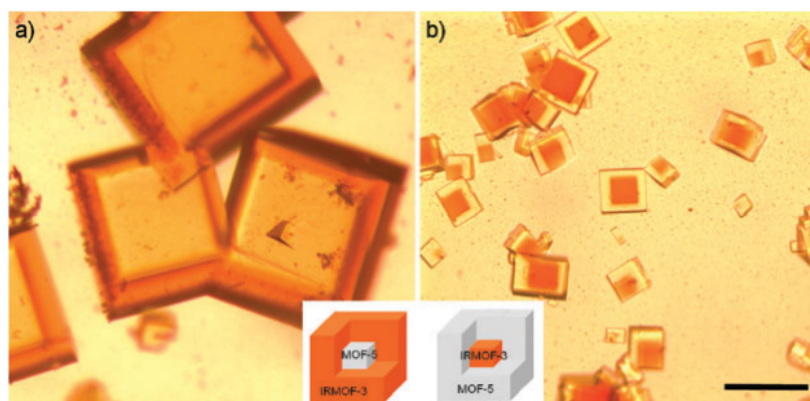


Figure 8.6.2: Optical micrographs of core-shell MOFs (a) IRMOF-3(shell)@MOF-5(core), (b) MOF-5(shell)@IRMOF-3(core). Scale bar: 200 μm .^[343] Reproduced by permission of The Royal Society of Chemistry.

The compatibility of both linkers was demonstrated by immersing single crystals of MOF-5 into a growth solution containing the IRMOF-3 building blocks, yielding crystals with a colorless core and an orange shell on the outer side (Fig. 8.6.2, left), and vice versa (Fig. 8.6.2, right). Quite evidently, the heteroepitaxial growth scheme is well transferable to planar systems such as MOF thin films, if the lattice parameters and in-plane connecting groups are identical, as Wöll and co-workers could show by growing $[\text{Zn}_2(\text{ndc})_2(\text{dabco})]$ on $[\text{Cu}_2(\text{ndc})_2(\text{dabco})]$ crystals *via* the LPE procedure.^[327]

This modular synthesis scheme holds great promise for the judicious and spatially well-defined integration of various functionalities in one single, yet heterogeneous MOF monolith, without sacrificing desired properties of the core framework, such as high surface area and pore volume.

8.7 MECHANISTIC INSIGHTS AND DIMENSION CONTROL – A CASE STUDY

As outlined in the previous chapters, the variety of nanomorphologies that has been synthesized to date is impressive, as is the variety of synthetic methodologies employed. Since a deeper insight into the nucleation and growth stages of nanoMOF formation is pivotal for the directed design of particular nanomorphologies, the complexity of the parameter space in nanoMOF synthesis necessitates radical simplification, and *in situ* techniques adept at monitoring the early stages of nucleation and growth need to be made available. Equally important though, the diversity of systems studied may complicate the elaboration of common underlying themes in the growth mechanisms of different MOF systems. Therefore, rational access to MOF nanomorphologies should be gained by exploring a sufficiently representative system in all its facets, and by subsequently transferring generally applicable motifs to other, more complex systems.

Owing to their stability, ease of synthesis, and rather straightforward solution chemistry, zeolitic imidazolate frameworks (ZIFs), a subclass of MOFs and already among the “*drosophilas*” in MOF science, lend themselves very well as model systems for an in-depth study of controlling morphology and crystal growth.^[46, 47, 160, 239, 344-347]

Both ZIF-8 and ZIF-7, first synthesized by Yaghi and co-workers, are composed of Zn ions joined by imidazolate ligands (ZIF-8: 2-methylimidazole (*mim*), ZIF-7: benzimidazole (*bim*)).^[41] The frameworks with composition $\text{Zn}(\text{mim}/\text{bim})_2$ are composed of zeolite-like tetrahedral nets with sodalite topology owing to the geometrical similarity between Zn—*mim/bim*—Zn and Si—O—Si bond angles. Whereas ZIF-8 crystallizes in the cubic space group *I*-43*m* and hence is expected to form isotropic nanocrystals, ZIF-7 (hexagonal, space group *R*-3) features an anisotropic channel network and therefore is ideally suited to study not only the size, but also shape selective synthesis of ZIF-7 nanocrystals. In the following, we will briefly discuss the insights recently gained into the growth mechanism of ZIF-8 nanocrystals and complete this review by surveying recent achievements in the shape-selective synthesis of ZIF-7 nanomorphologies.

8.7.1 GROWTH MECHANISM OF ZIF-8 NANOPARTICLES

The first steps toward ZIF-8 nanoparticles were made in the seminal work by Wiebcke and co-workers, who were able to synthesize ZIF-8 nanoparticles of ≈ 45 nm with a narrow size distribution in a room temperature synthesis by adding the bridging ligand 2-methylimidazole (*Hmim*) in eightfold excess with respect to the Zn source.^[237] This protocol was later on refined by the addition of modulating ligands that modify both coordination and deprotonation equilibria during nucleation and growth, thereby liberating the “active” linker methylimidazolate.^[282] Interestingly, although extremely small ZIF-8 nanocrystals (< 10 nm) were obtained in the presence of *n*-butylamine, the authors concluded that the most efficient size limiting effect is exerted by the bridging ligand, whose

concentration must be high. The ZIF-8 growth process without modulating ligand (solution composition $\text{Zn}/\text{Hmim}/\text{MeOH} = 1:4:1000$) was monitored by time-resolved *in situ* static light scattering (SLS) and SEM.^[282] Careful correlation between the time-dependent size and number distribution of the solution species with the particles observed *ex situ* confirm that ZIF-8 nucleation is continuous and comparatively slow, whereas crystal growth is rapid in the early stages of nanocrystal formation. Similar nucleation-controlled crystallization behaviour with continuous formation of nucleation sites over the timescale of minutes has been observed in other systems such as HKUST-1, studied by *in situ* WAXS and light scattering.^[348, 349] Somewhat unintuitively, for ZIF-8 a narrowing of the particle size distribution is evident after 1 h, resulting in rather monodisperse particles with an average size of 40 nm. The observed size focusing is rationalized by the termination of fast particle growth at a radius of gyration around 20 nm, which in turn is attested to colloidal stabilization of the primary particles by surface-attached *Hmim* ligands, in line with the measured zeta potential of $\xi = +55$ mV. Although size defocusing by Ostwald ripening subsequently broadens the particle size distribution, rhombic dodecahedral nanoparticles of only 65 nm are obtained even after a reaction time as long as 24 h at RT.

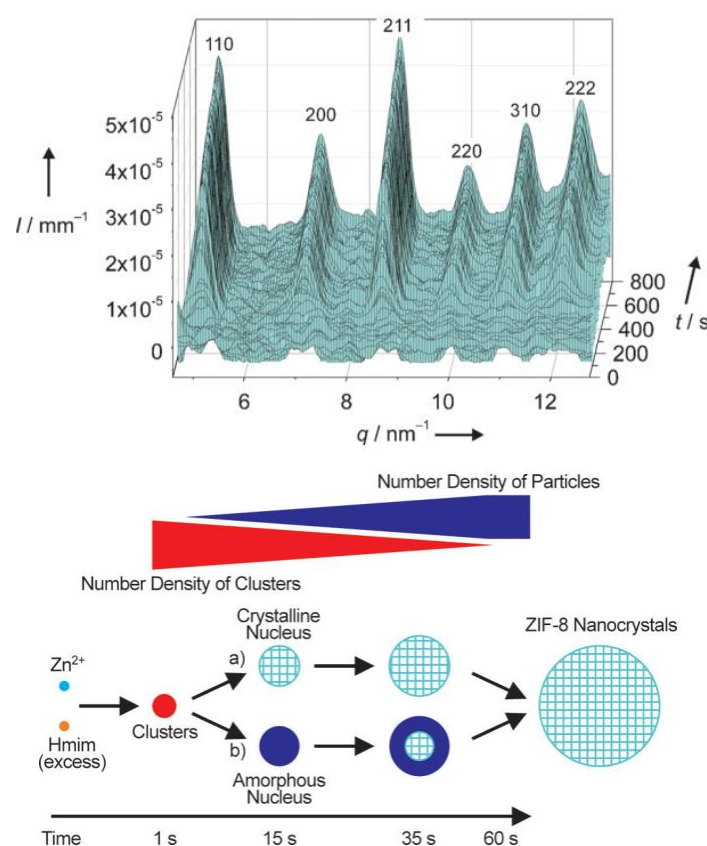


Figure 8.7.1: Top: Time resolved WAXS pattern during the formation of ZIF-8 nanocrystals between 1 s and 800 s. The time interval between succeeding patterns is 1 s. Bottom: Species occurring during nucleation and growth of ZIF-8 nanocrystals under conditions of high supersaturation. Two possible alternative crystallization pathways (a) and (b) are considered. Reprinted with permission from ref. ^[302]. Copyright ©2011 by John Wiley & Sons, Inc.

Complementary *in situ* SAXS/WAXS studies on ZIF-8 nucleation and growth by Cravillon *et al.* (Fig. 8.7.1), are largely in line with the previously reported SLS data. Owing to the excellent time resolution, prenucleation clusters of approximately 2 nm in size could be detected, suggesting a rather complex crystallization process familiar from the topologically related class of zeolites. Importantly, periodic ZIF-8 particles are formed after 22 s by a monomer/cluster addition mechanism, but not by coalescence. Finally, an important, yet previously somewhat controversial finding reveals the phase-pure formation of ZIF-8 nanocrystals without passing through another transient crystalline phase.^[350]

8.7.2 MORPHOLOGY CONTROL OF ZIF-7 NANOSTRUCTURES

The control of size and shape of ZIF-7 nanocrystals has recently been presented in a comprehensive study by Caro and co-workers. This study nicely demonstrates that particular MOF systems may act as a „morphological chameleon“ based on the premise that the reaction parameters are adjusted in a suitable way.^[318] For the synthesis of spherical ZIF-7 nanocrystals with uniform sizes tunable between 40 and 140 nm the authors proposed a simple „one-pot“ strategy using stoichiometric amounts of zinc nitrate and *bim* (molar ratio 1:2) in a polyethyleneimine-dimethylformamide (PEI-DMF) solution at room temperature (Fig. 8.7.2, left).^[318] PEI is acting as a base for *bim*, thus leading to a high nucleation rate which is critical for the formation of nanoparticles. In order to alter the growth kinetics of the different crystal faces and, hence, increase the aspect ratio of the nanoparticles, the authors employed zinc chloride instead of zinc nitrate as precursor. As a rationale, the authors invoke the “hard soft acid base” theory (HSAB), which classifies zinc and chloride as “intermediate” acids and bases, respectively, indicating strong interactions between them. Therefore, the differences in growth kinetics of the low index faces, characterized by the attachment energy,^[351] will be more distinct in the presence of chloride ions, resulting in enlarged differences in the growth rates of the {003} and {110}/{101} faces and thus, prismatic hexagonal crystals with high aspect ratios (Fig. 8.7.2, middle). When adding diethylamine (DEA), the size and aspect ratio of the ZIF-7 crystals could further be adjusted by varying the amount of DEA acting as deprotonation agent for the *bim* linker. Having established protocols for tailoring the crystal size and morphology, the authors succeeded in growing highly oriented ZIF-7 membranes starting from randomly oriented seed layers, which exhibit a clear morphological relation to the nanorods observed by non-supported growth (Fig. 8.7.2, right).

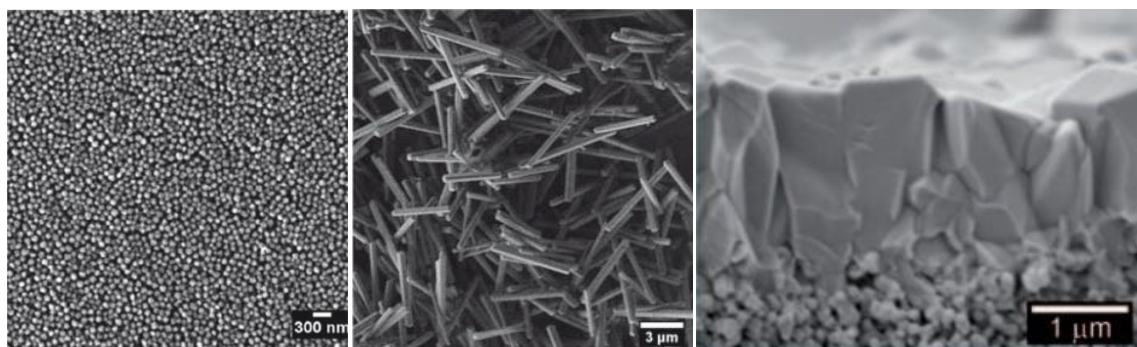


Figure 8.7.2: Nanoparticles synthesized from $\text{Zn}(\text{NO}_3)_2$ as metal source (left), nanorods grown in the presence of ZnCl_2 (middle), and ZIF-7 membrane on alumina disk (right). Reprinted with permission from ref. ^[318] and ^[319]. Copyright ©2010 by John Wiley & Sons, Inc.

In a previous report by the same authors, the growth of randomly oriented ZIF-7 membranes had been analysed.^[319] Permeation measurements through both oriented and non-oriented membrane types demonstrate the gas-separation capabilities of such ZIF films *via* a molecular sieving effect with an increased selectivity at elevated temperatures. Interestingly, the permeance of H_2 was found to be lower for the highly oriented membrane as compared to the randomly oriented layer, which the authors attribute to the anisotropic pore structure, as “neither the pyramidal termination $\{101\}$ faces nor the prismatic $\{110\}$ faces of the columnar crystals possess direct entrances for guest molecules.”^[318] The observed membrane performances further substantiate the efficiency of morphology tuning to enhance the functionality of nanoMOFs and devices made thereof.

8.8 CONCLUSION

This feature article has attempted to distil off the essence of state-of-the-art approaches toward nanoscale MOF architectures with different dimensionalities. Recent advances in the field have been highlighted with a particular focus on protocols (a) allowing for a high level of control with respect to composition and structure at the nanoscale, (b) enabling reliable tuning of the nanoscale morphology and, hence, dimensionality, or (c) elaborating conceptually new fabrication strategies to achieve the above goals. Besides, we have gathered insights into the mechanism of nucleation and growth processes in nanoMOF synthesis of representative MOF systems such as ZIF-8, which ultimately may be generalized to other MOF systems and enable a more purposeful fine-tuning of the reaction parameters in nanoMOF synthesis.

While the development of new nanoMOFs has considerably quickened its pace thanks to a plethora of different synthesis strategies that have significantly matured over the past years, many of the reported approaches are still essentially trial and error-based. Therefore, many nanoMOFs have been obtained by serendipity rather than rational design, yet a number of encouraging approaches has

recently been developed that point toward more directed morphology control. Among those, templating strategies enabling crystallographically oriented growth and interfacial control such as those in microfluidic environments excel by their straightforward concept, yet highly reproducible and tunable size and shape control. Also, the step-by-step liquid layer epitaxy for the immobilization of ultrathin MOF films allow for an unprecedented level of control of composition, topology and film thickness at the nanoscale. However, future MOF nanomorphologies will inevitably gain complexity – hollow and hybrid MOF spheres as well as hierarchically micro-mesoporous MOFs have given us a flavor of what is already possible.

As a perspective, the integration of different functionalities into one “hybrid” MOF platform will be a key asset. Highly oriented MOF-on-MOF heteroepitaxy on planar and curved surfaces has been trendsetting in this respect. Once this technology will be adapted to nanofabrication protocols, the stage is set for the design of tailor-made, multifunctional MOFs with spatially distinct porosity and surface properties.

The inherent shape-dependent properties of nanomaterials and the prospect of a vast spectrum of nanoMOF applications, ranging from drug delivery, catalysis and sensing to smart membranes, leave the synthetic chemist with the challenge to create various nanomorphologies of one and the same material. A look into the toolbox of modern nanoscale synthesis may do the trick – the tools are at hand.

8.9 ACKNOWLEDGEMENT

The authors acknowledge financial support by the Priority Program 1362 “Porous Metal-Organic Frameworks” of the Deutsche Forschungsgemeinschaft (DFG), the Nanosystems Initiative Munich (NIM) and the Center for NanoScience (CeNS).

9 APPENDIX

9.1 CHAPTER 4 - SUPPORTING INFORMATION

to the chapter "Surfactant-directed synthesis of mesostructured zinc imidazoles"

Table S1: Chemicals used in this work and their respective suppliers and purity.

Chemical name	Supplier	Purity
Zinc acetate dihydrate	Merck	ACS
Imidazole	Acros Organics	99 %
2-Methylimidazole	Merck	99 %
N,N-dimethyltetradecylamine	Sigma Aldrich	≥ 95 %
N,N-dimethylhexadecylamine	Sigma Aldrich	≥ 95 %
N,N-dimethyloctadecylamine	Sigma Aldrich	≥ 95 %
1,4-dibromobutane	Alfa Aesar	99 %
1,5-dibromopentane	Alfa Aesar	98 %
1,6-dibromohexane	Alfa Aesar	96 %
1,7-dibromoheptane	Acros Organics	97 %
1,8-dibromooctane	Acros Organics	98 %
1,9-dibromononane	Acros Organics	97 %
1,10-dibromodecane	Acros Organics	97 %
Cetyltrimethylammoniumbromide (CTAB)	Alfa Aesar	98 %
n-heptane	Sigma Aldrich	99 %
1-hexanol	Alfa Aesar	99 %
THF	Chemetall	99.9 %
Diethylether	VWR	99.7 %
2-propanol	Sigma Aldrich	99.5 %
Dioxan	Sigma Aldrich	≥ 99 %

Ehtylacetate	VWR	99 %
Methanol	Sigma Aldrich	99.9 %
Ethanol	Bundesmonopolverwaltung für Brandwein	99.8 %
Acetone	Sigma Aldrich	≥ 99 %

Table S2: *d*-spacings of the first observable stacking reflections in the powder XRD measurements of all as-made MIF materials synthesized with 16-10-16 gemini surfactants, as a function of the solvent used.

Solvent	IM MIF	MeIM MIF
Microemulsion (n-heptane/1-hexanol)	33.2	33.0
THF	33.5	32.8
Diethylether	34.0	32.7
2-Propanol	33.1	32.6
Dioxan	33.4	32.4
Ethylacetate	34.0	32.4
Ethanol	33.4	32.4
Methanol	33.4	32.4
Acetone	32.9	32.2

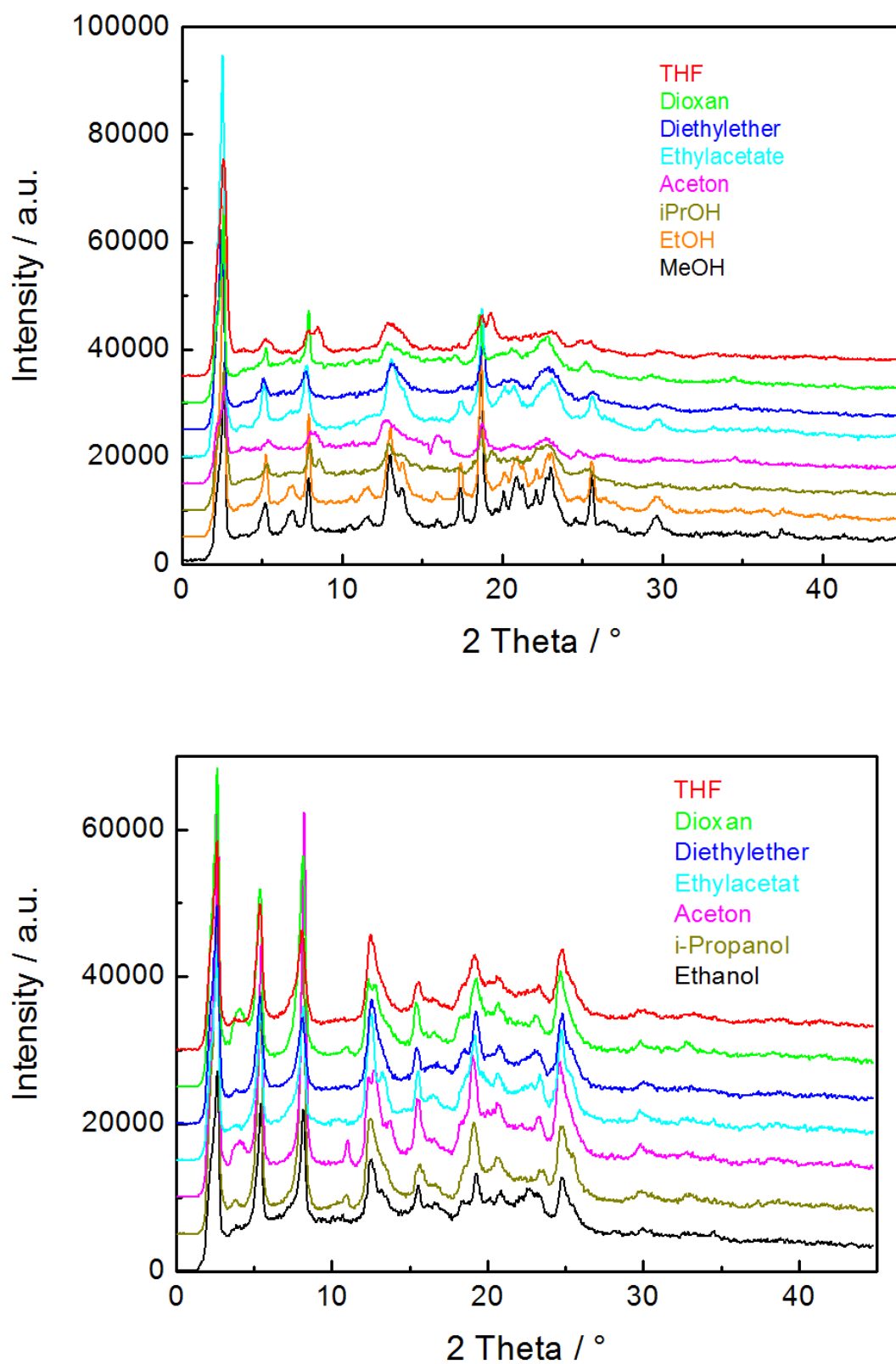


Figure S1: Powder XRD patterns obtained for IM MIF (top) and MeIM MIF (bottom) synthesized with 16-10-16 gemini surfactants in various solvents.

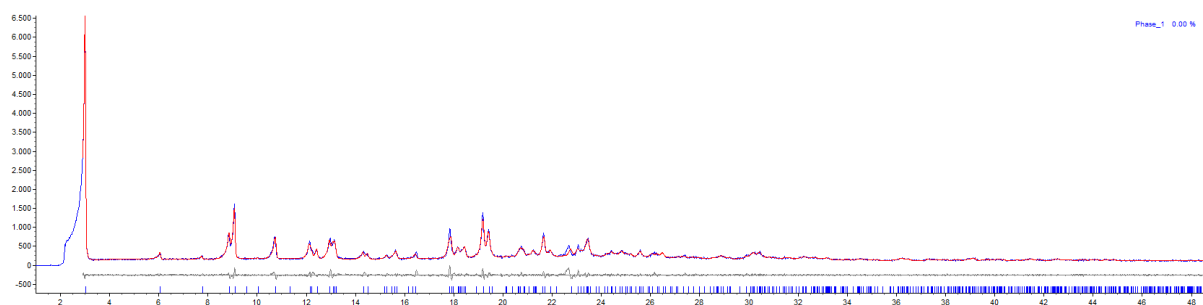


Figure S2: Pawley fit for IM MIF ($C2$, $a = 11.5829 \text{ \AA}$, $b = 58.253 \text{ \AA}$, $c = 9.2415 \text{ \AA}$, $\theta = 88.94^\circ$, $wR = 7.57$, $GoF = 1.286$) synthesized with 16-8-16 gemini surfactants.

Table S3: Percent elemental compositions from bulk elemental analyses of various MIF compounds and comparisons with the expected values for stoichiometric compositions of the hybrid materials with 1 zinc : 1 IM/MeIM : 2 bromine : 0.5 surfactant.

14-6-14, Im, MIF	Zn	C	N	H	Br
Measured values	8.0	55.9	6.9	9.9	19.3
Expected values	7.9	56.5	6.8	9.6	19.3
Difference	0.1	-0.6	0.1	0.3	0.0

16-10-16, Im, MIF	Zn	C	N	H	Br
Measured values	6.6	60.4	5.8	10.3	16.7
Expected values	7.0	59.9	6.0	10.2	17.0
Difference	-0.4	0.5	-0.2	0.1	-0.3

18-10-18, Im MIF	Zn	C	N	H	Br
Measured values	6.7	61.6	5.6	9.9	16.2
Expected values	6.6	61.4	5.6	10.4	16.0
Difference	0.1	0.2	0.0	-0.5	0.2

14-6-14, 2MIm, MIF	Zn	C	N	H	Br
Measured values	7.5	57.3	6.5	9.6	18.8
Expected values	7.8	57.0	6.6	9.7	19.0
Difference	-0.3	0.3	-0.1	-0.1	-0.2

16-10-16, 2MIm, MIF	Zn	C	N	H	Br
Measured values	6.9	59.9	6.0	10.1	17.0
Expected values	6.9	60.4	5.9	10.2	16.7
Difference	0.0	-0.5	0.1	-0.1	0.3

18-10-18, 2MIm MIF	Zn	C	N	H	Br
Measured values	6.5	61.7	5.5	10.6	15.7
Expected values	6.5	61.7	5.5	10.5	15.8
Difference	0.0	0.0	0.0	0.1	-0.1

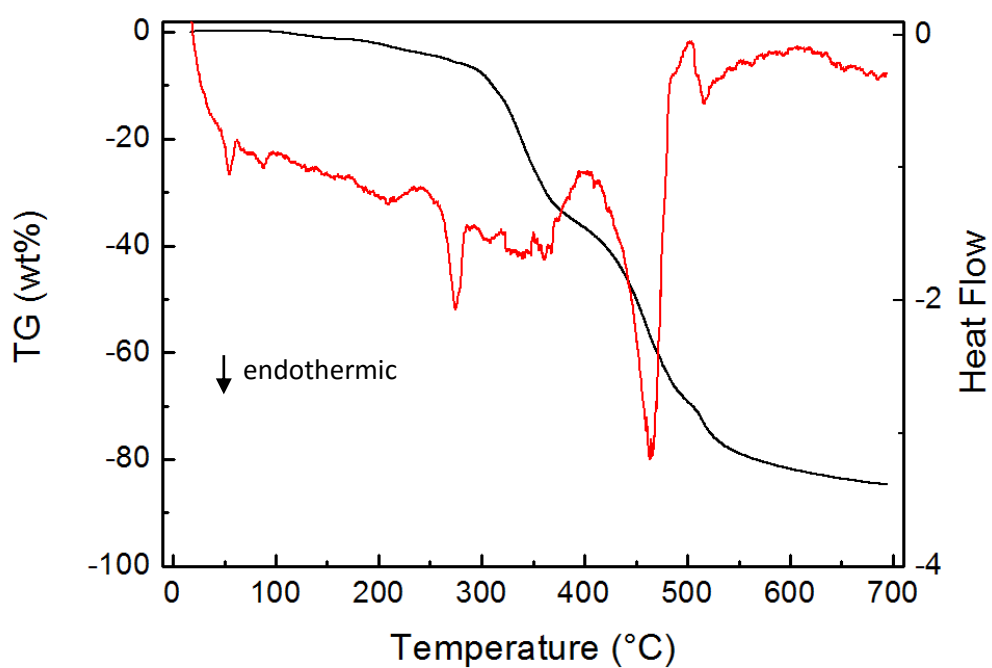
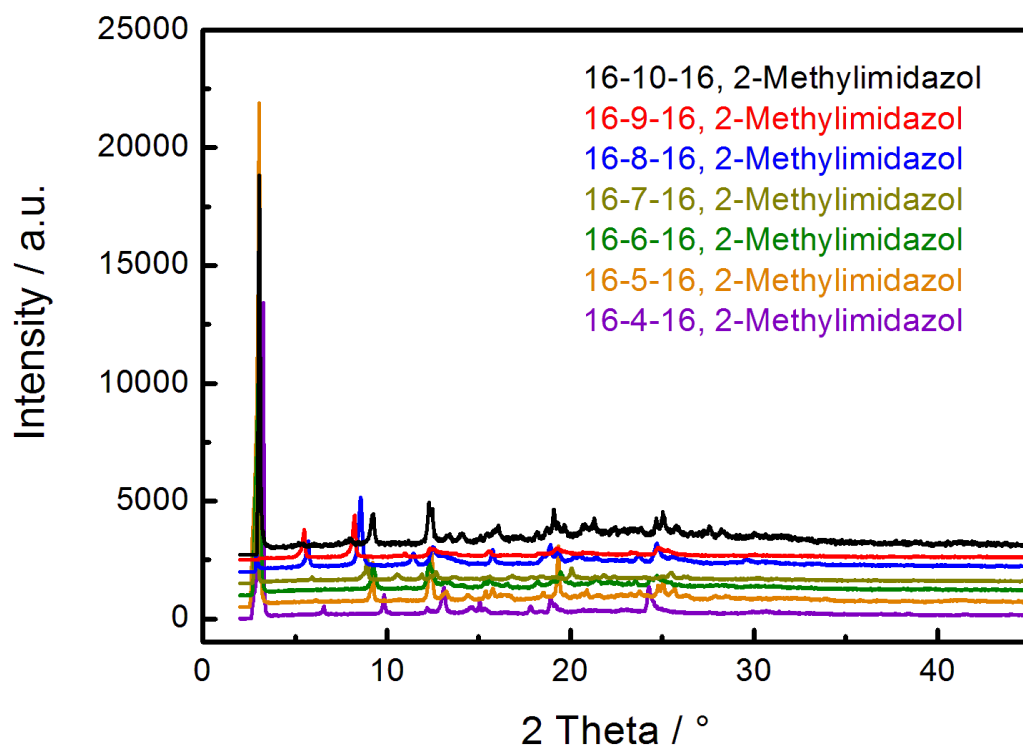
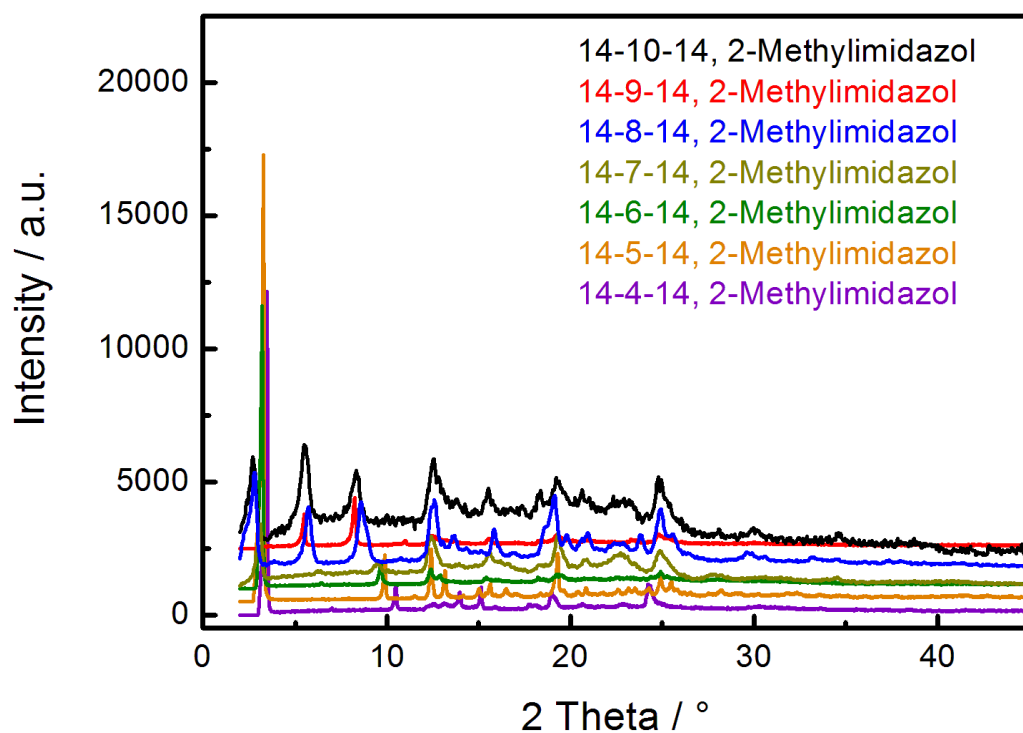
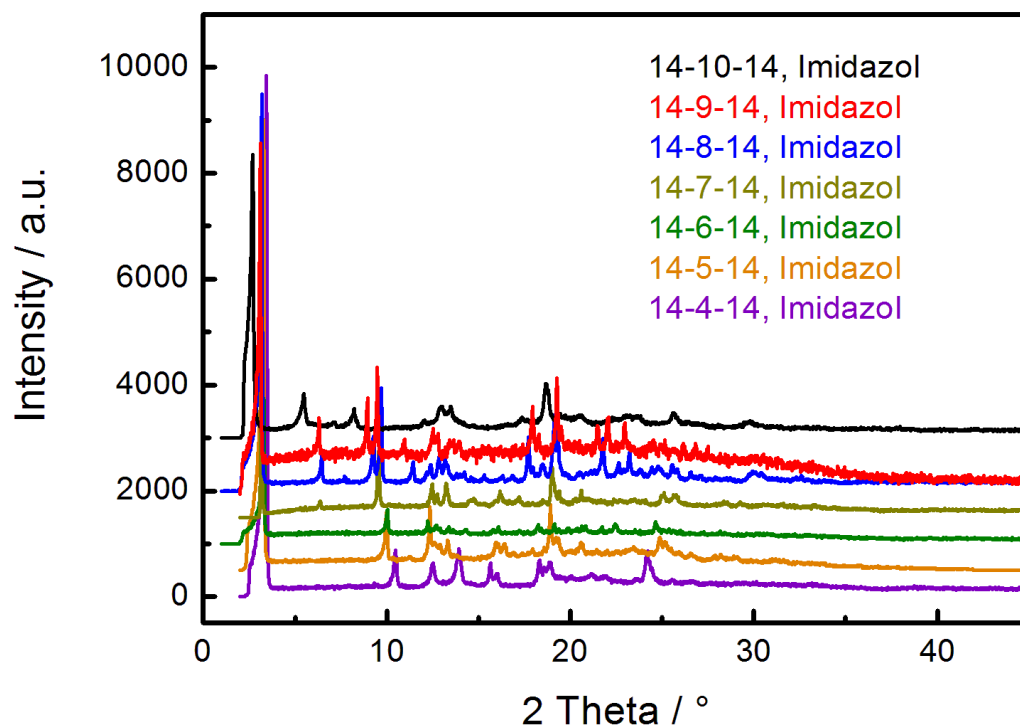
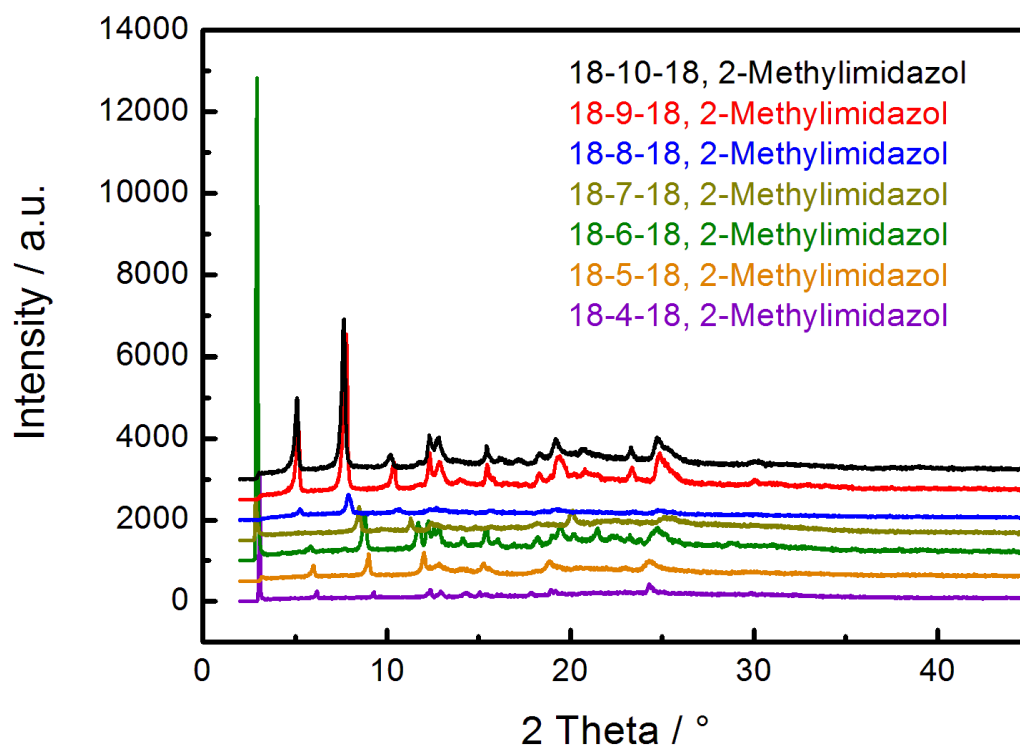


Figure S3: DTA/TG curves of 16-10-16 MeIm bridged MIF, suggesting thermal stability up to 300°C. The endothermic heat flow below 300 °C likely reflects thermally activated rearrangements and quasi-melting of the surfactants in the hybrid material.





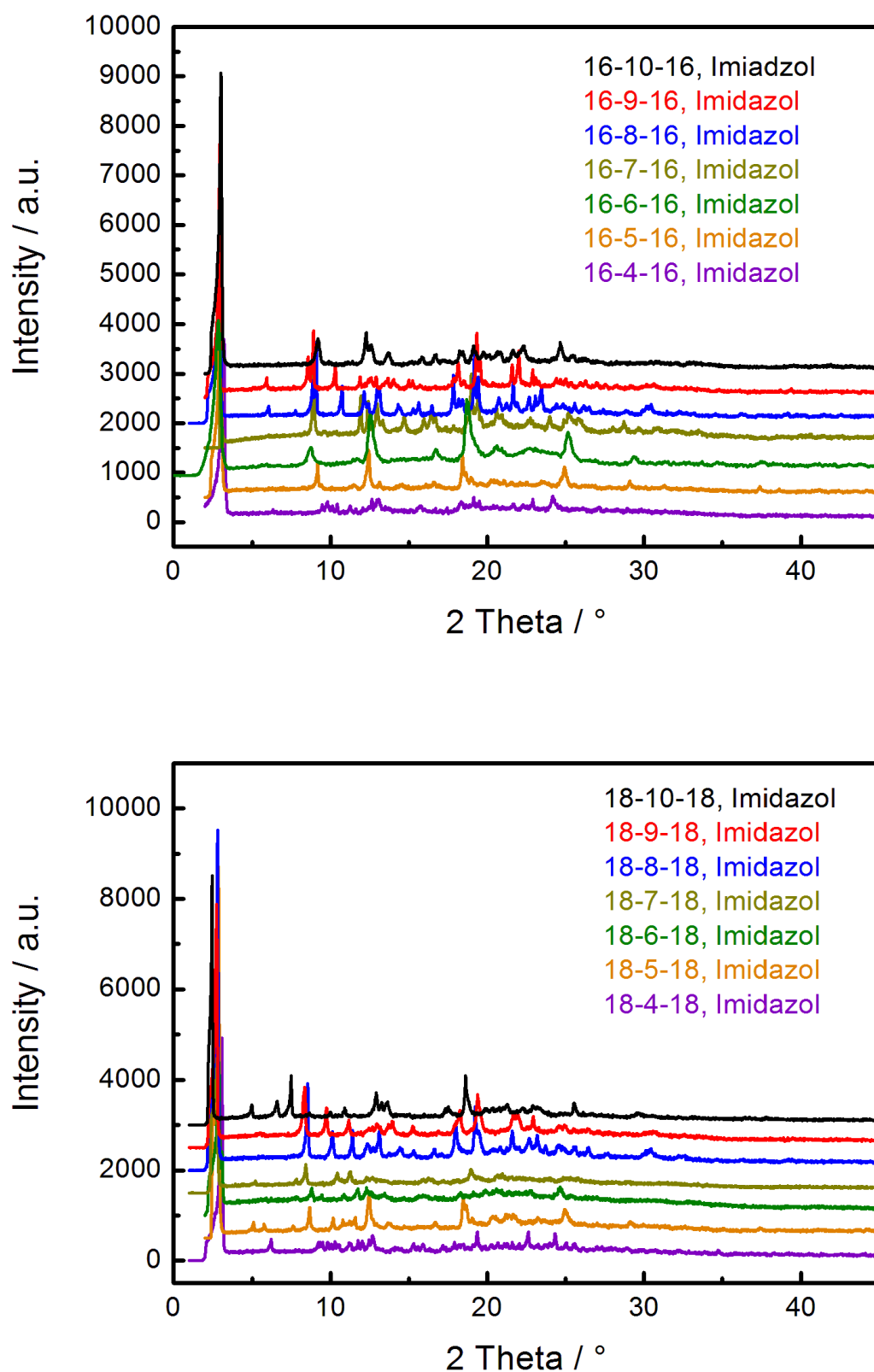


Figure S4: Powder XRD patterns of MeIM- and IM-bridged MIFs synthesized with different gemini surfactants. From top to bottom: 14-*m*-14 MeIM, 16-*m*-16 MeIM, 18-*m*-18 MeIM, 14-*m*-14 IM, 16-*m*-16 IM, 18-*m*-18 IM.

Table S4: *d*-spacings of the first observable stacking reflections in the powder XRD measurements of all as-synthesized MIF materials.

Tail Length	Spacer Length	IM MIF	MeIM MIF
14	4	25.4	25.3
14	5	26.8	26.9
14	6	26.6	27.5
14	7	27.6	28.1
14	8	27.5	29.5
14	9	28.2	30.4
14	10	32.6	31

Tail Length	Spacer Length	IM MIF	MeIM MIF
16	4	28.1	27.0
16	5	29.1	28.8
16	6	28.9	28.7
16	7	29.5	29.7
16	8	29.4	31.0
16	9	30.0	32.3
16	10	33.2	33.0

Tail Length	Spacer Length	IM MIF	MeIM MIF
18	4	28.6	28.6
18	5	30.7	29.4
18	6	30.4	30.2
18	7	31.8	31.2
18	8	31.4	33.6
18	9	32.1	34.1
18	10	35.7	34.7

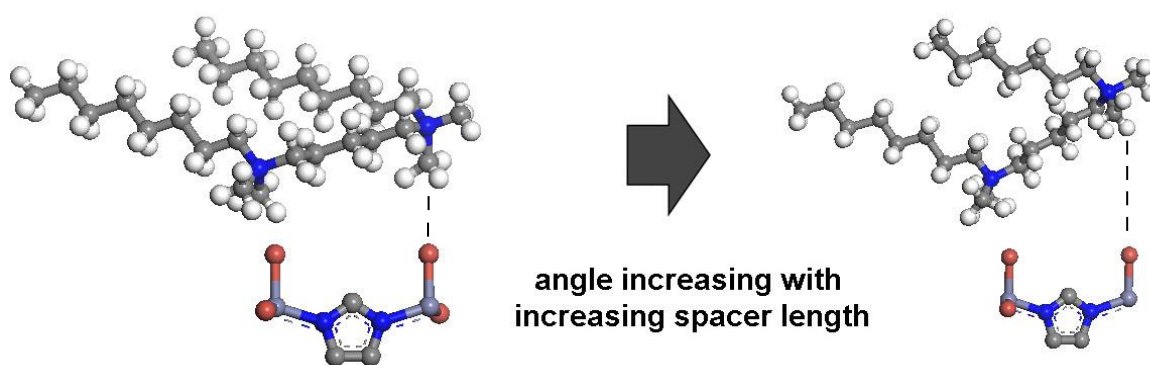


Figure S5: Proposed charge compensation by geometric rearrangement of the surfactant headgroups to comply with the charge density of the inorganic slabs. The angle between surfactant spacer and zinc imidazolate chains increases with growing spacer length. To simplify this image, only a single $[\text{ZnIMBr}_2]^-$ unit is shown and the carbon tail-groups (m) of the surfactants have been shortened.

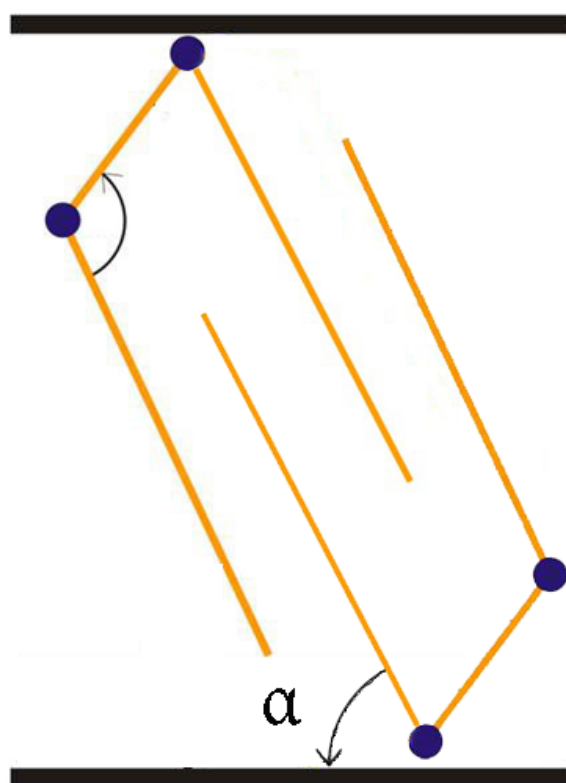


Figure S6: Schematic diagram depicting the proposed tilted interdigitated, anti-parallel arrangement of the surfactant in the as-synthesized MIF materials, showing the angle α between the tail groups and the zinc imidazolate layers.

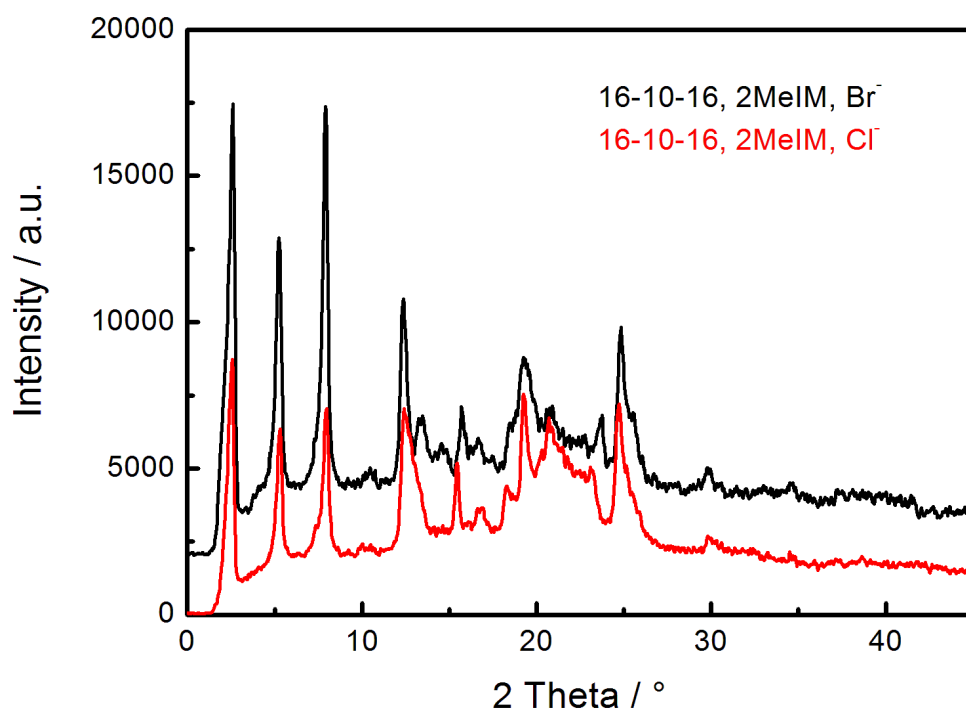


Figure S7: Powder XRD patterns of MeIM-bridged MIFs synthesized in the presence of different halogenide ions.

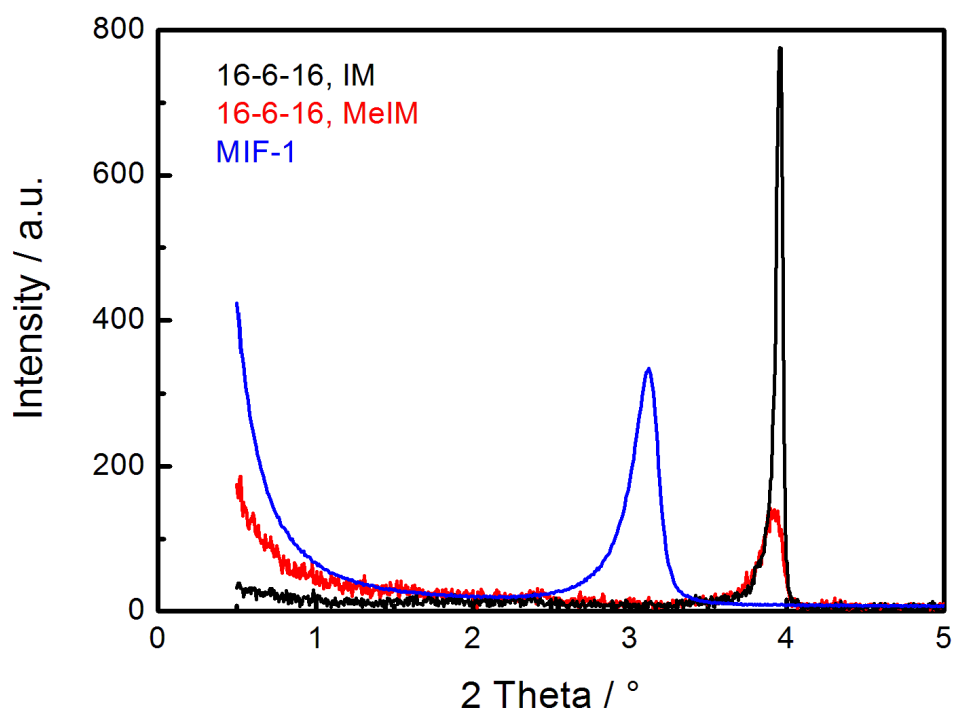


Figure S8: Small-angle XRD patterns of gemini-directed materials and MIF-1 showing the first reflections corresponding to the lamellar stacking of the as-synthesized materials.

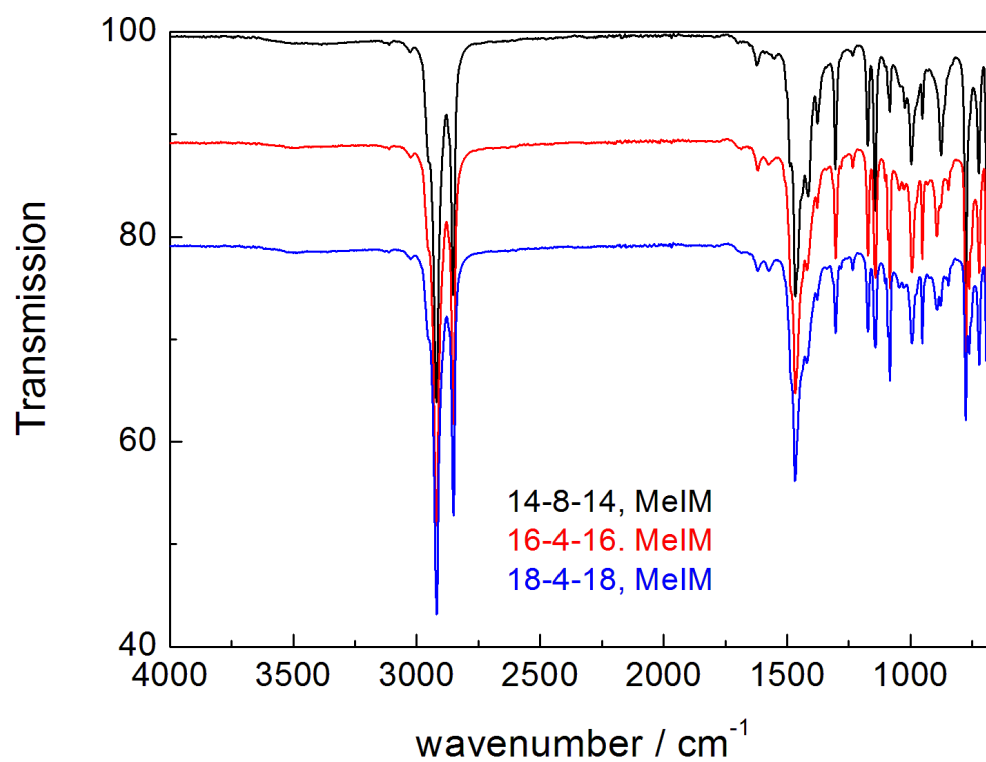
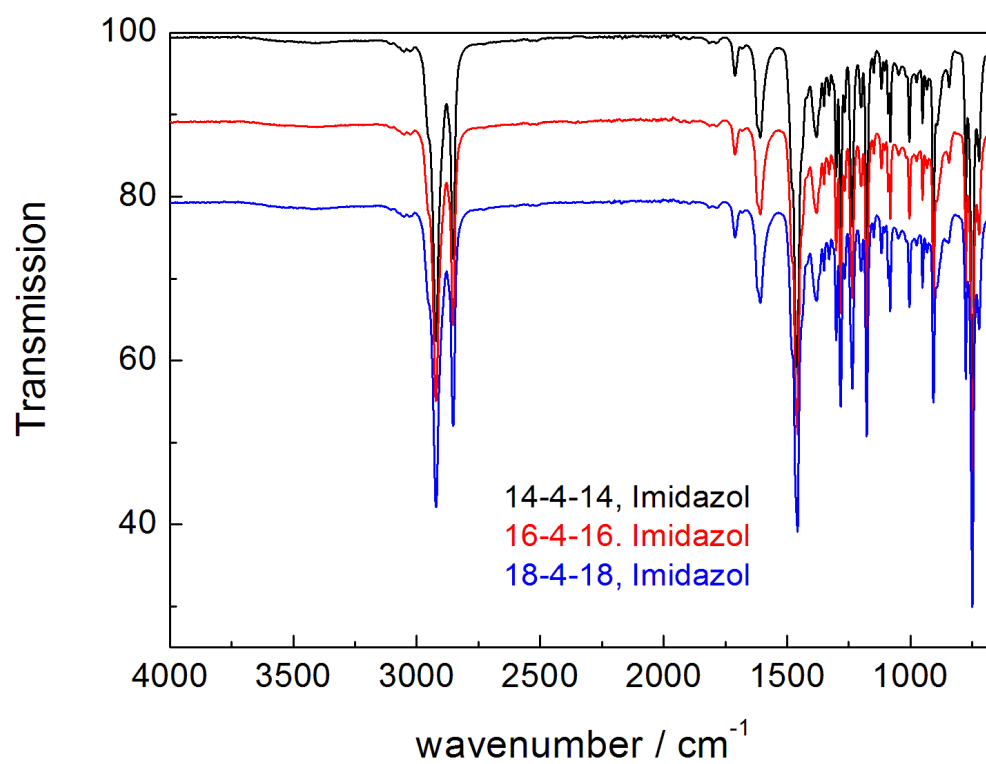


Figure S9: Infrared spectra showcasing the similarity between the MeIM/IM MIFs templated by different gemini-surfactants.

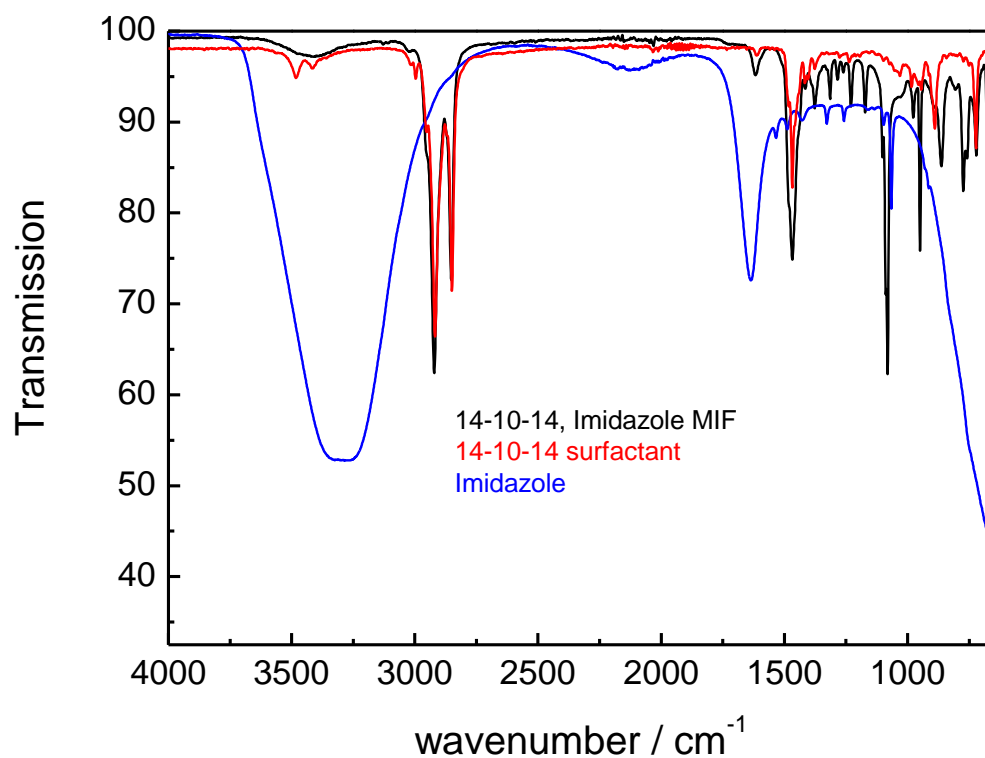


Figure S10: Infrared spectra showcasing the similarities and purity of the synthesized MIF materials in comparison to the starting materials used.

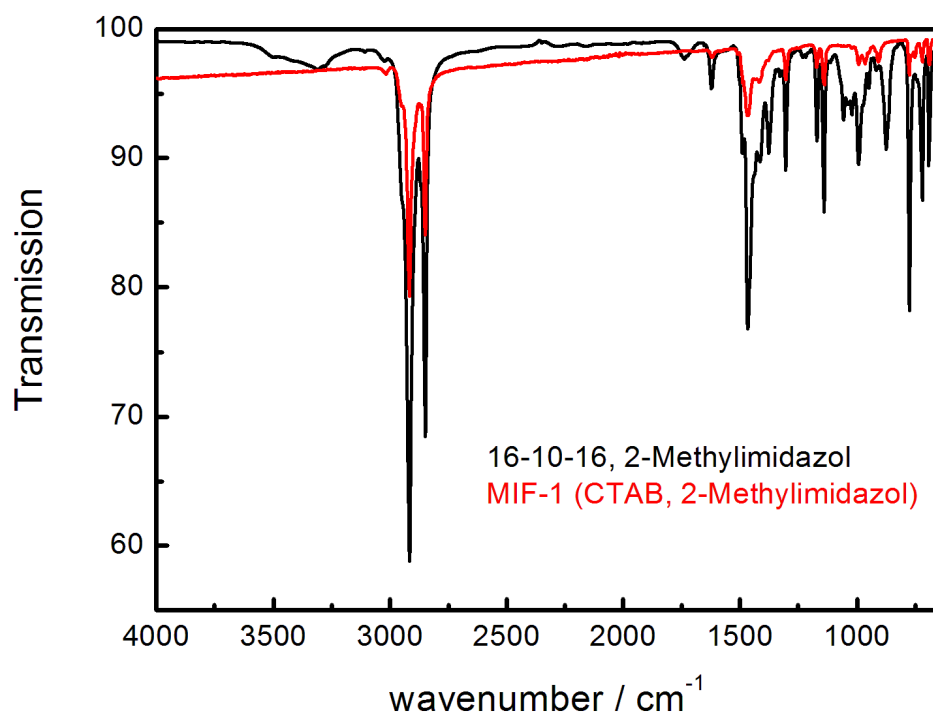


Figure S11. Infrared spectra showcasing the similarities between prototypic MIF-1 (CTAB/MeIM) and the MIF obtained from synthesis with 16-10-16 gemini surfactant.

9.2 CHAPTER 5 - SUPPORTING INFORMATION

Tabelle S1: Experimental parameter for the solid-state ^{13}C and ^{15}N NMR measurements

^{13}C	Rotational frequency [kHz]	Recycle delay [sec]	Contact time [μsec]	Number of scans
Zn[BeIM]OPr	10	4.0	3000	256
Zn[BeIM]OBut	10	8.0	3000	1752
Zn[BeIM]OBut (solid state)	10	4.0	3000	256
Zn[NO ₂ -BeIM]OAc	10	2.0	3000	256
Zn[NH ₂ -BeIM]OAc	10	8.0	3000	1752
Zn[NH ₂ -BeIM]OAc (functionalized)	10	4.0	3000	12488

^{15}N	Rotational frequency [kHz]	Recycle delay [sec]	Contact time [μsec]	Number of scans
Zn[BeIM]OPr	10	8.0	3000	20700
Zn[BeIM]OBut	10	8.0	3000	20328
Zn[BeIM]OBut (solid state)	10	8.0	3000	14200
Zn[NO ₂ -BeIM]OAc	10	2.0	3000	20700
Zn[NH ₂ -BeIM]OAc	10	8.0	3000	20700
Mixed linker; x=0.25	10	1.0	3000	19200
Mixed linker; x=0.5	10	2.0	3000	31616

9.3 CHAPTER 6 - SUPPORTING INFORMATION

Tabelle S1: Experimental parameter for the solid-state ^{13}C and ^{15}N NMR measurements

	Rotational frequency [kHz]	Recycle delay [sec]	Contact time [μsec]	Number of scans
^{13}C	10	1.0	3000	548
^{15}N	10	1.0	3000	15236

9.4 CHAPTER 7 - SUPPORTING INFORMATION

9.4.1 EXPERIMENTAL PROCEDURES

Chemicals. All chemicals and solvents were purchased from commercial suppliers and used without further purification: Hexadecyltrimethylammonium bromide (Alfa Aesar, 98%), cobalt(II)acetate tetrahydrate (Acros Organics, 98+%), imidazole (Alfa Aesar, 99%), n-heptane (Grüssing, 99%), 1-hexanol (Sigma Aldrich, 98%), iso-propanol (Sigma Aldrich, 99%). Deionized water was used throughout all procedures.

Co^{II}₃Co^{III}₂(Im)₁₂. In a typical synthesis, 948 mg (2.6 mmol) hexadecyltrimethylammonium bromide (CTAB) were added to a mixture of 22 mL n-heptane and 2.3 mL 1-hexanol. To the turbid mixture, 1675 µL aqueous imidazole solution (1.8M) were added and the mixture was stirred until a clear solution was formed. To this solution, 150 mg (0.603 mmol) cobaltacetate tetrahydrate were added and the resulting mixture was refluxed at 105°C for 2 hours. The resulting precipitate was removed from the solution by filtration, washed with iso-propanol to remove unreacted species and dried at room temperature.

Characterization. X-ray diffraction (XRD) analysis, inductively coupled plasma atomic emission spectroscopy (ICP-AES), elemental analysis, transmission electron microscopy, differential thermal analysis coupled with thermogravimetric measurements (DTA/TG), magnetic measurements, photoelectron spectroscopy (XPS), infrared spectroscopy (IR) and UV/VIS spectroscopy were used to identify the material.

XRD data of powders were collected using a STOE Stadi P (STOE&Cie GmbH, Darmstadt) device operating in Guinier geometry with an imaging plate as detector.

ICP-AES was done using a VISTA RL CCD and ICP-AES analyzer system (Agilent Technologies, Waldbronn). An Elementar vario EL (Elementar Analysensysteme, Hanau) was employed for elemental analysis.

TEM measurements were performed on a JEOL JSM-6500F (Jeol Ltd., Tokyo) with accelerating voltages in the range from 2 to 25 kV.

DTA/TG were performed using a Netzsch STA 409C (Netzsch GmbH, Selb).

Magnetic measurements were performed in the temperature range between 5 and 350 K using a MPMS 7.0 (Quantum Design, San Diego). X-ray photoelectron spectroscopy (XPS) was carried out on an Axis Ultra X-ray photoelectron spectrometer (Kratos Analytical, Manchester).

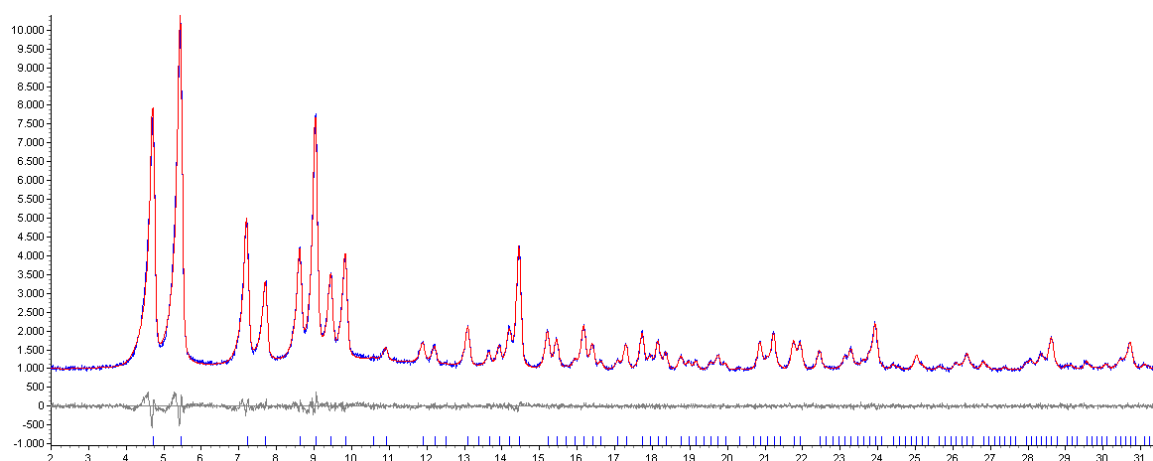
Infrared spectra were recorded using a Perkin Elmer Spectrum BXII featuring an attenuated total reflectance unit (Perkin Elmer Inc., Waltham).

UV/VIS spectra were recorded using a Varian Cary 500 Scan UV-Vis-NIR spectrometer (Agilent Technologies, Waldbronn).

Electrochemical characterization. The material was deposited onto the working electrode, either fluorine-doped tin oxide coated glass (FTO, exposed diameter of 18 mm, Aldrich, $7\ \Omega\ \text{sq}^{-1}$) or glassy carbon electrode (GCE, 3 mm, ALS Japan), using the drop-cast method. For the FTO, a loading of 1 mg was achieved by repeated deposition of 100 μL aliquots of a $1\ \text{mg mL}^{-1}$ aqueous suspension, followed by drying in air. For the GCE, 5 μL aliquot of the same suspension was drop-cast onto the electro-active area of the electrode. For the non-aqueous experiments, a platinum foil and a platinum wire were used as the counter and quasi-reference electrode, respectively. The electrolyte was an acetonitrile (dried over 4 Å molecular sieve) solution of tetra-*n*-butylammonium hexafluorophosphate (0.1 M). Potential was referenced to the ferrocene redox couple.

Cyclic voltammetry was performed on a Princeton Applied Research VersaSTAT MC scanning from 3 V to -3 V at $10\ \text{mV s}^{-1}$. In aqueous conditions, a saturated calomel electrode (SCE, +0.244 V vs standard hydrogen electrode, SHE) was used as the reference electrode. Cyclic voltammetry was conducted in NaOH solution (1 M) scanning from -0.2 to 1 V vs SCE at $50\ \text{mV s}^{-1}$ repeatedly until the voltammogram was reproducible, then at $1\ \text{mV s}^{-1}$ (for clarity, only this voltammogram was plotted). Electrochemical stability and faradaic efficiency experiments were performed in chronoamperometry/chronocoulometry mode using NaOH solution (1 M) and the oxygen in the cell headspace was quantified by gas chromatography (Thermo Scientific TRACE GC Ultra) equipped with a TCD detector using argon as the carrier gas. The working electrode was held at 800 mV vs SCE for 60 min, and the headspace was analyzed before and after the applied potential. The leak rate of the cell was also taken into account in the estimation of the faradaic efficiency, which assumes a 4-electron process under alkaline conditions: $4\text{OH}^- \rightarrow \text{O}_2 + 2\text{H}_2\text{O} + 4e^-$. The spent catalyst was recovered by scrapping off the FTO, washed with water, then dried at 60 °C in a vacuum oven prior to characterization. Reaction order with respect to $[\text{OH}]^-$ was determined using the chronoamperometry method employing concentrations of 1.0, 0.49, 0.23 and 0.010 M for the NaOH solutions; ionic strengths of these 4 solutions were kept at 1.0 M using Na_2SO_4 . The working electrode was held at a potential of 520 mV vs SCE, which is the midpoint of the non-diffusion-limited linear region of the Tafel plot, and the steady current was used for the reaction order plot.

9.4.2 STRUCTURE ELUCIDATION

**Figure S1** Rietveld refinement of the measured PXRD data.**Table S1:** Crystal data obtained from the analysis of $\text{Co}^{\text{II}}_3\text{Co}^{\text{III}}_2(\text{Im})_{12}$.

Empirical formula	$\text{Co}_5\text{C}_{36}\text{H}_{36}\text{N}_{24}$
Formula weight	1099.51
Crystal system	Cubic
Space group	$Ia-3d$
$a = b = c$ (Å)	21.0825
$\alpha = \beta = \gamma$	90
V (Å ³)	9370.56
Z	8
GOF	1.163
R_{exp}	2.995
R_{p}	2.514
R_{wp}	3.186

Table S2: Atom positions found for $\text{Co}^{\text{II}}_3\text{Co}^{\text{III}}_2(\text{Im})_{12}$.

Atom	Wyck.	x	y	z
N1	96h	-0.176 (1)	0.070 (1)	-0.033 (1)
N2	96h	-0.088 (1)	0.022 (1)	-0.032 (1)
C1	96h	-0.124 (1)	0.062 (1)	0.008 (1)
C2	96h	-0.115 (1)	0.012 (1)	-0.092 (1)
C3	96h	-0.169 (1)	0.040 (1)	-0.092 (1)
Co1	16a	0	0	0
Co2	24c	0	-0.25	0.125

Angels and Distances

$$\text{Co1} - \text{N1} = 1.8425 \text{ \AA}$$

$$\text{Co2} - \text{N2} = 1.9015 \text{ \AA}$$

$$\text{N1} - \text{C2} = 1.5281 \text{ \AA}$$

$$\text{N1} - \text{C1} = 1.5284 \text{ \AA}$$

$$\text{N2} - \text{C3} = 1.5281 \text{ \AA}$$

$$\text{N2} - \text{C1} = 1.5282 \text{ \AA}$$

$$\text{C2} - \text{C3} = 1.5286 \text{ \AA}$$

$$\text{C1} - \text{H1} = 1.0800 \text{ \AA}$$

$$\text{C2} - \text{H2} = 1.0800 \text{ \AA}$$

$$\text{C3} - \text{H3} = 1.0800 \text{ \AA}$$

$$\text{N1} - \text{Co1} - \text{N1} = 85.72^\circ / 94.28^\circ / 180^\circ$$

$$\text{N2} - \text{Co2} - \text{N2} = 110.29^\circ / 107.85^\circ$$

$$\text{C2} - \text{N1} - \text{C1} = 108.00^\circ$$

$$\text{C2} - \text{N1} - \text{Co1} = 119.46^\circ$$

$$\text{C1} - \text{N1} - \text{Co1} = 132.32^\circ$$

$$\text{C3} - \text{N1} - \text{C1} = 108.00^\circ$$

$$\text{C3} - \text{N2} - \text{Co2} = 141.31^\circ$$

$$\text{C1} - \text{N2} - \text{Co2} = 110.45^\circ$$

$$\text{N2} - \text{C1} - \text{H1} = 125.99^\circ$$

$$\text{N1} - \text{C1} - \text{H1} = 126.00^\circ$$

$$\text{N1} - \text{C1} - \text{N2} = 108.01^\circ$$

$$\text{N1} - \text{C2} - \text{C3} = 108.00^\circ$$

$$\text{N1} - \text{C2} - \text{H2} = 126.00^\circ$$

$$\text{H2} - \text{C2} - \text{C3} = 126.00^\circ$$

$$\text{C2} - \text{C3} - \text{N2} = 108.00^\circ$$

$$\text{C2} - \text{C3} - \text{H3} = 125.98^\circ$$

$$\text{H3} - \text{C3} - \text{N2} = 126.02^\circ$$

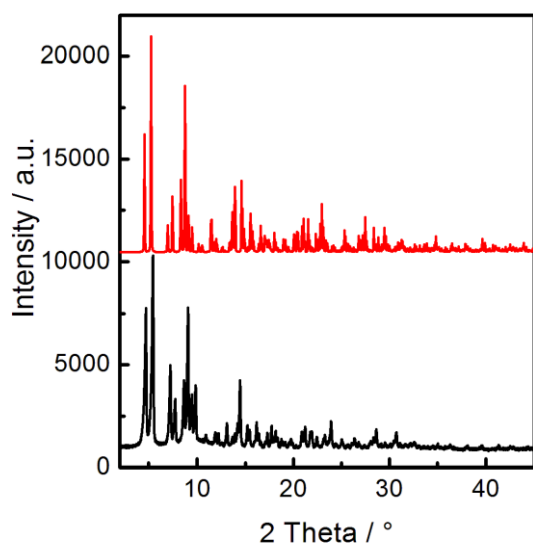


Figure S2 Comparison of the experimental pattern of $\text{Co}^{\text{II}}_3\text{Co}^{\text{III}}_2(\text{Im})_{12}$ (black) and the simulated pattern of ZIF-5 ($\text{Zn}_3\text{In}_2\text{Im}_{12}$) showcasing good agreement between the metrics of the two materials.

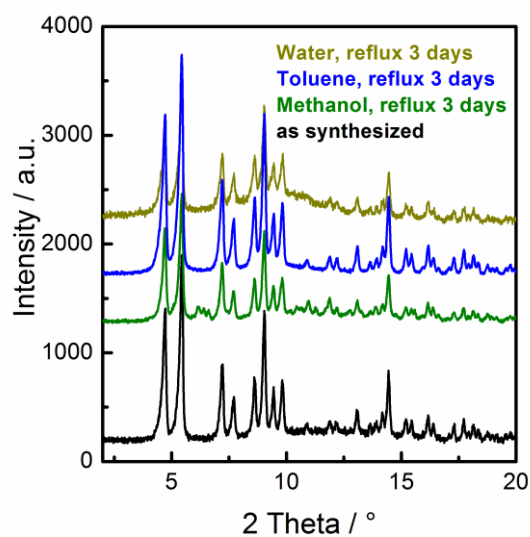


Figure S3: Powder XRD patterns of $\text{Co}^{\text{II}}_3\text{Co}^{\text{III}}_2(\text{Im})_{12}$ before (black) and after 3 days refluxing in methanol (green), toluene (blue) or water (yellow).

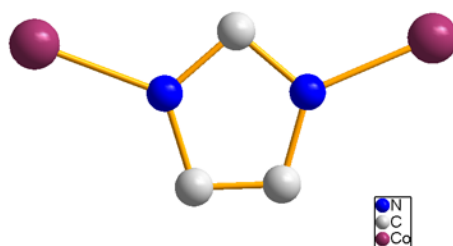


Figure S4: Asymmetric unit with isotropic temperature factors drawn at the 50 percent probability level.

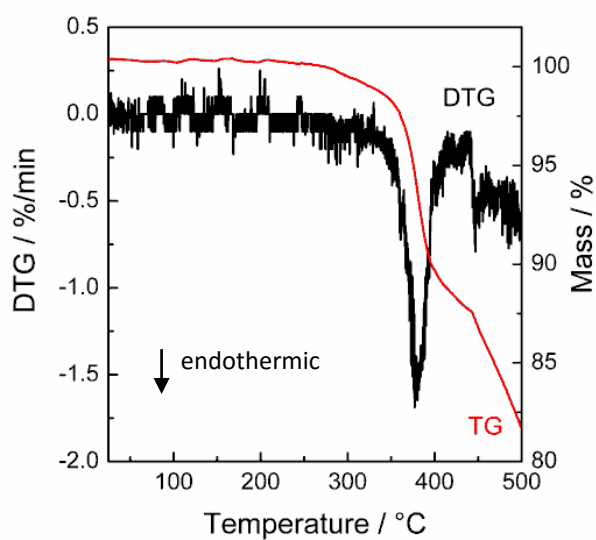


Figure S5 DTA/TG measurement of the sample showing the thermal stability up to 320 °C without phase transitions below the decomposition temperature.

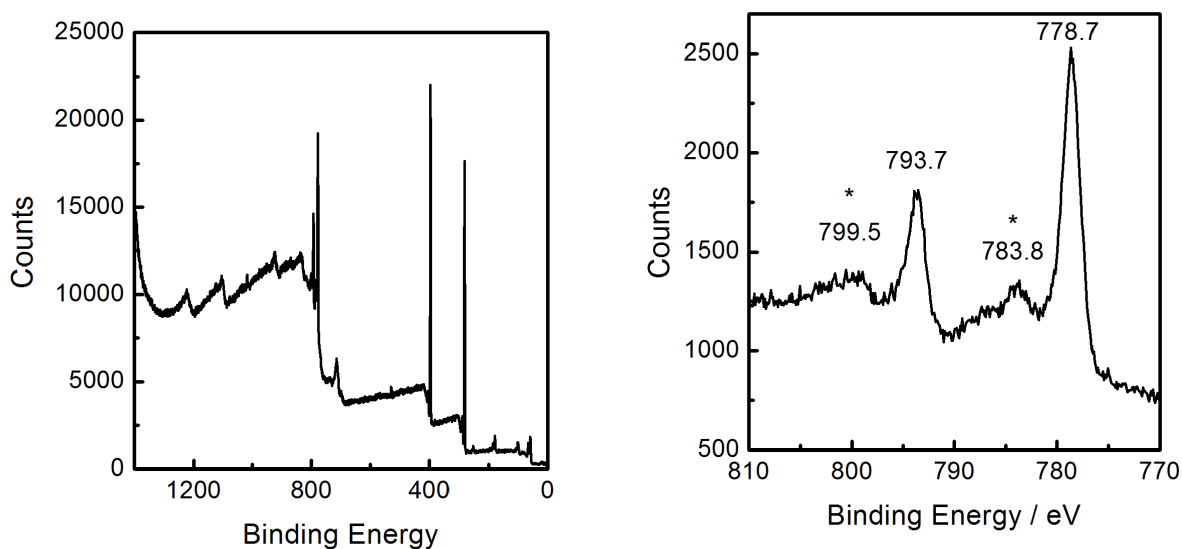


Figure S6 Overview XPS measurement (left) and zoom into the binding energies for Cobalt 2p_{1/2} at 793.7 eV and 2p_{3/2} at 778.7 eV (right). Satellites are marked with asterisks.

Electrochemical measurements

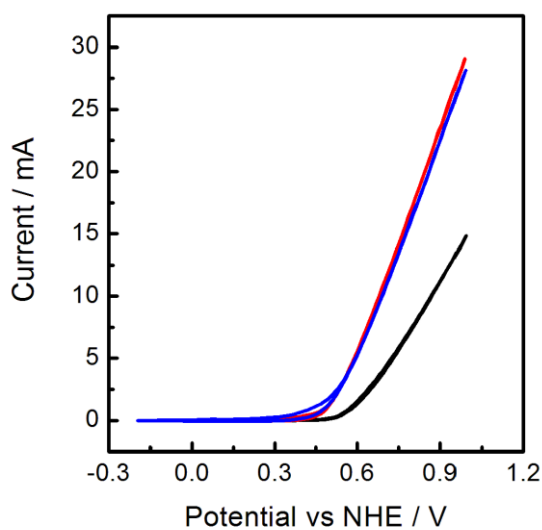


Figure S7: Cyclic voltammograms of $\text{Co}^{\text{II}}_3\text{Co}^{\text{III}}_2(\text{Im})_{12}$ before (black) and after calcination of the material in air (red) and argon (blue) on FTO in NaOH solution (1 M) at a scan rate of 1 mV s^{-1} . Note that leaking of Co into the solution is only observed for the calcined samples, but not for the pristine MOF.

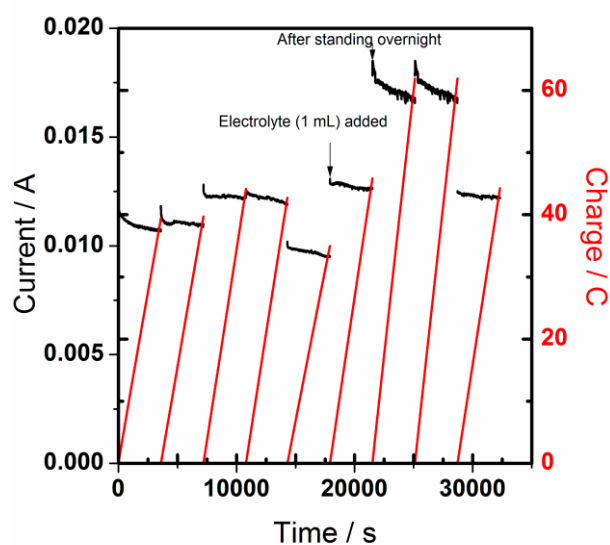


Figure S8: Determination of electrochemical stability and faradaic efficiency of the $\text{Co}^{\text{II}}_3\text{Co}^{\text{III}}_2(\text{Im})_{12}$ framework in chronoamperometry/chronocoulometry mode, showing the current in black and the charge passed in red.

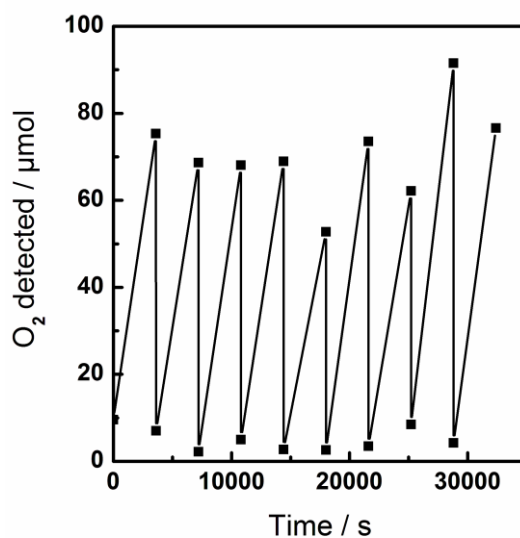


Figure S9: Detection of oxygen in the headspace of the electrochemical cell in the chronoamperometry/chronocoulometry experiment of Figure S6. Note that oxygen quantification *via* gas chromatography is hampered by using Ar as carrier gas; in addition, oxygen dissolved in the solution is not accounted for.

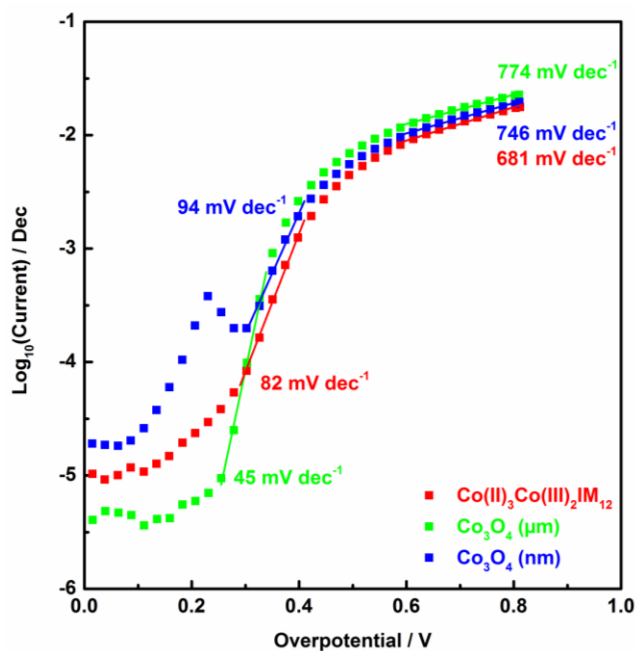


Figure S10: Tafel plots of the $\text{Co}^{\text{II}}_3\text{Co}^{\text{III}}_2(\text{Im})_{12}$ framework in NaOH (1 M), compared with μm - and nm -sized Co_3O_4 powders. Tafel slopes obtained by linear fitting (blue, red and green lines) in the low overpotential region were used for analysis of the reaction mechanism (see text); Tafel slopes in the high overpotential region (> 0.6 V) were large and attributable to diffusion limitations.^[352]

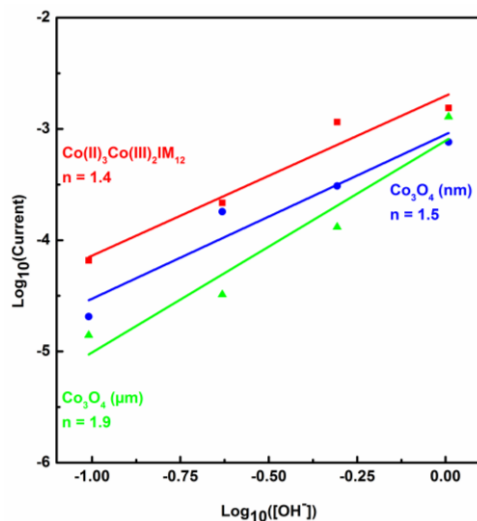


Figure S11: Reaction orders (n , the slope of the linear fit) with respect to OH^- of the $\text{Co}^{\text{II}}_3\text{Co}^{\text{III}}_2(\text{Im})_{12}$ framework and the μm - and nm -sized Co_3O_4 powders.

Scheme S1: Literature reaction mechanism of oxygen evolution, where S denotes an active site on the electrocatalyst (i.e. Co^{IV}).

1)	$S + \text{OH}^- \rightarrow S\text{-OH} + e^-$
2)	$S\text{-OH} + \text{OH}^- \rightarrow S\text{-H}_2\text{O}_2 + e^-$
3)	$2S\text{-H}_2\text{O}_2 \rightarrow 2S + 2\text{H}_2\text{O} + \text{O}_2 \uparrow$

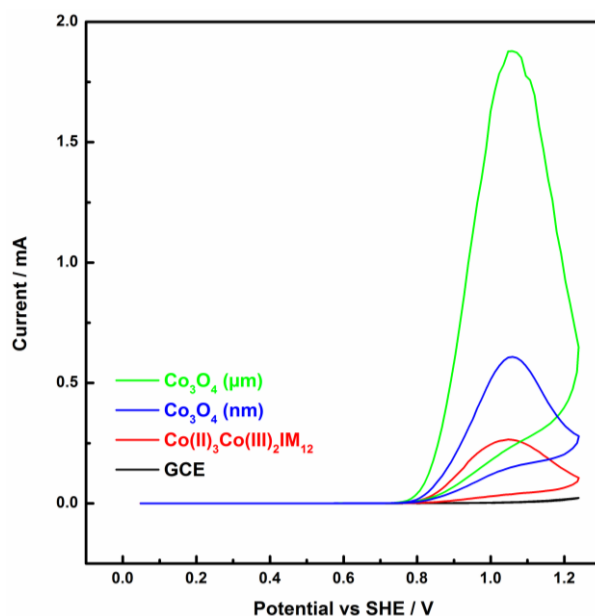


Figure S12: Cyclic voltammograms of the $\text{Co}^{\text{II}}_3\text{Co}^{\text{III}}_2(\text{Im})_{12}$ framework, compared to the μm - and nm-sized Co_3O_4 powders, using GCE as the substrate in NaOH solution (1 M).

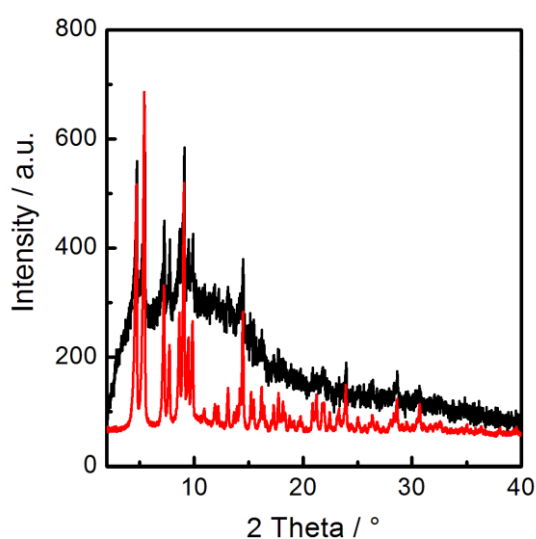


Figure S13: PXRD measurement of the sample before (red) and after chronoamperometry measurement (black) proving the stability of the material under the electrochemical conditions. The low signal to noise ratio in the measurement after chronoamperometry is due to the small amount of sample used for chronoamperometry and the subsequent XRD measurement.

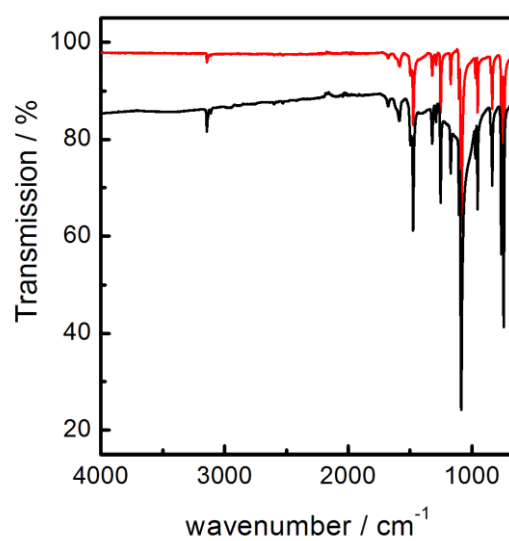


Figure S14: IR spectra of the as-prepared sample (red) and after chronoamperometry measurement (black), proving the stability of the material under the electrochemical conditions.

10 REFERENCES

- [1] D. C. Lacy, C. C. L. McCrory, J. C. Peters, *Inorg. Chem.* **2014**, *53*, 4980-4988.
- [2] J.-R. Li, R. J. Kuppler, H.-C. Zhou, *Chem. Soc. Rev.* **2009**, *38*, 1477-1504.
- [3] C.-Y. Huang, M. Song, Z.-Y. Gu, H.-F. Wang, X.-P. Yan, *Environ. Sci. Technol.* **2011**, *45*, 4490-4496.
- [4] S. Cobo, J. Heidkamp, P.-A. Jacques, J. Fize, V. Fourmond, L. Guetaz, B. Jousselme, V. Ivanova, H. Dau, S. Palacin, M. Fontecave, V. Artero, *Nat. Mater.* **2012**, *11*, 802-807.
- [5] Y. Y. Li, F. d. r. Cunin, J. R. Link, T. Gao, R. E. Betts, S. H. Reiver, V. Chin, S. N. Bhatia, M. J. Sailor, *Science* **2003**, *299*, 2045-2047.
- [6] P. Horcajada, C. Serre, G. Maurin, N. A. Ramsahye, F. Balas, M. a. Vallet-Reg  , M. Sebban, F. Taulelle, G. r. F  rey, *J. Am. Chem. Soc.* **2008**, *130*, 6774-6780.
- [7] H. R. Luckarift, S. R. Sizemore, K. E. Farrington, J. Roy, C. Lau, P. B. Atanassov, G. R. Johnson, *Appl. Mater. Interfaces* **2012**, *4*, 2082-2087.
- [8] W.-S. Chae, D. V. Gough, S.-K. Ham, D. B. Robinson, P. V. Braun, *Appl. Mater. Interfaces* **2012**, *4*, 3973-3979.
- [9] R. H. Coridan, K. A. Arpin, B. S. Brunschwig, P. V. Braun, N. S. Lewis, *Nano Lett.* **2014**, *14*, 2310-2317.
- [10] Y. Surendranath, M. W. Kanan, D. G. Nocera, *J. Am. Chem. Soc.* **2010**, *132*, 16501-16509.
- [11] A. Harriman, I. J. Pickering, J. M. Thomas, P. A. Christensen, *Journal of the Chemical Society, Faraday Transactions 1: Physical Chemistry in Condensed Phases* **1988**, *84*, 2795-2806.
- [12] J. Zhang, S. Wang, M. Xu, Y. Wang, B. Zhu, S. Zhang, W. Huang, S. Wu, *Cryst. Growth Des.* **2009**, *9*, 3532-3537.
- [13] E. Biemmi, A. Darga, N. Stock, T. Bein, *Micropor. Mesopor. Mater.* **2008**, *114*, 380-386.
- [14] F. M. Hinterholzinger, A. Ranft, J. M. Feckl, B. Ruhle, T. Bein, B. V. Lotsch, *J. Mater. Chem.* **2012**, *22*, 10356-10362.
- [15] K. S. W. Sing, D. H. Everett, R. A. W. Haul, L. Moscou, R. A. Pierotti, J. Rouquerol, T. Siemieniewska, *Pure Appl. Chem.* **1985**, *57*, 603.
- [16] B. Kersting, <http://www.uni-leipzig.de/~bkerst/MCM41.ppt>. Leipzig, **2013**.
- [17] A. F. Cronsted, *Akad. Handl. Stockholm* **1756**, 120.
- [18] L. Pauling, *Nat. Acad. Sci* **1930**, 453.
- [19] W. H. Taylor, *Z. Kristallogr.* **1930**, 74.
- [20] R. M. Barrer, *J. Chem. Soc.* **1948**, 2158.
- [21] R. M. Barrer, *J. Chem. Soc.* **1948**, 127.
- [22] R. M. Barrer, D. W. Riley, *J. Chem. Soc.* **1948**, 133.
- [23] J. Weitkamp, *Solid State Ionics* **2000**, *131*, 175-188.
- [24] S. T. Wilson, B. M. Lok, C. A. Messina, T. R. Cannan, E. M. Flanigen, *J. Am. Chem. Soc.* **1982**, *104*, 1146-1147.

- [25] <http://www.iza-structure.org/databases>.
- [26] <http://www.integral-health-guide.com/powdered-zeolite/>.
- [27] C. Martínez, A. Corma, *Coord. Chem. Rev.* **2011**, 255, 1558-1580.
- [28] B. Yilmaz, U. Müller, *Top. Catal.* **2009**, 52, 888-895.
- [29] H. Eichhorn, *Ann. Rev. Phys. Chem.* **1958**, 105, 126.
- [30] D. I. Tchernev, *Rev. Mineral. Geochem.* **2001**, 45, 589.
- [31] M. Vallet-Regí, F. Balas, M. Colilla, M. Manzano, *Solid State Sci.* **2007**, 9, 768-776.
- [32] G. Dogliotti, A. E. Malavazos, S. Giacometti, U. Solimene, M. Fanelli, M. M. Corsi, E. Dozio, *J Clin Biochem Nutr* **2012**, 50, 195-198.
- [33] C. Platas-Iglesias, L. Vander Elst, W. Zhou, R. N. Muller, C. F. G. C. Geraldès, T. Maschmeyer, J. A. Peters, *Chem-Eur J* **2002**, 8, 5121-5131.
- [34] H. Chiku, M. Matsui, S. Murakami, Y. Kiyozumi, F. Mizukami, K. Sakaguchi, *Anal. Biochem.* **2003**, 318, 80-85.
- [35] J. Caro, *Micropor. Mesopor. Mater.* **2009**, 125, 79-84.
- [36] M. G. Nijkamp, J. E. M. J. Raaymakers, A. J. van Dillen, K. P. de Jong, *Applied Physics A* **2001**, 72, 619-623.
- [37] C. Y. Liu, K.-i. Aika, *J. Jpn. Pet. Inst.* **2003**, 46, 301-307.
- [38] T. Düren, L. Sarkisov, O. M. Yaghi, R. Q. Snurr, *Langmuir* **2004**, 20, 2683-2689.
- [39] X.-C. Huang, Y.-Y. Lin, J.-P. Zhang, X.-M. Chen, *Angew. Chem. Int. Ed.* **2006**, 45, 1557-1559.
- [40] A. Phan, C. J. Doonan, F. J. Uribe-Romo, C. B. Knobler, M. O'Keeffe, O. M. Yaghi, *Acc. Chem. Res.* **2009**, 43, 58-67.
- [41] K. S. Park, Z. Ni, A. P. Côté, J. Y. Choi, R. Huang, F. J. Uribe-Romo, H. K. Chae, M. O'Keeffe, O. M. Yaghi, *P Natl Acad Sci USA* **2006**, 103, 10185-10191.
- [42] R. Banerjee, A. Phan, B. Wang, C. Knobler, H. Furukawa, M. O'Keeffe, O. M. Yaghi, *Science* **2008**, 319, 939.
- [43] B. Wang, A. P. Côté, H. Furukawa, M. O'Keeffe, O. M. Yaghi, *nature* **2008**, 453, 207-211.
- [44] Z. Zhang, S. Xian, Q. Xia, H. Wang, Z. Li, J. Li, *AIChE J.* **2013**, 59, 2195-2206.
- [45] H. Bux, F. Liang, Y. Li, J. Cravillon, M. Wiebcke, J. r. Caro, *J. Am. Chem. Soc.* **2009**, 131, 16000-16001.
- [46] Y. Liu, E. Hu, E. A. Khan, Z. Lai, *J. Membr. Sci.* **2010**, 353, 36-40.
- [47] G. Lu, J. T. Hupp, *J. Am. Chem. Soc.* **2010**, 132, 7832-7833.
- [48] N. Liédana, A. Galve, C. Rubio, C. Téllez, J. Coronas, *Appl. Mater. Interfaces* **2012**, 4, 5016-5021.
- [49] J. Zhuang, C.-H. Kuo, L.-Y. Chou, D.-Y. Liu, E. Weerapana, C.-K. Tsung, *ACS Nano* **2014**, 8, 2812-2819.
- [50] E. A. Tomic, *J. Appl. Polym. Sci.* **1965**, 9, 3745-3752.
- [51] O. M. Yaghi, G. Li, H. Li, *NATURE* **1995**, 378, 703.
- [52] M. Eddaoudi, J. Kim, N. Rosi, D. Vodak, J. Wachter, M. O'Keeffe, O. M. Yaghi, *Science* **2002**, 295, 469-472.
- [53] S. R. Batten, R. Robson, *Angew. Chem. Int. Ed.* **1998**, 37, 1460-1494.
- [54] J. L. C. Rowsell, O. M. Yaghi, *Angew. Chem. Int. Ed.* **2005**, 44, 4670-4679.
- [55] H. Deng, S. Grunder, K. E. Cordova, C. Valente, H. Furukawa, M. Hmadeh, F. Gándara, A. C. Whalley, Z. Liu, S. Asahina, H. Kazumori, M. O'Keeffe, O. Terasaki, J. F. Stoddart, O. M. Yaghi, *Science* **2012**, 336, 1018-1023.
- [56] S. B. Choi, H. Furukawa, H. J. Nam, D.-Y. Jung, Y. H. Jhon, A. Walton, D. Book, M. O'Keeffe, O. M. Yaghi, J. Kim, *Angew. Chem. Int. Ed.* **2012**, 51, 8791-8795.
- [57] J. L. C. Rowsell, O. M. Yaghi, *Micropor. Mesopor. Mater.* **2004**, 73, 3-14.
- [58] O. M. Yaghi, M. O'Keeffe, N. W. Ockwig, H. K. Chae, M. Eddaoudi, J. Kim, *Nature* **2003**, 423, 705-714.

- [59] M. O'Keeffe, M. A. Peskov, S. J. Ramsden, O. M. Yaghi, *Acc. Chem. Res.* **2008**, *41*, 1782-1789.
- [60] D. J. Tranchemontagne, Z. Ni, M. O'Keeffe, O. M. Yaghi, *Angew. Chem. Int. Ed.* **2008**, *47*, 5136-5147.
- [61] M. O'Keeffe, *Chem. Soc. Rev.* **2009**, *38*, 1215-1217.
- [62] F. Millange, C. Serre, G. Férey, *Chem. Commun.* **2002**, 822-823.
- [63] C. Serre, F. Millange, S. Surblé, G. Férey, *Angew. Chem. Int. Ed.* **2004**, *43*, 6285-6289.
- [64] S. R. Miller, G. M. Pearce, P. A. Wright, F. Bonino, S. Chavan, S. Bordiga, I. Margiolaki, N. Guillou, G. Férey, S. Bourrelly, P. L. Llewellyn, *J. Am. Chem. Soc.* **2008**, *130*, 15967-15981.
- [65] M. Taddei, F. Costantino, F. Marmottini, A. Comotti, P. Sozzani, R. Vivani, *Chem. Commun.* **2014**, *50*, 14831-14834.
- [66] Z.-T. Zhang, Q.-Y. Wang, W.-W. Li, Q.-H. Meng, X.-L. Zhang, *CrystEngComm* **2012**, *14*, 5042-5052.
- [67] B. Wu, J. Yang, Y. Liu, F. Zhuge, N. Tang, X.-J. Yang, *CrystEngComm* **2010**, *12*, 2755-2761.
- [68] X.-C. Huang, Y.-Y. Lin, J.-P. Zhang, X.-M. Chen, *Angew. Chem. Int. Ed.* **2006**, *45*, 1557-1559.
- [69] W.-Y. Gao, W. Yan, R. Cai, K. Williams, A. Salas, L. Wojtas, X. Shi, S. Ma, *Chem. Commun.* **2012**, *48*, 8898-8900.
- [70] P. Cui, Y.-G. Ma, H.-H. Li, B. Zhao, J.-R. Li, P. Cheng, P. B. Balbuena, H.-C. Zhou, *J. Am. Chem. Soc.* **2012**, *134*, 18892-18895.
- [71] C. Valente, E. Choi, M. E. Belowich, C. J. Doonan, Q. Li, T. B. Gasa, Y. Y. Botros, O. M. Yaghi, J. F. Stoddart, *Chem. Commun.* **2010**, *46*, 4911-4913.
- [72] Y.-L. Zhao, L. Liu, W. Zhang, C.-H. Sue, Q. Li, O. Š. Miljanić, O. M. Yaghi, J. F. Stoddart, *Chem-Eur J* **2009**, *15*, 13356-13380.
- [73] R. A. Smaldone, R. S. Forgan, H. Furukawa, J. J. Gassensmith, A. M. Z. Slawin, O. M. Yaghi, J. F. Stoddart, *Angew. Chem. Int. Ed.* **2010**, *49*, 8630-8634.
- [74] M. Mizutani, N. Maejima, K. Jitsukawa, H. Masuda, H. Einaga, *Inorg. Chim. Acta* **1998**, *283*, 105-110.
- [75] Y. Zhang, M. K. Saha, I. Bernal, *CrystEngComm* **2003**, *5*, 34-37.
- [76] L. Bellarosa, S. Calero, N. Lopez, *Phys. Chem. Chem. Phys.* **2012**, *14*, 7240-7245.
- [77] G. Férey, C. Mellot-Draznieks, C. Serre, F. Millange, J. Dutour, S. Surblé, I. Margiolaki, *Science* **2005**, *309*, 2040-2042.
- [78] D. J. Tranchemontagne, J. R. Hunt, O. M. Yaghi, *Tetrahedron* **2008**, *64*, 8553-8557.
- [79] Y.-Q. Tian, Z.-X. Chen, L.-H. Weng, H.-B. Guo, S. Gao, D. Y. Zhao, *Inorg. Chem.* **2004**, *43*, 4631-4635.
- [80] Z. Ni, R. I. Masel, *J. Am. Chem. Soc.* **2006**, *128*, 12394-12395.
- [81] A. Pichon, S. L. James, *CrystEngComm* **2008**, *10*, 1839-1847.
- [82] E. R. Parnham, R. E. Morris, *Acc. Chem. Res.* **2007**, *40*, 1005-1013.
- [83] J. S. Beck, J. C. Vartuli, W. J. Roth, M. E. Leonowicz, C. T. Kresge, K. D. Schmitt, C. T. W. Chu, D. H. Olson, E. W. Sheppard, *J. Am. Chem. Soc.* **1992**, *114*, 10834-10843.
- [84] C. T. Kresge, M. E. Leonowicz, W. J. Roth, J. C. Vartuli, J. S. Beck, *NATURE* **1992**, *359*, 710-712.
- [85] L.-C. Juang, C.-C. Wang, C.-K. Lee, *Chemosphere* **2006**, *64*, 1920-1928.
- [86] S. B. Yoon, J. Y. Kim, J.-S. Yu, *Chem. Commun.* **2001**, 559-560.
- [87] R. Ryoo, S. H. Joo, S. Jun, *J. Phys. Chem. B* **1999**, *103*, 7743-7746.
- [88] D. Zhao, J. Feng, Q. Huo, N. Melosh, G. H. Fredrickson, B. F. Chmelka, G. D. Stucky, *Science* **1998**, *279*, 548-552.

-
- [89] G. Van den Bossche, R. Sobry, F. Fontaine, J.-M. Clacens, Z. Gabelica, *J. Appl. Crystallogr.* **1997**, 30, 1065-1074.
- [90] J. M. Gomez-Vega, K. Teshima, A. Hozumi, H. Sugimura, O. Takai, *Surf. Coat. Technol.* **2003**, 169-170, 504-507.
- [91] B. Tian, X. Liu, C. Yu, F. Gao, Q. Luo, S. Xie, B. Tu, D. Zhao, *Chem. Commun.* **2002**, 1186-1187.
- [92] N. Lang, A. Tuel, *Chem. Mater.* **2004**, 16, 1961-1966.
- [93] S. Kawi, *Chem. Commun.* **1998**, 1407-1408.
- [94] H. Rehage, *Chem. Unserer Zeit* **2005**, 39, 36-44.
- [95] P. T. Tanev, T. J. Pinnavaia, *Science* **1995**, 267, 865-867.
- [96] G. Herrier, J.-L. Blin, B.-L. Su, *Langmuir* **2001**, 17, 4422-4430.
- [97] D. Zhao, J. Sun, Q. Li, G. D. Stucky, *Chem. Mater.* **2000**, 12, 275-279.
- [98] M. Imp  rator-Clerc, P. Davidson, A. Davidson, *J. Am. Chem. Soc.* **2000**, 122, 11925-11933.
- [99] A. Taguchi, F. Sch  th, *Micropor. Mesopor. Mater.* **2005**, 77, 1-45.
- [100] K. Na, C. Jo, J. Kim, K. Cho, J. Jung, Y. Seo, R. J. Messinger, B. F. Chmelka, R. Ryoo, *Science* **2011**, 333, 328-332.
- [101] R. Zana, M. Benrraou, R. Rueff, *Langmuir* **1991**, 7, 1072-1075.
- [102] E. Alami, H. Levy, R. Zana, A. Skoulios, *Langmuir* **1993**, 9, 940-944.
- [103] E. Alami, G. Beinert, P. Marie, R. Zana, *Langmuir* **1993**, 9, 1465-1467.
- [104] E. Buhler, E. Mendes, P. Boltenhagen, J. P. Munch, R. Zana, S. J. Candau, *Langmuir* **1997**, 13, 3096-3102.
- [105] R. Oda, S. J. Candau, R. Oda, I. Huc, *Chem. Commun.* **1997**, 2105-2106.
- [106] R. Oda, I. Huc, D. Danino, Y. Talmon, *Langmuir* **2000**, 16, 9759-9769.
- [107] M. Sikiri  , I. Primo  i  , N. Filipovi  -Vincekovi  , *J. Colloid Interface Sci.* **2002**, 250, 221-229.
- [108] F. M. Menger, J. S. Keiper, *Angew. Chem. Int. Ed.* **2000**, 39, 1906-1920.
- [109] F. M. Menger, C. A. Littau, *J. Am. Chem. Soc.* **1991**, 113, 1451-1452.
- [110] F. M. Menger, C. A. Littau, *J. Am. Chem. Soc.* **1993**, 115, 10083-10090.
- [111] F. M. Menger, J. S. Keiper, V. Azov, *Langmuir* **2000**, 16, 2062-2067.
- [112] Z. Wei, X. Wei, D. Sun, J. Liu, X. Tang, *J. Colloid Interface Sci.* **2011**, 354, 677-685.
- [113] H. Akba  , M. Boz, A. Elemenli, *Fluid Phase Equilib.* **2014**, 370, 95-100.
- [114] G. P. Sorenson, K. L. Coppage, M. K. Mahanthappa, *J. Am. Chem. Soc.* **2011**, 133, 14928-14931.
- [115] P. V. D. Voort, M. Mathieu, F. Mees, E. F. Vansant, *J. Phys. Chem. B* **1998**, 102, 8847-8851.
- [116] Y. Zhao, J. Zhang, B. Han, J. Song, J. Li, Q. Wang, *Angew. Chem. Int. Ed.* **2011**, 50, 636-639.
- [117] L.-B. Sun, J.-R. Li, J. Park, H.-C. Zhou, *J. Am. Chem. Soc.* **2012**, 134, 126-129.
- [118] L. H. Wee, C. Wiktor, S. Turner, W. Vanderlinden, N. Janssens, S. R. Bajpe, K. Houthoofd, G. Van Tendeloo, S. De Feyter, C. E. A. Kirschhock, J. A. Martens, *J. Am. Chem. Soc.* **2012**, 134, 10911-10919.
- [119] X.-D. Do, V.-T. Hoang, S. Kaliaguine, *Micropor. Mesopor. Mater.* **2011**, 141, 135-139.
- [120] X.-X. Huang, L.-G. Qiu, W. Zhang, Y.-P. Yuan, X. Jiang, A.-J. Xie, Y.-H. Shen, J.-F. Zhu, *CrystEngComm* **2012**, 14, 1613-1617.
- [121] S. C. Junggeburth, K. Schwinghammer, K. S. Virdi, C. Scheu, B. V. Lotsch, *Chem-Eur J* **2012**, 18, 2143-2152.
- [122] S. C. Junggeburth, L. Diehl, S. Werner, V. Duppel, W. Sigle, B. V. Lotsch, *J. Am. Chem. Soc.* **2013**, 135, 6157-6164.
- [123] Z. Wang, S. M. Cohen, *J. Am. Chem. Soc.* **2007**, 129, 12368-12369.
-

-
- [124] K. K. Tanabe, Z. Wang, S. M. Cohen, *J. Am. Chem. Soc.* **2008**, *130*, 8508-8517.
- [125] S. M. Cohen, *Chemical Science* **2010**, *1*, 32-36.
- [126] C. Volkringer, S. M. Cohen, *Angew. Chem. Int. Ed.* **2010**, *49*, 4644-4648.
- [127] M. Kim, J. F. Cahill, K. A. Prather, S. M. Cohen, *Chem. Commun.* **2011**, *47*, 7629-7631.
- [128] K. K. Tanabe, S. M. Cohen, *Chem. Soc. Rev.* **2011**, *40*, 498-519.
- [129] J. S. Seo, D. Whang, H. Lee, S. I. Jun, J. Oh, Y. J. Jeon, K. Kim, *Nature* **2000**, *404*, 982-986.
- [130] C. J. Doonan, W. Morris, H. Furukawa, O. M. Yaghi, *J. Am. Chem. Soc.* **2009**, *131*, 9492-9493.
- [131] Z. Wang, S. M. Cohen, *Angew. Chem. Int. Ed.* **2008**, *47*, 4699-4702.
- [132] S. C. Jones, C. A. Bauer, *J. Am. Chem. Soc.* **2009**, *131*, 12516-12517.
- [133] X. Zhang, F. X. Llabrés i Xamena, A. Corma, *J. Catal.* **2009**, *265*, 155-160.
- [134] C. Martín, F. Molina, E. Alvarez, T. R. Belderrain, *Chem-Eur J* **2011**, *17*, 14885-14895.
- [135] Y. E. Cheon, M. P. Suh, *Angew. Chem. Int. Ed.* **2009**, *48*, 2899-2903.
- [136] C. Zlotea, R. Campesi, F. Cuevas, E. Leroy, P. Dibandjo, C. Volkringer, T. Loiseau, G. Férey, M. Latroche, *J. Am. Chem. Soc.* **2010**, *132*, 2991-2997.
- [137] D. Dybtsev, C. Serre, B. Schmitz, B. Panella, M. Hirscher, M. Latroche, P. L. Llewellyn, S. p. Cordier, Y. Molard, M. Haouas, F. Taulelle, G. r. Férey, *Langmuir* **2010**, *26*, 11283-11290.
- [138] K. M. L. Taylor-Pashow, J. D. Rocca, Z. Xie, S. Tran, W. Lin, *J. Am. Chem. Soc.* **2009**, *131*, 14261-14263.
- [139] W. Morris, C. J. Doonan, H. Furukawa, R. Banerjee, O. M. Yaghi, *J. Am. Chem. Soc.* **2008**, *130*, 12626-12627.
- [140] S. Bernt, V. Guillermin, C. Serre, N. Stock, *Chem. Commun.* **2011**, *47*, 2838-2840.
- [141] K. K. Tanabe, C. A. Allen, S. M. Cohen, *Angew. Chem. Int. Ed.* **2010**, *49*, 9730-9733.
- [142] A. Modrow, D. Zargarani, R. Herges, N. Stock, *Dalton Trans.* **2012**, *41*, 8690-8696.
- [143] H. C. Kolb, M. G. Finn, K. B. Sharpless, *Angew. Chem. Int. Ed.* **2001**, *40*, 2004-2021.
- [144] W. H. Binder, R. Sachsenhofer, *Macromol. Rapid Commun.* **2007**, *28*, 15-54.
- [145] P. Wu, M. Malkoch, J. N. Hunt, R. Vestberg, E. Kaltgrad, M. G. Finn, V. V. Fokin, K. B. Sharpless, C. J. Hawker, *Chem. Commun.* **2005**, 5775-5777.
- [146] D. D. Díaz, K. Rajagopal, E. Strable, J. Schneider, M. G. Finn, *J. Am. Chem. Soc.* **2006**, *128*, 6056-6057.
- [147] S. S. Gupta, J. Kuzelka, P. Singh, W. G. Lewis, M. Manchester, M. G. Finn, *Bioconjugate Chem.* **2005**, *16*, 1572-1579.
- [148] A. J. Dirks, S. S. van Berkel, N. S. Hatzakis, J. A. Opsteen, F. L. van Delft, J. J. L. M. Cornelissen, A. E. Rowan, J. C. M. van Hest, F. P. J. T. Rutjes, R. J. M. Nolte, *Chem. Commun.* **2005**, 4172-4174.
- [149] A. J. Link, D. A. Tirrell, *J. Am. Chem. Soc.* **2003**, *125*, 11164-11165.
- [150] K. E. Beatty, F. Xie, Q. Wang, D. A. Tirrell, *J. Am. Chem. Soc.* **2005**, *127*, 14150-14151.
- [151] D. Britt, H. Furukawa, B. Wang, T. G. Glover, O. M. Yaghi, *Proc. Natl. Acad. Sci. U.S.A.* **2009**, *106*, 20637-20640.
- [152] S. Ma, H.-C. Zhou, *Chem. Commun.* **2010**, *46*, 44-53.
- [153] S. Keskin, S. Kizilel, *Ind. Eng. Chem. Res.* **2011**, *50*, 1799-1812.
- [154] V. W. T. Liu, P. L. Huang, *J. Cardio. Res.* **2008**, 19-29.
- [155] J. Della Rocca, D. Liu, W. Lin, *Acc. Chem. Res.* **2011**, *44*, 957-968.
- [156] O. R. Evans, W. Lin, *Acc. Chem. Res.* **2002**, *35*, 511-522.
- [157] G. Nickerl, A. Henschel, R. Grönker, K. Gedrich, S. Kaskel, *Chem. Ing. Tech.* **2010**, *83*, 90-103.
-

- [158] F. X. Llabrés i Xamena, O. Casanova, R. Galiasso Tailleur, H. Garcia, A. Corma, *J. Catal.* **2008**, 255, 220-227.
- [159] S. Neogi, M. K. Sharma, P. K. Bharadwaj, *J. Mol. Catal. A: Chem.* **2009**, 299, 1-4.
- [160] A. Demessence, C. Boissiere, D. Grosso, P. Horcajada, C. Serre, G. Ferey, G. J. A. A. Soler-Illia, C. Sanchez, *J. Mater. Chem.* **2010**, 20, 7676-7681.
- [161] L. T. L. Nguyen, K. K. A. Le, H. X. Truong, N. T. S. Phan, *Catalysis Science & Technology* **2012**, 2, 521-528.
- [162] R. Halder, S. K. Reddy, V. M. Suresh, S. Mohapatra, S. Balasubramanian, T. K. Maji *Chem-Eur J* **2014**, 20, 4347-4356.
- [163] E. Proietti, F. Jaouen, M. Lefèvre, N. Larouche, J. Tian, J. Herranz, J.-P. Dodelet, *Nat Commun* **2011**, 2, 416.
- [164] G. A. Goenaga, S. Ma, S. Yuan, D.-J. Liu, *ECS Trans.* **2010**, 33, 579-586.
- [165] S. Ma, G. A. Goenaga, A. V. Call, D.-J. Liu, *Chem-Eur J* **2011**, 17, 2063-2067.
- [166] C. Wang, Z. Xie, K. E. deKrafft, W. Lin, *J. Am. Chem. Soc.* **2011**, 133, 13445-13454.
- [167] K. F. Babu, M. A. Kulandainathan, I. Katsounaros, L. Rassaei, A. D. Burrows, P. R. Raithby, F. Marken, *Electrochem. Commun.* **2010**, 12, 632-635.
- [168] C. C. L. McCrory, S. Jung, J. C. Peters, T. F. Jaramillo, *J. Am. Chem. Soc.* **2013**, 135, 16977-16987.
- [169] WINXPOW, Powder Diffraction Software Package, v2.12, Stoe & Cie GmbH, Darmstadt (Germany) **2005**.
- [170] JCPDS, PDF v2, International Center for Diffraction Data, Swathmore (USA) **1992**.
- [171] K. Schmidt-Rohr, H. W. Spiess, *Multidimensional Solid State NMR and Polymers*, Academic Press, London, **1994**.
- [172] D. D. Laws, H.-M. L. Bitter, A. Jerschow, *Angew. Chem. Int. Ed.* **2002**, 41, 3096-3129.
- [173] Z. Shi, J. Peng, X. Yu, Y. Shen, Z. Zhang, K. Alimaje, X. Wang, *Inorg. Chem. Commun.* **2013**, 28, 85-89.
- [174] G. Wielgoszewski, http://commons.wikimedia.org/wiki/File:AFM_schematic_%28EN%29.svg, **2011**.
- [175] J. Fan, Y. Hao, A. Cabot, E. M. J. Johansson, G. Boschloo, A. Hagfeldt, *Appl. Mater. Interfaces* **2013**, 5, 1902-1906.
- [176] J.-S. Qin, D.-Y. Du, W.-L. Li, J.-P. Zhang, S.-L. Li, Z.-M. Su, X.-L. Wang, Q. Xu, K.-Z. Shao, Y.-Q. Lan, *Chemical Science* **2012**, 3, 2114-2118.
- [177] W. Xuan, C. Zhu, Y. Liu, Y. Cui, *Chem. Soc. Rev.* **2012**, 41, 1677-1695.
- [178] S.-L. Li, Q. Xu, *Energy & Environmental Science* **2013**, 6, 1656-1683.
- [179] O. K. Farha, I. Eryazici, N. C. Jeong, B. G. Hauser, C. E. Wilmer, A. A. Sarjeant, R. Q. Snurr, S. T. Nguyen, A. Ö. Yazaydın, J. T. Hupp, *J. Am. Chem. Soc.* **2012**, 134, 15016-15021.
- [180] J. A. Thompson, N. A. Brunelli, R. P. Lively, J. R. Johnson, C. W. Jones, S. Nair, *The Journal of Physical Chemistry C* **2013**, 117, 8198-8207.
- [181] J.-L. Wang, C. Wang, W. Lin, *ACS Catalysis* **2012**, 2, 2630-2640.
- [182] H. Hosseini, H. Ahmar, A. Dehghani, A. Bagheri, A. Tadjarodi, A. R. Fakhari, *Biosensors and Bioelectronics* **2013**, 42, 426-429.
- [183] W. Ma, Q. Jiang, P. Yu, L. Yang, L. Mao, *Anal. Chem.* **2013**, 85, 7550-7557.
- [184] P. Horcajada, T. Chalati, C. Serre, B. Gillet, C. Sebrie, T. Baati, J. F. Eubank, D. Heurtaux, P. Clayette, C. Kreuz, J.-S. Chang, Y. K. Hwang, V. Marsaud, P.-N. Bories, L. Cynober, S. Gil, G. Ferey, P. Couvreur, R. Gref, *Nat. Mater.* **2010**, 9, 172-178.
- [185] H.-L. Jiang, Y. Tatsu, Z.-H. Lu, Q. Xu, *J. Am. Chem. Soc.* **2010**, 132, 5586-5587.
- [186] N. Klein, I. Senkovska, K. Gedrich, U. Stoeck, A. Henschel, U. Mueller, S. Kaskel, *Angew. Chem. Int. Ed.* **2009**, 48, 9954-9957.

- [187] B. Mu, P. M. Schoenecker, K. S. Walton, *The Journal of Physical Chemistry C* **2010**, *114*, 6464-6471.
- [188] M. Choi, K. Na, J. Kim, Y. Sakamoto, O. Terasaki, R. Ryoo, *nature* **2009**, *461*, 246-249.
- [189] K. Na, M. Choi, W. Park, Y. Sakamoto, O. Terasaki, R. Ryoo, *J. Am. Chem. Soc.* **2009**, *132*, 4169-4177.
- [190] R. Zana, Y. Talmon, *Nature* **1993**, *362*, 228-230.
- [191] K. Karaborni, K. Esselink, P. A. J. Hilbers, B. Smit, J. Karthäuser, N. M. van Os, R. Zana, *Science* **1994**, *266*, 254-256.
- [192] H. I. Lee, C. Pak, S. H. Yi, J. K. Shon, S. S. Kim, B. G. So, H. Chang, J. E. Yie, Y.-U. Kwon, J. M. Kim, *J. Mater. Chem.* **2005**, *15*, 4711-4717.
- [193] B. Elena, G. de Paëpe, L. Emsley, *Chem. Phys. Lett.* **2004**, *398*, 532-538.
- [194] Q. Huo, D. I. Margolese, G. D. Stucky, *Chem. Mater.* **1996**, *8*, 1147-1160.
- [195] K. Lund, N. Muroyama, O. Terasaki, *Micropor. Mesopor. Mater.* **2010**, *128*, 71-77.
- [196] C. K. Lee, M. J. Ling, I. J. B. Lin, *Dalton Trans.* **2003**, 4731-4737.
- [197] G. A. V. Martins, P. J. Byrne, P. Allan, S. J. Teat, A. M. Z. Slawin, Y. Li, R. E. Morris, *Dalton Trans.* **2010**, *39*, 1758-1762.
- [198] X. Ji, C. Liu, C. Liu, J. Li, X. Yu, P. Su, J. Huang, J. Jia, J. Wu, L. Chen, C. Chen, Y. Wu, Y. Fan, J. Lin, B. Cheng, C. Tang, *Mater. Lett.* **2014**, *122*, 309-311.
- [199] A. R. Campanelli, L. Scaramuzza, *Acta Crystallographica Section C* **1986**, *42*, 1380-1383.
- [200] X. Yu, Z. Xu, S. Han, *J. Porous Mater.* **2010**, *17*, 99-105.
- [201] N. Hedin, R. Graf, S. C. Christiansen, C. Gervais, R. C. Hayward, J. Eckert, B. F. Chmelka, *J. Am. Chem. Soc.* **2004**, *126*, 9425.
- [202] S. C. Christiansen, D. Zhao, M. Janicke, C. C. Landry, G. D. Stucky, B. F. Chmelka, *J. Am. Chem. Soc.* **2001**, *123*, 4519.
- [203] A. C. Mayer, M. F. Toney, S. R. Scully, J. Rivnay, C. J. Brabec, M. Scharber, M. Koppe, M. Heeney, I. McCulloch, M. D. McGehee, *Adv. Funct. Mater.* **2009**, *19*, 1173.
- [204] N. C. Miller, E. Cho, M. J. N. Junk, R. Gysel, C. Risko, D. Kim, S. Sweetnam, C. E. Miller, L. J. Richter, R. J. Klinke, M. Heeney, I. McCulloch, A. Amassian, D. Acevedo-Feliz, C. Knox, M. R. Hansen, D. Dudenko, B. F. Chmelka, M. F. Toney, J. L. Brédas, M. D. McGehee, *Adv. Mater.* **2012**, *24*, 6071-6079.
- [205] H. Hayashi, A. P. Cote, H. Furukawa, M. O'Keeffe, O. M. Yaghi, *Nat. Mater.* **2007**, *6*, 501-506.
- [206] R. Liu, Y. Shi, Y. Wan, Y. Meng, F. Zhang, D. Gu, Z. Chen, B. Tu, D. Zhao, *J. Am. Chem. Soc.* **2006**, *128*, 11652-11662.
- [207] A. P. Alivisatos, *Science* **1996**, *271*, 933-937.
- [208] L. Arai, M. A. Nadeem, M. Bhadbhade, J. A. Stride, *Dalton Trans.* **2010**, *39*, 3372-3374.
- [209] X.-M. Li, *Acta Crystallographica Section E* **2007**, *63*, m1984.
- [210] S. Junggeburth, *PhD Thesis*, LMU Munich, **2013**.
- [211] W. Morris, C. J. Stevens, R. E. Taylor, C. Dybowski, O. M. Yaghi, M. A. Garcia-Garibay, *J. Phys. Chem. C* **2012**, *116*, 13307-13312.
- [212] K. Manna, T. Zhang, F. X. Greene, W. Lin, *J. Am. Chem. Soc.* **2015**, *137*, 2665-2673.
- [213] Y.-T. Liao, S. Dutta, C.-H. Chien, C.-C. Hu, F.-K. Shieh, C.-H. Lin, K. W. Wu, *J. Inorg. Organomet. Polym. Mater.* **2015**, *25*, 251-258.
- [214] Y.-Q. Tian, C.-X. Cai, X.-M. Ren, C.-Y. Duan, Y. Xu, S. Gao, X.-Z. You, *Chem-Eur J* **2003**, *9*, 5673-5685.
- [215] B. Seoane, A. Dikhtiarenko, A. Mayoral, C. Tellez, J. Coronas, F. Kapteijn, J. Gascon, *CrystEngComm* **2015**, *17*, 1693-1700.

- [216] Y. Pan, D. Heryadi, F. Zhou, L. Zhao, G. Lestari, H. Su, Z. Lai, *CrystEngComm* **2011**, *13*, 6937-6940.
- [217] R. Lehnert, F. Seel, *Z. Anorg. Allg. Chem.* **1980**, *464*, 187-194.
- [218] P. Shao, R. Y. M. Huang, *J. Membr. Sci.* **2007**, *287*, 162-179.
- [219] SDBS, Spectral Database for Organic Compounds, National Institute of Advanced Industrial Science and Technology (AIST), Japan, 2014.
- [220] F. Afsahi, H. Vinh-Thang, S. Mikhailenko, S. Kaliaguine, *J. Power Sources* **2013**, *239*, 415-423.
- [221] A. Corma, H. Garcia, F. X. Llabresi Xamena, *Chem. Rev.* **2010**, *110*, 4606-4655.
- [222] Y.-Q. Tian, Y.-M. Zhao, Z.-X. Chen, G.-N. Zhang, L.-H. Weng, D.-Y. Zhao, *Chem. Eur. J.* **2007**, *13*, 4146-4154.
- [223] B. P. Biswal, T. Panda, R. Banerjee, *Chem. Commun.* **2012**, *48*, 11868-11870.
- [224] D. J. Tranchemontagne, J. L. Mendoza-Cortes, M. O'Keeffe, O. M. Yaghi, *Chem. Soc. Rev.* **2009**, *38*, 1257-1283.
- [225] C. Janiak, J. K. Vieth, *New J. Chem.* **2010**, *34*, 2366-2388.
- [226] T. Dewa, T. Saiki, Y. Aoyama, *J. Am. Chem. Soc.* **2000**, *123*, 502-503.
- [227] J. Gascon, U. Aktay, M. D. Hernandez-Alonso, G. P. M. van Klink, F. Kapteijn, *J. Catal.* **2009**, *261*, 75-87.
- [228] U. P. N. Tran, K. K. A. Le, N. T. S. Phan, *ACS Catalysis* **2011**, *1*, 120-127.
- [229] J. Zakzeski, A. Dębczak, P. C. A. Bruijninx, B. M. Weckhuysen, *Applied Catalysis A: General* **2011**, *394*, 79-85.
- [230] S. Wang, Y. Hou, S. Lin, X. Wang, *Nanoscale* **2014**, *6*, 9930-9934.
- [231] J. B. Gerken, J. G. McAlpin, J. Y. C. Chen, M. L. Rigsby, W. H. Casey, R. D. Britt, S. S. Stahl, *J. Am. Chem. Soc.* **2011**, *133*, 14431-14442.
- [232] S. C. Petitto, E. M. Marsh, G. A. Carson, M. A. Langell, *J. Mol. Catal. A: Chem.* **2008**, *281*, 49-58.
- [233] G. Wang, L. Zhang, J. Zhang, *Chem. Soc. Rev.* **2012**, *41*, 797-828.
- [234] L. N. Saunders, M. E. Pratt, S. E. Hann, L. N. Dawe, A. Decken, F. M. Kerton, C. M. Kozak, *Polyhedron* **2012**, *46*, 53-65.
- [235] S.-Y. Zhang, B. Xu, L. Zheng, W. Chen, Y. Li, W. Li, *Inorg. Chim. Acta* **2011**, *367*, 44-50.
- [236] E. L. First, C. A. Floudas, *Micropor. Mesopor. Mater.* **2013**, *165*, 32-39.
- [237] J. Cravillon, S. Munzer, S.-J. Lohmeier, A. Feldhoff, K. Huber, M. Wiebcke, *Chem. Mater.* **2009**, *21*, 1410-1412.
- [238] G. Ferey, *Chem. Soc. Rev.* **2008**, *37*, 191-214.
- [239] Y. Pan, Y. Liu, G. Zeng, L. Zhao, Z. Lai, *Chem. Commun.* **2011**, *47*, 2071-2073.
- [240] N. S. McIntyre, M. G. Cook, *Anal. Chem.* **1975**, *47*, 2208-2213.
- [241] S. K. Das, M. K. Bhunia, M. Motin Seikh, S. Dutta, A. Bhaumik, *Dalton Trans.* **2011**, *40*, 2932-2939.
- [242] T. J. Chuang, C. R. Brundle, D. W. Rice, *Surf. Sci.* **1976**, *59*, 413-429.
- [243] C. K. Jørgensen, R. Pappalardo, H.-H. Schmidtke, *J. Chem. Phys.* **1963**, 1422-1430.
- [244] M. Gerloch, *Magnetism and Ligand-Field Analysis*, Cambridge University Press, Cambridge, **1983**.
- [245] B. N. Figgis, M. A. Hitchman, *Ligand-Field Theory and Its Applications*, Wiley-VCH, New York, **2000**.
- [246] M. Gerloch, L. R. Hanton, *Inorg. Chem.* **1980**, *19*, 1692-1698.
- [247] T. Peppel, M. Köckerling, *Cryst. Growth Des.* **2011**, *11*, 5461-5468.
- [248] D. A. Johnson, A. G. Sharpe, *Journal of the Chemical Society A: Inorganic, Physical, Theoretical* **1966**, 798-801.
- [249] X. Xie, W. Shen, *Nanoscale* **2009**, *1*, 50.
- [250] F. Cheng, Z. Tao, J. Liang, J. Chen, *Chem. Mater.* **2007**, *20*, 667-681.

- [251] J. He, Y. Peng, Z. Sun, W. Cheng, Q. Liu, Y. Feng, Y. Jiang, F. Hu, Z. Pan, Q. Bian, S. Wei, *Electrochim. Acta* **2014**, *119*, 64-71.
- [252] H. Pang, F. Gao, Q. Chen, R. Liu, Q. Lu, *Dalton Trans.* **2012**, *41*, 5862-5868.
- [253] R. N. Singh, M. Hamdani, J. F. Koenig, G. Poillerat, J. L. Gautier, P. Chartier, *J. Appl. Electrochem.* **1990**, *20*, 442-446.
- [254] J. O. Bockris, M., *The Journal of Chemical Physics* **1956**, *24*, 817-827.
- [255] S. P. Singh, S. Samuel, S. K. Tiwari, R. N. Singh, *Int. J. Hydrogen Energy* **1996**, *21*, 171-178.
- [256] L. Yang, S. Kinoshita, T. Yamada, S. Kanda, H. Kitagawa, M. Tokunaga, T. Ishimoto, T. Ogura, R. Nagumo, A. Miyamoto, M. Koyama, *Angew. Chem. Int. Ed.* **2010**, *49*, 5348-5351.
- [257] E. A. Flugel, A. Ranft, F. Haase, B. V. Lotsch, *J. Mater. Chem.* **2012**, *22*, 10119-10133.
- [258] S. Hausdorf, W. Seichter, E. Weber, F. O. R. L. Mertens, *Dalton Trans.* **2009**, 1107-1113.
- [259] C.-Y. Huang, M. Song, Z.-Y. Gu, H.-F. Wang, X.-P. Yan, *Environ. Sci. Technol.* **2011**, *45*, 4490-4496.
- [260] H. Wu, W. Zhou, T. Yildirim, *J. Am. Chem. Soc.* **2007**, *129*, 5314-5315.
- [261] B. Kesanli, Y. Cui, M. R. Smith, E. W. Bittner, B. C. Bockrath, W. Lin, *Angew. Chem. Int. Ed.* **2005**, *44*, 72-75.
- [262] H. Bux, A. Feldhoff, J. Cravillon, M. Wiebcke, Y.-S. Li, J. Caro, *Chem. Mater.* **2011**, *23*, 2262-2269.
- [263] S. R. Venna, M. A. Carreon, *J. Am. Chem. Soc.* **2009**, *132*, 76-78.
- [264] E. Biemmi, A. Darga, N. Stock, T. Bein, *Micropor. Mesopor. Mater.* **2008**, *114*, 380-386.
- [265] L. E. Kreno, J. T. Hupp, R. P. Van Duyne, *Anal. Chem.* **2010**, *82*, 8042-8046.
- [266] J. Liu, F. Sun, F. Zhang, Z. Wang, R. Zhang, C. Wang, S. Qiu, *J. Mater. Chem.* **2011**, *21*, 3775-3778.
- [267] X. Zhang, M. A. Ballem, Z.-J. Hu, P. Bergman, K. Uvdal, *Angew. Chem. Int. Ed.* **2011**, *50*, 5729-5733.
- [268] W. Hatakeyama, T. J. Sanchez, M. D. Rowe, N. J. Serkova, M. W. Liberatore, S. G. Boyes, *Appl. Mater. Interfaces* **2011**, *3*, 1502-1510.
- [269] R. Ananthoji, J. F. Eubank, F. Nouar, H. Mouttaki, M. Eddaoudi, J. P. Harmon, *J. Mater. Chem.* **2011**, *21*, 9587-9594.
- [270] D. Zhao, S. Tan, D. Yuan, W. Lu, Y. H. Rezenom, H. Jiang, L.-Q. Wang, H.-C. Zhou, *Adv. Mater.* **2010**, *23*, 90-93.
- [271] H.-L. Jiang, Q. Xu, *Chem. Commun.* **2011**, *47*, 3351-3370.
- [272] W. Lin, W. J. Rieter, K. M. L. Taylor, *Angew. Chem. Int. Ed.* **2009**, *48*, 650-658.
- [273] F. o. Fajula, A. Galarneau, F. D. Renzo, *Micropor. Mesopor. Mater.* **2005**, *82*, 227-239.
- [274] J. Wang, J. D. Byrne, M. E. Napier, J. M. DeSimone, *Small* **2011**, *7*, 1919-1931.
- [275] H. B. Na, I. C. Song, T. Hyeon, *Adv. Mater.* **2009**, *21*, 2133-2148.
- [276] R. E. Morris, *Nature Chem.* **2011**, *3*, 347-348.
- [277] N. Fukao, K.-H. Kyung, K. Fujimoto, S. Shiratori, *Macromolecules* **2011**, *44*, 2964-2969.
- [278] A. M. Spokoyny, D. Kim, A. Sumrein, C. A. Mirkin, *Chem. Soc. Rev.* **2009**, *38*, 1218-1227.
- [279] O. Shekhah, J. Liu, R. A. Fischer, C. Woll, *Chem. Soc. Rev.* **2011**, *40*, 1081-1106.
- [280] T. Tsuruoka, S. Furukawa, Y. Takashima, K. Yoshida, S. Isoda, S. Kitagawa, *Angew. Chem. Int. Ed.* **2009**, *48*, 4739-4743.

- [281] P. Horcajada, C. Serre, D. Grosso, C. Boissière, S. Perruchas, C. Sanchez, G. Férey, *Adv. Mater.* **2009**, *21*, 1931-1935.
- [282] J. Cravillon, R. Nayuk, S. Springer, A. Feldhoff, K. Huber, M. Wiebcke, *Chem. Mater.* **2011**, *23*, 2130-2141.
- [283] N. A. Khan, I. J. Kang, H. Y. Seok, S. H. Jung, *Chem. Eng. J.* **2011**, *166*, 1152-1157.
- [284] L.-G. Qiu, Z.-Q. Li, Y. Wu, W. Wang, T. Xu, X. Jiang, *Chem. Commun.* **2008**, 3642-3644.
- [285] Z.-Q. Li, L.-G. Qiu, W. Wang, T. Xu, Y. Wu, X. Jiang, *Inorg. Chem. Commun.* **2008**, *11*, 1375-1377.
- [286] S. Diring, S. Furukawa, Y. Takashima, T. Tsuruoka, S. Kitagawa, *Chem. Mater.* **2010**, *22*, 4531-4538.
- [287] Z.-Q. Li, L.-G. Qiu, T. Xu, Y. Wu, W. Wang, Z.-Y. Wu, X. Jiang, *Mater. Lett.* **2009**, *63*, 78-80.
- [288] K. S. Suslick, *Ultrasound: Its Chemical, Physical and Biological Effects*, VCH, Weinheim, Germany, **1988**.
- [289] K. S. Suslick, *Science* **1990**, *247*, 1439-1445.
- [290] K. Baba, H. Kasai, S. Okada, H. Oikawa, H. Nakanishi, *Opt. Mater.* **2003**, *21*, 591-594.
- [291] C. Nitschke, S. M. O'Flaherty, M. Kröll, W. J. Blau, *J. Phys. Chem. B* **2003**, *108*, 1287-1295.
- [292] E. Haque, N. A. Khan, J. H. Park, S. H. Jung, *Chem. Eur. J.* **2010**, *16*, 1046-1052.
- [293] M. Schlesinger, S. Schulze, M. Hietschold, M. Mehring, *Micropor. Mesopor. Mater.* **2011**, *132*, 121-127.
- [294] Z. Xiang, D. Cao, X. Shao, W. Wang, J. Zhang, W. Wu, *Chem. Eng. Sci.* **2010**, *65*, 3140-3146.
- [295] N. A. Khan, E. Haque, S. H. Jung, *Phys. Chem. Chem. Phys.* **2010**, *12*, 2625-2631.
- [296] T. Chalati, P. Horcajada, R. Gref, P. Couvreur, C. Serre, *J. Mater. Chem.* **2011**, *21*, 2220-2227.
- [297] J. Liu, S. Cheng, J. Zhang, X. Feng, X. Fu, B. Han, *Angew. Chem. Int. Ed.* **2007**, *46*, 3313-3315.
- [298] K. P. Johnston, K. L. Harrison, M. J. Clarke, S. M. Howdle, M. P. Heitz, F. V. Bright, C. Carlier, T. W. Randolph, *Science* **1996**, *271*, 624-626.
- [299] R. Ameloot, F. Vermoortele, W. Vanhove, M. B. J. Roefsaers, B. F. Sels, D. E. De Vos, *Nat Chem* **2011**, *3*, 382-387.
- [300] H. Guo, Y. Zhu, S. Qiu, J. A. Lercher, H. Zhang, *Adv. Mater.* **2010**, *22*, 4190-4192.
- [301] D. Zacher, R. Schmid, C. Wöll, R. A. Fischer, *Angew. Chem. Int. Ed.* **2011**, *50*, 176-199.
- [302] J. Cravillon, C. A. Schröder, R. Nayuk, J. Gummel, K. Huber, M. Wiebcke, *Angew. Chem. Int. Ed.* **2011**, *50*, 8067-8071.
- [303] Q. Shi, Z. Chen, Z. Song, J. Li, J. Dong, *Angew. Chem. Int. Ed.* **2010**, *50*, 672-675.
- [304] A. G. Wong-Foy, A. J. Matzger, O. M. Yaghi, *J. Am. Chem. Soc.* **2006**, *128*, 3494-3495.
- [305] T. M. Reineke, M. Eddaoudi, M. Fehr, D. Kelley, O. M. Yaghi, *J. Am. Chem. Soc.* **1999**, *121*, 1651-1657.
- [306] W. J. Rieter, K. M. L. Taylor, H. An, W. Lin, W. Lin, *J. Am. Chem. Soc.* **2006**, *128*, 9024-9025.
- [307] K. M. L. Taylor, A. Jin, W. Lin, *Angew. Chem. Int. Ed.* **2008**, *47*, 7722-7725.
- [308] K. M. L. Taylor, W. J. Rieter, W. Lin, *J. Am. Chem. Soc.* **2008**, *130*, 14358-14359.
- [309] K. P. Brazhnik, W. N. Vreeland, J. B. Hutchison, R. Kishore, J. Wells, K. Helmersen, L. E. Locascio, *Langmuir* **2005**, *21*, 10814-10817.

- [310] A. L. Thangawng, P. B. Howell Jr, J. J. Richards, J. S. Erickson, F. S. Ligler, *Lab Chip* **2009**, 9, 3126-3130.
- [311] J. Puigmartí-Luis, D. Schaffhauser, B. R. Burg, P. S. Dittrich, *Adv. Mater.* **2010**, 22, 2255-2259.
- [312] J. Puigmartí-Luis, M. Rubio-Martinez, U. Hartfelder, I. Imaz, D. Maspoch, P. S. Dittrich, *J. Am. Chem. Soc.* **2011**, 133, 4216-4219.
- [313] Q. Zhang, S.-J. Liu, S.-H. Yu, *J. Mater. Chem.* **2009**, 19, 191-207.
- [314] M. Jahan, Q. Bao, J.-X. Yang, K. P. Loh, *J. Am. Chem. Soc.* **2010**, 132, 14487-14495.
- [315] M. Eddaoudi, H. Li, O. M. Yaghi, *J. Am. Chem. Soc.* **2000**, 122, 1391-1397.
- [316] D. Zacher, A. Baunemann, S. Hermes, R. A. Fischer, *J. Mater. Chem.* **2007**, 17, 2785-2792.
- [317] S. Hermes, F. Schröder, R. Chelmowski, C. Wöll, R. A. Fischer, *J. Am. Chem. Soc.* **2005**, 127, 13744-13745.
- [318] Y.-S. Li, H. Bux, A. Feldhoff, G.-L. Li, W.-S. Yang, J. Caro, *Adv. Mater.* **2010**, 22, 3322-3326.
- [319] Y.-S. Li, F.-Y. Liang, H. Bux, A. Feldhoff, W.-S. Yang, J. Caro, *Angew. Chem. Int. Ed.* **2010**, 49, 548-551.
- [320] R. Ameloot, L. Pandey, M. V. d. Auweraer, L. Alaerts, B. F. Sels, D. E. De Vos, *Chem. Commun.* **2010**, 46, 3735-3737.
- [321] M. Kind, C. Wöll, *Prog. Surf. Sci.* **2009**, 84, 230-278.
- [322] A. Schoedel, C. Scherb, T. Bein, *Angew. Chem. Int. Ed.* **2010**, 49, 7225-7228.
- [323] O. Shekhah, H. Wang, S. Kowarik, F. Schreiber, M. Paulus, M. Tolan, C. Sternemann, F. Evers, D. Zacher, R. A. Fischer, C. Wöll, *J. Am. Chem. Soc.* **2007**, 129, 15118-15119.
- [324] O. Shekhah, H. Wang, M. Paradinas, C. Ocal, B. Schupbach, A. Terfort, D. Zacher, R. A. Fischer, C. Woll, *Nat. Mater.* **2009**, 8, 481-484.
- [325] G. Decher, J. D. Hong, J. Schmitt, *Thin Solid Films* **1992**, 210, 831-835.
- [326] H. K. Arslan, O. Shekhah, J. Wohlgemuth, M. Franzreb, R. A. Fischer, C. Wöll, *Adv. Funct. Mater.* **2011**, DOI: 10.1002/adfm.201101592.
- [327] O. Shekhah, K. Hirai, H. Wang, H. Uehara, M. Kondo, S. Diring, D. Zacher, R. A. Fischer, O. Sakata, S. Kitagawa, S. Furukawa, C. Wöll, *Dalton Trans.* **2011**, 40, 4954-4958.
- [328] D. Zacher, K. Yusenko, A. Bétard, S. Henke, M. Molon, T. Ladnorg, O. Shekhah, B. Schüpbach, T. de los Arcos, M. Krasnopolski, M. Meilikhov, J. Winter, A. Terfort, C. Wöll, R. A. Fischer, *Chem-Eur J* **2011**, 17, 1448-1455.
- [329] O. Shekhah, H. Wang, D. Zacher, R. A. Fischer, C. Wöll, *Angew. Chem. Int. Ed.* **2009**, 48, 5038-5041.
- [330] P.-Z. Li, Y. Maeda, Q. Xu, *Chem. Commun.* **2011**, 47, 8436-8438.
- [331] D. Zacher, O. Shekhah, C. Woll, R. A. Fischer, *Chem. Soc. Rev.* **2009**, 38, 1418-1429.
- [332] A. Demessence, P. Horcajada, C. Serre, C. Boissiere, D. Grosso, C. Sanchez, G. Ferey, *Chem. Commun.* **2009**, 7149-7151.
- [333] H. Li, M. Eddaoudi, T. L. Groy, O. M. Yaghi, *J. Am. Chem. Soc.* **1998**, 120, 8571-8572.
- [334] B. F. Hoskins, R. Robson, *J. Am. Chem. Soc.* **1990**, 112, 1546-1554.
- [335] W. J. Rieter, K. M. L. Taylor, W. Lin, *J. Am. Chem. Soc.* **2007**, 129, 9852-9853.
- [336] M. D. Rowe, D. H. Thamm, S. L. Kraft, S. G. Boyes, *Biomacromolecules* **2009**, 10, 983-993.
- [337] R. C. Huxford, J. Della Rocca, W. Lin, *Curr. Opin. Chem. Biol.* **2010**, 14, 262-268.
- [338] M. Vallet-Regí, F. Balas, D. Arcos, *Angew. Chem. Int. Ed.* **2007**, 46, 7548-7558.
- [339] R. C. Huxford, J. Della Rocca, W. Lin, *Curr. Opin. Chem. Biol.* **2010**, 14, 262-268.

- [340] S. Furukawa, K. Hirai, K. Nakagawa, Y. Takashima, R. Matsuda, T. Tsuruoka, M. Kondo, R. Haruki, D. Tanaka, H. Sakamoto, S. Shimomura, O. Sakata, S. Kitagawa, *Angew. Chem. Int. Ed.* **2009**, *48*, 1766-1770.
- [341] S. Furukawa, K. Hirai, Y. Takashima, K. Nakagawa, M. Kondo, T. Tsuruoka, O. Sakata, S. Kitagawa, *Chem. Commun.* **2009**, 5097-5099.
- [342] K. Hirai, S. Furukawa, M. Kondo, H. Uehara, O. Sakata, S. Kitagawa, *Angew. Chem. Int. Ed.* **2011**, *50*, 8057-8061.
- [343] K. Koh, A. G. Wong-Foy, A. J. Matzger, *Chem. Commun.* **2009**, 6162-6164.
- [344] J. Yao, D. Dong, D. Li, L. He, G. Xu, H. Wang, *Chem. Commun.* **2011**, *47*, 2559-2561.
- [345] L. Hertäg, H. Bux, J. Caro, C. Chmelik, T. Remsungnen, M. Knauth, S. Fritzsche, *J. Membr. Sci.* **2011**, *377*, 36-41.
- [346] T. D. Bennett, J.-C. Tan, S. A. Moggach, R. Galvelis, C. Mellot-Draznieks, B. A. Reisner, A. Thirumurugan, D. R. Allan, A. K. Cheetham, *Chem. Eur. J.* **2010**, *16*, 10684-10690.
- [347] W. Morris, C. J. Doonan, H. Furukawa, R. Banerjee, O. M. Yaghi, *J. Am. Chem. Soc.* **2008**, *130*, 12626-12627.
- [348] F. Millange, M. I. Medina, N. Guillou, G. Férey, K. M. Golden, R. I. Walton, *Angew. Chem. Int. Ed.* **2009**, *49*, 763-766.
- [349] D. Zacher, J. Liu, K. Huber, R. A. Fischer, *Chem. Commun.* **2009**, 1031-1033.
- [350] S. R. Venna, J. B. Jasinski, M. A. Carreon, *J. Am. Chem. Soc.* **2010**, *132*, 18030-18033.
- [351] P. Hartman, W. G. Perdok, *Acta Crystallogr. A* **1955**, *8*, 525-529.
- [352] A. J. Bard, L. R. Faulkner, *Electrochemical Methods: Fundamentals and Applications*, 2nd edition, Wiley: New York **2001**.

Curriculum vitae

Personal Data

<i>Name</i>	Erik Andreas Flügel
<i>Date of Birth:</i>	05. Februar 1985
<i>Place of Birth</i>	Munich
<i>Citizenship</i>	German

Education /Course of studies

	2004	Gymnasium München Moosach, Abitur in 2004
<i>University Education</i>	2005 –2009	Basic studies in chemistry and biochemistry, Ludwig- Maximilians Universität München
	2009	<i>Bachelor of Science (B.Sc.)</i>
	2009-2011	Graduate studies in chemistry, Ludwig-Maximilians Universität München
	2011	Master of Science (M. Sc.)
	Since 2011	PhD Student, Ludwig-Maximilians Universität München (Functional Nanostructures) and Max-Planck Institute for solid-state research in Stuttgart (Nanochemistry), supervisor: Prof. Bettina Lotsch

Publications

Published as Part of this Thesis

1. Surfactant-directed syntheses of mesostructured zinc imidazoles: formation mechanism and structural insights

E. A. Flügel, M. T. Aronson, S. C. Junggeburth, B. F. Chmelka and B. V. Lotsch, *CrystEngComm*, **2015**, 17, 463-470. - DOI: 10.1039/C4CE01512F

2. Homonuclear mixed-valent cobalt imidazolate framework for oxygen evolution electrocatalysis

E. A. Flügel, V. W.-h. Lau, H. Schlömer, R. Glaum and B. V. Lotsch, *Chem. Commun.*, **2015**, submitted

3. Synthetic routes toward MOF nanomorphologies

E. A. Flügel, A. Ranft, F. Haase and B. V. Lotsch, *J. Mater. Chem.*, **2012**, 22, 10119-10133.

Contributions to Conferences

Oral Presentations

From Porous Materials to Mesostructured Zinc Imidazoles

E. Flügel, S. C. Junggeburth, S. Hug, Max Plack Society, Ringberg 2012.

Poster Presentations

1. **Hierarchically structured imidazolate frameworks by supramolecular templating**

E. Flügel, S. Junggeburth and B. V. Lotsch, Advisory Board Meeting at the Max-Planck-Institute for solid-state research, Stuttgart, 2012.

2. **Mesostructured imidazolate frameworks**

E. Flügel and B. V. Lotsch, CeNS workshop, Venice, 2012.

3. **Towards hierarchically structured imidazolate frameworks**

E. Flügel, S. Junggeburth, H. Schlomberg, V. Duppel and B. V. Lotsch, Third International Conference on Multifunctional, Hybrid and Nanomaterials, Sorrento, 2013.